THERMAL HYDRAULIC DESIGN OF A 2400 MW_{th} DIRECT SUPERCRITICAL CO_2-COOLED FAST REACTOR

By

Michael A. Pope

B.S. Nuclear Engineering
Texas A&M University, 2002

S.M. Nuclear Engineering
Massachusetts Institute of Technology, 2004

SUBMITTED TO THE DEPARTMENT OF NUCLEAR SCIENCE AND ENGINEERING IN PARTIAL FULFILLMENT OF THE REQUIREMENTS FOR THE DEGREE OF

DOCTOR OF PHILOSOPHY IN NUCLEAR SCIENCE AND ENGINEERING
AT THE
MASSACHUSETTS INSTITUTE OF TECHNOLOGY

SEPTEMBER 2006

Signature of Author: _____
Department of Nuclear Science and Engineering
August 10, 2006

Certified by: _____
Michael J. Driscoll – Thesis Supervisor
Professor Emeritus of Nuclear Science and Engineering

Certified by: _____
Dr. Pavel Hejzlar – Thesis Reader
Principal Research Scientist

Accepted by: _____
Dr. Jeffrey A. Coderre
Chairman, Department Committee on Graduate Students

THERMAL HYDRAULIC DESIGN OF A 2400 MW_{th} DIRECT SUPERCRITICAL CO_2-COOLED FAST REACTOR

By

Michael A. Pope

Submitted to the Department of Nuclear Science and Engineering on August 10, 2006 in partial fulfillment of the requirements for the degree of Doctor of Philosophy in Nuclear Science and Engineering

Abstract

The gas cooled fast reactor (GFR) has received new attention as one of the basic concepts selected by the Generation-IV International Forum (GIF) for further investigation. Currently, the reference GFR is a helium-cooled direct cycle plant with core outlet temperatures in the 850°C to 1000°C range. Pursued in the interest of high cycle efficiency and the provision of process heat for hydrogen production by thermochemical water cracking, these high temperatures present materials challenges which may prove difficult to overcome in the near future. By taking advantage of the low compressibility of CO_2 near its critical point, the supercritical CO_2 (S-CO_2) recompression cycle can achieve an efficiency of 48% with a relatively low core outlet temperature of 650°C. The 4-loop 2400 MW_{th} direct S-CO_2 cooled fast reactor under investigation at MIT is thus a lower-temperature alternative to the mainstream helium cooled GFR design.

A steady state core design was developed which utilizes an innovative, high fuel volume fraction, vented Tube-In-Duct (TID) fuel assembly. Through an extensive series of iterative calculations, RELAP5-3D was then used to evaluate the natural circulation performance of an active/passive hybrid Shutdown/Emergency Cooling System (SCS/ECS). Routes were identified by which significant post-LOCA core bypass could occur and degrade the decay heat removal performance. Moderately-sized blowers were shown to be capable of overcoming even extreme core bypass routes. An active SCS/ECS was thus adopted for the reference design.

The loss of external load (LOEL) event is analyzed and a bypass valve scheme is recommended which prevents shaft overspeed and excessive core coolant mass flow rate. A large dry pressurized water reactor (PWR) containment building having a free volume of 70,000 m^3 and a peak design pressure of 6 bar is selected for this design based on a 100 in^2 cold duct break. During this same loss of coolant accident (LOCA), the depressurization time is shown to be in excess of 10 minutes. No action need be taken by the SCS/ECS blowers before this time in order to prevent core damage. After this time, a total blower power less than 90 kW is sufficient to cool the core out to 10,000 seconds. A loss of flow (LOF) transient in which a PCS loop is instantaneously isolated and no mitigating action is taken (i.e. no reactor scram) is also shown not to cause core damage.

It is concluded that a large S-CO_2 cooled GFR coupled to a supercritical Brayton power conversion system can withstand the thermal hydraulic challenges posed by the usual menu of severe accident scenarios.

Thesis Supervisor: Michael J. Driscoll
Title: Professor Emeritus of Nuclear Science and Engineering

Thesis Reader: Pavel Hejzlar
Title: Principal Research Scientist

Acknowledgements

I would first like to thank my advisor, Professor Emeritus Michael Driscoll, for his patient guidance in this project and throughout my time at MIT. His direction, ideas and vast knowledge have made this work possible. I feel very fortunate to be one of the many students over the years to call him an advisor.

I would also like to express my deepest gratitude to Dr. Pavel Hejzlar for his careful scrutiny of the technical content of my work and for his sharing of expertise in seemingly every aspect of nuclear science and engineering. His enthusiasm for his work is contagious and his presence has been invaluable to this and many other projects at MIT.

Chris Handwerk provided a great deal of support to this work through his reactor physics work related to the S-CO_2 GFR. In addition to his technical contributions, Chris has made a great collaborator and friend.

On behalf of myself and all involved in this project, I would like to thank Cliff Davis (INL) for his support in this effort. In addition to answering my questions related to the use of RELAP5-3D, Cliff spent many hours of his own time updating the RELAP code. The transient analyses presented in this thesis would not be possible without his tireless efforts.

Theron Marshall helped to facilitate my learning of the RELAP code by mentoring me during a summer internship at the Idaho National Laboratory, for which I am grateful. Theron also arranged for partial financial support of one of my semesters at MIT.

Jan Outcalt and Richard St. Clair made some of the figures used in this work. For this I am grateful to them.

Finally, I'd like to thank my parents for their support and encouragement throughout my entire education. No amount of success in my life would be possible if not for them.

Table of Contents

List of Figures

List of Tables

1 Introduction

1.1 Motivation

In order to satisfy the growing world demand for energy in the coming decades while limiting greenhouse gas emissions, nuclear energy must play a significant role. Currently, 438 nuclear plants generate 16% of the world's electricity. As the world population grows along with per capita demand for energy, a larger fraction of energy should be produced from nuclear and other emission-free sources in order to reduce the impact of global climate change. It is also desirable to develop the technology to use nuclear energy for applications other than production of electricity such as water desalinization and hydrogen production. Recognizing the need for a new generation of nuclear plants which would be able to satisfy the demand for energy in a safe, clean and economically competitive way, the Generation-IV (Gen-IV) International Forum (GIF) selected six basic concepts for further development for deployment by 2030. This would coincide with a time when many operating plants are near the end of their licensed life. [U.S. DOE, 2002]

Studied extensively in the 1960-1980 time frame, Gas-cooled Fast Reactors (GFRs) have received new attention since their selection by the GIF as one of the six Gen-IV concepts for further development. Although never built, the most mature design of a GFR to date was developed by General Atomics (GA); the concept was called a GCFR during that time. European and British versions were also developed concurrently. The reference GA GCFR had an indirect cycle with a helium primary coolant system and the secondary coolant system was a steam Rankine power cycle. [General Atomic Company, 1980] Since then, GFRs (and thermal spectrum gas cooled reactors) with direct helium Brayton cycles having peak temperatures between 800°C and 1000°C have been pursued in order to achieve high

thermodynamic efficiency and to provide high-temperature process heat for hydrogen production by thermochemical water splitting. [Garnier, et. al., 2003] [Chauvin, et. al., 2003] These temperatures present materials challenges which may prove difficult to overcome in the near future. An alternative to this cycle is the supercritical CO_2 (S-CO_2) cycle. Taking advantage of the low compressibility of CO_2 near its critical point, the S-CO_2 cycle can achieve high efficiencies with much lower temperatures than the helium cycles. This is done with compact and relatively simple power conversion systems.

This work is part of an ongoing research project at MIT with the objective of developing an optimized and competitive design for a 2400 MW_{th} direct S-CO_2 cooled GFR. This concept has a number of characteristics which make it a promising candidate for deployment as a Gen-IV design, several of which are discussed later in Section 1.5 within the framework of the GIF goals. A need for detailed design and analysis exists, however, in order to further assess its potential as a Gen-IV design, which is the purpose of this and related project tasks at MIT.

1.2 Objectives and Contributions of this Work

In general, the objective of this work is to contribute to the design process from the standpoint of thermal-hydraulics. This includes design of the reactor core and other reactor vessel internals, design and analysis of the Shutdown/Emergency Cooling System (SCS/ECS) and analysis of the performance of the plant under various accident conditions, primarily Loss Of Coolant Accidents (LOCAs), using RELAP5-3D. It is widely recognized that decay heat removal under all plausible situations is the principal challenge in GFR design because of the unavoidably high core power density and low heat capacity of the coolant. Design of the reactor core was performed in collaboration with C.S. Handwerk (MIT), who provided reactor physics analysis in support of this effort.

The primary contributions of this work are:

- The development of a core design (in collaboration with Handwerk) for a 2400 MW_{th} direct S-CO_2 cooled GFR coupled to a supercritical CO_2 recompression cycle.

- Characterization of the effects of post LOCA coolant bypass on both natural circulation and forced circulation cooling.
- Development of a basic design for an active Shutdown/Emergency Cooling System (SCS/ECS).
- A recommended arrangement of bypass valves which can be used to mitigate the effects of the Loss of External Load (LOEL) event.
- Evaluation of the performance of the design during a simulated LOCA.
- Estimation of the required emergency blower power.
- Development of working RELAP models of the GFR plant for future contributors to use for thermal-hydraulic simulations.
- Identification of areas in need of further analysis and/or refinement of the design.

1.3 Supercritical CO_2 Recompression cycle

In Brayton cycles operating well above the critical point of the working fluid, such as helium Brayton cycles, the compressor work (or "backwork") is a significant fraction of the turbine work. This is due to the compressibility of an ideal gas and the high volumetric flow rate in gas cycles. The very high temperatures in the 800°C-1000°C range at the turbine inlet which are being pursued for helium Brayton cycles are necessary in order to achieve high efficiencies with working fluids that behave as an ideal gas. These high temperatures introduce a number of materials challenges which will be difficult to resolve. Supercritical-CO_2 (S-CO_2) cycles take advantage of the non-ideal properties of CO_2 near its critical point. The temperature and pressure at the inlet to the compression stage in the S-CO_2 cycle are cooled to just above the critical point, where the fluid is very dense and its compressibility is very low. The effect of this is that the compressor work is a much smaller fraction of the turbine work in S-CO_2 cycles than in typical helium Brayton cycles. This allows high thermodynamic efficiency at significantly lower temperatures.

Though several variations exist on the S-CO_2 cycle, the recompression cycle was selected as the most promising S-CO_2 cycle for Gen-IV service and optimization of the cycle was performed in previous work at MIT. [Dostal, et. al., 2004] [Dostal, et. al., 2006] [Dostal (b), et. al., 2006] The general layout of the cycle is shown in Figure 1.1 and the cycle statepoints are given in Table 1-1. This table includes temperatures and pressures at the statepoints of both the reference design, which is the primary focus of this work, and a lower-temperature "fallback" design. The reference design has a peak temperature of 650°C and a main compressor inlet temperature of 32°C. In case a more conservative turbine inlet (core outlet) temperature is desired in later work, the fallback design has a peak temperature of 550°C. Table 1-2 gives other parameters of interest for both the reference and the fallback power cycles. In this thesis, the reference power cycle is always assumed unless otherwise specified.

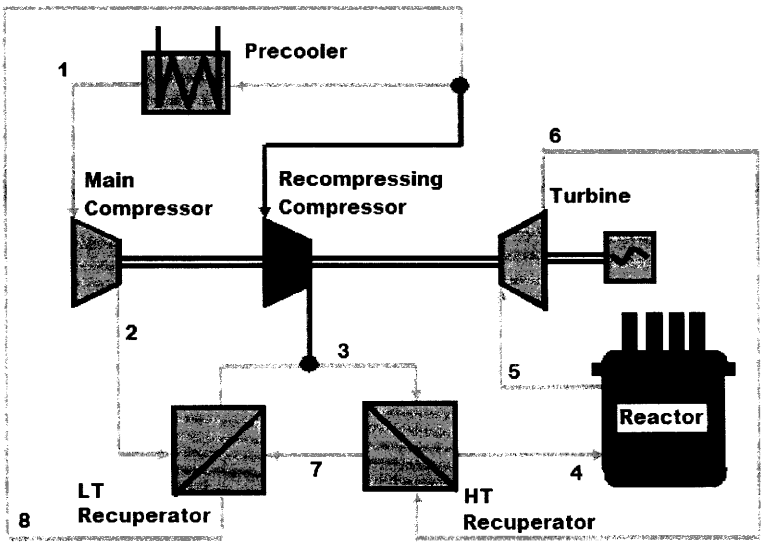

Figure 1.1. Layout of S-CO_2 recompression cycle. [from Dostal, et. al., 2004]

In the recompression cycle, S-CO_2 turbine exhaust flows through the hot sides of the high and low temperature recuperators, then encounters a split in the flow. At this point, some of the flow (42% in this design) is diverted to the recompressing compressor while the remainder is cooled to very close to the critical point in the precooler by counter-flow with a water stream. The critical point of CO_2 is at a pressure of 7.38 MPa, temperature of 31°C

and a fluid density of 467.6 kg/m^3. At the inlet to the main compressor, the fluid temperature and pressure are 7.69 MPa and 32°C, respectively. At these compressor inlet conditions, the density of the fluid is approximately 600 kg/m^3 and the compressibility is very low; the main compressor takes the pressure from 7.69 MPa to about 20 MPa while only increasing the density to 720 kg/m^3. This requires very little work compared to ideal gas compression, making the cycle quite efficient. Flow from the outlet of the main compressor is heated in the low temperature recuperator and then it mixes with the flow from the outlet of the recompressing compressor (this latter device is needed to avoid having temperature pinch point in the recuperator). The fluid is then heated in the high temperature recuperator before returning to the heat source. Both compressors and the turbine are on a single shaft and are much more compact than those for helium, reducing capital cost significantly. The absence of intercoolers is also a capital cost-reducing advantage of this cycle over helium cycles.

Table 1-1. Optimized power cycle statepoints of reference and fallback power cycles.

Statepoint*	Reference Design		Fallback Design	
	Pressure (MPa)	Temperature (°C)	Pressure (MPa)	Temperature (°C)
1	7.69	32.0	7.69	32.0
2	20.0	60.9	20.0	61.1
3	19.99	159.1	19.76	159.1
4	19.95	485.5	19.09	417.0
5	19.45	650.0	18.59	550.0
6	7.93	529.9	8.44	454.9
7	7.82	167.3	8.00	164.9
8	7.71	70.9	7.75	72.9

Table 1-2. Other power cycle parameters for reference and fallback designs.

Parameter	Reference Design	Fallback Design
Total mass flow rate (kg/s)	11,708	14,568
Core Thermal Power (MW_{th})	2400	2400
Recompressed fraction (%)	42.0	45.2
Thermodynamic efficiency (%)	50.8	45.3

* Statepoint numbers refer to labels in Figure 1.1.

1.4 Heatric® Printed Circuit Heat Exchangers

In previous work, Printed Circuit Heat Exchangers (PCHE's) were identified as ideal candidates for use as recuperators and precoolers in the S-CO_2 recompression cycle. A major advantage of the S-CO_2 cycle is its compactness, a feature which would not be retained if large shell-and-tube heat exchangers were used for recuperators and precoolers. For a shell and tube heat exchanger to be made sufficiently compact, the required tube diameters would be very small, especially for recuperators where the supercritical fluid is more gas-like and heat transfer coefficients are low. Furthermore, the pressure difference across the recuperators is large (in excess of 12 MPa), thus the tubes would have to be quite thick. Therefore, classical shell and tube heat exchangers are not well suited for use as recuperators and precoolers in this design and they were discarded in favor of compact heat exchangers. The two types of compact heat exchangers that were considered are plate and fin and PCHE's. Though sufficiently compact and highly effective, plate and fin heat exchangers were discarded due to their inability to withstand the pressure difference required of them in this design without excessively large parting plate thicknesses. PCHE's were thus selected for use in this power cycle. A more detailed summary of this downselection process can be found in [Dostal, et. al., 2004].

Heatric® PCHE's are robust heat exchangers which combine compactness, low pressure drop, high effectiveness and the ability to operate with a very large pressure differential between hot and cold sides. They are constructed by chemically etching small semicircular channels into plates as shown in Figure 1.2(a). Plates are then stacked alternating between hot and cold side as shown in Figure 1.2(b), then diffusion bonded together to form a monolithic heat exchanger core. Figure 1.2(c) shows a photomicrograph of a cross section of three hot and three cold channels after bonding. [a), b) and c) are from www.heatric.com] In this design, the precoolers and recuperators have flow channels with 2 mm semicircular diameters. The design of the precooler and recuperator headers and their arrangement within the PCS loops is not addressed in this work. A comprehensive analysis of Heatric® PCHE's, albeit for use as intermediate heat exchangers in an indirect cycle GFR, can be found in [Gezelius, et. al., 2004]. In the present context, heat exchanger type is important because of their energy storage during transients and their pressure drop.

Decay heat removal heat exchangers in the SCS/ECS will be assumed during this work to be Heatric® PCHE's with flow channels having semicircular diameter of 5 mm, but in future work, plate fin heat exchangers may be analyzed for potential use.

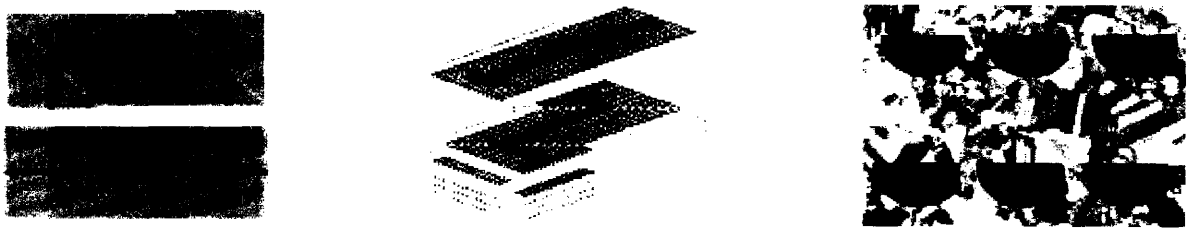

(a) (b) (c)

Figure 1.2. Heatric Printed Circuit Heat Exchangers. [from www.heatric.com]

1.5 Achieving GIF Goals with a 2400 MW_{th} Direct S-CO_2 Cooled GFR

This section describes some of the ways in which the 2400 MW_{th} direct S-CO_2 cooled GFR design is well suited for Gen-IV service from the standpoint of satisfying the goals of the GIF. The emphases embodied in these goals, summarized by [Driscoll, et. al., 2005] are sustainability, safety and economics.

Sustainability goals as defined by the GIF include high utilization of natural uranium resources, waste minimization and avoidance of proliferation of nuclear weapons. The fast neutron spectrum and high target burnup of 120 MWd/kg in this design provide high resource utilization. In GFR designs in the past, fertile blankets had been specified in order to achieve this high utilization, but in order to make this plant more proliferation resistant, fertile blankets are not specified, greatly reducing the amount of weapons-usable plutonium produced. The S-CO_2 GFR core is also designed to be capable of burning transuranics (TRU) including minor actinides, reducing the long-term radiotoxicity and thus the waste burden of the fuel cycle.

Gen-IV concepts are also expected to provide greater safety and reliability than present-day reactors. The GFR project at MIT includes PRA-guided design of safety

systems. In this thesis, two variations of an SCS/ECS are evaluated for post-LOCA decay heat removal; one is an active/passive hybrid design and the other relies on active cooling. Both consist of 200% cooling capability in a 4x50% (2 out of 4) arrangement of coolant loops, which has performed well in PRA analyses [Jourdan, et. al., 2004]. Also relevant to the safety of the system are the concurrent efforts at MIT to reduce the coolant void reactivity* of the core by use of BeO diluent in the fuel and by integrating a S-CO_2 radial reflector volume which provides enhanced leakage upon coolant voiding. [Handwerk, et. al., 2006] The target void reactivity sought in these efforts is zero or negative.

Gen-IV plants must also be economically favorable compared to other (non-nuclear) energy sources without greater financial risk. In present-day light water reactors (LWRs), 60% of the electricity generation cost results from the capital cost of the building the plant. [Hejzlar, et. al., 2006] Therefore, reduction of capital cost is a major objective in making a Gen-IV reactor economically competitive. The relatively large thermal power of 2400 MW_{th} pursued in this design takes advantage of economies of scale. Also, the S-CO_2 recompression cycle is very compact and simple with a single shaft (per power conversion system loop) and no intercoolers, which provides a significant reduction in capital cost, in particular due to its suitability for modular construction in a factory setting. Selection of a direct cycle rather than an indirect reduces capital cost by eliminating the need for intermediate heat exchangers (IHXs). This reduction in capital cost reduces the overall risk of the investment and decreases the electricity generation cost. The high efficiency of the S-CO_2 cycle decreases electricity cost, as does the added efficiency from using a direct cycle rather than an indirect one. The use of a direct cycle in the subject design is an important attribute, which, as will be shown, has an important impact on transient performance and accident scenarios.

Though not specified as one of the goals of the Gen-IV program listed above, the capability of the GFR system to provide energy for efficient hydrogen production is desirable. The most common approach among designers of the gas-cooled Gen-IV plants is

---

* Not to be confused with the definition of void reactivity used in analyzing a core with two-phase coolant, void reactivity as defined in this work refers to the reactivity insertion by complete instantaneous depressurization.

to use core outlet temperatures in the 800-1000°C range for thermochemical water splitting. The lower temperatures in the MIT design preclude this hydrogen production process, but high temperature steam electrolysis (HTSE) has been shown to be a highly efficient means of hydrogen production when coupled to the S-CO_2 cycle. [Yildiz, et. al., 2006]

1.6 Potential Accidents and Transients

The array of events which can disrupt a nuclear power plant from steady state operation is wide, as is their range of severity and frequency. At this stage in design, it is useful to list the potential events which will need to be evaluated. Table 1-3 shows a list of potential transients and accidents along with a brief description and comments on the applicability to the GFR design under investigation in this work. Transients involved in ordinary operation of the plant such as startup, shutdown and slow power ramps are not included in this and will not be addressed in this thesis. Clearly the direct cycle impacts the nature of the transients and accidents as does the parallel arrangement of the four PCS loops. Although most, if not all, of the accidents and transients listed in Table 1-3 will need to be analyzed eventually as this design matures, three were selected for analysis in this work due to either their severity or their occurrence during other transients and accidents. Those selected for analysis here are the Loss of external Load (LOEL), the Loss of Coolant Accident (LOCA) and the Loss of Flow (LOF). The following paragraphs briefly describe each of these and discuss their application to the S-CO_2 cooled GFR.

LOEL – In this transient, the generator becomes decoupled from the electrical grid. This removes the large negative torque on the generator causing rapid acceleration of the shaft. Fast-acting bypass valves are used in order to prevent shaft overspeed and damage to turbomachinery. Because the turbomachinery is smaller in gas cycles than that of steam Rankine cycles, this transient is particularly challenging due to the small moments of inertia of components attached to the shafts. S-CO_2 turbomachinery is even smaller still than helium turbomachinery and so the LOEL transient is even more challenging still in this design.

LOCA – This is a breach in the primary system through which coolant inventory escapes into the containment volume. Part of the design basis accident in present-day LWRs,

this is generally considered to be the most severe accident in gas-cooled reactors as well. The LOCA creates a particular challenge in a gas-cooled reactor because of the fast depressurization rate of the gas coolant versus liquid. Selection of break size is a major consideration affecting the severity of the accident. In the GCFR design by GA, a break size of 100 in^2 (645 cm^2) was selected as being a conservatively large break. [General Atomics Company, 1980] Based on this precedent, a 100 in^2 break size is analyzed in this work. * Smaller break sizes are typically analyzed as well in order to capture the effects of ruptures in smaller pipes or instrumentation lines, but these will be left for future work in this design.

In the 4-loop direct S-CO_2 GFR, isolation valves are used to seal off the individual PCS loop responsible for the LOCA, preserving the coolant inventory. For the analyses performed in this work, those valves are assumed not to have functioned and the system is allowed to blow down to equilibrium with the containment. The case where the isolation valve does function in the event of a faulted PCS is captured by the LOF transient.

LOF – In general, an LOF transient is a sudden loss of coolant flow in the core such that the power/flow ratio increases and the core heats up unless some action is taken. In water-cooled reactors, LOF transients can be initiated by circulating pump failures of various kinds. In the S-CO_2 direct cycle where turbomachinery is on a single shaft, an LOF could occur as a result of damage to a compressor or a shaft seizure.

In the 4-loop arrangement of the GFR under investigation here, isolation valves will be used in order to seal individual PCS loops in case of a serious fault. For example, in the case of a LOCA in one of the PCS loops, the isolation valves to that loop should close immediately upon its detection, suddenly decreasing core flow by 25%. After the isolation of the PCS loop, the rest of the system will function independent of it. Isolation valve closure could also be initiated inadvertently even if no PCS loops are faulted. In this case, the analysis does not change significantly from that of a small break LOCA or other fault in which the response of the system is relatively slow. Therefore, isolation valve closure alone

---

* Although SI units are preferable for this (or virtually any) scientific publication, use of square inches in the designation of the size of a pipe break has taken deep root in the parlance of nuclear power plant safety analysis. These units will therefore be used in the discussion of the LOCA in this report.

envelopes other transients involving faults in PCS loops so long as the valves function as designed.

Table 1-3. Potential accidents and transients in the direct S-CO_2 cooled GFR.

Name (acronym)	Description	Comments
Loss of Coolant Accident (LOCA)	Break in piping or instrumentation line causes loss of coolant inventory	Considered the most severe accident. Break sizes analyzed for gas reactors typically range from 10 in^2 (64.5 cm^2) to 100 in^2 (645 cm^2) in cold leg. Isolation valves on PCS ducts mitigate this accident.
Loss of External Load (LOEL)	Generator is decoupled from grid and shaft speed increases rapidly.	Fast-acting bypass valves used to avoid shaft overspeed and turbomachinery damage.
Loss of Heat Sink (LOHS)	Heat rejection to ultimate heat sink is lost.	In the direct S-CO_2 cooled GFR, this would be loss of heat rejection in precoolers due to a loss or decrease of water-side flow in one or all PCS loops.
Loss of Flow (LOF)	Sudden decrease of coolant flow due to loss of compressor function or PCS isolation valve closure.	In the direct S-CO_2 cooled GFR, the LOF may be due to a compressor failure. PCS isolation valve closure comprises a rapid 25% LOF. This could be inadvertent or in response to a PCS loop failure (e.g. LOCA).
Transient Overpower (TOP)	Event which increases the reactor power above 100%, such as an unexpected control rod withdrawal.	Dependent on reactor physics parameters such as Doppler and void coefficients. These types of events are left for future work.
Anticipated Transient Without Scram (ATWS)	A reactor event occurs and a system which provides the means to shut down the reactor fails.	Several different events occurring without scram could fall under the ATWS designation (e.g. control rod withdrawal, LOEL, LOF, TOP, LOHS)

1.7 Selected Previous Work at MIT

As is the case with most projects of this nature, a great deal of progress had been made by other contributors before the work described in this thesis commenced. Aside from the work mentioned in the previous sections related to the selection and optimization of the S-CO_2 recompression cycle and the investigation of Heatric® PCHE's, the following other contributions have provided a prerequisite knowledge base for this work in a direct way:

- At the outset of this work, significant previous progress had been made by P. Hejzlar and W.C. Williams [see Williams, et. al., 2004] on the design of an active/passive hybrid SCS/ECS system as part of an International Nuclear Energy Research Initiative (INERI). This work was performed in collaboration with Argonne National Laboratory (ANL) and the French Commissariat à l'Energie Atomique (CEA). In the present work, the SCS/ECS system is redesigned somewhat to rely on active cooling, but it remains based largely on the pre-existing hybrid design.

- In studies performed by [Handwerk, et. al., 2006], the use of BeO as diluent in oxide fuel was recommended for this application. This diluent is assumed in the estimation of thermal conductivity in this work. The concept of a S-CO_2 radial reflector used in this work also comes from the above reference. His work also established the core power shapes and power peaking factors needed for thermal-hydraulic analyses.

- Performance curves for turbines and axial compressors were developed at MIT by [Wang, et. al., 2004]. Although the axial compressors will later be discarded in favor of radial compressors, these curves will be used in the modeling of the GFR plant in this work.

1.8 Organization of this Thesis

Chapter 2 gives the motivation for and a description of an innovative vented Tube-In-Duct (TID) fuel assembly.

Chapter 3 discusses the selection of the fuel form for this design. The benefits of using BeO diluent are discussed and the question of whether to use pellets or vibrationally compacted fuel is addressed.

Chapter 4 describes the methodology used in the preliminary studies aimed at determining the set of core parameters which meet design requirements. Correlations used in calculating form and frictional losses are given along with heat transfer coefficients. Assumptions made in the calculation of the temperature rise across the cladding, fuel and fuel-clad gap are presented. An estimate of the thermal conductivity of the specified fuel is also developed in this chapter.

Chapter 5 gives the results of the preliminary analysis of core parameters and provides recommended lattice parameters based on calculations accounting for two channel types with no bypass. The potential for heat transfer augmentation and coolant channel orificing is also discussed. The impact of a lower-temperature power cycle on the design of the core is investigated.

Chapter 6 develops a more realistic core design including sizing and arrangement of fuel assemblies in the core. Flow between TID fuel assemblies is accounted for and an estimate of the heating rate through duct walls is made. The S-CO_2 radial reflector is introduced and cooling of radial shielding assemblies is considered. Selection of the reactor vessel type is also discussed and its key dimensions are given.

Chapter 7 gives results of a steady state evaluation of the post-LOCA performance of an active/passive hybrid Shutdown/Emergency Cooling System (SCS/ECS). The RELAP model used for this analysis is discussed, but because the model would be significantly changed in later work, detailed description is withheld until Chapter 9. The post-LOCA performance is evaluated and several parametric studies are performed to quantify the effects of channel roughening, grid spacers, and bypass through PCS loops or pipe breaks.

Chapter 8 describes an active version of the SCS/ECS design from Chapter 7. This was pursued based on the results of analyses reported in Chapter 7. Details on heat exchanger design and placement inside the reactor vessel are given.

Chapter 9 presents a description of the RELAP model used to simulate the GFR plant in the remainder of this work.

Chapter 10 maps the demand for active cooling using the RELAP model described in Chapter 9 under steady state conditions.

Chapter 11 investigates methods for mitigation of the Loss of External Load (LOEL) event. Different locations for bypass valves are evaluated and a recommended scheme is presented which performs well for an LOEL event starting from steady state full power conditions.

Chapter 12 analyzes several LOCA events of varying break size and evaluates the measures which must be taken in order to prevent core melting and the delay which is allowable before such measures are taken.

Chapter 13 summarizes the findings of this work and identifies several areas where future work is needed.

2 Vented Tube-In-Duct Fuel Assemblies

2.1 Introduction

This design presents a unique set of neutronic, chemical, and thermal-hydraulic conditions. In order to satisfy the goals of this design, an innovative vented Tube-In-Duct (TID) fuel assembly was conceptualized. This chapter outlines the motivation for this design. This explanation progresses from the motivation for high fuel volume fraction to the benefits of inverted fuel geometry over pins. The reasoning for discarding block-type matrix fuel elements is then presented followed by a description of the TID fuel assembly concept. Appendix C contains a preliminary manufacturing sequence for the vented TID assembly.

2.2 Motivation for High Fuel Volume Fraction

There are several drivers for the use of a high fuel volume fraction in this design. Fast reactors are typically designed with a conversion ratio greater than unity in order to achieve attractive natural uranium resource utilization. Fertile blankets were typically implemented in order to achieve this, a practice which produces significant amounts of plutonium with high ^{239}Pu content. This plutonium could potentially be used to make nuclear weapons, and thus fertile blankets are now seen as an excessive proliferation risk. Because this design does not use fertile blankets, a higher fuel volume fraction is necessary to boost the internal conversion ratio and to increase the reactivity-limited burnup.

It is also desirable to have fuel which is chemically stable in CO_2 at 650°C. Carbide and nitride fuels, favorable neutronically due to their high heavy metal densities, are not chemically stable in CO_2 at the temperatures of interest. Therefore, the fuel form of choice is oxide. The disadvantage of the low heavy metal density of oxide fuel is also overcome by

use of high fuel volume fraction. Since fast reactors typically have positive coolant void reactivity, low coolant volume fraction (thus high fuel volume fraction) is desirable from a safety standpoint as well. High fuel volume fraction also gives a higher thermal inertia which helps to withstand power excursions. A coolant volume fraction of ~25% has been set as a constraint for this design with a goal in mind of achieving a coolant void reactivity that is less than $1 assuming an instantaneous and complete depressurization.

2.3 Thermal-Hydraulic Benefits of Inverted Fuel Geometry over Pins

The constraint of 25% coolant in the core presents a challenge in designing a core with sufficiently low cladding and fuel temperatures without incurring a prohibitively high pressure drop. Significant thermal-hydraulic advantages can be gained by using "inverted" fuel rather than the more conventional pin-type fuel used in most nuclear reactors. In this work, the concept of "inverted" fuel refers to a geometry in which fuel resides not inside cylindrical pins with coolant outside, but rather surrounding cylindrical coolant channels. An example of inverted fuel geometry is the prismatic block-type fuel specified in the design of the High Temperature Gas Reactor (HTGR).

If we consider a hexagonal lattice of fuel pins and neglect cladding (i.e. only fuel and coolant are present), it can be shown that for constant fuel conductivity and power density the temperature rise across the fuel is related to fuel volume fraction by; [Hankel, 1960]

$$\left[\frac{16k_f}{sp\cdot\rho_{HM}\cdot D_e}\right]\Delta T_{f,pin}=\left(\frac{v_f}{1-v_f}\right)^2 \qquad \textbf{(2-1)}$$

where k_f is fuel thermal conductivity, sp is specific power, ρ_{HM} is heavy metal density, D_e is equivalent (hydraulic) diameter, $\Delta T_{f,pin}$ is the temperature rise across the fuel in the pin arrangement and v_f is the fuel volume fraction. For an inverted fuel arrangement, having a hexagonal array of coolant channels in fuel and again neglecting cladding, the temperature rise across the fuel is related to the fuel volume fraction by; [Hankel, 1960]

$$\left[\frac{16k_f}{sp\cdot\rho_{HM}\cdot D_e}\right]\Delta T_{f,inv}=\frac{-\ln\left(1-v_f\right)-v_f}{1-v_f} \tag{2-2}$$

where $\Delta T_{f,inv}$ is the temperature rise across the fuel in the inverted fuel arrangement. To compare a pin and inverted arrangement, we assume that both cases have the same power density, fuel volume fraction and constant fuel conductivity. Setting the hydraulic diameter constant between the two geometries allows comparison on the basis of the same pressure drop across the core since the flow areas are also the same. Under these constraints, the parts of Equations 3-1 and 3-2 in square brackets are equivalent and the ratio of fuel temperature rise in pins to that in inverted fuel is given by;

$$\frac{\Delta T_{f,pin}}{\Delta T_{f,inv}}=\frac{v_f^2}{\left[-\ln\left(1-v_f\right)-v_f\right]\left(1-v_f\right)} \tag{2-3}$$

which is plotted in Figure 2.1 over a range of fuel volume fractions encompassing all reasonable values. This shows that for a given pressure drop, coolant volume fraction and power density, the maximum fuel temperature will be much higher in pins than in inverted fuel. Furthermore, for the same pressure drop, the fuel temperature benefit of inverted geometry over pins increases at an increasing rate as the fuel volume fraction is increased.

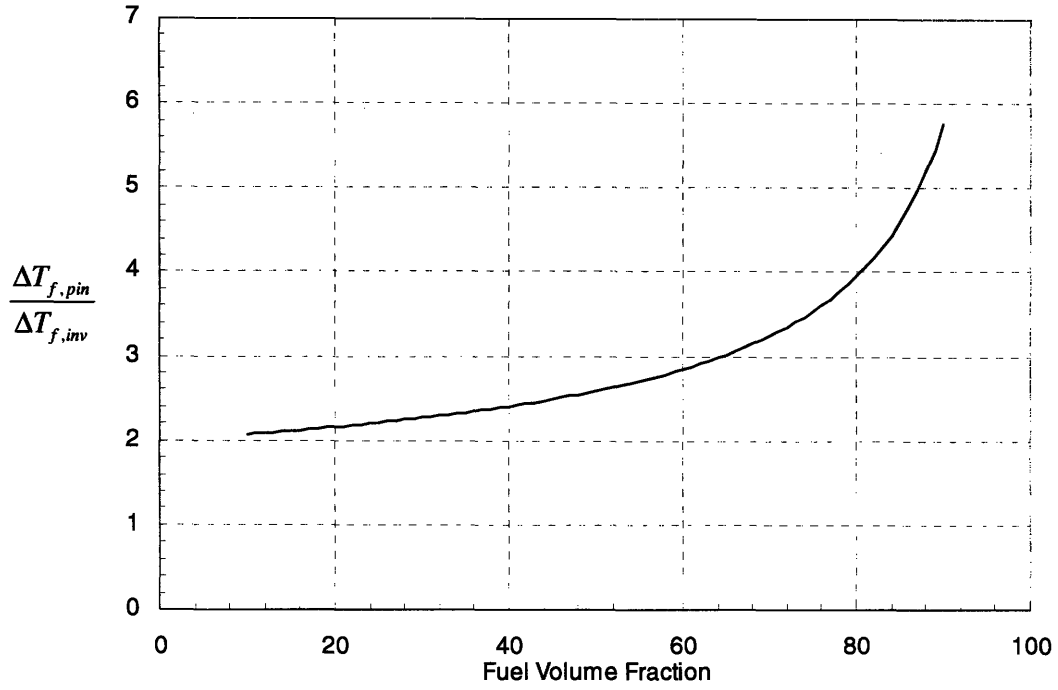

Figure 2.1. Ratio of fuel temperature rise in pins to inverted fuel with the same pressure drop.

In inverted fuel with a hexagonal array of channels, the coolant volume fraction is related to the channel pitch and diameter by;

$$v_c = \frac{\pi\sqrt{3}}{6\left(P_{chan}/D_{chan}\right)^2} \tag{2-4}$$

where v_c is the coolant volume fraction, P_{chan} is the coolant channel pitch and D_{chan} is the coolant channel diameter. A coolant volume fraction of 25% gives a P_{chan}/D_{chan} of 1.905. Because the coolant flow area consists of round channels, the equivalent (hydraulic) diameter in the inverted fuel is simply the coolant channel diameter, D_{chan}. In a hexagonal array of fuel pins, the coolant volume fraction is given by;

$$v_c = 1 - \frac{\pi\sqrt{3}}{6\left(P_{pin}/D_{pin}\right)^2} \tag{2-5}$$

where P_{pin} is the fuel pin pitch and D_{pin} is the fuel pin diameter. A coolant volume fraction of 25% in this case yields a P_{pin}/D_{pin} of 1.100. The hydraulic diameter of a hexagonal array of fuel pins is related to its lattice parameters by;

$$D_{e,pin} = D_{pin}\left(\frac{2\sqrt{3}}{\pi}\left(P_{pin}/D_{pin}\right)^2 - 1\right) \tag{2-6}$$

where $D_{e,pin}$ is the equivalent (hydraulic) diameter of the array of fuel pins. In order to compare the pin and inverted fuel types on the basis of constant pressure drop, we set the coolant volume fractions of each to 25%. This gives the pitch-to-diameter ratios mentioned above for each geometry. The hydraulic diameters are then set equal, which gives the following relationship;

$$D_{chan} = D_{pin}\left(\frac{2\sqrt{3}}{\pi}\left(P_{pin}/D_{pin}\right)^2 - 1\right) \tag{2-7}$$

If the value of 1.100 calculated above for P_{pin}/D_{pin} is substituted into Equation 3-7, one finds that for 25% coolant fraction and equivalent hydraulic diameters between the two geometries, the fuel pin diameter is equal to about 3 times the coolant channel diameter in the inverted fuel. As will be seen, this leads to consideration of small TID coolant channels. Figure 2.2 shows a schematic of an inverted fuel lattice (left) and a pin-type lattice (right) having the same coolant volume fraction and hydraulic diameter. Because the total wetted perimeter (which in these cases is equal to the heated perimeter) is the same in both of these lattices, the surface heat flux is the same and so the clad temperatures are nearly equal between the two geometry types. Because the fuel pin diameter is so large, the number of pins is small and thus the linear power of each pin is large. This leads to the high fuel temperatures in the pin core. In order to lower the fuel temperature in the pin core, the fuel pin diameter would have to be decreased while preserving the pitch-to-diameter ratio. This would increase the wetted perimeter, and then the pressure drop would exceed the inverted fuel geometry value.

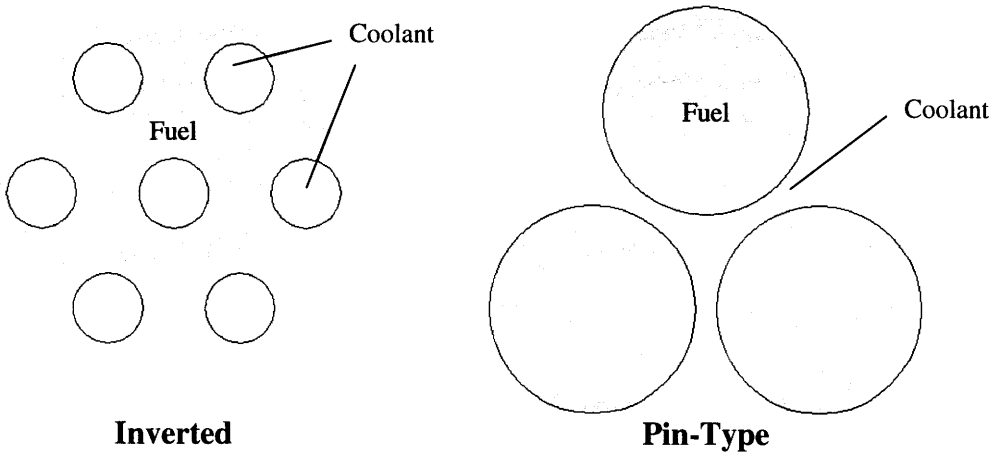

Figure 2.2. Inverted and pin-type fuel lattices having equivalent coolant volume fraction and hydraulic diameter.

It follows from these inherent characteristics that a given fuel temperature limit can be met using an inverted arrangement with a much lower pressure drop than in pin-type fuel. Inverted fuel also eliminates the need for grid spacers, which are a significant source of pressure losses in pin cores. These avoided pressure drops then become available in the clad and fuel temperature reduction tradeoff process.

2.4 Consideration of Matrix Fuel Forms

Matrix fuel forms are essentially blocks of structural material having fuel dispersed within. Fuel exclusion zones surrounding coolant channels provide a buffer between coolant and fuel. Matrix fuels may consist of ceramic fuel and matrix (cer-cer), ceramic fuel and metallic matrix (cer-met) or both metallic fuel and matrix (met-met). In early work by [Kaufmann, 1962], it was recommended that no more than 30% fuel by volume be used in matrix fuel so that it retains structural integrity during burnup. Previous studies at MIT concluded that in order to achieve sufficiently high burnup in a fast reactor using $(U,Pu)O_2$ fuel and no fertile blankets, greater than 60% fuel by volume was necessary, thus precluding the use of matrix fuels in this design. [Pope, et. al., 2004]

2.5 Tube-In-Duct Fuel Assembly Concept

In order to achieve high fuel volume fraction with inverted-geometry fuel elements which would not be corroded excessively by hot CO_2 and maintain structural integrity with burnup, a Tube-In-Duct (TID) fuel assembly was conceptualized. TID fuel assemblies consist of a hexagonal duct with coolant tubes inside. Fuel would be placed around coolant tubes and inside the hexagonal duct. Figure 2.3 shows a horizontal cross-sectional view of a TID fuel assembly. Figure 2.4 shows a vertical cross-sectional view of a TID fuel assembly with some of its features sketched schematically. This figure shows only one coolant tube whereas there actually would be many per assembly as is shown in Figure 2.3. Axial reflector and shielding material are placed at the top and bottom of the assembly inside the same cell volume envelope as the fuel. Coolant enters the assembly from the bottom through a debris filter and flows into the coolant channels. Because some of the heat generated in the assembly will be transferred through the outer duct wall, a fraction of flow is diverted just before the coolant channels through holes in the duct wall to the outside of the duct. This flow between adjacent assemblies is addressed in a later chapter.

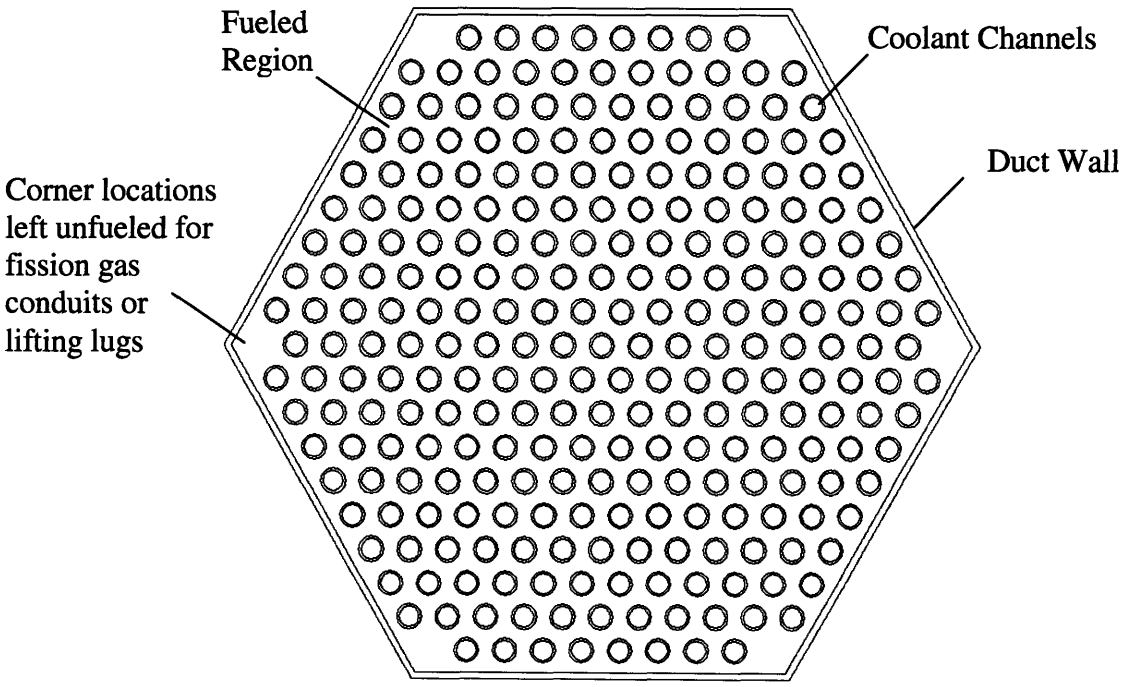

Figure 2.3. Horizontal cross-section view of TID fuel assembly.

2.6 Venting System for TID Fuel

Since the duct wall and the coolant tubes (cladding) are susceptible to pressure induced creep, the fueled region is vented to an offgas system to reduce wall stresses during steady state and LOCA conditions. A venting system similar to this was specified in the design of the General Atomics pin-type GCFR of the 1970's. [Capana, et. al., 1974] Vented fuel was also evaluated favorably for LMFBR service [O'Neill, et. al., 1965] and was used successfully on the Peach Bottom HTGR. [de Hoffmann, et. al., 1965]

As shown in Figure 2.4, fission gases which diffuse through the fuel and upper reflector encounter an absorber region which increases the holdup of fission products. A small plenum at the top of the assembly allows the fuel volume to communicate with fission gas conduits. These conduits lead fission gases to a debris trap and then to a "flower-holder" type lower plate, the center plenum of which leads to the offgas system.

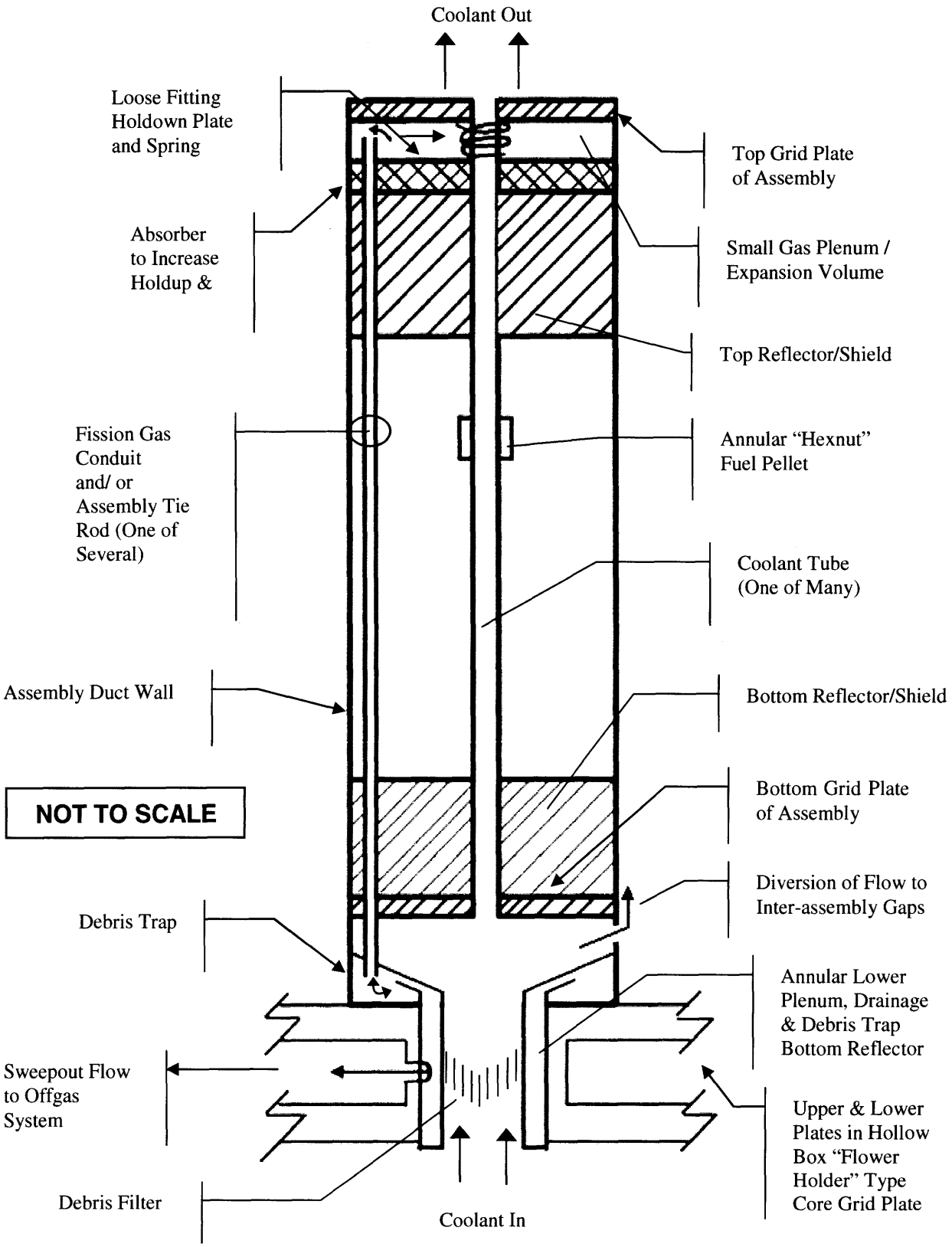

Figure 2.4. Vertical cross-section view of TID fuel assembly features.

2.7 Summary

In this chapter, the motivation for and a description of the TID fuel assembly concept was given. Sizing of coolant channels and basic dimensioning of these assemblies will be addressed in later chapters. A detailed design of the TID assembly and analysis of the performance of the fission gas venting system are left for future work. A preliminary suggested manufacturing sequence is given in Appendix C.

3 Selection of Fuel Form

3.1 Introduction

In the previous chapter, the use of oxide fuel was identified as the best candidate due to its chemical compatibility with CO_2. The objective of this chapter is to describe the neutronic and thermal-hydraulic benefits of using beryllium oxide (BeO) as a diluent in the fuel. The question of whether to specify vibrationally compacted or pellet-type fuel for the design is also addressed. A reference fuel form is identified along with some fall back options for possible later revisions of the design.

3.2 Motivation for use of BeO Diluent

If (U,TRU)O_2 fuel is loaded into TID fuel assemblies with no diluent, the resulting core has several unfavorable features, both neutronic and thermal-hydraulic. The following bullets identify some of these problems and describe how using BeO diluent serves to mitigate them.

- The primary driver for using BeO diluent in the direct S-CO_2 GFR is to reduce coolant void reactivity. The coolant void reactivity with (U,TRU)O_2 fuel alone and no diluent has been shown to be in excess of $1 assuming a complete and instantaneous depressurization. [Handwerk, et. al., 2005] BeO diluent can reduce the void reactivity to below $1 by providing neutron moderation which remains after coolant is voided.

- Even with the relatively low heavy metal density in oxide fuel, the critical TRU enrichment with (U,TRU)O_2 fuel only is quite low, leading to a conversion ratio

well in excess of unity. The resulting large reactivity increase between startup and mid-cycle would require many control rods which displace fuel in the core. The presence of a diluent raises the critical TRU enrichment by softening the neutron spectrum, displacing heavy metal, and favoring non-fission absorptions. The diluent can thus be used to reduce the conversion ratio to just above unity creating a much flatter reactivity profile and reducing the number and worth of control rods, with a concurrent reduction in rod ejection probability and severity.

- Adding BeO diluent to (U,TRU)O_2 fuel while keeping the core power density (in kW/liter core) constant increases the specific power (in kW/kg HM), which is beneficial from an economic standpoint.

- Although the radial power distribution can be flattened at BOL by enrichment zoning, this initial power shape does not hold during burnup and instead returns to a center-peaked J_0 shape. On the other hand, the power shape can be held quite steady by using zones of varying diluent volume fractions. This was demonstrated using BeO diluent by [Handwerk, et. al., 2006]

- With only 25% coolant by volume, fuel temperatures tend to be quite high due to the low thermal conductivity of oxided fuel. It will be discussed later that due to the unusually high thermal conductivity of 300 W/m·K [Tainsh, et. al., 1964] (quite high for an oxide), addition of BeO to oxide fuel increases its thermal conductivity significantly. [Sarma, et. al., 2005]

The use of BeO blended with oxide fuel has received a great deal of attention since as early as the 1940's. Due to the low atomic number of beryllium (thus high moderating power), it has primarily been evaluated as a means of neutron moderation. In 1946, a study lead by Dr. Farrington Daniels was performed evaluating the feasibility of a power reactor moderated by BeO and fueled by a BeO/UO_2 blend. [Gilbreath, et. al., 1958] During the 1950's, a fuel having BeO dispersed in UO_2 was also developed as part of the Aircraft Nuclear Propulsion (ANP) Program. This fuel was never tested in a reactor due to the cancellation of the program. [Holden, 1967] In 1963, construction began on the Experimental Beryllium Oxide Reactor (EBOR) in Idaho but the project was cancelled in

1966 before its completion. The purpose of this project was to evaluate BeO as a moderator in a gas-cooled thermal reactor. [Stacey, 2000] Also during the 1960's, the Australians evaluated the potential for a dispersion of $(U,Th)O_2$ and BeO for a CO_2-cooled pebble bed reactor. [Smith, 1964] The Southwest Experimental Fast Oxide Reactor (SEFOR), operated from 1969 to 1972, was a sodium cooled fast reactor built for the purpose of studying the Doppler effect in fast reactors. BeO was added to fuel in order to enhance the Doppler effect through neutron moderation.

Silicon Carbide (SiC) is also a well established material in nuclear applications which provides thermal and neutronic advantages over oxide fuel alone in the S-CO_2 GFR. [Handwerk, et. al., 2005] Like BeO, SiC has a high melting point, high thermal conductivity, lowers coolant void reactivity from the oxide-only value, and helps shape radial power during burnup. The benefits, however, are not as pronounced as with the BeO diluent. Nevertheless, at this stage in design, SiC should be kept as an alternate diluent material.

3.3 Consideration of Vibrationally Compacted Fuel (VIPAC or Sphere-Pac)

The process of loading fuel into TID assemblies will have to be a remote because the fuel will be enriched with highly radioactive TRU from spent LWR fuel. The fuel must be loaded into an unusually-shaped volume surrounding the hexagonally-arrayed pins. These factors make VIPAC or Sphere-Pac attractive fuel forms. VIPAC fuel consists of small fuel particles of irregular shape which are loaded into fuel assemblies (typically pins) and subjected to high-frequency vibrations. Particles of two or three different sizes are used to achieve useful fuel densities. Sphere-Pac fuel consists of a vibrationally compacted particle bed as well, only with more regularly-shapes spheres of different sizes. Because they present an economical means of remote loading of fuel assemblies, both VIPAC and Sphere-Pac fuels have been studied extensively, primarily for mixed oxide-fueled reactors burning either spent fuel TRU or weapons-grade plutonium.

Of major concern for any reactor application, especially one with such a small coolant volume fraction, is the thermal conductivity of the fuel. The conductivity of particle beds has been studied extensively for many years both for nuclear and non-nuclear applications. Although a particle bed fuel with a fill gas will typically have a lower thermal conductivity

than a solid pellet of the same composition, the bed usually sinters upon startup and the thermal conductivity of the sintered region becomes similar to that of pelletized fuel. The peak temperature of VIPAC or Sphere-Pac fuel has been shown to be lower than that of pelletized fuel at the same linear power primarily due to the reduction in fuel-clad interface conductance (analogous to gap conductance in pellet fuel) resulting from fuel particles being in contact with the surface of the cladding. As the particle bed fuel in a cylindrical pin sinters, a central void develops in a similar way to a pellet.

In the prediction of thermal conductivity of VIPAC or Sphere-Pac BeO/(U,TRU)O_2 for this application, care must be taken in use of the available experimental data and models because of the unique composition and geometry presented by this application. The buildup of fission gases, primarily xenon and krypton, has significant impact on the thermal conductivity of nuclear fuel. This is especially true in the case of particle bed fuels since much of the conduction is through the fill gas. The production of fission gases in vibrationally compacted fuel is well documented and rather straightforward to predict, but since the TID fuel assemblies will be vented to an off-gas system which is not yet designed in detail, the rate of build up of fission product gases in the fuel assemblies is not yet known. Venting also allows CO_2 to enter the assembly, fuel interstices and any gaps present. CO_2 has a lower thermal conductivity than helium, the common fill gas for sealed pins.

In most previous studies of vibrationally compacted fuel performance, cylindrical pins were used. After the initial heatup, the fuel sinters in a similar way to a pelletized fuel producing a central void. During sintering, the fuel remains in contact with the clad surface, essential in maintaining the advantage of low fuel-clad interface conductance. In the TID geometry, sintering would still occur, but whether or not the fuel would remain in contact with the clading surface is a question which can only be answered by irradiation of a prototypical assembly.

Due to the unique composition, unusual geometry and need for high burnup, prediction of the thermal performance of BeO/(U,TRU)O_2 in the form of VIPAC or Sphere-Pac fuel in TID assemblies is unreliable without irradiating a prototypical assembly. Because of the favorable characteristics of vibrationally compacted fuel and the complicated fuel

volume in TID assemblies, however, this option should be left open as a possible alternative fuel form for a future iteration on this design.

3.4 BeO/(U,TRU)O_2 Pellet Fuel

In recent work at Purdue University, enhanced thermal conductivity oxide fuels have been developed by pressing cylindrical pellets of UO_2 with a continuous BeO inert matrix. This fuel has exhibited a 50% higher thermal conductivity than ordinary UO_2 fuel with 10 percent BeO by volume present. [Sarma, et. al., 2005] This increase in thermal conductivity was observed over a range of temperatures. [Solomon, 2005]

In order to fit into a TID fuel assembly, pellets must be made in geometries other than conventional cylindrical shapes. Figure 3.1 shows how annular pellets having circular holes and hexagonal outer shapes (here called "hex-nut" pellets) can fit into the TID assembly.

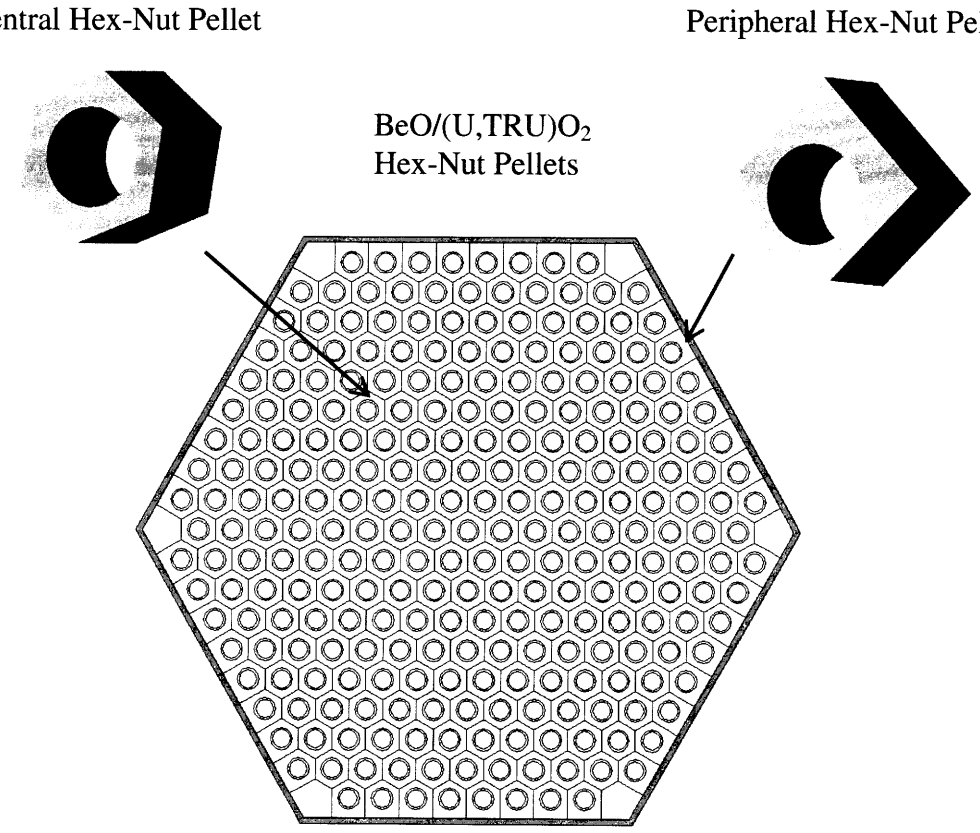

Figure 3.1. Horizontal cross-section of TID fuel assembly with hex-nut pellets.

Peripheral pellets would have one flat side which would fit adjacent to the duct wall. Annular oxide fuel pellets have been successfully manufactured at Westinghouse as part of a NERI project. [Hejzlar, et. al., 2004] Manufacturing hex-nut pellets is expected to be possible by a similar process with an appropriately-shaped die.

3.5 Summary

Pressed pellets in hex-nut shapes containing oxide fuel with a continuous BeO matrix (denoted by BeO/(U,TRU)O_2) are identified as the reference fuel form for use in the TID fuel assemblies. VIPAC or Sphere-Pac fuel could potentially offer a number of advantages such as small thermal resistance at the fuel-clad interface and ease in remote fuel loading. However, due to uncertainty in the behavior of such fuel with the composition and geometry specified for this design, these fuel forms are not selected as the reference design, but rather left as possible alternatives to the palletized fuel conceptualized here. SiC, though not selected as the diluent for the reference design, has many favorable neutronic and thermal properties. It is thus kept as an alternative diluent for possible revision of the design in later work.

4 Methodology Used in Core Parameter Studies

4.1 Introduction

Initial scoping analyses were performed aimed at determining core parameters such as coolant channel diameter and pitch, core height and core diameter. The associated calculations were performed using a FORTRAN code called FLOWSPLIT. This code was written by Pavel Hejzlar at MIT and is capable of determining cladding temperatures in multiple channel types with user-specified power levels, hydraulic diameters, roughness, etc. Updated to calculate fuel temperatures as well, this code provides a convenient input and short computation time relative to more robust software packages such as RELAP. This allows for evaluation of many core configurations and the determination of the allowable design space.

In this chapter, the methodology used in FLOWSPLIT is described starting with the constitutive equations for heat transfer and pressure drop in coolant channels. The methodology and assumptions used in calculation of the temperature rise across the cladding, fuel-clad gap and the fuel are then discussed. Variables will be defined as they are introduced in the following sections, several of which are shown in the diagram of a unit TID cell in Figure 4.1.

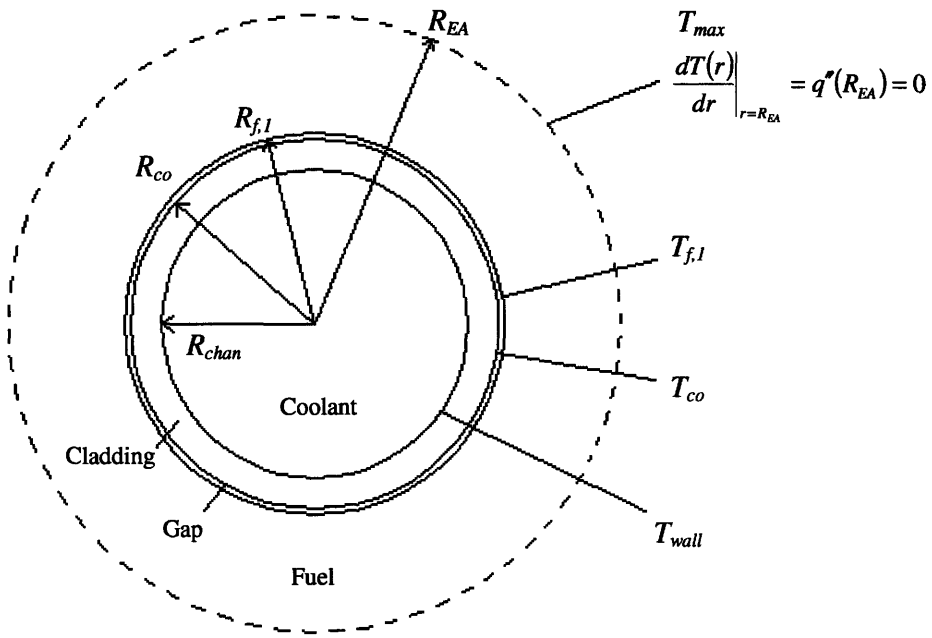

Figure 4.1. Diagram of cylindricized TID fuel unit cell with nomenclature for thermal-hydraulic calculations.

4.2 Constitutive Models for Core Thermal-Hydraulic Calculations

4.2.1 Form Losses at Core Inlet and Exit

Form pressure losses occurring at the entrance and exit of the core coolant channels can be calculated using the following equations;

$$\Delta P_i = \zeta_i \rho \frac{v^2}{2} \tag{4-1}$$

$$\Delta P_o = \zeta_o \rho \frac{v^2}{2} \tag{4-2}$$

where ΔP_i is the inlet form pressure loss, ΔP_o is the outlet form pressure loss, ζ_i is the inlet form loss coefficient, ρ is the fluid density, v is fluid average velocity inside the channel, and ζ_o is the outlet form loss coefficient. The velocity term (v) is always the higher velocity of the fluid with an expansion or a contraction, so in this case, it is always the flow inside the

coolant channels, since the flow area of the plena are larger. The values of the inlet and exit loss coefficients (ζ_i and ζ_o) depend on the geometry of the system.

In the case of the entrance loss coefficient, rounding the edge of the hole leading to the coolant channel can reduce significantly the value of ζ_i. If the radius of the round is greater than or equal to 12% of the hydraulic diameter of the channel, ζ_i is reduced to approximately 0.1 down from the sharp-edge value of 0.5. With a P/D_{chan} of 1.905 (set by the 25% coolant by volume constraint), this is possible without the entrance rounds of adjacent channels coming into contact with one-another. On the other hand, rounding the edges of the channel exits is not as effective at reducing the exit loss coefficient (ζ_o) below the sharp-edge value of 1.0. For thermal-hydraulic calculations in this work, ζ_i and ζ_o are therefore taken to be 0.1 and 1.0, respectively.

4.2.2 Friction Pressure Drop in Coolant Channels

Most of the pressure loss encountered by coolant moving through the core is a result of friction along the rod surfaces. The frictional pressure drop in coolant channels is calculated by;

$$\Delta P_f = \frac{1}{2} f \frac{L}{D_e} \rho v^2 \tag{4-3}$$

where ΔP_f is the frictional pressure drop, f is the Darcy (or Moody) friction factor, L is the channel length, D_e is the equivalent (or hydraulic) diameter ρ is the fluid density, and v is the fluid velocity. The frictional pressure drop is calculated along with acceleration and gravitational pressure drops at each axial node (20 in active core, 5 in bottom reflector, 5 in top reflector) to get the pressure of the next node.

The friction factor model used in the analyses is the Zigrang-Sylvester correlation given by; [Zigrang, et. al., 1985]

$$\frac{1}{\sqrt{f}} = -2\log\left\{\frac{\varepsilon}{3.7D_e} + \frac{2.51}{\mathrm{Re}}\left[1.14 - 2\log\left(\frac{\varepsilon}{D_e} + \frac{21.25}{\mathrm{Re}^{0.9}}\right)\right]\right\} \tag{4-4}$$

where ε is the surface roughness and Re is the Reynolds number. An explicit approximation to the transcendental Colebrook-White correlation, the Zigrang-Sylvester equation is valid for Re ≥ 3,000. Reynolds number (Re) is a dimensionless parameter proportional to the ratio of kinetic energy to viscous forces and is given by;

$$\mathrm{Re} = \frac{\rho v D_e}{\mu} \tag{4-5}$$

where μ is the fluid viscosity evaluated at the bulk fluid temperature.

4.2.3 Film Heat Transfer Model

The cladding wall temperature is related to the heat flux using a heat transfer coefficient as follows;

$$\Delta T_{film} \equiv T_{wall} - T_{bulk} = \frac{q''_{wall}}{h} \tag{4-6}$$

Where ΔT_{film} is the temperature difference between the clad surface and the bulk fluid, T_{wall} is the clad surface temperature, T_{bulk} is the bulk fluid temperature, q''_{wall} is the heat flux at the clad surface in contact with coolant, and h is the heat transfer coefficient.

The heat transfer coefficient is dependent on geometry, fluid properties and flow conditions and is typically predicted using empirical models. The model used in all turbulent-regime convective heat transfer calculations in this work is that suggested by [Gnielinski, 1975];

$$Nu = \frac{hD_e}{k} = \frac{\left(f/8\right)(\mathrm{Re}-1000)\mathrm{Pr}}{1+12.7\sqrt{(f/8)}\left(\mathrm{Pr}^{2/3}-1\right)}\left[1+\left(\frac{D_e}{L_h}\right)^{2/3}\right]K \tag{4-7}$$

where Nu is Nusselt number, f is the friction factor, Pr is the Prandtl number evaluated at the bulk fluid temperature, L_h is the heated length (distance traveled past the onset of heating), h is the heat transfer coefficient and k is the coolant conductivity evaluated at the bulk

temperature. The friction factor used in this equation is the smooth-wall isothermal Darcy (or Moody) friction factor given by; [Gnielinski, 1975]

$$f = \frac{1}{(1.82\log(\mathrm{Re}) - 1.64)^2} \tag{4-8}$$

Note that this is different than the friction factor used to estimate pressure losses in the channels. The square-bracketed term of Equation 5-7 accounts for the heated development length and the K term accounts for the fluid having different properties at the wall temperature than at the bulk temperature and is given by; [Gnielinski, 1975]

$$K = \left(\frac{T_{bulk}}{T_{wall}}\right)^{0.45} \tag{4-9}$$

where K is a factor used to capture the heated wall effect, T_{bulk} is the bulk coolant temperature and T_{wall} is the temperature of the cladding at the surface in contact with coolant. This particular expression for the factor K is meant to be used for a gas only. The viscosity of a gas increases with increasing temperature, so because the gas near the heated wall of a coolant channel is at a higher temperature than the bulk fluid, the viscosity of the gas near the wall is higher. This inhibits turbulent mixing and so the heated wall effect in the case of a gas serves to decrease the overall heat transfer coefficient. Because the K term in Equation 5-7 contains a T_{wall} term, the clad surface temperature calculation at each node is an iterative solution.

4.3 Calculation of Temperatures in Cladding and Fuel

4.3.1 Temperature Rise in Cladding

Since the cladding wall thickness is relatively small compared to its diameter and the temperature change across the cladding is small relative to the total temperature difference between coolant and peak fuel, heat transfer through the cladding can be treated with reasonable accuracy as one-dimensional heat transfer through a constant-conductivity medium. This temperature rise across the cladding can thus be estimated by;

$$\Delta T_{clad} \equiv T_{co} - T_{wall} = \frac{q''_{clad}}{k_{clad}} t_c \qquad \textbf{(4-10)}$$

where ΔT_{clad} is the temperature rise across the cladding, T_{co} is the clad surface temperature on the fuel side, T_{wall} is the clad surface temperature in contact with the coolant, q''_{clad} is the heat flux at the center of the clad wall k_{clad} is the thermal conductivity of the cladding and t_c is the thickness of the cladding.

4.3.2 Temperature Rise across Fuel-Clad Gap

The temperature rise across the gap between cladding and fuel is dependent on a complex set of factors related to fill gas thermal conductivity, surface emissivity, degree of contact between fuel and cladding, etc.

4.3.2.1 Gap Size and Effect of Initial Heatup

Fuel and coolant tubes must be manufactured with sufficient clearance to load hex-nut pellets onto the tubes without interference. The initial heat up associated with the rise to full power causes fuel and cladding to expand based on their cold-to-hot temperature increases and their respective coefficients of thermal expansion. Depending on these material properties and their associated temperature changes, this can result in a net increase or decrease in gap thickness as the reactor is brought to full power. In this section, estimates are made of the desired initial cold and hot gap sizes. The subscript "hot" is adopted to represent dimensions at a hot full power condition with zero burnup, and the subscript "cold" indicates dimensions as-fabricated before initial heat up of the fuel. Two major assumptions are used in order to simplify the estimation of the dimensional changes in cladding and fuel with heat up; one is that an average temperature increase from cold to hot conditions can be assumed in the fuel and the cladding. In other words, the temperature is assumed to be independent of position in each material. The other major assumption is that the coefficients of thermal expansion for fuel and cladding are independent of temperature. With these assumptions, the thickness of the fuel-clad gap under cold conditions is given by;

$$t_{gap(cold)} = R_{f,1(cold)} - R_{co(cold)} = \frac{D_{f,1(cold)} - D_{co(cold)}}{2} \qquad \textbf{(4-11)}$$

where t_{gap} is the thickness of the fuel-clad gap, $R_{f,l}$ is the fuel pellet inner radius, R_{co} is the cladding outer radius, the variable D represents the diameter corresponding to the radius with the same subscript and the parenthetical subscript *cold* indicates that these are dimensions in fresh fuel in a cold condition with zero burnup. The changes in $D_{f,l}$ and D_{co} as a result of initial heatup are given by the product of the temperature change and the coefficient of thermal expansion as follows;

$$D_{f,l(hot)} = D_{f,l(cold)} \alpha_f \overline{\Delta T}_f \tag{4-12}$$

$$D_{co(hot)} = D_{co(cold)} \alpha_c \overline{\Delta T}_c \tag{4-13}$$

where the subscript *hot* denotes a condition just after full power is reached but before significant burnup is achieved, α_f is the constant linear coefficient of thermal expansion of the fuel, α_c is the constant linear coefficient of thermal expansion of the cladding, $\overline{\Delta T}_f$ is the average temperature increase in the fuel from cold to hot conditions and $\overline{\Delta T}_c$ is the average temperature increase in the cladding from cold to hot conditions. The hot gap size is then given by replacing the *cold* subscript with *hot* in Equation 5-11 and substituting Equations 5-12 and 5-13 into the resulting equation. The resulting expression for hot gap size is as follows;

$$t_{gap(hot)} = R_{f,l(hot)} - R_{co(hot)} = \frac{D_{f,l(hot)} - D_{co(hot)}}{2} = \frac{D_{f,l(cold)} \alpha_f \overline{\Delta T}_f - D_{co(cold)} \alpha_c \overline{\Delta T}_c}{2} \tag{4-14}$$

For this analysis, the coefficient of thermal expansion of ODS MA956 was taken to be 12.3×10^{-6} /°C, the value at 400°C according to [Special Metals, 2004]. For the fuel, the coefficient of thermal expansion was taken to be 10.1×10^{-6} /°C, the average value for pure UO_2 over the range from 400°C to 1400°C. [Todreas, et. al., 1990] The average temperature increases from ambient to full power in the cladding and fuel were taken to be 750°C and 1100°C, respectively. Three coolant channel inner diameters (D_{chan}) were evaluated with the cladding thickness held constant at 0.7 mm. Table 4-1 shows the hot gap thickness based on these assumptions for three different coolant channel inner diameters and a range of cold gap thicknesses. From these data, one may conclude that the fuel-clad gap thickness increases by

about 10 μm with the initial heatup of fuel. In order to minimize the hot gap thickness (and thus the temperature rise across the gap), the cold gap thickness must be made smaller. This is limited, however, by the need to insert cladding (coolant flow tubes) into the hex-nut pellet holes without interference. 60 μm was selected as a relatively small, yet manufacturable, cold gap thickness. This gives a hot gap thickness of 70 μm, a value which is carried through the remainder of this work.

Table 4-1. Hot gap thickness for several cold thicknesses and three coolant channel diameters.

$t_{gap(cold)}$ (μm)	$t_{gap(hot)}$ (μm)		
	$D_{chan(cold)}$ = 6 mm	$D_{chan(cold)}$ = 8 mm	$D_{chan(cold)}$ = 10 mm
40	47	49	51
50	58	59	61
60	68	70	71
70	78	80	82
80	88	90	92

4.3.2.2 Gap Conductance Model

The temperature rise across the gap is calculated by defining an effective gap conductance relating ΔT_{gap} to the heat flux across the gap as follows;

$$\Delta T_{gap} \equiv T_{f,1} - T_{co} = \frac{q''_{gap}}{h_{gap}} \tag{4-15}$$

where ΔT_{gap} is the temperature rise across fuel-clad gap, h_{gap} is the conductance of fuel-clad interface and q''_{gap} is the heat flux at the center of the gap. At the beginning of fuel life, heat transfer between cladding and fuel can be modeled as a combination of conduction through the fill gas and radiation between the fuel and cladding surfaces. This methodology is based on the assumption that the fuel is perfectly centered about the cladding and the fuel and cladding do not touch in any place. The gap conductance adapted to reflect the notation shown in Figure 4.1 with the first term accounting for conduction through the gas and the second term accounting for radiation is given by; [adapted from Todreas, et. al., 1990]

$$h_{gap} = \frac{k_{gas}}{t_{gap}} + \frac{\sigma}{\frac{1}{\varepsilon_c} + \frac{1}{\varepsilon_f} - 1}\left(\frac{T_{f,1}^4 - T_{co}^4}{T_{f,1} - T_{co}}\right) \quad \textbf{(4-16)}$$

where k_{gas} is the thermal conductivity of the fill gas, t_{gap} is the fuel-clad gap thickness, ε_c is the emissivity of the cladding surface, ε_f is the emissivity of the fuel surface, and σ is the Stefan-Boltzmann constant (5.67×10^{-8} W/m^2·K^4). Several terms in this equation must be estimated in order to proceed with the analysis. The conductivity of the gas in the gap is an important factor as the conduction term is often larger than the radiation term.

Figure 4.2 shows the thermal conductivity of CO_2 at 20 MPa in the temperature range of interest for the fuel-clad gap. Thermal conductivities of helium, xenon and krypton are also shown for comparison. All solid lines on the graph represent data from the NIST database. The dotted lines in the cases of helium, xenon and kypton are defined by the equations of the form $k=AT^x$ with the constants A and x given in Table 4-2 for these gases from [de Podesta, 1996]. In the case of CO_2, the dotted line is the result of fitting NIST data to an equation of the same form as above for temperatures sufficiently far from the critical point to achieve good agreement in the temperature range of interest. Moving to the left in Figure 4.2, the solid lines (NIST data) for all of these gases deviate significantly from the equations defined in Table 4-2 because they are approaching their respective critical temperatures. Moving to the right in the figure, the temperature is moving farther from the critical temperatures and the solid lines begin to converge to the dotted lines.

For calculations using FLOWSPLIT, the thermal conductivity of the CO_2 fill gas was taken to be 0.08 W/m·K, the value at 875°C. This is conservative since average gap temperatures will exceed this temperature at the core axial centerline, the approximate location of the highest fuel temperature. This also avoids excessive extrapolation of available conductivity data for CO_2. The thickness of the gap between fuel and cladding after initial heatup was taken at this point to be 70 μm as discussed in the previous section. In the literature, the gap thickness term in Equation 5-16 is an effective thickness taking into account discontinuities at the gas-solid interface. [Todreas, et. al., 1990] In this work, the real gap thickness is used. Emissivity values of cladding and fuel surfaces (ε_c and ε_f) were

taken to be 0.90 and 0.79, respectively. The methodology of FLOWSPLIT is such that an initial value of $T_{f,1}$ is calculated using Equation 5-15 and an assumed h_{gap}, then Equation 5-16 is used to recalculate h_{gap}. The program iterates on this procedure until the calculated $T_{f,1}$ ceases to change appreciably from one iteration to the next.

Given the estimated parameters above (k_{gas} = 0.08 W/m·K and t_{gap} = 70 μm), the gap conductance resulting from conduction alone (the first term in Equation 5-16) has a value of 1000 W/m^2·K. For this application, the conduction term tends to be larger than the radiation term, and total gap conductance values in the range from 1000 to 1500 W/m^2·K can be expected. This is much lower than in helium-filled gaps due to the lower thermal conductivity of CO_2, approximately a factor of 5 lower than helium at comparable temperature and pressure. This means that the temperature rise across the gap may be significant in fresh fuel with this design. After irradiation, the fuel will swell, closing the fuel-clad gap and increasing the gap conductance.

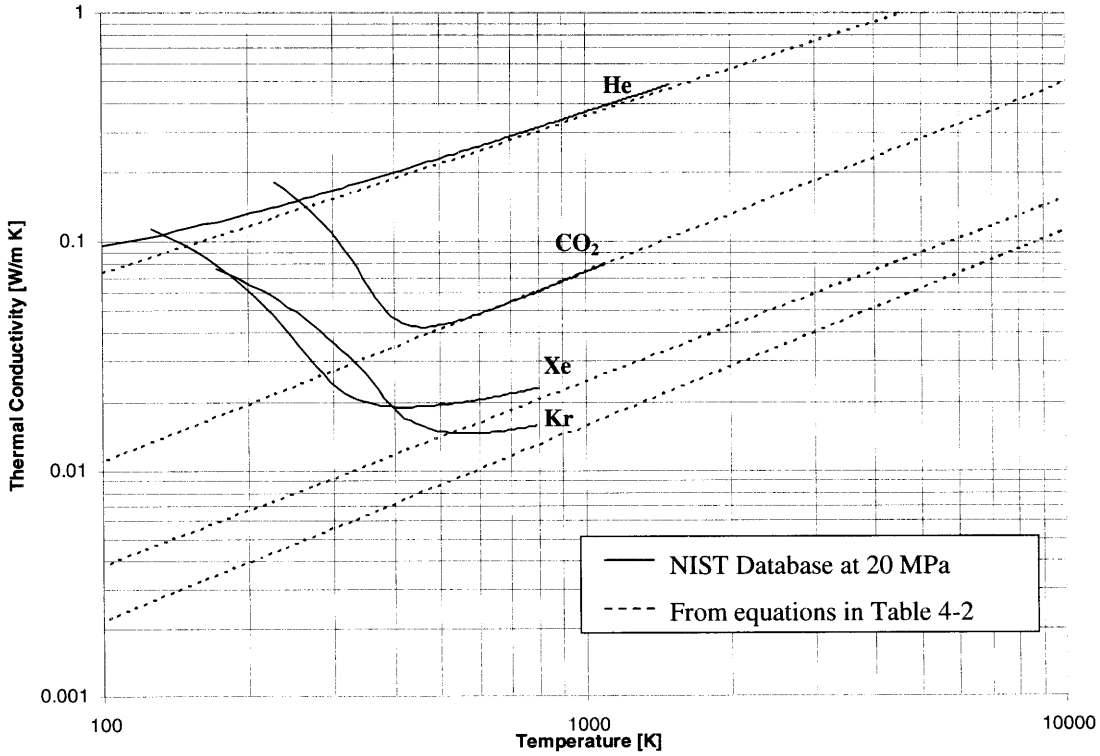

Figure 4.2. Isobaric thermal conductivity of gases at 20 MPa.

Table 4-2. Constants for $k = AT^x$ where T is temperature in Kelvins and k is conductivity in W/m·K from [de Podesta, 1996].

Gas	A	x
Helium	30.91×10^{-4}	0.685
CO_2*	2.4×10^{-4}	0.829
Kr	0.93×10^{-4}	0.806
Xe	0.42×10^{-4}	0.857

* Fit to NIST data for 20 MPa and temperatures 570K < T < 1070K

During burnup, gap conductance changes as a result of several phenomena including thermal expansion of fuel and cladding, radiation-induced swelling and cracking of fuel and buildup of fission products in the fuel and buildup of fission product gases (primarily xenon and krypton) in the fuel-gaps. In conventional pin-type rods with oxide fuel, the effects of burnup typically result in a net increase in gap conductance. [Todreas, et. al., 1990]

In the "inside-out" arrangement of TID fuel, these changes have competing effects on gap conductance. Thermal expansion of the cladding will serve to decrease gap thickness and increase gap conductance, while thermal expansion of the hex-nut pellets will partially offset this effect. Radiation-induced swelling and cracking of the pellet will have the effect of closing the gap. Of the fission product gases produced during burnup, the most prevalent are xenon and krypton. Since these gases have significantly lower thermal conductivity than CO_2, their introduction into the system will decrease the conductivity of the fill gas, thus degrading gap conductance. This affect is less pronounced, however, in a CO_2-filled gap than a helium-filled gap since the conductivity of CO_2 is much lower than helium. In other words, the difference in conductivities is more pronounced between fission product gases and helium than between fission product gases and CO_2. Also, with venting, excessive buildup of fission product gases in the gap is not expected. Although a more thorough treatment of these competing effects on gap conductance is necessary, for now it is assumed that the lowest gap conductance is at beginning of fuel life immediately following the rise to full power and will increase with burnup.

4.3.3 Fuel Temperatures

Determination of fuel temperatures is important in order to ensure that no melting occurs during normal operation and to predict fission gas release. An estimate of the thermal conductivity of the fuel must be made in order to determine these temperatures. A great deal of data is available pertaining to the thermal conductivity of conventional fuels and how they are affected by temperature, plutonium content, porosity, burnup, stoichiometry, etc. In this design, however, the specified fuel geometry and composition has not been irradiated in a prototypical experiment and thus some approximations must be made in order to estimate temperatures during operation.

4.3.3.1 Equivalent Fuel Annulus Assumption

In a hexagonal array of coolant channels distributed in a fuel matrix (in this case comprised of hex-nut pellets), a two or three-dimensional solution to the heat conduction equation giving temperature everywhere in the fuel is not practical for most thermal-hydraulic calculations. Therefore, for an application such as this, the concept of an equivalent fuel annulus is typically employed. Figure 4.3 shows a schematic of a coolant channel and its associated hex-nut fuel pellet. The largest circle drawn represents the size of an annular fuel region such that the volume of fuel surrounding the coolant channel is preserved. An insulated boundary condition is used at the outer periphery of the equivalent annulus of fuel as indicated in Figure 4.1. The conduction equation can then be efficiently solved in one-dimensional cylindrical coordinates for each axial node to find the temperature at the edge of the equivalent fuel annulus. While this temperature is slightly lower than the actual peak fuel temperature (located at the corners of the hex-nut pellets), it is assumed to be the peak fuel temperature with reasonable accuracy.

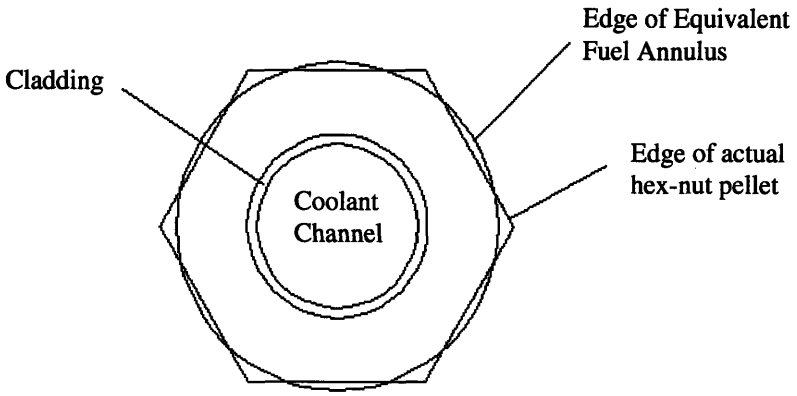

Figure 4.3. TID fuel unit cell diagram illustrating the concept of an equivalent fuel annulus.

4.3.3.2 Estimate of Fuel Thermal Conductivity

As mentioned in Chapter 3, the fuel is a blend of BeO, natural uranium oxide and trans-uranic oxides, denoted by BeO/(U,TRU)O_2. The TRU composition is taken to be 90 w/o PuO_2 and 10 w/o oxides of minor actinides, each having isotopic composition similar to spent LWR fuel. The TRU enrichment will vary between core regions, but will typically be between 15 and 20 w/o. The percent BeO will also be varied in order to shape power and mitigate coolant void reactivity.

In estimating the thermal conductivity of the BeO/(U,TRU)O_2 fuel, the thermal conductivity of stoichiometric (oxygen/metal atom ratio = 2.00) mixed oxide fuel (MOX) of 20% plutonium and 80% uranium at 95% theoretical density is used as a starting point. An empirical formula for this conductivity is given by; [Waltar, et. al., 1981]

$$k(T) = \frac{1}{0.042 + 2.71\times10^{-4}(T+273)} + 6.9\times10^{-11}(T+273)^3 \qquad \textbf{(4-17)}$$

where T is temperature in °C and k is thermal conductivity of fresh MOX fuel in W/m·K. Two factors are used to modify this conductivity; one to account for the presence of BeO, and one to account for change of the conductivity resulting from burnup. A major assumption made at this point is that these two effects are separable. In other words, the temperature-dependent thermal conductivity given in Equation 5-17 will be multiplied by two factors, one to account for each of these effects.

It has been shown that 10% by volume BeO present in UO_2 gives approximately a 50% increase in thermal conductivity over UO_2 alone. [Sarma, et. al., 2005] This enhancement was observed over a range of temperatures. [Solomon, 2005] For the fuel temperature calculations performed here, this factor of 1.5 will be applied over the entire range of temperatures used. It is important to note that BeO is known to exhibit anisotropic crystal growth when exposed to fast neutron flux, which can lead to microcracking and pulverization at high fluence. These effects are reduced by irradiation at higher temperatures and by manufacturing fuel with finer grain sizes. [Hickman, et. al., 1964] These effects are difficult to quantify without experiments at the current state of knowledge and need attention in future work.

The thermal conductivity of fuel tends to decrease with burnup resulting from a number of structural and composition changes. Thermal cycling causes cracking in fuel pellets which lowers thermal conductivity. Introduction of fission products into the fuel matrix during fuel life also lowers thermal conductivity. The relative change in thermal conductivity of BeO/(U,TRU)O_2 fuel with burnup is assumed to be proportional to that of MOX fuel without BeO diluent.

An empirical formula for the thermal conductivity of MOX fuel as a function of temperature, burnup and the ratio of thermal conductivity of MOX fuel to that of UO_2 based on fuel temperature measurements in an LWR is given by; [Lee, et. al., 2002]

$$k(T) = \frac{f_{mox}}{0.1149 + 0.0035 \cdot B + \left(2.475 \times 10^{-4} - 7.921 \times 10^{-7} \cdot B\right) \cdot T} + 0.0132 e^{0.00188 \cdot T} \quad \textbf{(4-18)}$$

where k is thermal conductivity of fresh MOX fuel in W/m·K, f_{mox} is the ratio of thermal conductivities of MOX to UO_2 fuels, B is the fuel burnup in MWd/kgHM and T is the temperature in °C. This equation was used to develop a burnup degradation factor (F_{bu}) to multiply by Equation 5-17. The value of f_{mox} was taken to be 0.9. Over a range of temperatures, the value of this expression was calculated for burnups of 0 and 120 MWd/kg.

The ratio of these gave the burnup degradation factor as a function of temperature, which was fit with the following polynomial expression;

$$F_{bu}\left(120 MWd/_{kg}\right) = -3.2\times10^{-8}T^2 + 0.00035T + 0.2231 \quad \textbf{(4-19)}$$

where F_{bu} is the burnup degradation factor at 120 MWd/kg and T is the temperature in °C. This burnup degradation factor (F_{bu}) is shown graphically in Figure 4.4. Multiplying the fresh MOX fuel conductivity by this factor gives the estimate of conductivity at 120 MWd/kg. The estimate of thermal conductivity of the BeO/(U,TRU)O_2 is now given by the expression;

$$k(T) = 1.5F_{bu}\left[\frac{1}{0.042 + 2.71\times10^{-4}(T+273)} + 6.9\times10^{-11}(T+273)^3\right] \quad \textbf{(4-20)}$$

where k is thermal conductivity in W/m·K and T is temperature in °C. The factor of 1.5 accounts for the 50% increase in conductivity from the presence of the BeO diluent and the burnup degradation factor F_{bu} is evaluated at 120 MWd/kg as indicated in Equation 5-19. Figure 4.5 shows the resulting thermal conductivity versus temperature. The integral of thermal conductivity was calculated numerically and is also shown in the figure.

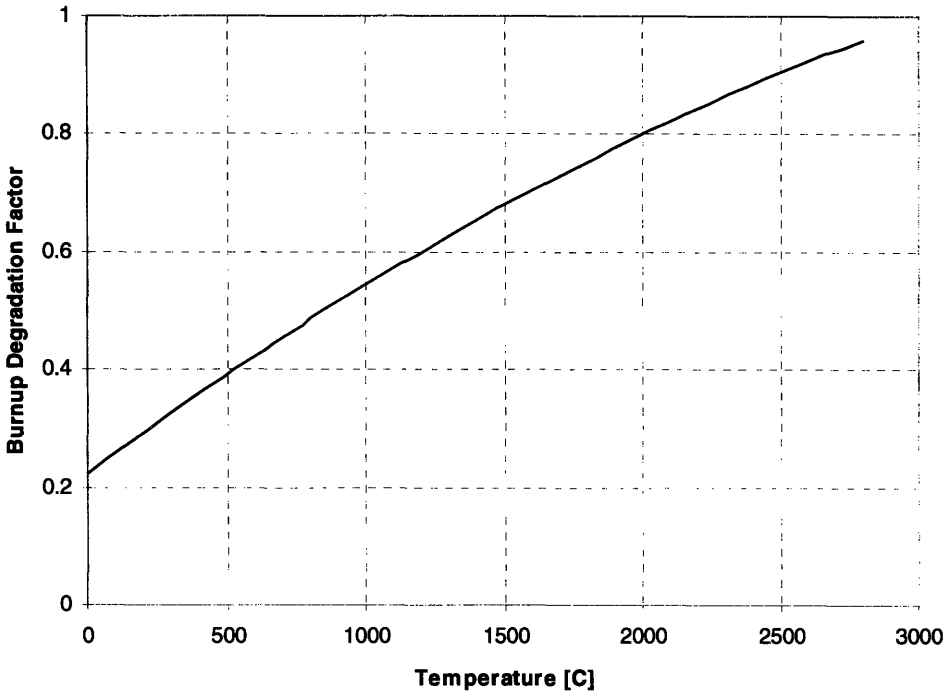

Figure 4.4. Burnup conductivity degradation factor versus temperature at 120 MWd/kg.

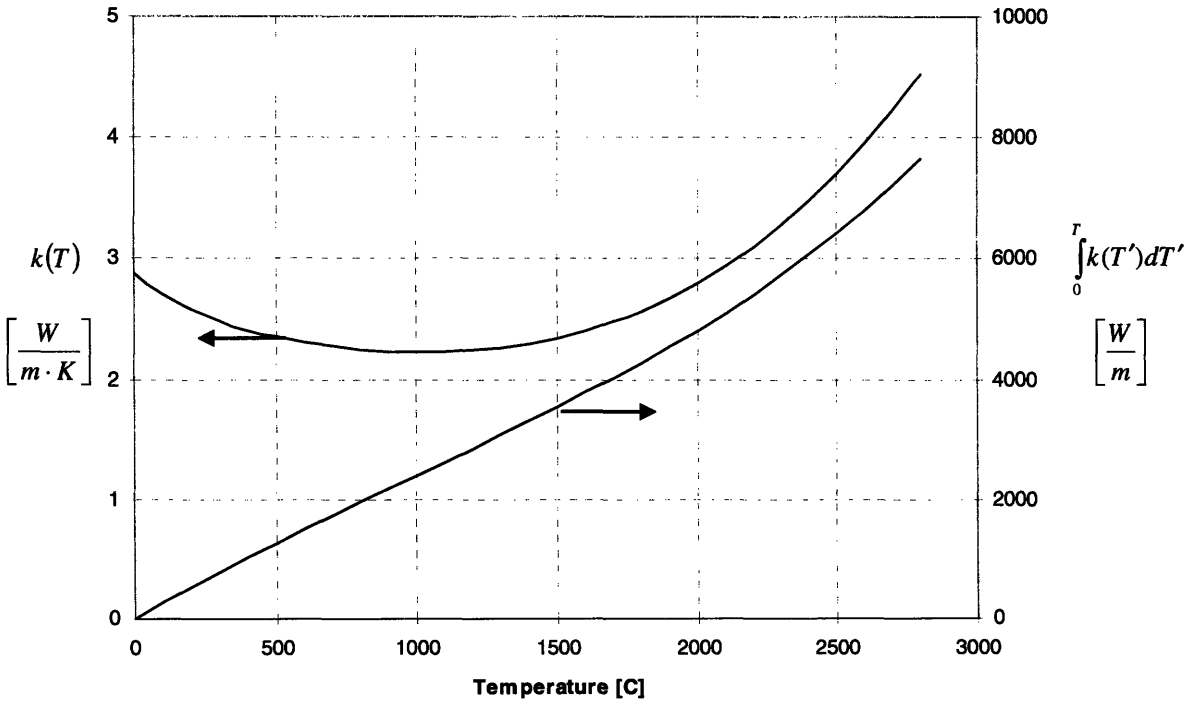

Figure 4.5. Estimated thermal conductivity of BeO/(U,TRU)O_2 fuel.

4.3.3.3 *Fuel Temperature Calculations in FLOWSPLIT*

It can be shown that for an annulus of fuel with uniform heat generation, no net axial or azimuthal conduction and a zero heat flux boundary condition at the outermost periphery of the equivalent fuel annulus, the following is the solution to the one-dimensional heat transfer equation;

$$-\int_{T_{f,1}}^{T_{max}} k_f(T)\,dT = q'''\left[\frac{\left(R_{EA}^2 - R_{f,1}^2\right)}{4} - \frac{R_{EA}^2}{2}\ln\left(\frac{R_{EA}}{R_{f,1}}\right)\right] \qquad \textbf{(4-21)}$$

where $k_f(T)$ is the temperature-dependent thermal conductivity of the fuel, T is the local temperature of the fuel, T_{max} is the maximum fuel temperature in the cell, $T_{f,1}$ is the temperature of the fuel surface adjacent to the cladding, q''' is the heat generation rate inside the fuel, R_{EA} is the radius of the equivalent annulus of fuel surrounding a coolant channel and $R_{f,1}$ is the radius of the inner fuel surface. The left-hand side of this equation can be expanded into the difference of two integrals, which results in the following expression;

$$\int_{0}^{T_{f,1}} k_f(T)\,dT - \int_{0}^{T_{max}} k_f(T)\,dT = q'''\left[\frac{\left(R_{EA}^2 - R_{f,1}^2\right)}{4} - \frac{R_{EA}^2}{2}\ln\left(\frac{R_{EA}}{R_{f,1}}\right)\right] \qquad \textbf{(4-22)}$$

The integral of fuel thermal conductivity shown in Figure 4.5 was determined by numerical integration, and so in order to easily solve for fuel temperatures, it was fit with a 2nd order polynomial. The right-hand side of Equation 5-22 is known based on the geometry and power of an axial calculational node. After the calculation of ΔT_{gap}, the value of the inner fuel surface temperature ($T_{f,1}$) is known, and so the first term on the left-hand side of Equation 5-22 is determined by substituting $T_{f,1}$ into the polynomial expression for the integral of $k_f(T)$. T_{max} is then determined by solving the polynomial expression of the conductivity integral for the value of T_{max} which satisfies Equation 5-22.

4.4 Summary

This chapter summarizes the methodology employed by FLOWSPLIT in calculating core pressure drop and temperatures in cladding and fuel. The next chapter uses this code for a preliminary assessment of what arrangements of core parameters satisfy the design limits imposed on the problem. In a later section, a comparison of results will be given between FLOWSPLIT and RELAP for the final reference design at steady state.

It should be noted that the fuel temperature calculations performed based on the above estimate of fuel thermal conductivity and treatment of the fuel-clad gap conductance are conservative. The assumed burnup of 120 MWd/kg is at the end of fuel life in the core which gives the lowest thermal conductivity value. The handling of the fuel-clad gap, on the other hand, is developed assuming that no burnup and the associated swelling of the fuel has occurred, also giving a conservative result. In reality, fuel at high burnup will likely have a higher gap conductance due to radiation-induced swelling and so the worst cases of gap conductance and fuel thermal conductivity will not occur at the same point in time. In future work, better understanding of the behavior of this fuel form should be sought in order not to overburden the design process with needless conservatism.

5 Core Parameters Study

5.1 Introduction

This chapter discusses the process by which the fluid flow and heat transfer models described in the previous chapter were used to determine a set of core parameters which satisfies relevant limits. These calculations were perfomed taking into account only two channel types, hot and average. Inter-assembly heating and flow, along with core bypass flow, are not accounted for. This should therefore be considered a preliminary assessment of core parameters serving as a first iteration on core design. Detailed design of fuel assemblies and actual core layout is reserved for the following chapter.

The prospect of reducing cladding temperatures via heat transfer augmentation is considered in this chapter, along with the potential for coolant channel orificing. The benefits of the lower-temperature alternative power cycle on core design are investigated as well in this chapter.

5.2 Preliminary Thermal-Hydraulic Analysis of Reference Core

5.2.1 Constant Parameters Used in Assessment

From the optimized cycle statepoints in Table 1-1 for the reference design, the inlet and outlet temperatures are set at 485°C and 650°C, respectively. The total core mass flow rate is set to 11,708 kg/s from the previous cycle optimization work. The axial power shape is assumed to be a chopped cosine in both the peak and average channels with a peaking factor of 1.3. The radial power peaking factor was assumed to be 1.15 at this point, a value which is expected to be obtainable through the use of BeO diluent zoning to flatten the radial

power shape. Upper and lower inactive lengths are specified in order to allow for reflector, shielding, the small plenum at the top of the assembly and upper and lower assembly plates which serve as manifolds. Table 5-1 shows a summary of these and other parameters held constant in these preliminary calculations.

Table 5-1. Parameters used in preliminary thermal hydraulic calculations.

Parameter (units)	**Value**
Thermal power (MW_{th})	2400
Mass flow rate (kg/s)	11,708
Inlet pressure (MPa)	20
Inlet temperature (°C)	485
Outlet temperature (°C)	650
Axial power shape	Chopped cosine
Axial peaking factor	1.3
Radial peaking factor	1.15
Lower inactive length (m)	1.1
Upper inactive length (m)	1.0
Coolant volume fraction (%)	25
Clad thickness (mm)	0.7
Clad thermal conductivity (W/m·K)	23
Entrance loss coefficient	0.1
Exit loss coefficient	1.0
Fuel conductivity	See Figure 4.5
Channel surface roughness (m)	$1x10^{-5}$
Core power density (kW/liter core)	100
Active core volume (m^3)	24
Gap CO_2 conductivity (W/m·K)	0.08
Hot gap thickness (μm)	70
Fuel emissivity	0.79
Cladding emissivity	0.90

5.2.2 Parametric Study Methodology

The core parameters of interest at this stage of the investigation were active core height, core effective diameter (assuming a lattice of channels in fuel with no duct walls, etc.), coolant channel diameter and number of coolant channels. A core height and a coolant channel diameter are initially selected. Since the core volume was set at 24 m^3, the core

transverse cross-sectional area (as viewed from above) can be determined by dividing the core volume by the channel active height. The core area, along with the constraint of 25% coolant by volume gives the number of channels for this core H/D and channel size. The channel pitch is also set by this coolant volume fraction to 1.905 times the coolant channel diameter. The power distribution in the channels can then be determined based on the average power density of 100 kW/liter core. FLOWSPLIT is then used to calculate the peak clad surface temperature, peak fuel temperature and core pressure drop. Core H/D values ranging from 0.3 to 0.425 were evaluated. For each core H/D, a range of coolant channel inner diameters from 6 mm to 10 mm was evaluated.

5.2.3 Design Limits Used in Parametric Study

The design limits against which the results of FLOWSPLIT calculations were compared are shown in Table 5-2. The midwall peak clad temperature limit set by designers of the GA GCFR in the 1970's was 750°C. [General Atomic Company, 1980] The ODS MA956 specified as the cladding material in this work has superior creep resistance to the stainless steel 316 specified for GCFR service. Since these fuel assemblies would be vented as were the GA GCFR assemblies, there will be no pressure differences across cladding which were also not present in the GCFR design. Due to these factors, the clad surface temperature limit was set to 800°C.

In fuel assemblies where the fuel volume is not vented to an offgas system, fuel temperature limits are typically based on 1) no fuel melting and 2) limiting fission gas release to prevent excessive pressure in fuel pins. In a vented assembly, however, the fission gas release does not cause increased pressure across cladding. This allows for higher fuel temperatures than in unvented assemblies. For example, the steady state peak fuel temperature limit set for the GA GCFR design was 2650°C, the lower bound of the UO_2 fuel melting temperature. The peak fuel temperature limit of 1800°C set for our present design is based on 1) no melting of $(U,TRU)O_2$ fuel, 2) no melting of BeO diluent, and 3) chemical stability of the $BeO/(U,TRU)O_2$ mixture. The melting point of the $(U,TRU)O_2$ is assumed to be equal to the value for $(U_{0.8}Pu_{0.2})O_2$ of 2750°C [Waltar, et. al., 1981] and BeO melts at around 2570°C. BeO is chemically stable with UO_2 and PuO_2 up to 2135°C. [Sarma, et. al.,

2005] Although in general it is desirable to have lower temperatures in fuel in order to reduce the stored energy at the outset of a transient, an exact steady state fuel temperature limit based on this constraint can only be determined through detailed transient calculations and is difficult to specify a priori.

The pressure drop across the core is an important design parameter. At full power operation, the core pressure drop directly impacts the compressor work (back work) and thus has direct bearing on the thermodynamic efficiency of the power cycle. The core's resistance to coolant flow also impacts blower power requirements during refueling and accident conditions. Also of great significance is the fact that a core with a high pressure drop will tend to perform poorly in natural circulation cooling at pressure or in a post-LOCA depressurized state. For this work, a full power core pressure drop limit of 500 kPa is set.

Typically in GFR design (and in otherwise-cooled fast reactors), a small core H/D is specified, commonly referred to as a "pancake" core. This is done in order to mitigate the typically-positive coolant void reactivity in fast reactors, and to reduce the pressure drop across the core. This ratio, however, cannot be reduced to an arbitrarily small value for two reasons: the core leakage would become too high to give an acceptable conversion ratio and the reactor vessel diameter requirements would be too large. This parametric study involves determining the smallest core diameter which can be used while satisfying the design limits set forth in Table 5-2, but the core diameter is not limited by a particular number at this point. In the following chapter, fuel assemblies will be sized and arranged into a core taking into account duct walls, inter-assembly gaps, reflector and shielding. Only then can the size of the required reactor vessel be ascertained.

Table 5-2. Imposed full power steady state design limits.

Parameter	**Value**
Peak clad surface temperature (°C)	800
Peak fuel temperature (°C)	1800
Total core pressure drop (kPa)	500

5.2.4 Results of Reference Core Parameters Study

FLOWSPLIT was used to calculate peak clad surface temperature, peak fuel temperature and core pressure drop over the range of core H/D and coolant channel diameters discussed above. Figure 5.1 shows the peak clad surface temperature versus core pressure drop. Each line represents a different core H/D and each point along a line represents a different coolant channel inner diameter in 0.5 mm increments. The shaded region shows the allowable design space bounded by the core pressure drop and peak clad surface temperature limits. As the channel diameter is decreased (corresponding to moving along lines in Figure 5.1 from top left to bottom right) and the number of channels is increased accordingly, the heat transfer area is increased, lowering heat flux and peak clad surface temperatures. Because this increases the wetted perimeter without changing the coolant flow area, the pressure drop increases as channel diameter is increased. From the standpoint of peak clad surface temperature, core H/D values greater than 0.4 can be ruled out, along with coolant channel diameters greater than 8.5 mm.

Figure 5.2 shows peak fuel temperatures versus coolant channel inner diameter for the range of core H/D values. Again, each datum on a line represents a different channel diameter in increments of 0.5 mm decreasing from 10 mm at the top left to 60 mm at the bottom right. The shaded region defines the design space bounded by the fuel temperature limit of 1800°C and the core pressure drop limit of 500 kPa. Based on these design limits, core H/D values greater than 0.35 can be ruled out, along with coolant channel inner diameters greater than 7 mm. This illustrates that based on the gap conductance and thermal conductivity estimates made in the last chapter, the fuel temperature limit is more constraining than the limit on clad surface temperature.

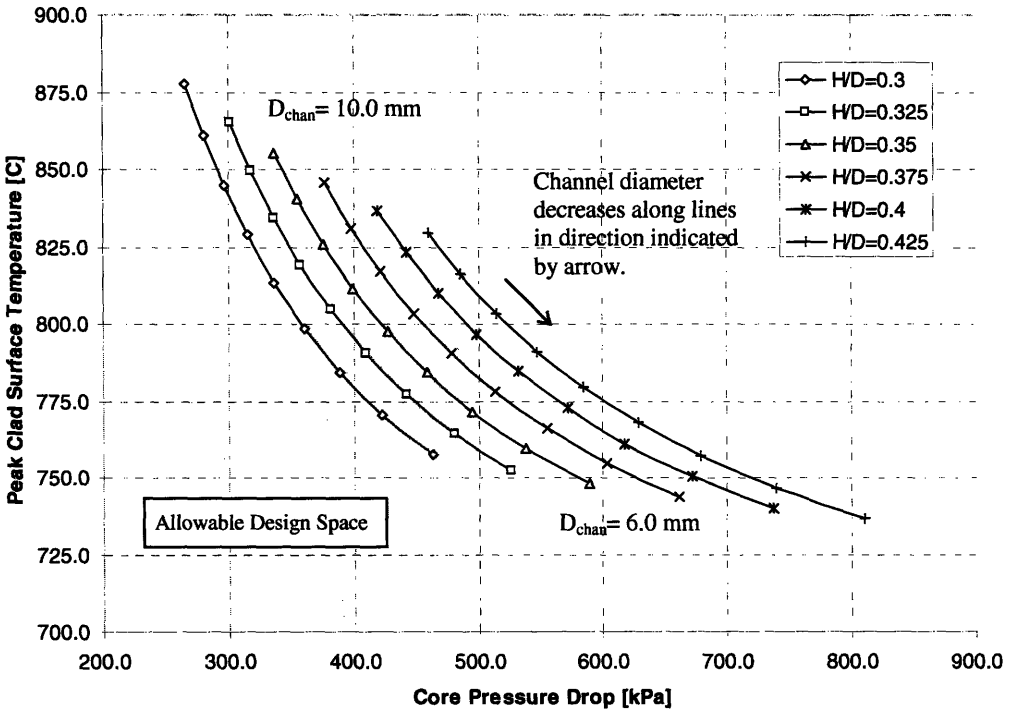

Figure 5.1. Peak clad surface temperature versus core pressure drop for various values of core H/D.

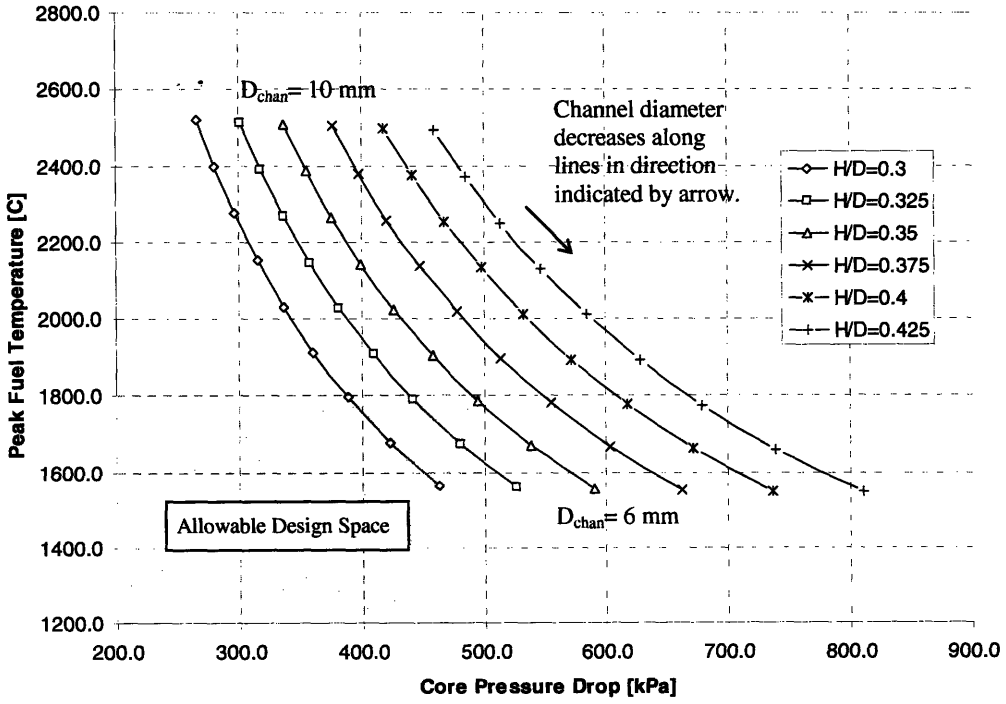

Figure 5.2. Peak fuel temperature versus core pressure drop for various values of core H/D.

In order to better examine the design space, data was arranged in the following way; for each core H/D evaluated, interpolation was performed in order to determine the coolant channel diameter which bounds the design space based on each of the design limits. Figure 5.3 shows the lines formed from these limiting channel diameters versus core effective diameter. The arrows indicate the direction one may move along the y-axis and continue to satisfy its associated limit. For example, the top line gives coolant channel inner diameters which give a peak cladding temperature of 800°C. The associated arrow points down, so for a given core diameter, smaller (and more numerous) coolant channels than those on the line will also satisfy the clad temperature limit of 800°C. Although not used as a design limit in this work, a line is shown giving the channel diameter necessary to achieve a peak clad surface temperature of 750°C. This is given in order to show that in order to achieve clad temperatures close to those limiting the GA GCFR design, a significantly larger core diameter would be required in order to avoid excessive pressure drop.

Several observations can be made from the data shown in Figure 5.3. While the maximum allowable coolant channel diameter required to satisfy clad temperature limits decreases significantly as the core diameter is increased, the peak fuel temperature limit is essentially satisfied by a coolant channel diameter of 7 mm or less over the range of core diameters investigated. More sensitive to core diameter is the minimum required coolant channel diameter which satisfies the pressure drop limit of 500 kPa. As seen in the previous two figures, the peak fuel temperature limit of 1800°C is a more limiting parameter than is the imposed clad temperature limit of 800°C. The selected design point, shown graphically on Figure 5.3 and numerically in Table 5-3, is a coolant channel inner diameter of 7 mm and a core effective diameter of 4.54 m. To maintain 25% coolant by volume, the number of channels required is around 101,000.

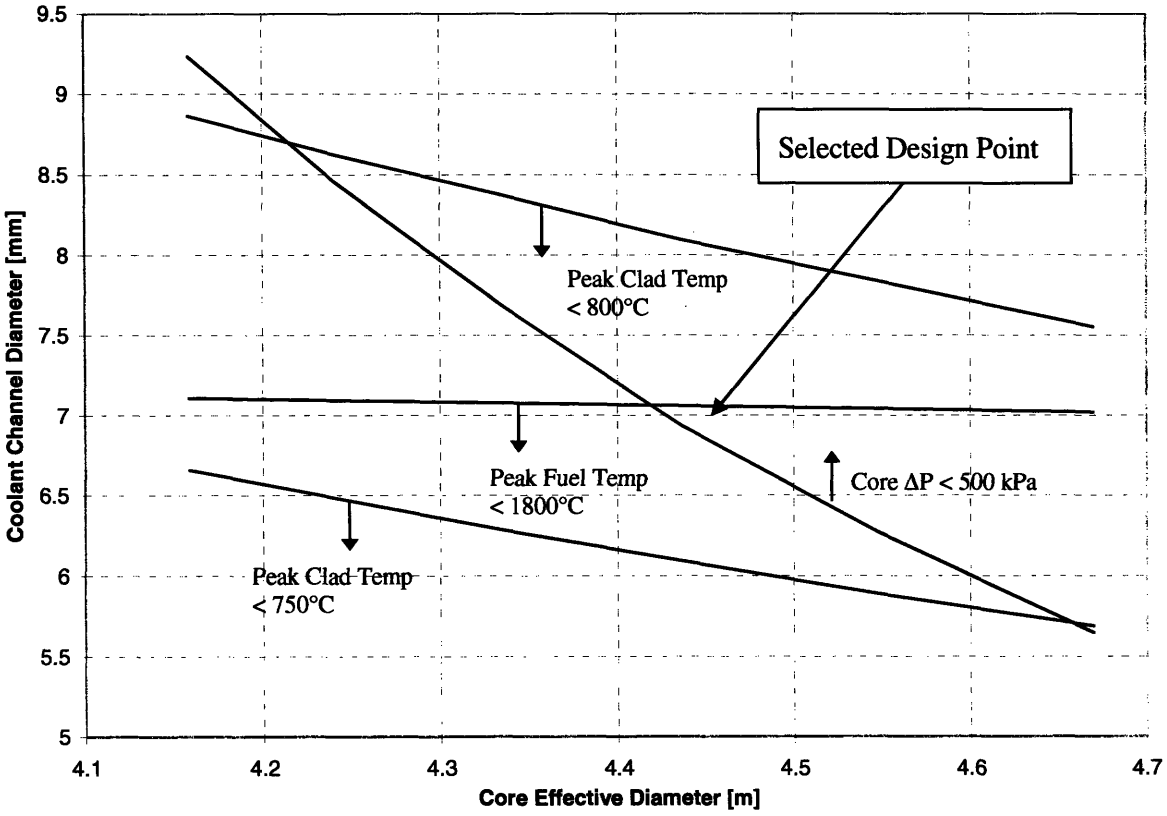

Figure 5.3. Coolant channel diameter required to satisfy selected design objectives versus core effective diameter.

Table 5-3. Recommended core parameters and performance based on two-channel calculations.

Parameter (units)	**Value**
Active core height (m)	1.54
Active core effective diameter (m)	4.45
Coolant channel inner diameter (mm)	7.0
Number of coolant channels	101,000
Peak fuel temperature in average channel (°C)	1646
Peak fuel temperature in hot channel (°C)	1787
Peak clad surface temperature in average channel (°C)	732
Peak clad surface temperature in hot channel (°C)	772
Total core pressure drop (kPa)	487

5.3 Potential for Heat Transfer Augmentation

Gases typically have lower convective heat transfer coefficients than other coolants. Therefore, heat transfer surfaces in the core are often altered in such a way that the heat transfer coefficient is increased to a greater value than for a smooth channel. Many different methods exist for increasing the heat transfer coefficient of a surface. The purpose of these methods is to either reduce the required size of a heat exchanger for a certain duty or to reduce the temperature of a surface in contact with a fluid for a given heat flux as in the case of a reactor core. Heat transfer augmentation has been studied extensively and the variety of methods available is quite wide. The GA GCFR design included specifications for transverse trapezoidal ribs raised from the surface of the fuel pins. [Eaton, et. al., 1975]

Methods of heat transfer augmentation include sandpaper-type roughening, repeated or spiral ribs of various shapes and pitches, wire coil wrapping (or inserts for an internal channel) [Ravigururajan, et. al., 1996], twisted tape inserts, dimpled surfaces [Ligrani, et. al., 2005], etc. The degree to which heat transfer coefficients are increased by the augmentation technique is typically given by the Nusselt multiplier (Nu/Nu_s) which gives the ratio of augmented to smooth Nusselt numbers, where the subscript s stands for the smooth surface. Any heat transfer augmentation comes with a friction factor penalty quantified using an analogous friction factor multiplier (f/f_s) which is the ratio of augmented friction factor to the smooth friction factor. Note that these smooth values are not referring to a perfectly smooth surface, but rather a real surface without any augmentation. The ratio of Nusselt multiplier to friction factor multiplier $(Nu/Nu_s)/(f/f_s)$ is referred to as the Reynolds analogy performance parameter. High values of this parameter indicate better heat transfer augmentation for a given pressure drop penalty. The highest values of this parameter are achieved by dimpled surfaces followed by repeated rib configurations. [Ligrani, et. al., 2003] A problem with dimpled surfaces for this application is that they are essentially a removal of material from the cladding, weakening the first fission product barrier. Repeated ribs protruding from the surface do not weaken the cladding and their size and pitch can be tailored to give the required augmentation, but manufacturing small ribs inside ODS tubing with an inner

diameter of 7 mm is an open issue and may increase costs significantly. Wire coil inserts are simpler to manufacture, but because their contact with the surface is loose compared to a raised rib, the heat conduction from the cladding wall to the coil is low causing low performance compared to integral protrusions. [Rohsenow, et. al., 1998] Twisted tape inserts are a type of swirl-flow device which increase heat transfer coefficients in heated flow. [Kreith, et. al., 1986] Both coil and twisted tape inserts may subject the tubing to fretting due to flow-induced vibrations.

In the case of the present work, core pressure drop is quite high even without heat transfer augmentation, due to the high Reynolds number (~500,000) of the flow in the core coolant channels. The friction factor penalty of augmented surfaces is therefore difficult to withstand without exceeding acceptable core pressure drop limits. Furthermore, the high fuel temperatures resulting from the use of oxide fuel and low coolant volume fraction are potentially more limiting than the clad surface temperature limit. Augmenting heat transfer on the cladding surfaces would not reduce significantly the maximum fuel temperatures because the temperature rise across the fuel is much larger than the bulk temperature rise. The friction factor penalty of augmented surfaces would require larger coolant channels and thus a larger pitch in order to simultaneously satisfy the core pressure drop limit and maintain approximately 25% coolant by volume. The resulting increase in fuel temperatures from this change in the lattice would counteract any lowering of fuel temperature from the augmentation alone. Heat transfer augmentation also significantly degrades the natural circulation capabilities of the system post-LOCA, an effect which will be revisited in a subsequent chapter.

At this point, heat transfer augmentation is discarded for the aforementioned reasons. However, implementation of one of these methods should be kept open in case fuel temperatures are found to be lower than current estimates due to either a change in specified fuel composition or new information about the thermal conductivity of the current fuel in the operating conditions and geometry specified for this design.

5.4 Potential for Coolant Channel Orificing

Channel orificing is used to satisfy a given design limit with as little coolant mass flow rate as possible. In a GFR, the limit of interest is either peak cladding temperature or peak fuel temperature. Flow to channels with low power density is constricted using a reduced-area orifice, forcing more flow into channels with higher power density. In this way, coolant is delivered at a rate appropriate to the power density of each fuel assembly or zone of the core, and a given temperature limit can be respected with a lower circulator power than in the un-orificed case. Because channel orificing is a method of manipulating the film temperature rise, which is much smaller than the temperature rise in the fuel, it is better suited to minimizing peak cladding temperatures than fuel maximum temperatures. This is therefore the most common objective of orificing in a gas cooled reactor design. An analytical treatment of coolant channel orificing for major nuclear reactor types, including a GFR, gives a methodology for determining the mass flow rates which will give equal peak cladding temperatures in all channel types based on their relative power. [Ribeiro, 1974] The author concludes, however, that this somewhat rigorous method is not necessarily worthwhile because the radial power shape changes with time, making this level of optimization excessive. A much simpler method is to orifice for uniform bulk coolant exit temperatures, which gives nearly constant peak cladding temperatures in all channels. This means that channel mass flow rates should be proportional to their integrated power.

In the present work, a coolant channel orificing scheme for fueled assemblies is not pursued for the following reasons;

- The benefits of orificing increase with radial peaking factor and the reference design is expected to have a radial peaking factor of 1.15 or less using diluent zoning in combination with control rods. Furthermore, the peaking factor remains essentially the same over the core's lifetime. [Handwerk, et. al., 2006] Therefore, the benefit from orificing in this design is minimal. Past fast reactor designs have used radial blankets, which have very low power at beginning of life. These assemblies were orificed in order to divert more flow to the higher-power driver fuel assemblies.

- If the core coolant channels (or subassembly inlets) are orificed, the coolant channel diameters would be made larger to compensate for the increased pressure drop. Because P/D_{chan} is fixed by the coolant volume fraction, the pitch would also be increased and the fuel temperatures would be higher. As illustrated in Figure 5.3, the peak fuel temperature is more limiting than the 800°C peak cladding surface temperature in the present design.

Although at this point in the design process, coolant channel orificing is not deemed favorable, final determination of whether orificing should be employed can only be made after a refueling and/or fuel shuffling scheme is developed. One possible refueling scheme for this design is a "battery" type core wherein a single batch of fuel remains in place without shuffling for its entire life. In this design, power shifts slightly between outer and inner fuel zones during the life of the batch. [Handwerk, et. al., 2006] Orifices or control rod programming would need to be adjusted either online or during an outage in order to keep an optimum configuration.

With the low peaking factors expected of this design, the absence of radial fertile blankets and the limiting fuel temperatures, orificing is discarded. However, if lower fuel temperatures are achieved in later work or if cladding surface temperatures prove too high from a materials standpoint, the potential gain from orificing should be revisited.

5.5 Lower-Temperature Alternative Core Design

If in later work, operating near the design limits set forth in Table 5-2 is found to be too aggressive from the standpoint of materials corrosion and creep, the desired parameters of this lower-temperature alternative core would differ from the reference design. It is therefore of interest to investigate the benefits of operating a lower temperature cycle from the standpoint of core design. The analysis performed here is basically the same as the one described in Section 5.2 with differences in core inlet and outlet temperatures and a higher mass flow rate. The lower-temperature design has core inlet and outlet temperatures of

417°C and 550°C and a mass flow rate of 14,568 kg/s. The remaining parameters used in this study are identical to those given in Table 5-1.

Figure 5.4 shows peak clad surface temperature versus core pressure drop for various values of core H/D and a range of coolant channel inner diameters. Figure 5.5 shows peak fuel temperature versus pressure drop for the same range of H/D and D_{chan}. Two lower values of H/D were added which were not analyzed in the 650°C case because the higher mass flow rate results in higher pressure drops. Figure 5.5 shows that the fuel temperature limit, which was the most constraining limit in the 650°C case, now cannot be met with in conjunction with the pressure drop limit of 500 kPa unless the core H/D is less than 0.3.

Therefore, the lower-temperature alternative cycle having the same pressure as the reference design offers no significant advantage over the reference design due to the significantly higher mass flow rate. Another option would be to increase the peak cycle pressure and lower the mass flow rate, but this would have a significant impact on reactor vessel design. A larger temperature rise across the core would also allow a smaller mass flow rate, but the higher density which would result would increase the coolant void reactivity.

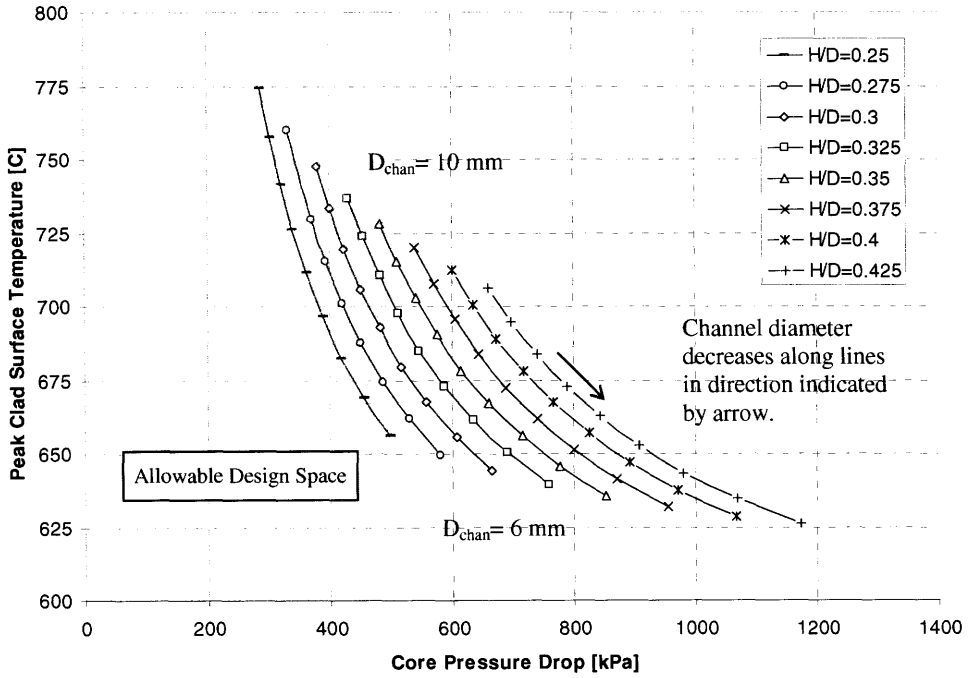

Figure 5.4. Peak clad surface temperature versus core pressure drop in 550°C alternative core.

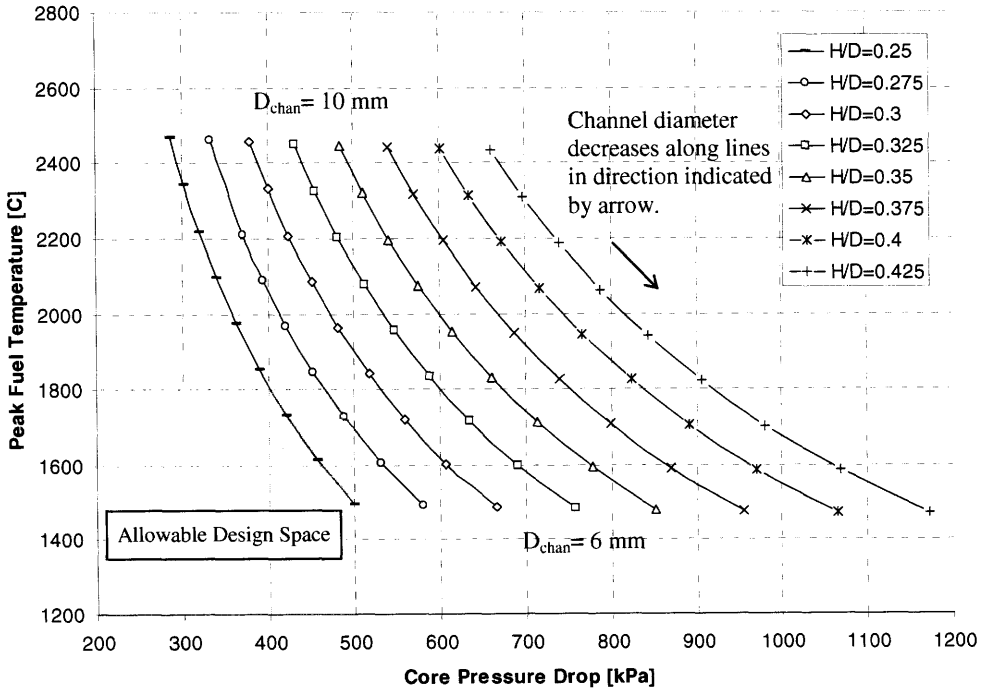

Figure 5.5. Peak fuel temperature versus core pressure drop in 550°C alternative core.

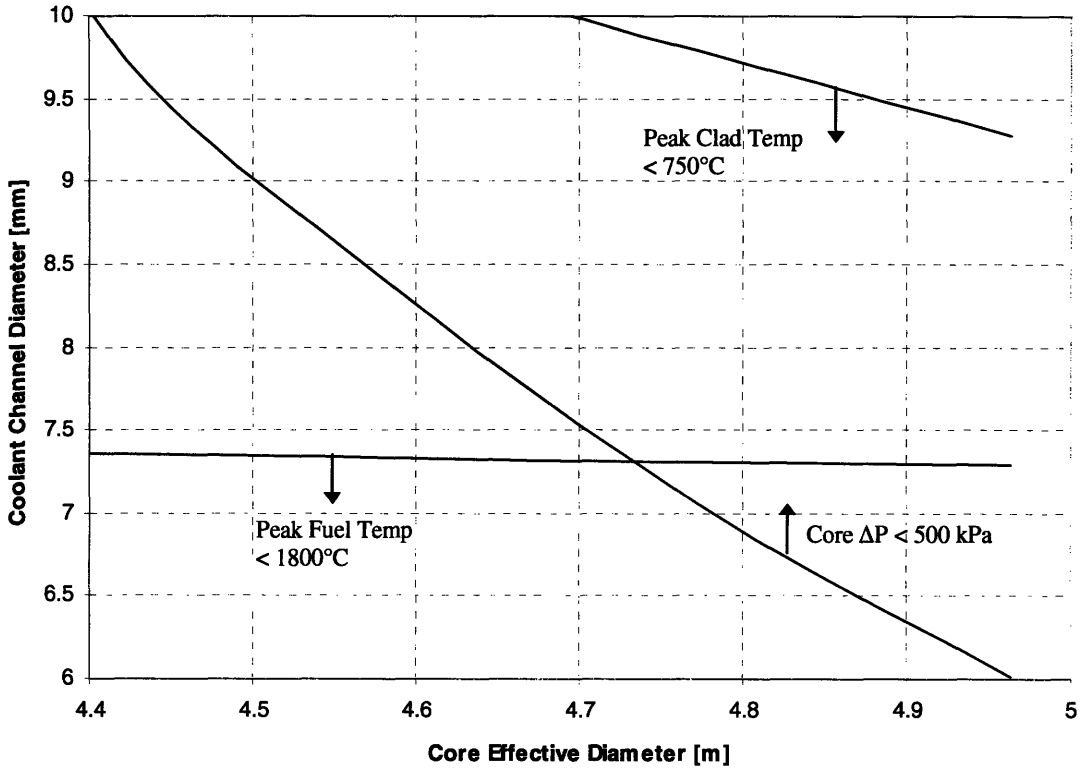

Figure 5.6. Coolant channel diameter required to satisfy selected design objectives versus core effective diameter in lower-temperature alternative core.

5.6 Summary

In this chapter, analyses were performed to determine the set of core parameters, particularly coolant channel pitch and diameter and core height and diameter, which satisfy the design limits for steady state full power operation selected for this design (shown in Table 5-2). The calculations were based on the assumption that all heat is transferred to coolant through cylindrical coolant channel walls only, and excluding duct walls. Bypass flow between assemblies and in the radial shield and reflectors was also neglected. The recommended core parameters based on this study are given in Table 5-3. In the following chapter, a more realistic core design having fuel assemblies with inter-assembly flow and heating, shielding assemblies and a reflector region, is developed.

Once these reference core parameters were established, three alternative core design options were discussed. Reduction of cladding temperatures by augmentation of heat transfer surfaces is discarded due to the already-large pressure drop in the core with smooth channels and the high fuel temperatures resulting from use of oxide fuel and low coolant volume fraction. It should also be noted that a significant manufacturing simplification is retained by specifying smooth coolant channels. Furthermore, the feasibility of some of the typical means of heat transfer augmentation on the inside of 7 mm diameter ODS steel tubes is an open issue. Use of coolant channel (or assembly) orificing was also discussed briefly in this chapter. As in the case of heat transfer augmentation, this was discarded due to some specific characteristics of the design. First, the very low radial power peaking expected of this design ($\leq$1.15) means that the benefit from orificing is minimal. As was mentioned in the case against heat transfer augmentation, the high fuel temperatures are potentially more limiting than cladding temperatures and they are not improved by implementing an orificing scheme. Also, because neither a fuel reloading and/or shuffling scheme or a control rod insertion sequence have been settled upon at this point, an orificing strategy cannot be fully designed. Both the potential for heat transfer augmentation and coolant channel orificing should be left as options for later revisions of the design if the conditions necessitate such measures.

Calculations were performed in order to determine the benefits on the core design of a lower-temperature alternative cycle having a core outlet temperature of 550°C. While a core for this cycle was found to have a significantly lower peak cladding surface temperature, the pressure drop was higher than the reference design due to a 24% larger mass flow rate. The core diameter required to simultaneously respect the limits on core pressure drop and peak fuel temperature is larger than that for the reference (650°C core outlet) design. While this lower-temperature alternative cycle may be attractive for materials reasons because of the lower temperatures, there is little benefit from the standpoint of meeting core design limits other than cladding temperature while maintaining a reasonably-sized core diameter and reactor vessel. A lower flow rate could be achieved by increasing the peak pressure, thus respecting the pressure drop limit.

6 Core Layout and Reactor Vessel Considerations

6.1 Introduction

In the previous section, simple thermal-hydraulic calculations were used to find core parameters which satisfy relevant core design goals and temperature limits. The parameters listed in Table 5-3 were recommended based on these calculations. These recommended core parameters, however, are based on the assumption of a lattice of coolant channels in fuel without heated inter-assembly spacing or core bypass to cool reflector or shielding assemblies. The size of fuel assemblies, the number of coolant channels per fuel assembly and the number of fuel assemblies in the core must be determined as well as the spacing between fuel assemblies. In this chapter, a more detailed core design is developed accounting for individual fuel assemblies and the bypass flow between them. Fuel assemblies are arranged in the core and the reflector and shielding regions are sized. Once the outer dimensions of the shielding are known, the barrel and downcomer can be sized. This sets the inner diameter of the reactor vessel. Because of this dependency, the selection of a reactor vessel type is included in this chapter.

6.2 Distribution of Coolant Channels among Fuel Assemblies

The number of coolant channels recommended in the last section (101,000) must be distributed among a number of fuel assemblies in an actual core design. In order to investigate options for this distribution, some nomenclature is first described. Assemblies are designated as having a number of "rings" which surround the central channel. For example, the lattice shown in Figure 6.1 has 2 rings because there is the central coolant channel and then two surrounding rings. The core is given an analogous designation, but with its number

of rings referring to the number of rows of assemblies surrounding the central assembly. Figure 6.2 shows a two ring arrangement for a core.

Table 6-1 shows combinations of different core and assembly sizes and the resulting number of channels in the core. The left-hand column gives number of rings in an assembly and the next column gives the resulting number of channels in that assembly. To the right on the table, the top row in bold gives number of assembly rings in the core with the number of resulting assemblies just below that in bold. The table then gives the resulting number of channels in the core.

It should be noted that Table 6-1 is based on two major assumptions which will not be true in the final design; one is that each assembly will have a fueled channel in all cells in its lattice. The other assumption is that the core will be arranged in a perfect hexagon with no control assemblies. In a real assembly, the six corner locations are assumed to be without fuel in favor of lifting lugs and fission gas conduits, and several of the assembly locations in the core will be occupied by control rods. The values of interest in Table 6-1 are those that exceed the 101,000 value, as it is known that some of the coolant channel locations accounted for in this table will actually be lost to controls, lifting lugs, fission gas conduits, etc.

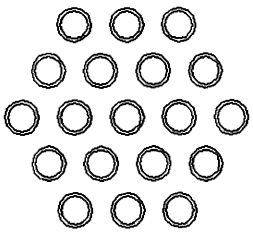

Figure 6.1. A two-ring arrangement of coolant channels in an assembly.

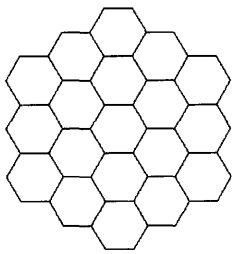

Figure 6.2. A two-ring arrangement of fuel assemblies in a core.

Table 6-1. Combinations of number of rings in assemblies and core and their resulting number of channels.

Channels per Assembly		Assemblies in core							
		Rings	8	9	10	11	12	13	14
Rings	Channels	Assemblies	217	271	331	397	469	547	631
4	61		13237	16531	20191	24217	28609	33367	38491
5	91		19747	24661	30121	36127	42679	49777	57421
6	127		27559	34417	42037	50419	59563	69469	80137
7	169		36673	45799	55939	67093	79261	92443	106639
8	217		47089	58807	71827	86149	101773	118699	136927
9	271		58807	73441	89701	***107587***	127099	148237	171001
10	331		71827	89701	109561	131407	155239	181057	208861

There are trade-offs involved in selecting a number of fuel assemblies and the number of channels per assembly. A large number of relatively small fuel assemblies will require a larger amount of core volume dedicated to duct walls and bypass flow between assemblies. A small number of large assemblies, on the other hand, reduces the number of options for control rod locations and refueling strategies. An 11-ring core with 9-ring assemblies was selected as a compromise in this trade-off. The resulting number of fuel assembly locations is 397, 19 of which will be set aside for control rod locations, leaving 378 fuel assemblies. This allows for about 6,500 extra channel locations beyond the 101,000, which will be used for the purposes described above.

Figure 6.3 shows a horizontal cross-section of the 9-ring TID fuel assembly with corner locations left empty. Outer dimensions of the duct are given in cm. As explained previously, P/D_{chan} is set at 1.905 and since the channel diameter was selected to be 7 mm, the pitch has a value of 13.3 mm. This value, along with the number of rings and the duct wall thickness of 2 mm, set the outer dimension of the duct at 22.7 cm flat-to-flat. Since steady state full power operations apply in these calculations, the specified dimensions are those at hot conditions.

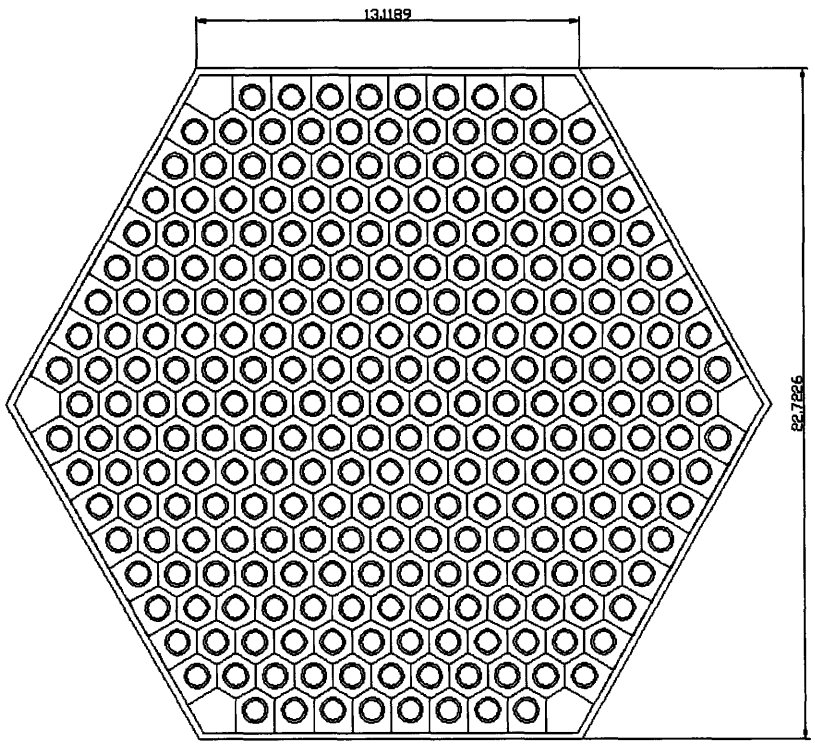

Figure 6.3. Horizontal cross-section of TID fuel assembly with hot dimensions in cm.

6.3 *Inter-Assembly Spacing*

The core will be arranged such that some coolant will bypass the coolant channels, and flow between adjacent fuel assemblies. This flow must be sufficient to remove heat from the duct wall, keeping its temperature below 800°C. The required spacing between ducts is dependent upon the fraction of heat which is transferred to coolant through the duct walls into the inter-assembly flow rather than through coolant channel walls. In this section, an estimate is made for that fraction and sufficient cooling of the duct wall is evaluated for a range of inter-assembly gap sizes and inlet loss coefficients using FLOWSPLIT. The assumed heat flux through the duct wall is later compared to results from using a finite element analysis (FEA) heat transfer package along with the FLOWSPLIT code.

6.3.1 Estimate of Heat Flux through Duct Wall

In moving from the infinite-lattice calculations performed in Chapter 5 to the design of actual assemblies, fuel is added by squaring one side of the hex-nut pellets at the fuel assembly periphery. This "excess" fuel is shown graphically in Figure 6.4. Some of the heat produced in the peripheral fuel pellets will be transferred to coolant through the duct wall and some will be transferred through the cladding into coolant in the channels. It is assumed at this point that heat generated in the excess fuel portion is transferred to coolant through the duct wall, with the remaining heat being transferred to coolant through the channel cladding. The excess fuel region shown in Figure 6.4 accounts for 4.5% of the total inventory of fuel. If a constant volumetric power in fuel is assumed, then the rate of heat transferred through the duct wall to inter-assembly coolant flow is 4.5% of the total core power, or 108 MW_{th}, leaving the remaining 2292 MW_{th} to be transferred through the coolant channel cladding. This relieves some of the heat removal duty from the coolant channels, but also diverts some of the flow away from them as well.

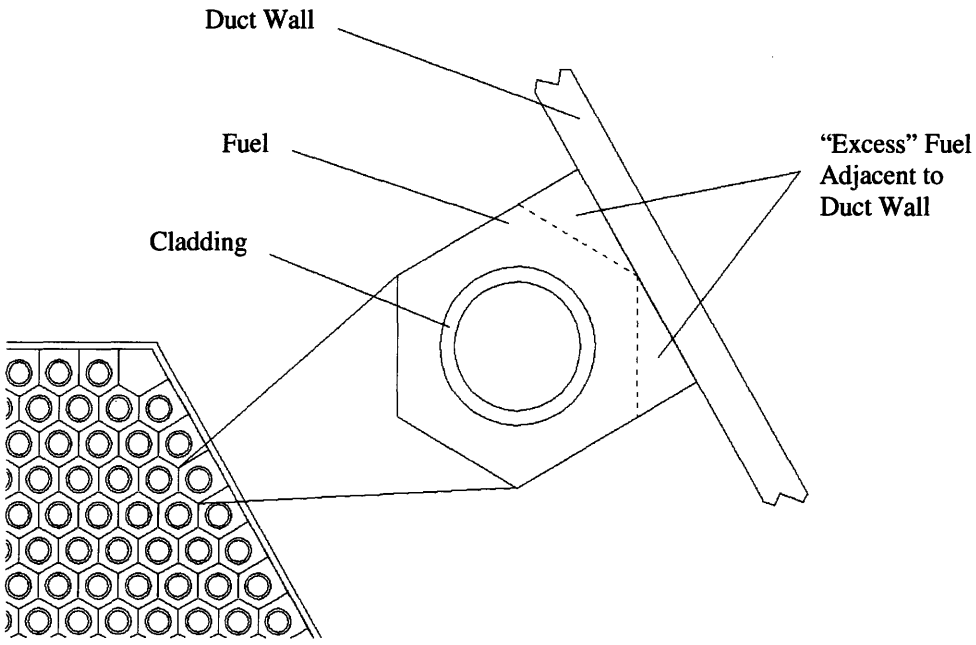

Figure 6.4. Excess fuel present in pellets adjacent to duct walls.

6.3.2 Sizing of Inter-Assembly Gaps

In this section, the sizing of inter-assembly gaps is investigated. In addition to the assumption made above dealing with the balance of heat transfer between coolant channels and duct walls, several other simplifications are made in this analysis. One is that the fraction of local power which is removed through the duct wall is constant axially. This gives a chopped cosine power distribution with peaking factor of 1.3 through the duct wall, just as in the round coolant channels. Another assumption is that the heat flux through a duct wall is constant along its perimeter (as viewed from above). Duct walls are assumed to have roughness of 45μm.

During initial heat-up of the fuel, the fuel assembly duct wall expands based on the temperature increase from cold to hot conditions and the coefficient of thermal expansion of the duct wall material. This expansion of the duct shrinks the width of inter-assembly gaps, thus constricting flow somewhat. For a conservative verification that the duct wall can be cooled by the flow in the inter-assembly gaps, a cold-to-hot average temperature change of 800°C was assumed and the coefficient of thermal expansion for MA956 is again taken to be 12.3×10^{-6} °C^{-1}. Given these values, the inter-assembly spacing after heatup is calculated and the gap size is reduced accordingly.

The flow between assemblies was modeled in FLOWSPLIT as a lumped single channel, the flow area of which was calculated by summing the area of the hot inter-asssembly gaps. This flow area changes significantly for each cold gap size used. The heated/wetted perimeter was found by simply adding the perimeters of all 378 fueled assemblies. The average heat flux at the interface between the duct wall and coolant was calculated by dividing the 108 MW_{th} by the total duct outer surface area, giving 2.3×10^5 W/m^2. Since the wetted/heated perimeter changes by only a few percent from thermal expansion, these values were not recalculated for the hot dimensions, as the inter-assembly flow area must be.

The flow paths between assemblies were initially modeled as having inlet and outlet loss coefficients of 0.5 and 1.0, respectively. Different cold gap sizes were used ranging from 4 to 6 mm. Other than the extra inter-assembly flow and the new distribution of heat

flux between coolant channels and duct wall, the remaining parameters detailed in Table 5-1 were used. The results of the calculations are shown in Table 6-2.

Table 6-2. Performance of inter-assembly flow paths for various gap sizes.

Inter-Assembly Gap (mm)		Inter-Assembly $\dot{m}$		Peak Coolant Channel T_{wall} (°C)	Inter-Assembly Outlet T_{bulk} (°C)	Peak Duct T_{wall} (°C)	Inter-Assembly Flow Pressure Losses (kPa)		
Cold	Hot	(kg/s)	(% of total)				Form	Friction	Total
4.0	1.8	427	3.7	781	688	713	16	439	463
4.5	2.3	628	5.4	786	624	651	21	419	448
5.0	2.8	860	7.4	792	587	616	26	397	430
5.5	3.3	1,108	9.5	799	564	595	30	375	412
6.0	3.8	1,369	11.7	806	550	582	34	353	394

Several observations can be made from the results in this table The total core flow rate is kept constant, and so some of the coolant which would have traveled in the coolant channels is diverted to between the assemblies. This hinders cooling inside the coolant channels. On the other hand, some of the heat removal is now taking place through the duct wall, partially offsetting the decreased flow inside channels. The net effect for the cases run here was that the peak coolant channel surface temperature increased slightly.

As the inter-assembly gap size is increased, the resistance to flow in these spaces decreases and the gaps receive more of the total core flow rate. The peak coolant channel temperature increases as the channels are deprived of flow. The flow rate in the inter-assembly gap increases, decreasing the coolant temperature at the outlet to these spaces. The heat transfer coefficient in the gaps also increases with this increase in flow, which, along with the lower coolant temperatures, decreases the peak duct wall surface temperature. The pressure drop across the entire core decreases with increasing inter-assembly gap size due to the fact that the assembly size was set prior to the calculations. Any addition of flow area between assemblies increases the core flow area, lowering total pressure drop of the core. This in turn increases the diameter of the core, albeit by a few centimeters in these cases.

These calculations can be used to set a lower bound on the spacing between assemblies, but larger inter-assembly gaps can be orificed in order to reduce the amount of

coolant bypassing the assemblies. Furthermore, in these calculations, the entrance loss coefficient for the inter-assembly gaps was set to 0.5, but in the actual design, the flow must be diverted somehow from the inlet plenum of the assembly to the region between ducts. From this, a large entrance loss coefficient is unavoidable. Therefore, it is worthwhile at this point to examine the sensitivity of the inter-assembly gap flow to entrance loss coefficient using a gap size sufficiently large to allow proper cooling with larger entrance loss coefficients for the inter-assembly gaps.

For these calculations, a cold gap of 5 mm (hot gap of 2.8 mm) was selected as it allows ample margin to increase the resistance to flow between assemblies and still provide sufficient cooling to the duct walls. The exit loss coefficient for all channels was left at 1.0, while the entrance loss coefficient to the flow between assemblies was varied from 0.5 to 10.0. Table 6-3 shows the results of these calculations. As the entrance loss coefficient to the inter-assembly flow is increased, the flow inside the coolant channels increases. This brings the cladding temperatures down and raises the duct wall temperature. From these results, it can be seen that a 5 mm cold gap (2.8 mm hot) is sufficient to cool the duct wall, even with a very large inter-assembly entrance loss coefficient. This gap size is thus selected as the inter-assembly spacing desired under hot full power conditions. The diversion of flow into the inter-assembly space will be sized in order to give an inter-assembly mass flow rate equivalent to the loss coefficient of 25.0 shown in Table 6-3.

Table 6-3. Performance of inter-assembly flow paths for various entrance loss coefficients and a hot inter-assembly gap size of 2.8 mm.

Entrance Loss Coefficient for Flow Between Assemblies	Inter-Assembly $\dot{m}$		Peak Coolant Channel T_{wall} (°C)	Inter-Assembly Outlet T_{bulk} (°C)	Peak Duct T_{wall} (°C)	Inter-Assembly Flow Pressure Losses (kPa)		
	(kg/s)	(% of total)				Form	Friction	Total
0.5	860	7.4	792	587	616	26	397	430
1.0	853	7.3	792	588	617	33	391	431
2.0	838	7.2	792	589	619	47	378	432
5.0	799	6.8	791	595	625	83	345	435
10.0	745	6.4	789	602	635	130	302	439
15.0	706	6.0	787	609	644	169	265	441
20.0	668	5.7	786	616	652	199	239	444
25.0	636	5.4	785	622	660	222	217	446

6.3.3 Design of Flow Diversion to Inter-assembly Gaps

In the previous section, the entrance losses associated with flow between fuel assemblies were modeled as a loss coefficient applied to the area of inter-assembly flow. In the real design, coolant must be diverted just before the lower plate of the assembly out through the duct wall and into the space between adjacent assemblies. This is shown schematically in Figure 2.4. This will be done by placing a round hole in each face of the duct just below the lower plate of the assembly. Since the form losses at the inlet to the inter-assembly flow channels will dominate the overall form losses, the hole used to divert flow to this section can be sized appropriately to give a form pressure loss of 222 kPa (the value shown for an entrance loss coefficient of 25.0 in Table 6-3). The total inter-assembly mass flow rate desired is 636 kg/s, as is also shown in the table. If this is divided by the number of fueled assemblies (378) and then by the number of sides of each TID duct (6) the mass flow rate which must pass through each hole is 0.28 kg/s. Note that each rectangular space between adjacent assemblies is fed by two holes in the duct wall. The pressure drop through the hole can be modeled with reasonable accuracy as flow through an orifice connecting two infinitely large plena by;

$$\Delta p = \zeta \frac{\rho v^2}{2} \tag{6-1}$$

where Δp is the form pressure loss at the entrance to the inter-assembly flow space, ζ is the loss coefficient, ρ is the fluid density, and v is the fluid velocity inside the orifice. For a relatively thin-walled orifice connecting two infinite plena, the loss coefficient is approximately equal to 2.8. [Idelchik, 1993] The velocity inside the orifice can be expressed by;

$$v = \frac{\dot{m}}{\rho A} \tag{6-2}$$

where A is the area of the orifice. If Equation 6-2 is substituted into Equation 6-1 and rearranged, the orifice area can be expressed as;

$$A = \dot{m}\sqrt{\frac{\zeta}{2\rho\Delta p}} \tag{6-3}$$

Substituting a mass flow rate of 0.28 kg/s, a loss coefficient of 2.8, a fluid density of 135 kg/m^3 and a pressure drop of 222 kPa (222,000 Pa) into Equation 6-3 gives an orifice area of 6×10^{-5} m. This is the area of a round hole with a diameter of about 9 mm. One of these can easily be drilled into each of the six sides of the TID assembly ducts just below the lower assembly plate in order to allow for sufficient cooling of duct walls. For the purpose of modeling flow through the inter-assembly channels in either RELAP or FLOWSPLIT, the loss coefficient of 25.0 will be applied to the entrance to the inter-assembly spaces as shown in the previous section.

6.4 Active Core Layout

Figure 6.5 shows the layout of the entire active core if arranged in a hexagonal shape without rounding corners. Two rows of reflectors (150 locations) are included along with three rows of shielding material (270 locations), each taking up the same space as fuel and control assemblies. Although 19 control assemblies are tentatively specified, their locations are not shown as this requires knowledge of power shapes, fuel shuffling schemes, etc., which will be determined only after the reactor physics design has been developed further. From the standpoint of thermal-hydraulics, their location does not affect calculations significantly.

The core barrel is a cylindrical structure which separates the core and the core bypass flow from the downcomer. If 5 cm clearance is allowed between the outermost shielding assembly and the inner surface of the core barrel, the inner diameter of the core barrel is set to 8.20 m. A thickness of 6 cm is specified for the core barrel making its outer diameter (downcomer inner diameter) 8.32 m. The downcomer width must be sufficiently large to allow for inspection of the reactor vessel and to achieve small pressure losses to maximize natural circulation flow after a LOCA. A width of 30 cm is specified here, a value which does not differ greatly from present-day LWR downcomer sizes. This sets the inner diameter of the reactor vessel to 8.92 m.

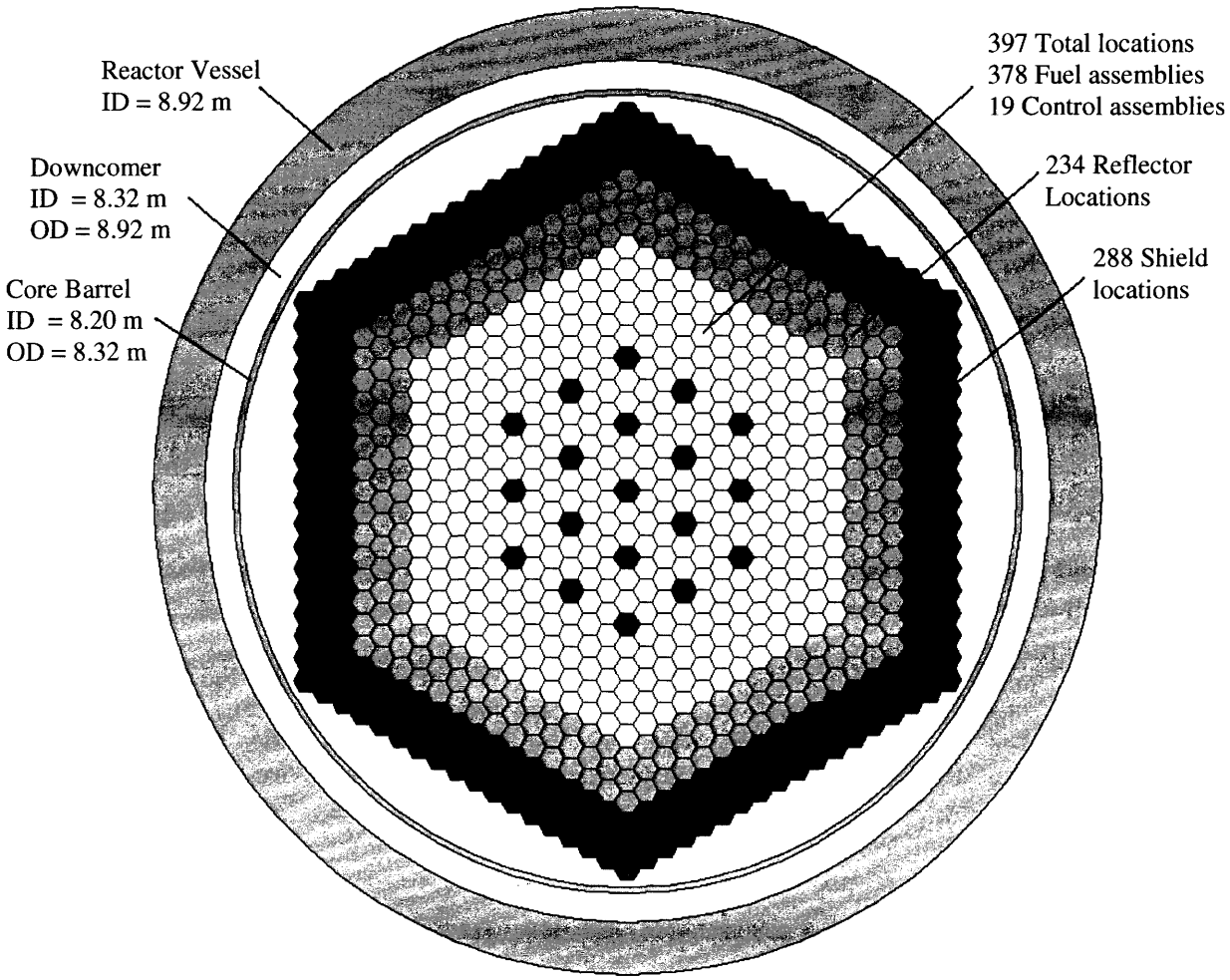

Figure 6.5. Horizontal cross-section view of core layout.

Table 6-4. Summary of parameters of active core.*

Parameter (units)	Value
Coolant Channels	
Inner diameter (mm)	7.0 (6.93)
Cladding thickness (mm)	0.7
Outer diameter (mm)	8.4 (8.32)
Channel pitch (mm)	13.3 (13.21)
Channel roughness (m)	1×10^{-5}
Lower inactive length (m)	1.1 (1.094)
Active length (m)	1.54 (1.530)
Upper inactive length (m)	1.0 (0.992)
Fuel Assembly Geometry	
Fueled locations per assembly	265
Unfueled locations per assembly (corners)	6
Duct wall flat-to-flat inner dimension (cm)	22.3 (22.1)
Duct wall thickness (mm)	2
Duct wall flat-to-flat outer dimension (cm)	22.7 (22.5)
Core Geometry	
Inter-assembly spacing (mm)	2.8 (5.0)
Fuel assemblies	378
Control assemblies	19
Reflector assembly locations	234
Shielding assemblies	288
Active core volume including control assemblies (m^3)	28.0
Active core effective diameter (m)	4.81
Active core H/D	0.32
Active core area including control assemblies (m^2)	18.2
Active core area excluding control assemblies (m^2)	17.3
Area Fractions (neglecting control assemblies)	
Coolant flow area (%)	24.7
Coolant in channels (%)	22.3
Coolant in inter-assembly gaps (%)	2.4
Steel (%)	13.2
Steel in coolant channel cladding (%)	9.8
Steel in duct walls (%)	3.4
Fuel (%)	59.6
Corner locations for vent tubes or lifting lugs (%)	2.5

* Hot dimensions are given with selected cold dimensions in parenthesis.

6.5 Radial Reflector and Cooling of Shield Assemblies

Axial reflectors and shielding are located within the TID fuel assemblies above and below the core. A fraction of the total thermal power appears as heat in the reflectors and shielding as a result of direct neutron and gamma heating. This relieves some of the heat removal duty of the active core. However, this has been shown to be quite small in this reactor (< 1% of the total thermal power), and thus analysis of the heat removal from axial reflector and shield regions is not performed. All heat transfer to coolant is assumed to take place in the active core. The constant-diameter coolant channels and inter-assembly gaps which span the length of the active core are more than sufficient to cool the much lower power density regions above and below the active core.

The radial reflector region is occupied by stagnant S-CO_2 in order to increase the reactivity feedback resulting from enhanced leakage in the event of a LOCA. Coolant enters the reflector region at the inlet temperature and is allowed to exit the top section slowly such that the CO_2 at the exit of the reflector region is not heated to above the average core outlet temperature. This keeps the density of the CO_2 reflector sufficiently high to provide the reactivity feedback for which it is designed.

The first row of radial shielding is exposed to the greatest neutron flux of any shielding and thus the necessity of internal cooling of these assemblies should be evaluated. The shielding material selected is boron carbide (B_4C) enriched to 99w/o ^{10}B. Reactor physics calculations show that the direct heating rate per assembly of the first, second and third rows of shielding are 19.4 kW, 444 W, and 106 W, respectively. The shielding assemblies are the same size as fueled assemblies in the active core (22.7 cm flat-to-flat hexagonal shape). If a single first-row shielding element is assumed to be a cylinder of equivalent height and volume, the change in temperature from its outer surface to its centerline based on an assumption of a radially-constant internal heat generation is given by;

$$\Delta T_{cyl} = \frac{q'}{4\pi k} \tag{6-4}$$

where ΔT_{cyl} is the temperature rise from outer surface to the centerline of a cylinder with linear power q' and constant thermal conductivity k. For the first row of shielding, the

average linear power times a peaking factor of 1.3 is 16.4 kW/m. If the thermal conductivity of B_4C is taken to be 30 W/m·K, this gives a temperature rise of 44°C. The same calculation on the second row of radial shielding results in approximately a 1°C temperature rise. These simple calculations are based on a constant heat generation rate radially within a single shielding assembly, an assumption which would not hold given a more detailed treatment. However, the very low temperature rises calculated and the extremely high melting point of B_4C (2445°C) suggest that internal cooling requirements of the shielding assemblies is not significant and can be neglected at this stage of design.

The inter-assembly flow paths between adjacent shielding assemblies are sized the same as those in the active core and these will comprise most of the unheated core bypass. The total area of these inter-assembly flow paths between shielding assemblies is 0.319 m^2. The heat flux on the perimeter of the shielding assemblies assuming no internal cooling is still much lower than the heat flux at the surface of the duct walls of the active core TID assemblies. This is true even if all of the heat in the first row of assemblies is transferred to coolant through half of its surface area which would simulate the uneven heating of the shielding assembly. In order to give a conservatively high estimate of the bypass flow, however, the same entrance loss coefficient is applied to the inter-assembly flow in the shielding region as in the active core. This loss coefficient of 25.0 will again be achieved using one 9 mm diameter hole per assembly flat, just as for the active core. Because the fraction of power which appears as direct heating in reflector and shield regions is less than 1% of the total thermal power of the reactor, the flow channels used to simulate the flow between shielding assemblies are, for modeling purposes, assumed not to be heated. This channel will be referred to as simply "bypass" flow in later sections.

Figure 6.6 shows T_{wall} and T_{bulk} versus axial distance from the bottom of the core for average, hot and inter-assembly flow channels in the final reference core as calculated in FLOWSPLIT. Figure 6.7 shows maximum fuel temperatures in average and hot channels versus axial position in the reference core design. Because FLOWSPLIT fuel temperature calculations are intended for cylindrical geometries, this figure does not include them for the inter-assembly flow channels.

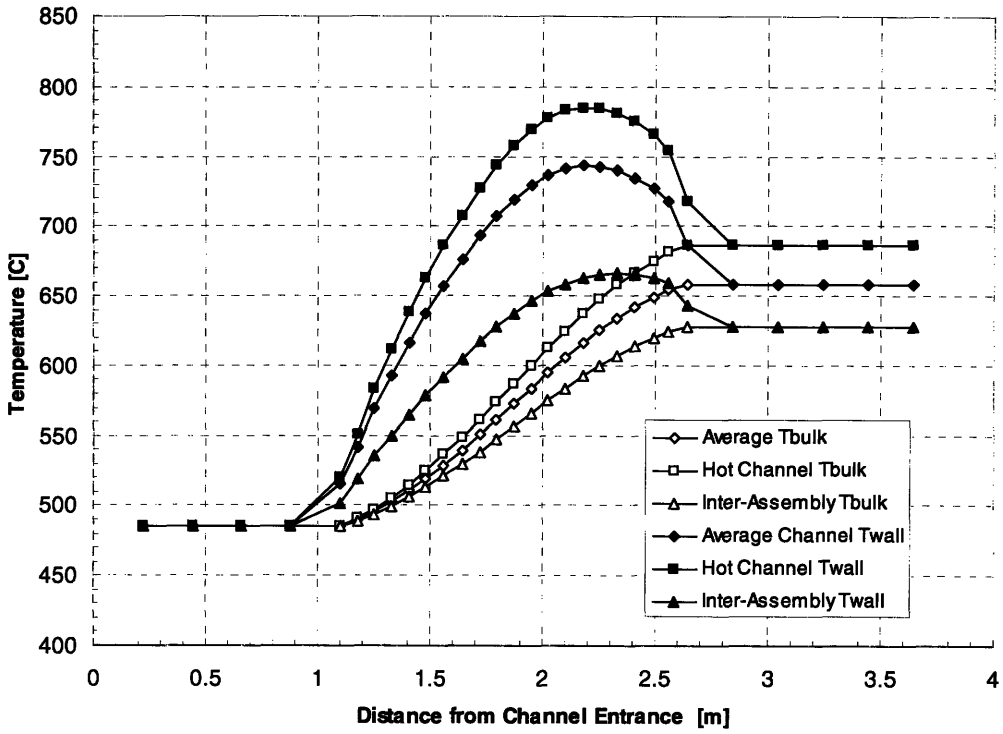

Figure 6.6. Bulk and wall temperatures for hot, average and inter-assembly channels in reference core design.

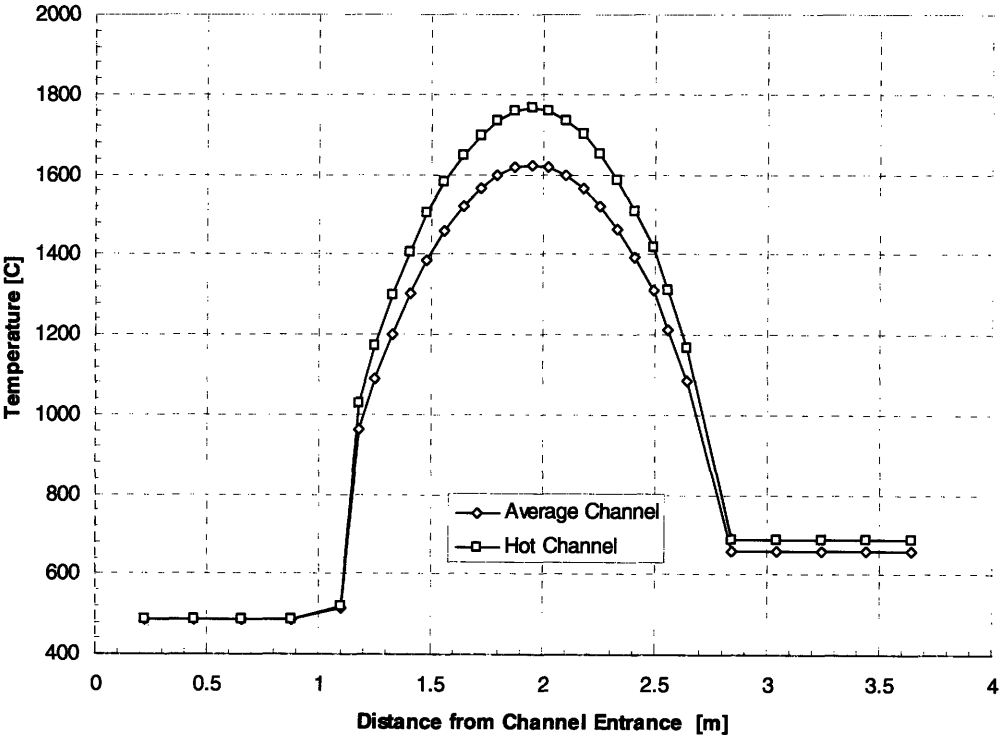

Figure 6.7. Maximum fuel temperatures in average and hot channels in reference core design.

6.6 Pre-stressed Cast Iron Vessel (PCIV)

As mentioned above, in order to accommodate this core with the radial S-CO_2 reflector and radial shielding while leaving sufficient room for a barrel and downcomer, the inner wall of the reactor vessel needs to be around 8.92 m in diameter. For this design, a Pre-stressed Cast Iron Vessel (PCIV) is specified, a brief description of which is provided here. A PCIV has been considered for nuclear reactor vessel applications in the past. For example, Figure 6.8 shows a drawing of a proposed PCIV design for a Very High Temperature Reactor from [Ravets, et. al., 1975]. [Fishkin, 2004] reviews the extensive work on this type of vessel carried out in Germany in the past.

A PCIV consists of cast iron blocks fabricated to fit around a steel liner to form a cylindrical vessel. The cast-iron blocks are compressed axially by a pre-stressing system consisting of many independent steel tendons extending the length of the vessel. Radial pre-stressing tendons are also present around the circumference of the vessel. Thus the cast iron only bears a compressive load and the steel tendons a tensile load. Cast iron is well suited to this application for a number of reasons; it has a very high compressive strength, it resists creep up to 400°C and it is a well known and relatively cheap material. The liner is present to make the vessel leak-tight and is composed of a low-strength, high-ductility material. Advantages of using a PCIV include; [Fishkin, 2004]

- The PCIV is constructed from smaller sections which are easily transported for on-site assembly.
- If a pressure loss occurs in a PCIV, gas escapes between cast iron blocks and the vessel regains leak-tightness once the pressure inside is relieved. Because unstable crack growth is not possible in a PCIV, the claim is made that they are burst-proof.
- A PCIV can accommodate larger diameters than a steel vessel for a given pressure.

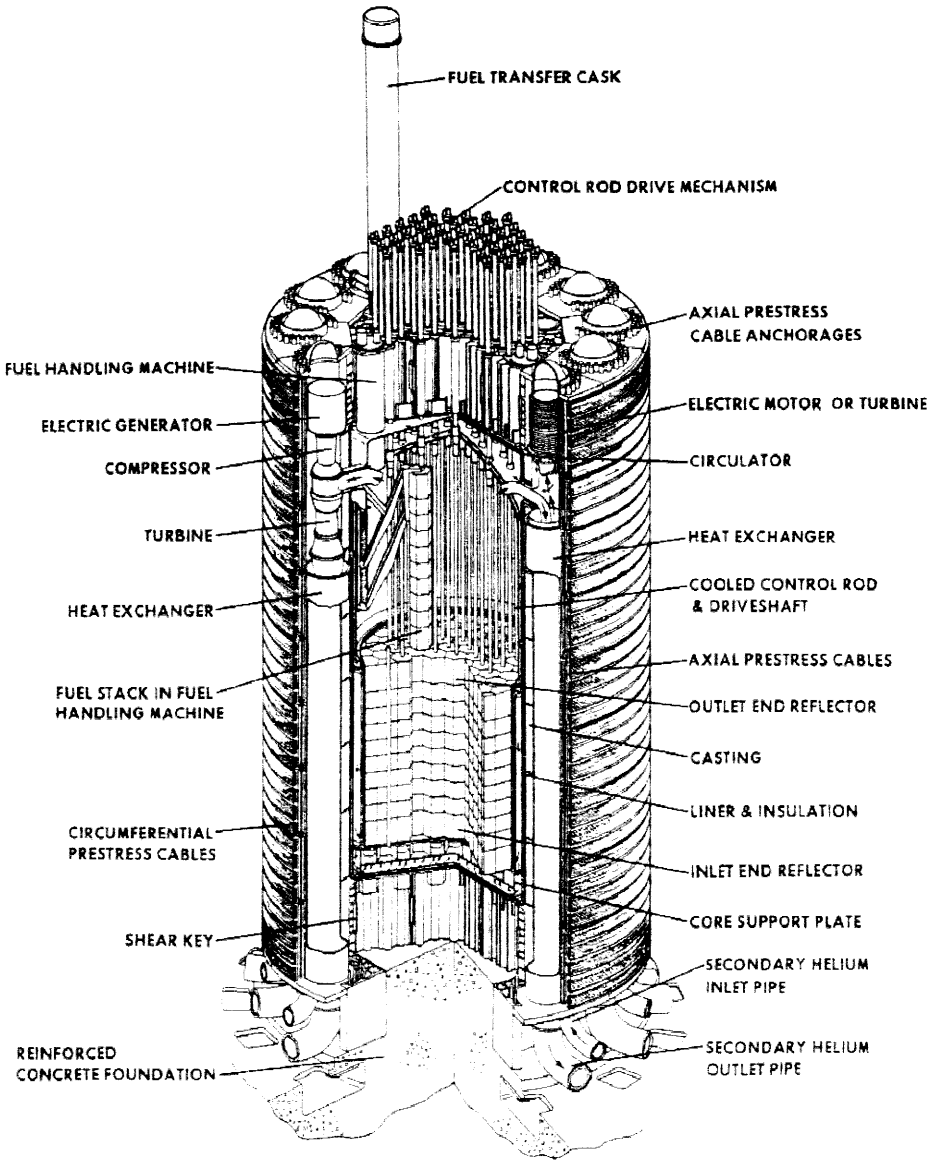

Figure 6.8. Cutaway view of PCIV for HTGR service. [from Ravets, et. al., 1975]

Figure 6.8 shows a PCIV with penetrations for coolant inlets and outlets located at the bottom of the vessel. However, for the present design, coaxial side penetrations are desired for connections to the PCS loops. Each side penetration creates a location where axial and radial prestressing tendons cannot be placed. This serves to limit the size and number of side penetrations which can be accommodated by the vessel. Figure 6.9 shows a cutaway drawing for a PCIV design which includes several side penetrations for gas circulation. This view illustrates how the cast iron blocks are fit together to form the cylindrical vessel. Figure

6.10 is a photograph of a finished PCIV with side penetrations. From this figure, one can clearly see the radial prestressing tendons and the region from which they are excluded surrounding the holes for gas circulator pipes along the side of the vessel. In the S-CO_2 cooled GFR design analyzed here, the vessel penetrations are fairly large (about 1.65 meters in diameter) and so the area which cannot have prestressing tendons is large. The structural integrity of the vessel given this fact is an open issue which should receive attention in future work. The size requirements for the vessel in this application are revisited in a later chapter as the design and location of the Shutdown/Emergency Cooling System heat exchangers impact the required height of the vessel. For the remainder of this work, it will be assumed that the components internal to the vessel can be accommodated by a PCIV.

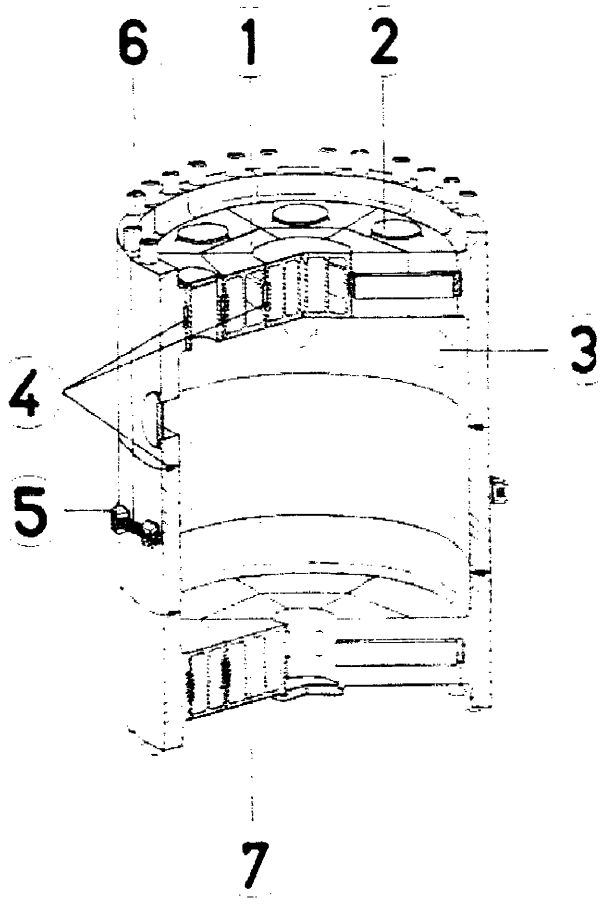

1. Top slab
2. Heat exchanger penetrations
3. Gas circulator penetrations
4. Horizontal and vertical down system
5. Horizontal prestressing system (schematically)
6. Vertical prestressing cables
7. Bottom slab

Figure 6.9. Cutaway view of PCIV with side penetrations. [from Schilling, et. al., 1973]

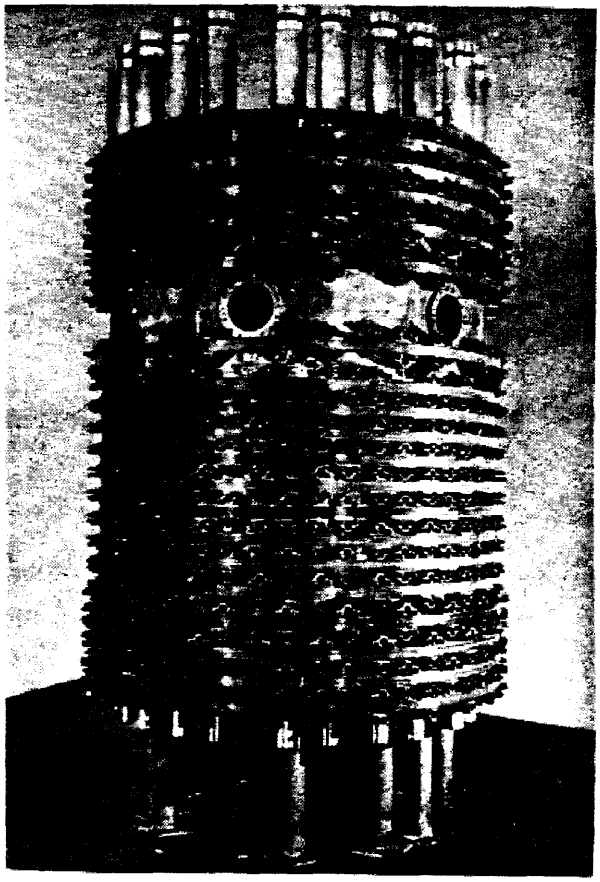

Figure 6.10. Photograph of a PCIV with gas circulator side penetrations. [from Schilling, et. al., 1973]

6.7 Summary

In this chapter, the core design was refined to include the number of coolant channels per fuel assembly, the number and arrangement of assemblies in the core and specifications for the reflector and shielding regions. These parameters were summarized in Table 6-4. The required spacing between assemblies was taken into account, resulting in a hot gap width of 2.8 mm; and the size of the hole on each of the assembly flats diverting inlet flow to the inter-assembly spacing was set to 9 mm in diameter. A major assumption which should be checked in future work is the assumed fraction of heat which is transferred to coolant through duct walls rather than through the cylindrical coolant channels. A more accurate estimate of this can be obtained by iteration between a two dimensional finite element analysis code and a 1-D thermal-hydraulic code such as FLOWSPLIT. With a S-CO_2 reflector region designed

to give low coolant void reactivity due to enhanced leakage and three rows of shielding, the vessel inner diameter must be at least 8.92 m. This diameter is too large for a steel vessel at the 20 MPa pressure required of the design. Therefore, a PCIV is specified for this application. The design of a PCIV with large side penetrations is an open issue at this point, which should be addressed in future work.

7 Evaluation of an Active/Passive Hybrid Decay Heat Removal System

7.1 Introduction

This chapter gives account of an evaluation of an active/passive hybrid Shutdown/Emergency Cooling System (SCS/ECS). The system uses blower-driven circulation as the primary means of decay heat removal, but the system would be designed such that the post-LOCA equilibrium pressures give sufficiently high mass flow rates to remove decay heat by natural circulation without exceeding cladding temperature limits. Thus natural circulation is a backup cooling mode for forced circulation. This design was originally developed by [Hejzlar, et. al., 2005] and was evaluated favorably in PRA analyses by [Jourdan, et. al., 2004].

The steady state natural circulation performance of the system is evaluated in this chapter. The effect of simulated grid spacers with and without Reynolds-dependent loss coefficients is also evaluated in order to demonstrate one of the favorable qualities of inverted fuel. The effects of channel roughening are also investigated and the results from RELAP are compared to those from LOCA-COLA, a code written at MIT. [Williams, et. al., 2004] Two routes of post-LOCA core bypass are also described and their effects on the decay heat removal performance of the system are evaluated in both natural and forced circulation.

It should be noted that the core model used for the analyses in this chapter does not share the same specifications as the core design detailed in the last chapter, nor is it the same as in subsequent chapters. The RELAP model in this section represents an earlier design

revision which was superceded by the design used in other parts of this thesis. These results are nonetheless informative.

7.2 Description of Active/Passive Hybrid Decay Heat Removal System

Figure 7.1 shows a diagram of the plant layout which served as the reference case at the time of this work. The SCS/ECS, shown in the upper-left hand corner of the figure, is based on GFR work within an I-NERI project at MIT in cooperation with ANL and CEA. [Hejzlar, et. al., 2005] Only one SCS/ECS module is shown in the figure, but in the real design, there would be four 50% capable loops. This 4x50% arrangement forms a 2-out-of-4 system where one SCS/ECS module (or loop) can be out of service for maintenance and a second loop can fail and sufficient decay heat removal is still provided by the two operational loops. This provides highly reliable decay heat removal in shutdown and postulated accident conditions.

In normal operation, the check valves are held shut by the core pressure drop and CO_2 in the SCS/ECS modules is nearly stagnant. During shutdown or emergency cooling, the check valves open, allowing CO_2 to leave the upper part of the chimney and enter the inner pipe of the coaxial cross-vessel duct arrangement. The CO_2 then enters Heatric® gas/water PCHE's where it is cooled by a water loop. After leaving the heat exchanger, blowers (4 per SCS/ECS loop) circulate the CO_2 through the open check valve and return it to the vessel downcomer. The water loop transfers heat from the gas/water heat exchanger to a water/water heat exchanger communicating with the ultimate heat sink, a spray pond located outside of the containment.

In a postulated accident condition, the most severe of which is a LOCA, the design would rely on the emergency blowers to circulate CO_2 and remove decay heat as the first line of defense-in-depth. However, the containment is sized such that the equilibrium pressure is sufficient to enable natural circulation flow rates that can remove decay heat without exceeding cladding temperature limits. Thus natural circulation serves as a backup cooling mode to forced blower-driven circulation.

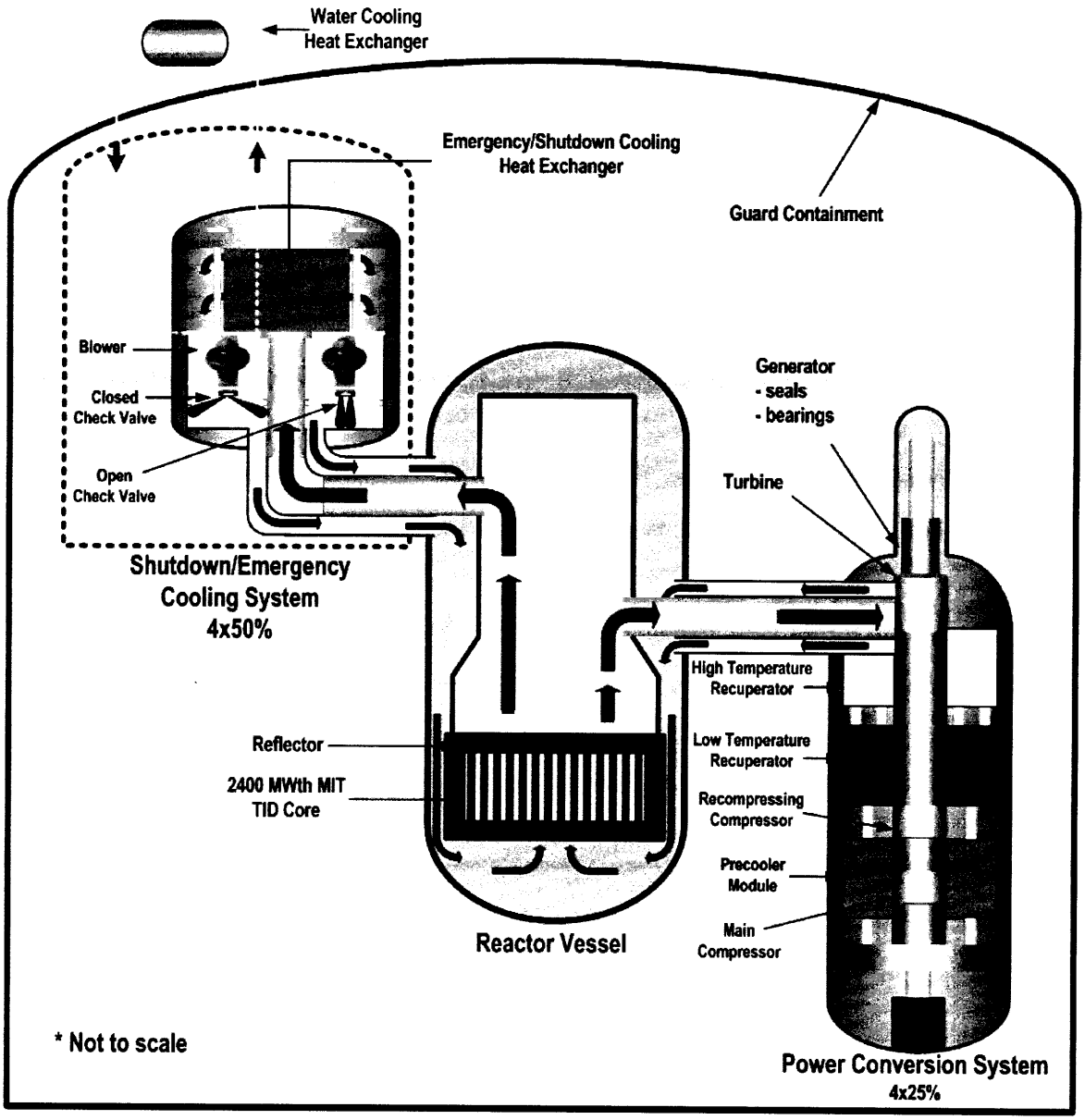

Figure 7.1. Plant layout with hybrid active/passive SCS/ECS. [adopted from Hejzlar, et. al., 2005]

7.3 RELAP Model Used in Analysis

Figure 7.2 and Figure 7.3 are nodalization diagrams of the RELAP model used to simulate the S-CO_2 cooled GFR plant for analysis of the active/passive hybrid SCS/ECS. These serve not only as tools for the RELAP user, but also as a way to communicate the methodology and assumptions used in representing the system. Numbers on hydrodynamic volumes, junctions and components represent their labels in the RELAP model and will be used to reference plant components in the text of this report. Hatch patterns indicate RELAP heat structures, which are used to account for the effects of physical structures in the plant that can store and conduct heat such as fuel, cladding, pipe walls and heat exchangers. Convergence in steady state calculations is accelerated in RELAP by artificially reducing the heat capacity of heat structures. Therefore, the only heat structures of significance in steady state calculations are those which can transfer heat from one hydrodynamic volume to another such as in the case of a heat exchanger. The core barrel also serves as a heat exchanger because heat is transferred through it from the chimney to the downcomer. The degradation of decay heat removal performance due to conduction through the core barrel is addressed later in the chapter.

The PCS loops are modeled as a single loop (volumes labeled 3XX on the left side of Figure 7.2) and a lumped 3x25% loop (volumes labeled 4XX on the left side of Figure 7.2). The valves located on the coaxial duct to the single PCS are used to model LOCAs. During normal operation, valves 302 and 398 are open. Different types and sizes of breaks can be modeled by opening valves 303, 304, 393 and 394 connecting the coolant system to the containment volume (900). Pressure control volumes (397 and 497) are attached at the main compressor inlets. These are used to help maintain the proper pressure in steady state operation. The valves to these volumes (396 and 496) are left open for the steady state calculations, but before a transient is run (as will be seen in later work) these valves are closed. Though this plant model differs significantly from what will later be described as the final reference design, the modeling of the PCS loops is not changed significantly throughout this work. A more detailed description of the modeling of various parts of the PCS loops including turbomachinery, recuperators and precoolers is reserved for a later chapter where the model of the entire plant is discussed at greater length.

The RELAP model includes two of the four SCS/ECS loops present in the plant lumped into one equivalent loop. The simulation of SCS/ECS blowers is performed by using a time-dependent junction (645) in the absence of a detailed design. A RELAP motor valve (650) is used to simulate the SCS/ECS check valves so that the timing of their opening can be controlled. During full power operation, junction 645 is set to zero flow and valve 650 is closed to simulate a closed check valve. In natural circulation, the mass flow rate in time-dependent junction 645 is set to zero and valve 650 is opened.

The water loop pressure is maintained nominally at a pressure of 5 bar by time-dependent volume 745. It will be shown later that for higher reactor powers, the water temperatures are high enough that this pressure must be increased to raise its saturation temperature. Junction 701 can be a time-dependent junction in order to force flow simulating a pump, or be changed to a single junction in the case of natural circulation. The water/water heat exchanger at the top of the water loop is modeled as horizontal pipes through which the water flows, having an outer surface temperature set to be constant at 25°C.

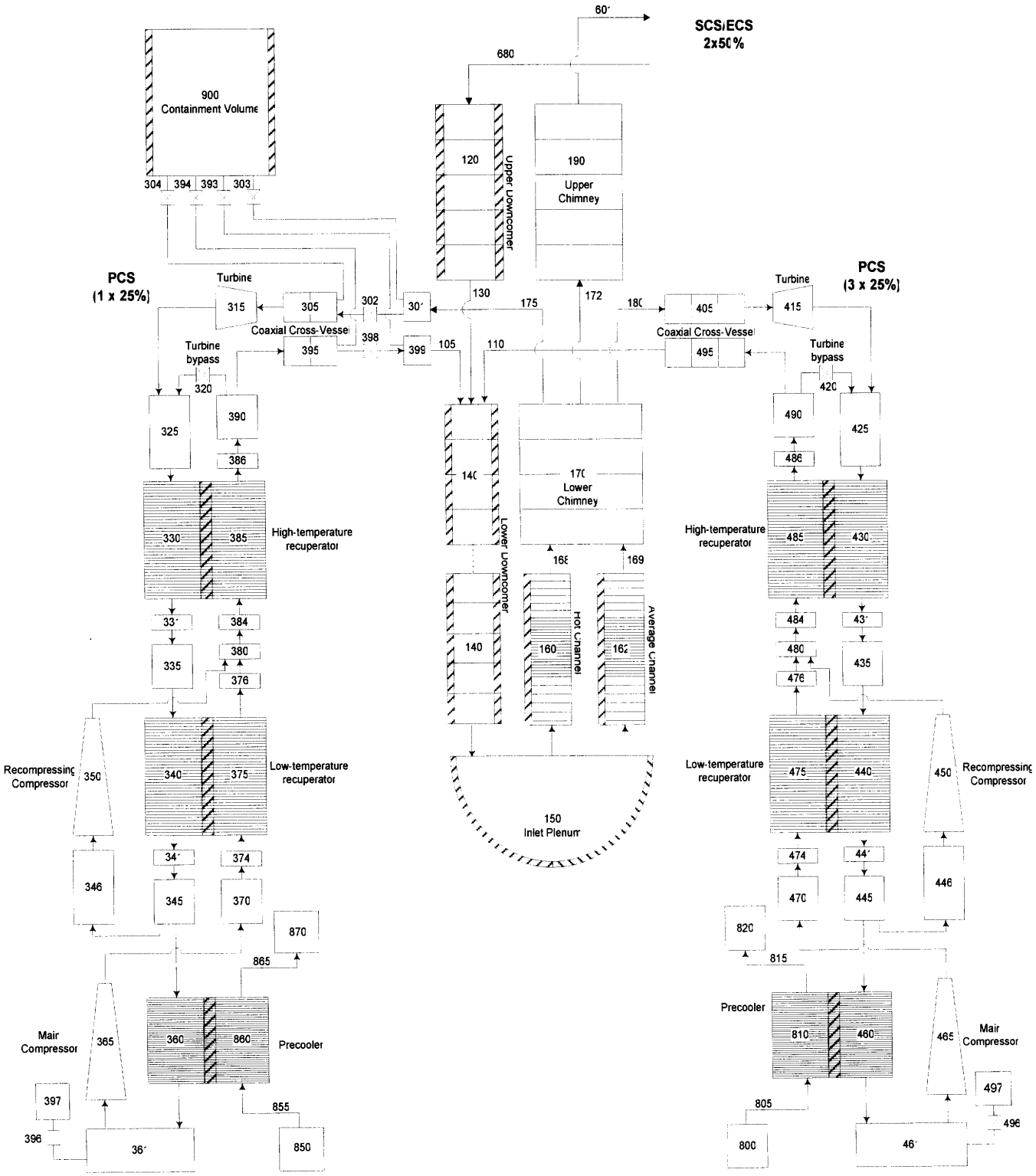

Figure 7.2. Nodalization diagram for RELAP5-3D model of plant excluding SCS/ECS.

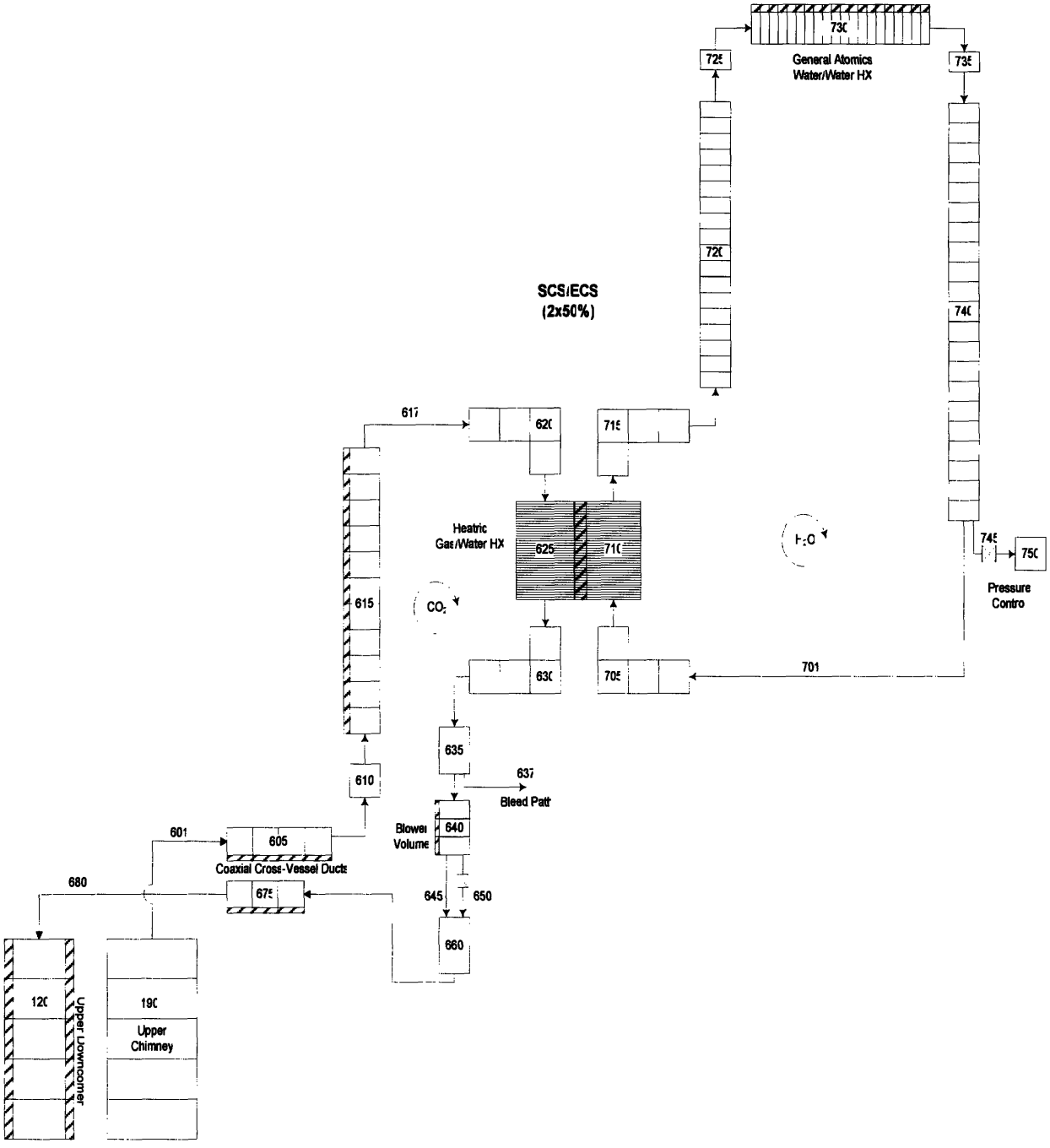

Figure 7.3. Nodalization diagram of RELAP5-3D model of active/passive hybrid SCS/ECS.

As mentioned before, the core used in this analysis was a previous version of the final design, and therefore differs from the core detailed in previous and subsequent chapters. Here the core is modeled using two channel types, hot and average, with no bypass for reflector or shielding. As before, the axial power shape is a chopped cosine with a peaking factor of 1.3 and the radial power peaking factor is 1.15. These and other key parameters of this core model are given in Table 7-1. Table 7-2 and Table 7-3 give detailed descriptions of the volumes that comprise the vessel and SCS/ECS flow paths with PCS loops omitted. Table 7-2 gives descriptions of the volumes that make up the CO_2 path during shutdown or post-accident cooling and Table 7-3 details the water flow path which transfers heat to the ultimate heat sink.

Table 7-1. Parameters of simplified core model used in analysis of active/passive hybrid SCS/ECS.

Parameter	**Value**
Thermal power (MW_{th})	2400
Mass flow rate (kg/s)	11,708
Pressure (MPa)	20
Inlet temperature (°C)	485
Outlet temperature (°C)	650
Axial power shape	Chopped cosine
Axial peaking factor	1.3
Radial peaking factor	1.15
Active core length (m)	1.7
Lower inactive length (m)	1.1
Upper inactive length (m)	1.0
Number of channels	122,287
Channel diameter (mm)	6.062
Channel pitch (mm)	11.55
Clad thickness (mm)	0.7
Coolant volume fraction (%)	25
Active core H/D	0.4

Table 7-2. Description of hydrodynamic volumes in vessel and active/passive SCS/ECS.

Node	Description	D_e (mm)	# of Channels	Length (mm)	Height (mm)*	Entrance k_{loss}	Roughness (m)	Flow Area per channel (m^2)
120	Upper Downcomer	2025	2	5000	-5000	0.5	$4.5x10^{-5}$	2.29
140	Lower Downcomer	699	1	7800	-7800	1.0	$4.5x10^{-5}$	7.30
150	Inlet Plenum	7000	1	2330	2330	0.0	$4.5x10^{-5}$	38.5
160	Core Hot Channel	6.062	100	3800	3800	0.1	$1.0x10^{-6}$	$2.886x10^{-5}$
162	Core Average Channel	6.062	122,187	3800	3800	0.1	$1.0x10^{-6}$	$2.886x10^{-5}$
170	Lower Chimney	6300	1	4000	4000	1.0	$4.5x10^{-5}$	31.2
190	Upper Chimney	5400	1	5000	5000	0.1	$4.5x10^{-5}$	22.9
605	Inner Co-axial Duct	1350	2	4000	0	1.23	$4.5x10^{-5}$	1.43
610	Lower DHR Riser	1800	2	1000	1000	0.0	$4.5x10^{-5}$	3.24
615	Upper DHR Riser	1636	4	4700	4700	0.1	$4.5x10^{-5}$	2.70
620	G/W HX Inlet Plenum†	150	4	1250	-500	0.23	$4.5x10^{-5}$	1.06
625	G/W HX Hot Side	3.055	611,766	600	-600	1.23	$1.0x10^{-5}$	$9.817x10^{-6}$
630	G/W HX Outlet Plenum	150	4	1250	-200	0.23	$4.5x10^{-5}$	1.06
635	Upper HX Downcomer	2026	4	1000	-1000	0.0	$4.5x10^{-5}$	5.5
640	Blower/Check Valve	1400	4	3000	-3000	3.23	$4.5x10^{-5}$	3.08
660	Lower HX Downcomer	2026	4	400	-400	13.23	$4.5x10^{-5}$	5.5
675	Outer Co-axial Duct	386	2	3000	0	0.23	$4.5x10^{-5}$	0.97

Table 7-3. Description of hydrodynamic volumes in SCS/ECS water loop.

Node	Description	D_e (mm)	# of Channels	Length (mm)	Height (mm)	Entrance k_{loss}	Roughness (m)	Flow Area per channel (m^2)
705	G/W HX Inlet Plenum	150	4	1250	500	0.5	$4.5x10^{-5}$	1.063
710	G/W HX Hot Side	3.055	611,766	600	600	1.23	$4.5x10^{-5}$	$9.817x10^{-6}$
715	G/W HX Outlet Plenum	150	4	1250	200	0.23	$4.5x10^{-5}$	1.063
720	Water loop Riser	333	4	8500	8500	0.0	$4.5x10^{-5}$	0.087
725	G/A HX Inlet Plenum	35.1	391	500	0	0.5	$4.5x10^{-5}$	$9.676 x10^{-4}$
730	G/A UHS HX	35.1	391	33240	0	0.0	$4.5x10^{-5}$	$9.676 x10^{-4}$
735	G/A HX Outlet Plenum	35.1	391	500	0	0.0	$4.5x10^{-5}$	$9.676 x10^{-4}$
740	Water loop Downcomer	333	4	9800	-9800	1.0	$4.5x10^{-5}$	0.087

* This column represents the relative vertical elevation change of a component. Because all attachments to the lower plenum (cell 150) occur from the top, its height must be neglected for the heights to sum to zero.

† G/W stands for Gas to Water

7.4 Steady-State Natural Circulation without Core Bypass

For these calculations, the PCS loops were removed from the model, reducing calculation time considerably. A pressure control volume was added at the core inlet plenum (150) to control pressure. The simulations were started with initial conditions such that the core was producing decay heat from time zero and both the CO_2 loop and the water loop to the ultimate heat sink had flow rates greater than the steady state natural circulation flow rates. The plant was then allowed to run without pumps or circulators until a steady state condition was reached. This was performed for pressures of 4, 6, 8, 10, and 12 bar. It is worth noting at this point that this analysis is incomplete in that it does not address how the plant goes from full power to this condition, and thus it cannot alone be used to conclusively prove the safety of the plant against an accident. It does, however, provide an envelope of achievable decay heat removal rates by natural circulation in the absence of core bypass routes. This helps determine the energy storage requirements for batteries or fuel cells and/or the rating of emergency diesels or microturbines used to provide emergency power.

7.4.1 Steady State Natural Circulation Decay Heat Removal without Core Bypass

Figure 7.4 shows peak clad temperature versus percent of full reactor power for the five backup pressures. The horizontal line drawn at 1200°C is the limit set on peak clad surface temperature. The points where this line intersects the other five form the plot in Figure 7.5. This plot gives the percent of full power which can be removed versus backup pressure without exceeding a clad surface temperature limit of 1200°C. The data verify that the decay heat removable by natural circulation exhibits near linear proportionality to the backup pressure in the range 4-12 bar, a proportionality predicted by prior analytic and numerical analyses. During efforts to extend the data down to atmospheric pressure, some difficulty was encountered in achieving a steady state condition. This is probably due to the fact that conduction through the core barrel is transferring heat from the chimney to the downcomer and thus degrading natural circulation. The effect of this degradation is briefly addressed in Section 7.4.2 on benchmarking with LOCA-COLA, and will receive more attention in future work.

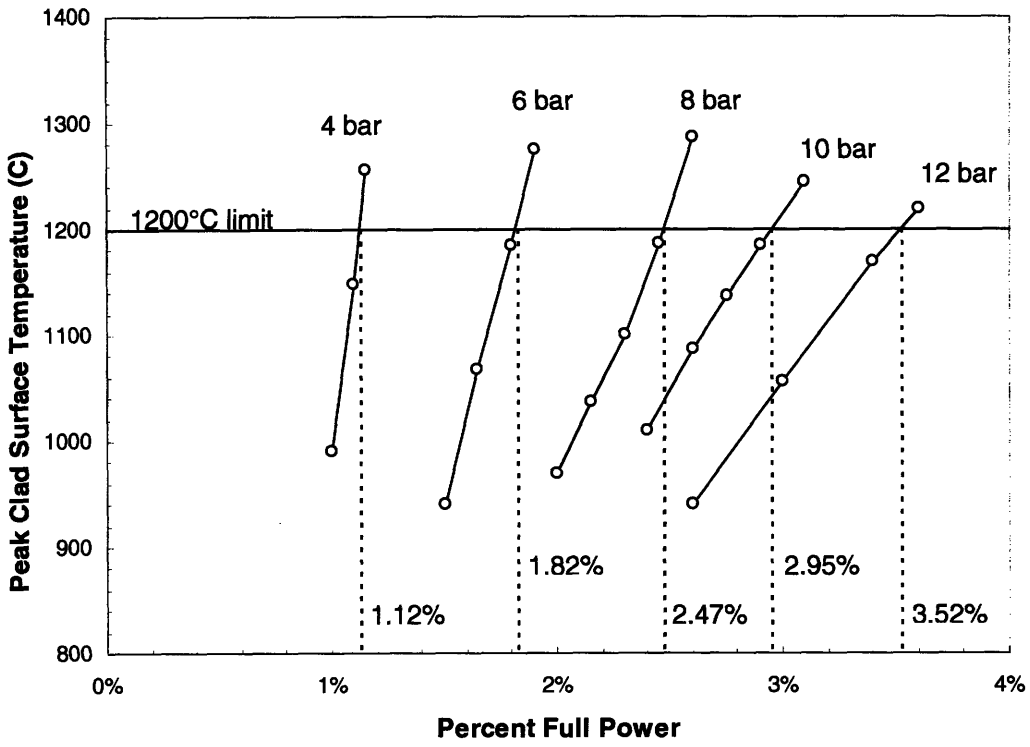

Figure 7.4. Peak clad surface temperature versus percent power in natural circulation.

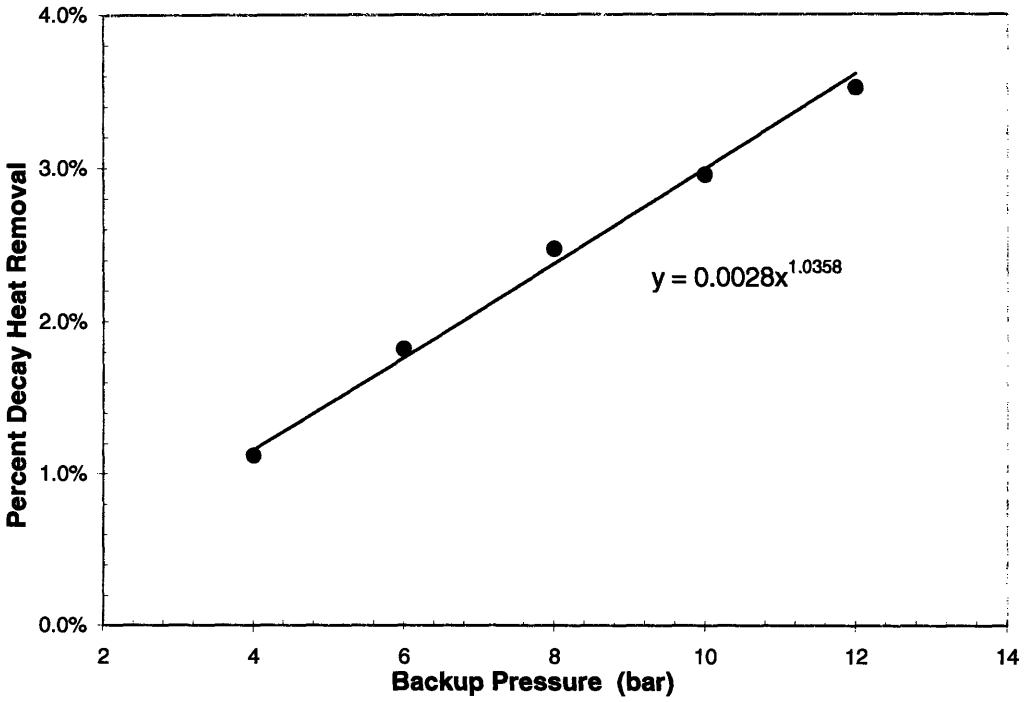

Figure 7.5. Percent decay heat removable by natural circulation versus post-LOCA pressure with line fit.

7.4.2 Benchmarking with LOCA-COLA

A single case was run using LOCA-COLA for comparison to the results of the RELAP model. The conditions were a pressure of 6 bar and a power level of 1.65% of full power. Temperatures calculated for the water loop in natural circulation using RELAP were used as boundary conditions in LOCA-COLA. The steady-state peak clad surface temperatures calculated by LOCA-COLA and RELAP were 1004°C and 1068°C, respectively. This difference was primarily caused by the fact that in the RELAP model, heat is transferred from the chimney to the downcomer through the barrel (from volumes 190 and 170 to volumes 120 and 140, respectively in Figure 7.2) as discussed in the previous section, degrading the natural circulation performance. This is not accounted for in the LOCA-COLA calculations. In a subsequent RELAP run, the core barrel was made perfectly insulated and the steady-state peak cladding temperature fell to 1014°C, which is in excellent agreement with the value calculated using LOCA-COLA. This exercise not only verified the modeling methodology used here, but also illustrated that conduction through the core barrel is important and therefore provision of sufficient insulation to minimize these losses needs attention in future work.

7.4.3 Effect of Channel Roughening

As was mentioned previously, in gas-cooled reactors, low heat transfer coefficients often motivate the use of augmentation techniques such as repeated ribs or a roughened surface. This not only increases the heat transfer coefficient, but carries a substantial penalty in friction factor. In the design evaluated in this chapter, heat transfer augmentation is not specified, and the channels have been made small and numerous in order to maintain a clad surface temperature of $\leq$ 750°C. One reason for this decision is the anticipated natural circulation penalty incurred by using a roughened surface.

In order to demonstrate the effect of an augmented surface on natural circulation decay heat removal, the 6 bar, 1.65% power case was used with a heat transfer coefficient multiplier of two and a roughness selected which gives three times the friction pressure drop (typical factors for roughened surfaces) at full power operation (Re ~ 500,000). Using

RELAP, the resulting peak clad surface temperature in steady state natural circulation decreased from 1064°C to 1020°C with the addition of the simulated augmentation.

LOCA-COLA was then used to compare the natural circulation performance of the smooth channels with the augmented channels. In this case, constant multipliers of 2 and 3 were used for heat transfer coefficients and friction factors, respectively. It was found that the backup pressure had to be increased from 6 bars to 9 bars in order to maintain the same peak clad temperature in the roughened case as in the smooth case using LOCA-COLA.

The reason for this discrepancy between the two codes is the handling of the wall roughness dependence of the friction factor at transition Reynolds numbers. In turbulent flow, the friction factor depends strongly on the wall roughness, whereas in the laminar regime, friction factor depends only on Reynolds number. Figure 7.6 shows friction factor versus Reynolds number for various wall relative roughness values. [from Idelchik, 1993] In the transition regime, there is significant dependence of friction factor on wall roughness and a local maximum in friction factor in this region. This is reflected in the way that the LOCA-COLA code calculates friction factor, but not in RELAP. Therefore, RELAP may be underpredicting the friction factor for roughened channels in transition flow.

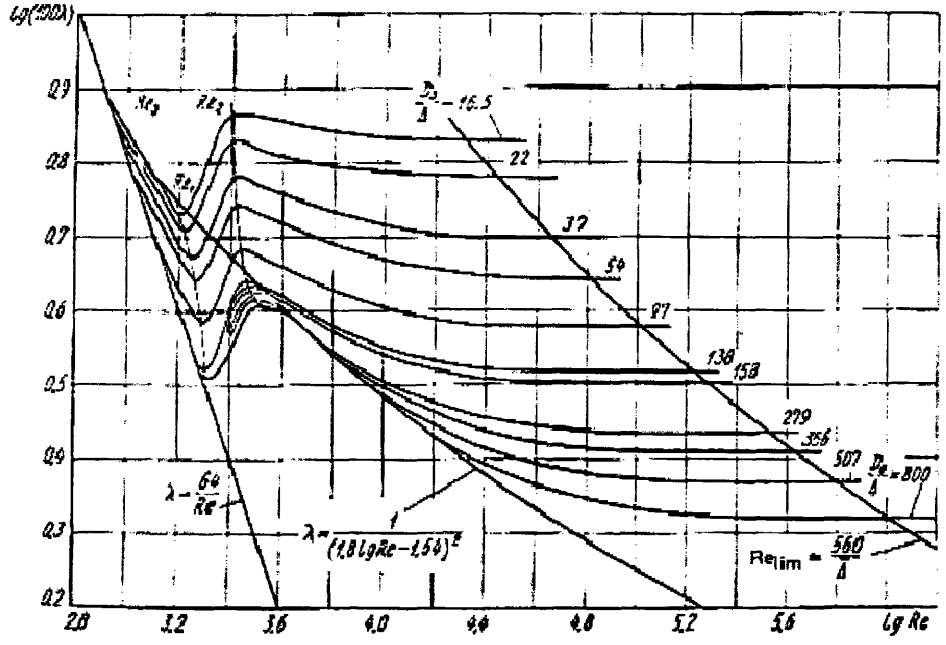

Figure 7.6. Transition Reynolds number friction factors. [from Idelchik, 1993]

7.4.4 Effect of Grid Spacers

A major motivation to use TID fuel assemblies is the avoidance of grid spacers which account for a large contribution to pressure drop in pin-type cores. The nominal pressure drop limit in this design is 500 kPa. The effect of grid spacers was simulated by increasing the core coolant channel exit loss coefficients such that a 50% increase in total core pressure drop results during normal full power operation so that the grid spacers account for around 1/3 of the total pressure drop, typical of gas-cooled reactors. The increase in exit loss coefficient required for this was found to be 4.91.

First, a constant loss coefficient was added in the 6 bar, 1.65% power case. Then a Reynolds-dependent loss coefficient was used which gives the desired grid loss coefficient at $Re = 5x10^5$, and also exhibits Re^{-1} proportionality in the transition and laminar regimes. The equation used for the Reynolds-dependent loss coefficient added to the channel exit losses is given by;

$$k_{grid} = 4.85 + \frac{28974}{Re} \qquad 7\text{-}1$$

Table 7-4 shows the peak clad temperature in steady state natural circulation for the nominal case, that with an added constant exit loss coefficient to simulate grid spacers, and then with an added Reynolds-dependent loss coefficient. This shows that the natural circulation advantage of not requiring grid spacers is significant, especially when the Reynolds-dependent losses are accounted for. Hence, in a pin type core, coolant volume fraction would have to increased to offset this penalty, but this would significantly penalize reactor physics performance.

Table 7-4. Results of simulated grid spacers in natural circulation at 6 bar and 1.65% power.

Condition	**Peak Clad Temp. (°C)**
No simulated grid spacers	1064
$k_{grid} = 4.91$	1173
$k_{grid} = 4.85 + 28974\ Re^{-1}$	1292

7.5 Analysis of Post-LOCA Core Bypass

After a LOCA, alternate paths may exist through which coolant may bypass the core in both natural and forced convection. Two paths identified as possible routes of post-LOCA core bypass are through a pipe break in which both the hot and cold legs of a coaxial duct connecting the vessel to a PCS loop are broken, or through the PCS loops in the absence or malfunction of isolation valves. The post-LOCA core bypass discussed in this section should not be confused with the core bypass in which coolant avoids flowing through the active core by way of radial reflectors and shielding. Later there will be instances where both take place at once, but in this chapter, only the core bypass via pipe breaks and PCS loops is considered.

7.5.1 Post-LOCA Core Bypass via Pipe Breaks

In the event of a LOCA involving breakage of both the hot and cold leg ducts connecting the vessel to a PCS unit, there is a potential for some coolant to bypass the core in favor of exiting through the broken pipe to containment. The coolant would travel out the pipe leading from the PCS to the downcomer and then return through the break in the leg which normally carries coolant from the core outlet to the PCS. This is shown graphically in Figure 7.7. The percent of coolant flow which bypasses the core will clearly be dependent upon the resistance of the alternate flow path relative to the core. In the case of a pipe break, this resistance is determined primarily by the break size and to a lesser degree the shape of the break because this determines the loss coefficients.

In order to identify the degree of performance degradation caused by this route of core bypass, RELAP calculations were performed in which pipe breaks were simulated using valves 393 and 303 in Figure 7.2. These valves were opened and the simulation was allowed to run until a steady state natural circulation condition was reached. The flow areas of these valves were adjusted in order to simulate varying break sizes. The system pressure was 6 bar and the core power was 1.82% of full. The containment volume was decreased by a factor of 10 in order to speed up the approach to steady state. Loss coefficients from the broken pipes

into containment were set to 1.0 and the loss coefficients from the containment into broken pipes were set to 0.5.

Figure 7.8 shows core and bypass fractional mass flow rates versus size of the simulated breaks to containment (break size given occurs in both the hot and cold legs of a single PCS duct). The peak cladding surface temperature is also shown versus the pipe break size on a secondary ordinate. The total system mass flow rate increases with increasing break size, but the core flow rate decreases as a larger fraction of coolant travels through the pipe breaks rather than through the core. Break sizes larger than about 1700 cm^2 resulted in breakdown of natural circulation through the core and subsequent overheating. The total flow area of the hot duct is 0.9 m^2 ($9x10^3$ cm^2) and that of the cold duct is 1.24 m^2 ($1.24x10^4$ cm^2). Therefore, sufficient cooling in the event of complete severance of a coaxial PCS duct is not achievable by natural circulation alone at this particular combination of core power and equilibrium backup pressure.

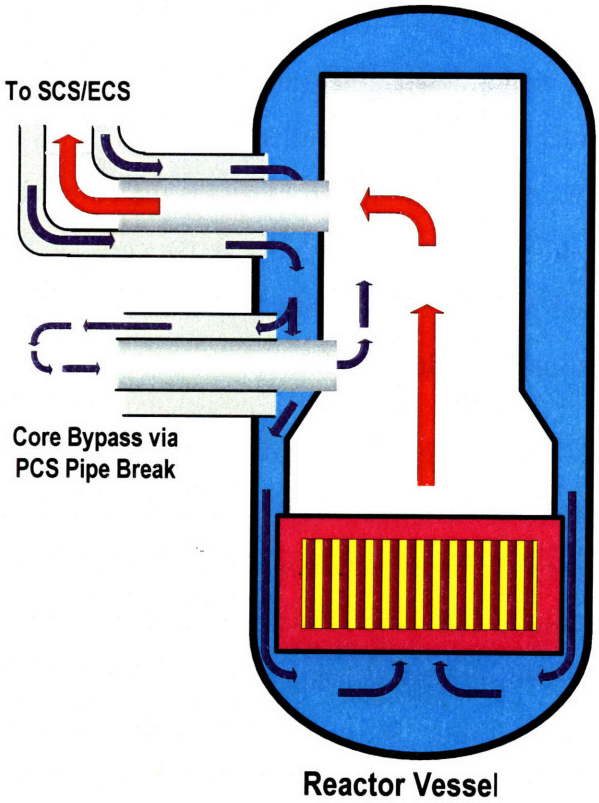

Figure 7.7. Post-LOCA core bypass through pipe break in both hot and cold legs

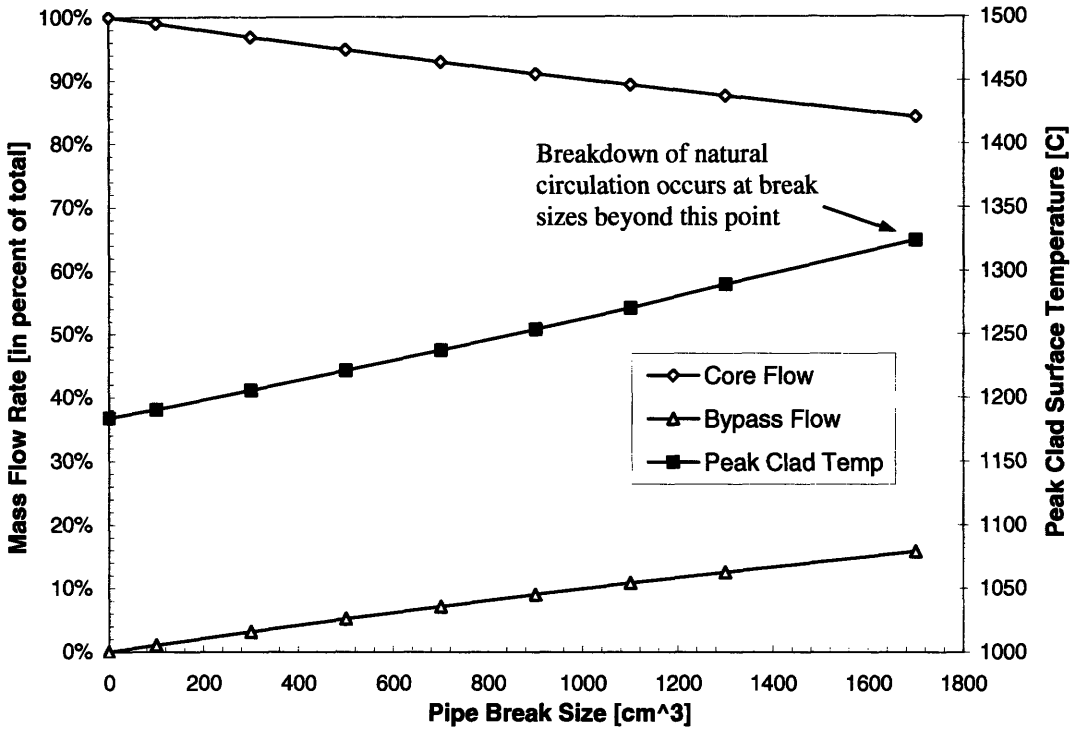

Figure 7.8. Steady state natural circulation mass flow rates in core and bypass for varying PCS pipe break sizes.

The operation of blowers was simulated (using junction 645 in Figure 7.3) with the system at the same pressure and power as before, but with a constant break size of 1300 cm^2 in both the hot and cold legs of the PCS duct. The blower mass flow rate was varied by about a factor of four from near the natural circulation value of 52.8 kg/s to 200 kg/s. Figure 7.9 shows core and bypass fractional mass flow rates versus total blower mass flow rate. The fraction of coolant which bypasses the core remains relatively the same (between 12% and 16% of total flow) even over this relatively large variation in total mass flow rate. The peak cladding surface temperature (again shown on a secondary ordinate) decreases to well below the accident limit of 1200°C for a relatively modest total flow rate.

The fact that the percent of coolant bypassing the core remains relatively constant between forced and natural circulation means that even in the case of a very large pipe break,

the blowers can be used to force flow such that the core will receive sufficient coolant to remove decay heat. Calculations were performed using the maximum break sizes possible (the full area of the coaxial PCS ducts). The inner (hot) duct area is again 0.9 m^2 and the outer (cold) is 1.24 m^2. These were fully opened and the blower mass flow rate was varied from 100 kg/s to 200 kg/s. Figure 7.10 shows core and bypass fractional flow rates versus total blower flow rate for the maximum pipe break sizes. The peak cladding surface temperature is also shown again on a secondary ordinate. Again, the bypass fraction remains relatively constant, this time between 54% and 60% of the total flow, while the total flow rate changes by a factor of two. The required blower power can be estimated by the following relationship;

$$\dot{Q}_B = \frac{1}{\eta_B} \dot{V} \Delta P \tag{7-2}$$

where $\dot{Q}_B$ is total blower power, η_B is the efficiency of the blowers (assumed to be 85%), ΔP is the pressure rise across the blowers and $\dot{V}$ is the volumetric flow rate in the blowers calculated from the mass flow rate divided by the average density in the blower. In the case of the total blower-driven mass flow rate of 200 kg/s shown in Figure 7.10, the total blower power calculated from the steady-state RELAP results was 92 kW. This shows that even in the case of a very large break in both the hot and cold legs of a PCS duct and the associated core bypass, relatively low-powered active systems can provide sufficient decay heat removal to avoid exceeding cladding temperature limits.

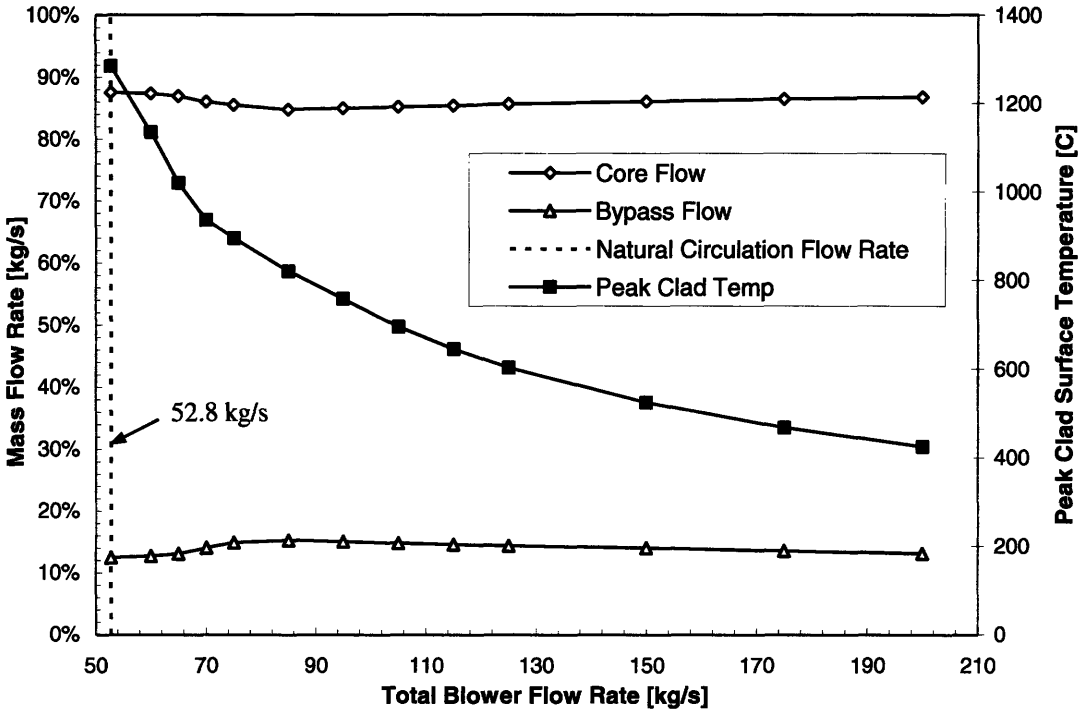

Figure 7.9. Core mass flow rate and bypass flow in forced circulation for 1300 cm^2 break size.

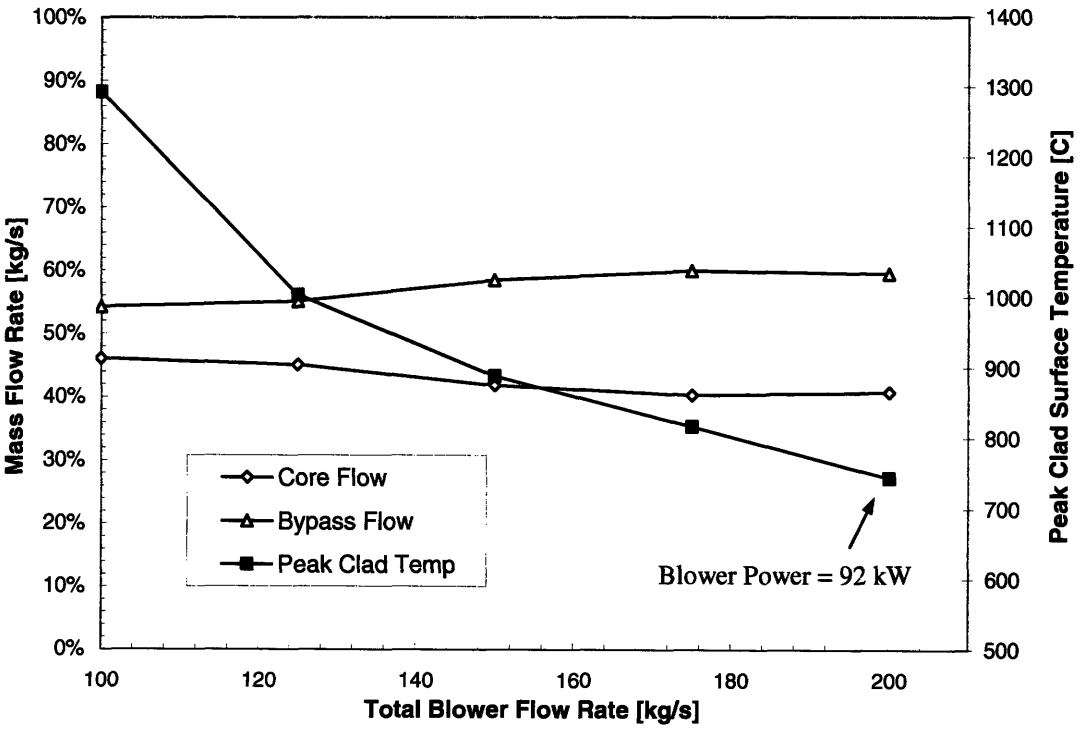

Figure 7.10. Core mass flow rate and bypass flow in forced circulation for maximum pipe break size (0.9 m^2 inner, 1.24 m^2 outer).

7.5.2 Post-LOCA Core Bypass via PCS Loops

The other means by which coolant may bypass the core during post-LOCA decay heat removal is by reverse flow through PCS loops after the turbomachinery has stopped. A simulation was performed to quantify this bypass flow again at a pressure of 6 bar and 1.82% of full power. Unlike previous calculations where the PCS units were removed from the model to reduce computation time, the entire plant model was used for this analysis. Turbomachinery was replaced with volumes of equivalent flow area and loss coefficients of 10, a typical value for stopped pumps, to approximate the resistance of a stalled PCS unit. Coolant was forced by simulated SCS/ECS blowers at a mass flow rate of 60 kg/s and the model was allowed to run until reaching a steady state. No coolant was allowed to bypass the core via pipe breaks as in the previous section, leaving only the PCS units as bypass routes. Turbine bypass valves (320 and 420 in Figure 7.2) were left closed and the precooler water-side flow was left running at its full-power rate. The bypass flow in this case was 11.2 kg/s (2.8 kg/s per PCS loop) which was 18.7% of total system flow. This means that the resistance to flow offered by the four PCS loops is less than that of the maximum break size shown in Figure 7.8. As would be expected, when the blowers are removed and the system is allowed to operate in natural circulation, RELAP calculations show that the core mass flow rate is too low due to bypass through the PCS loops and temperatures exceed allowable limits.

Passive check valves or active isolation valves should be used to seal off PCS loops in the event of a depressurization, but the design of these valves with sufficiently high reliability is an open issue. Startup motors could also be operated in order to resist this reverse flow through the PCS loops and even provide circulation of coolant, which would assist the SCS/ECS in decay heat removal. Another bypass route not examined here could occur if a PCS loop which is not sealed off from the vessel has a turbine bypass valve which is stuck open. This would decrease the resistance to bypass flow offered by the PCS. It is evident that numerous combinations of post-LOCA core bypass flow paths could be imagined. Because these bypass routes have the potential to deprive the system of sufficient decay heat removal, the mechanisms which cause them must be well characterized. This is particularly true if the design is to rely upon natural circulation alone.

7.6 Summary

Steady state calculations have confirmed an approximately linear proportionality between decay power removable by natural circulation and post-LOCA backup pressure. While a benchmark calculation between LOCA-COLA and RELAP showed good agreement with smooth channels, a simulated heat transfer augmentation case showed discrepancy due to the handling of the friction factor in the transition regime. The absence of grid spacers allowed by using TID fuel was shown to be a significant advantage in natural circulation.

Post-LOCA core bypass was shown to be a significant issue in post-LOCA decay heat removal. In the case of core bypass flow via PCS loops, all four loops without isolation valves provide a relatively small resistance to flow and thus give rise to a large bypass mass flow rate. Implementation of reliable isolation valves would eliminate this route of core bypass. If isolation valves are not used or have malfunctioned, active cooling using blowers can provide adequate decay heat removal to the core. Operation of PCS startup motors also can prevent this bypass mechanism from occurring.

In the case of a break in both the hot and cold legs of a PCS duct, the percent of flow which bypasses the core is dependent primarily on the pipe break size and shape and is relatively insensitive to total system mass flow rate. This was shown to be true whether free or forced circulation is employed. The use of a reliable and appropriately-sized active system can provide sufficient core cooling even in the extreme case of the maximum possible break sizes without excessive power demand. It should be noted that these break sizes analyzed are quite large. The maximum break size analyzed for the GA GCFR was 100 in^2 (645 cm^2) and was not assumed to have occurred in more than one leg. [General Atomic Company, 1980]

The post-LOCA natural circulation performance of the SCS/ECS is degraded significantly by core bypass through pipe breaks and PCS loops. The exclusion of these routes of core bypass without more knowledge of these mechanisms is difficult to defend. Natural circulation cooling may be aided by increasing the height of the convection loop or increasing the backup pressure, but these means are not cost effective, and a maximum credible bypass to be analyzed for is not available at this time. On the other hand, relying on

blowers capable of delivering mass flow rates of interest here would result in a modest cost penalty since blowers are already specified in the hybrid active/passive decay heat removal system. In the remainder of this work, it is therefore recommended that an active decay heat removal system with highly reliable blowers be specified. Since active decay heat removal will be relied upon, this removes the need for the extended heights of the decay heat removal loops. Decay heat removal heat exchangers could therefore be placed inside the reactor vessel along with the blowers. In the following chapter, the design of this type of active SCS/ECS is presented.

Another course of action which should be pursued is the limitation of duct break size, for example by clamping on a strongback with a circumferential rib cage. Instrumentation to detect leaks before breaks should also be provided. As noted earlier, reliable isolation valves are a high priority system design goal.

8 Design of Active Shutdown/Emergency Cooling System

8.1 Introduction

In the previous chapter, steady state natural circulation post-LOCA decay heat removal was evaluated for an earlier version of the SCS/ECS. It was shown that post-LOCA core bypass through pipe breaks and un-isolated PCS loops can potentially degrade cooling, and in extreme cases can render natural circulation cooling inadequate for meeting cladding temperature limits. It was also shown that, even in extreme cases of core bypass (such as complete severance of a coaxial PCS duct), relatively low-powered blowers could restore sufficient coolant flow through the core. It was therefore recommended that active decay heat removal be pursued using reliable blowers. In this chapter, an active SCS/ECS is described which employs decay heat removal heat exchangers similar to the ones in the previous chapter, only now located within the vessel.

8.2 Design of Active SCS/ECS

Because natural circulation cooling alone will not be relied upon in an accident, the loop elevations of the SCS/ECS need not be lengthened to augment this cooling mode. This allows placement of the gas/water decay heat removal heat exchangers within the reactor vessel. Figure 8.1 is a vertical cross-section of the reactor vessel showing how the decay heat removal heat exchangers can be arranged vertically in the upper part of the chimney between the core barrel and vessel inner wall. When the SCS/ECS is operating, hot CO_2 travels up to the narrow portion of the chimney and into the side of the decay heat removal heat exchanger modules where it transfers heat to the water loop which is in counter-flow relative to the

CO_2. Cold CO_2 exits the DHR-HX modules on the side of the heat exchanger adjacent to the vessel wall and travels down to the blowers and check valves.

Figure 8.2 shows a horizontal cross section of the top portion of the reactor vessel with key dimensions given in meters. This view illustrates the azimuthal arrangement of decay heat removal heat exchangers. It should be noted that a significant change in naming convention occurs at this point. Previously, there were four SCS/ECS modules capable of 200% decay heat removal (i.e. 50% each). Only two of the four modules were modeled in the RELAP calculations. Now, though the total heat exchanger capacity has not changed, they are grouped differently. Now there are eight total SCS/ECS modules present, each consisting of two submodules. Though in this view, one blower shaft is shown per module, the ideal number of blowers to specify in the SCS/ECS system has not been determined. This question is left for future work. The method for delivering torque to the blowers is also not yet determined and is thus not shown in the figures presented here. This should also be evaluated and designed in greater detail in future work. As before, the RELAP calculations assume that half of the decay heat removal capacity is out of service, so just 4 modules are modeled. Also note that the grouping of modules into submodules does not affect the RELAP calculations because the SCS/ECS loops are lumped into a single effective flow path in the model anyhow.

As was mentioned previously, the decay heat removal heat exchangers described in this chapter and used for the duration of the remaining analysis in this thesis have identical active volumes as those used in the analysis in the last chapter. The design of the headers, however, is not trivial in the case of PCHE's, and so consideration of this feature follows. Figure 8.3 shows diagrams of the hot and cold plates of a single decay heat removal heat exchanger submodule. The left-hand half of the figure shows a cold (water) side plate and the right-hand side shows a hot (CO_2) side plate. The vantage point from which the plates are viewed in this figure is from above such that the bottom of the figure would be attached to the core barrel and the top of the figure would be adjacent to the inner wall of the PCIV. Hot CO_2 flows radially outward from the upper chimney into the PCHE channels and the active heat exchanger volume. The cold CO_2 then exits the small channels and turns downward adjacent to the inner PCIV wall. The cold water flow enters the top of the heat

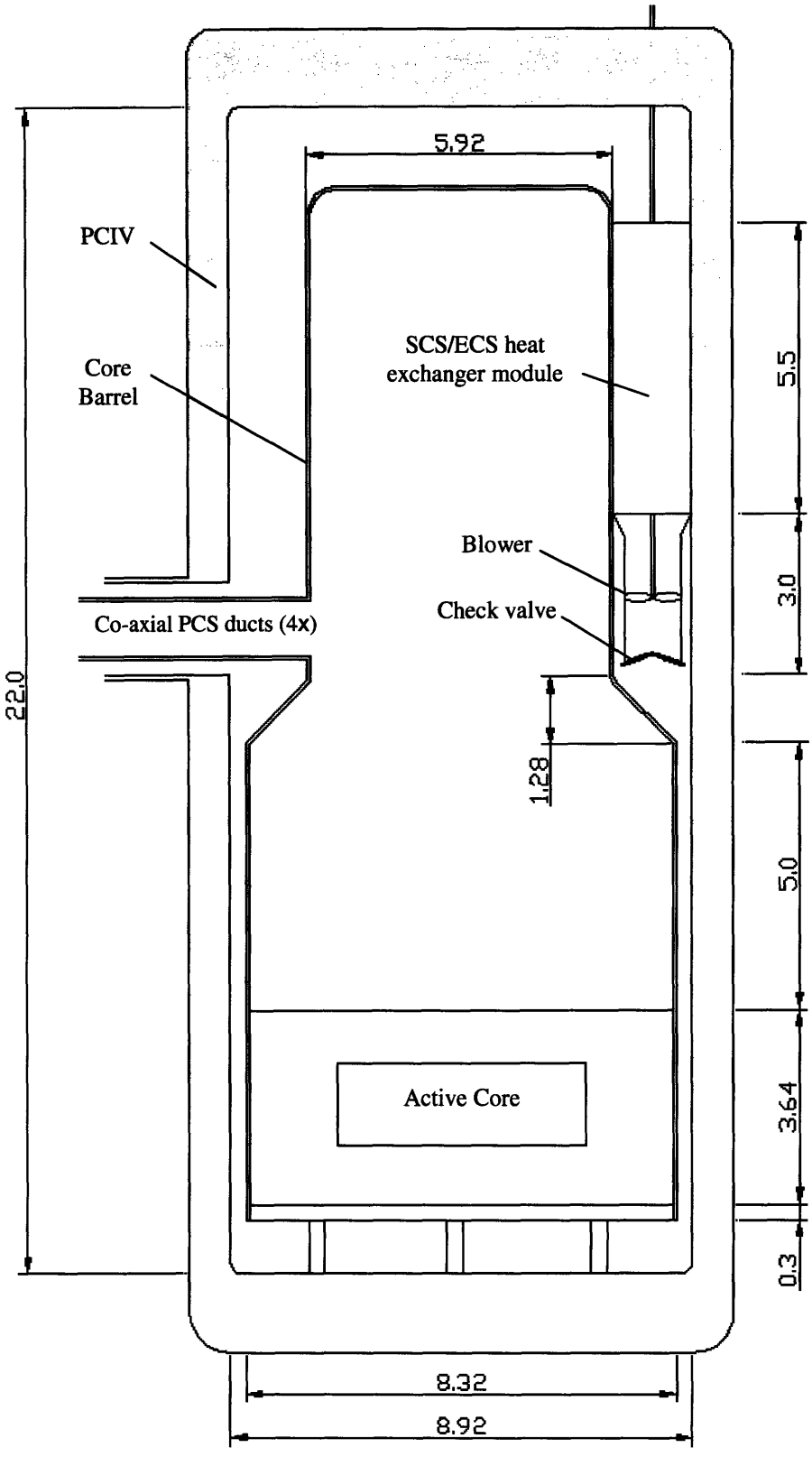

Figure 8.1. Vertical cross-section of reactor vessel and internals with key dimensions shown in meters.

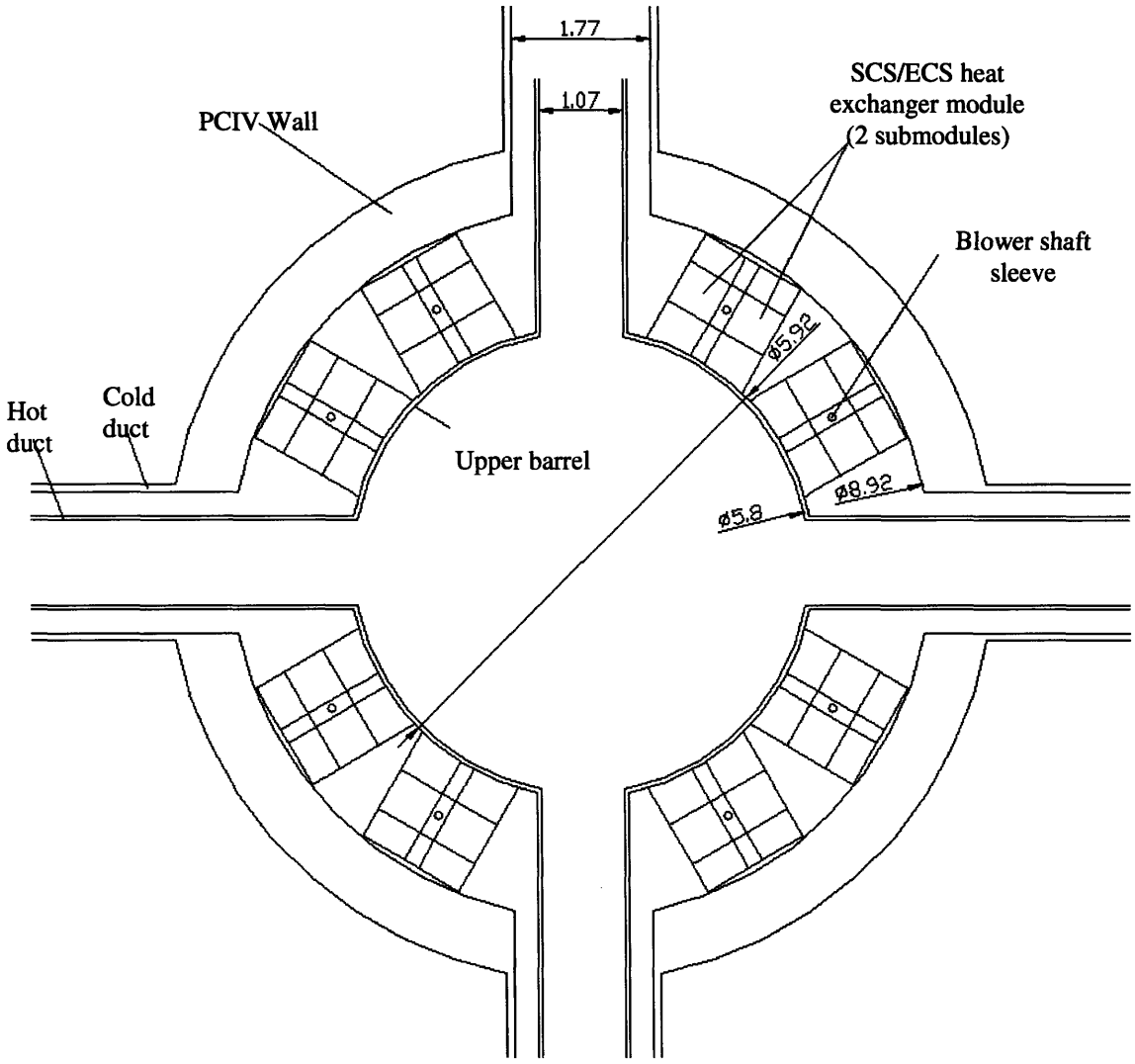

Figure 8.2. Cross-section of top portion of reactor vessel showing arrangement of DHR heat exchangers, with key dimensions shown in meters.

exchangers (into the page in Figure 8.3) then turns radially inward toward the core barrel to the active heat exchanger volume. The hot water then turns up out of the page as shown in the figure. The width of the plates is 60 cm, the maximum which can be currently manufactured by Heatric®.

To help clarify the configuration of the PCIV headers and the directions of the flow of the two streams, a three-dimensional rendering of a slice of one of the decay heat removal heat exchanger submodules is shown in Figure 8.4. Arrows indicate the

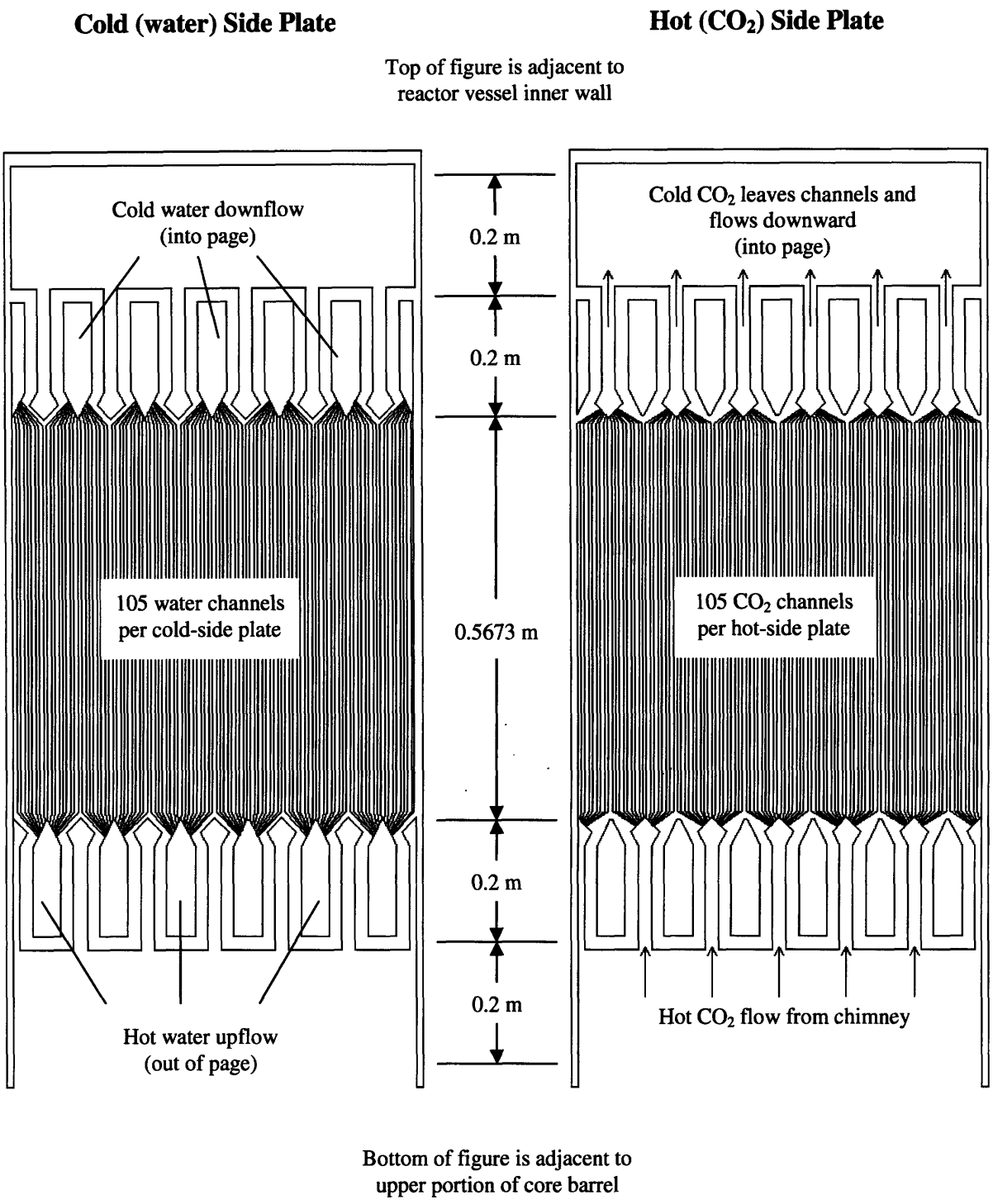

Figure 8.3. Top-view diagrams of water and gas side plates of Heatric® PCHE DHR heat exchanger submodules.

direction of flow of each stream. The cold CO_2 stream is not shown, but would travel out the back of the channels and down through the rectangular duct. An actual heat exchanger submodule would appear much taller if the entire height were used in the drawing.

Detailed geometric parameters for the decay heat removal heat exchangers are given in Table 8-1 for four of the eight SCS/ECS modules (100% decay heat removal). This is done so that consistency is maintained with the RELAP modeling methodology. The table also gives selected performance parameters of the decay heat removal heat exchangers. These values were obtained using a separate RELAP model of the heat exchangers with time-dependent volumes and junctions imposing the relevant boundary conditions on them.

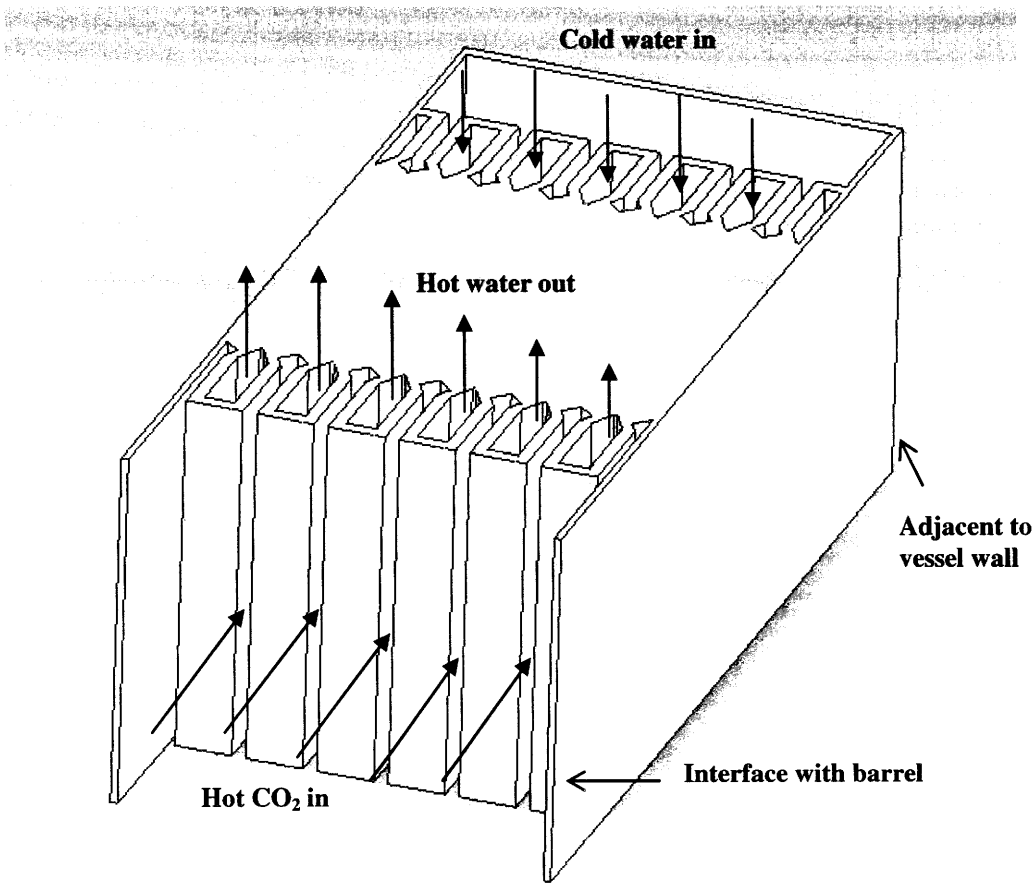

Figure 8.4. Three-dimensional slice of a DHR heat exchanger submodule.

Table 8-1. Decay heat removal heat exchanger geometry and nominal operating conditions.

Heat Exchanger Geometry*	
Number of submodules (100% decay heat removal capacity)	8
Number of submodules per module	2
Number of modules (100% decay heat removal capacity)	4
Channel semicircular diameter on hot side (mm)	5
Channel semicircular diameter on cold side (mm)	5
Channel pitch on hot side (mm)	5.71
Channel pitch on cold side (mm)	5.71
Plate thickness on hot side (mm)	3.7
Plate thickness on cold side (mm)	3.7
Number of hot-side plates per submodule	743
Number of cold-side plates per submodule	743
Number of hot-side channels per submodule	78,015
Number of cold-side channels per submodule	78,015
Number of hot-side channels	624,120
Number of cold-side channels	624,120
Active submodule volume height (m)	5.5
Active submodule volume width (m)	0.6
Active channel length(m)	0.5673
Submodule active volume (m^3)	1.872
Total active heat exchanger volume (m^3)	14.98
Nominal Operating Conditions†	
Power (MW)	48
Pressure in hot side – set at outlet (kPa) ‡	800
Pressure in cold side – set at outlet (kPa) ‡	500
Hot side pressure drop (Pa)	89
Cold side pressure drop (Pa)	2107
Mass flow rate on hot side (kg/s) ‡	92.4
Mass flow rate on cold side (kg/s) ‡	459.3
Temperature – hot side, cold leg (°C)	106.4
Temperature – cold side, cold leg (°C) ‡	75
Temperature – hot side, hot leg (°C) ‡	581
Temperature – cold side, hot leg (°C)	99.6
Cold side inlet velocity (m/s)	0.078
Hot side outlet velocity (m/s)	1.36
Reynolds number – hot side, cold leg	2496

* Geometry parameters refer to four modules (100% decay heat removal) for consistency with RELAP modeling methodology. The actual design has eight modules providing 200% decay heat removal capacity.

† These operating conditions are for design purposes, and performance data in this table are from a separate-effects RELAP model of the SCS/ECS heat exchangers only.

‡ Indicates an imposed boundary condition in the separate effects model of the SCS/ECS heat exchangers.

Note that the channel pitch, diameter and plate thickness given in Table 8-1 form a very thick web of coolant channels (channel pitch = 5.71 mm, channel diameter = 5.0 mm, plate thickness = 3.7 mm). Figure 8.5 shows a scaled drawing of a segment of one hot and one cold row of channels in the gas/water decay heat removal heat exchangers with dimensions given in mm.

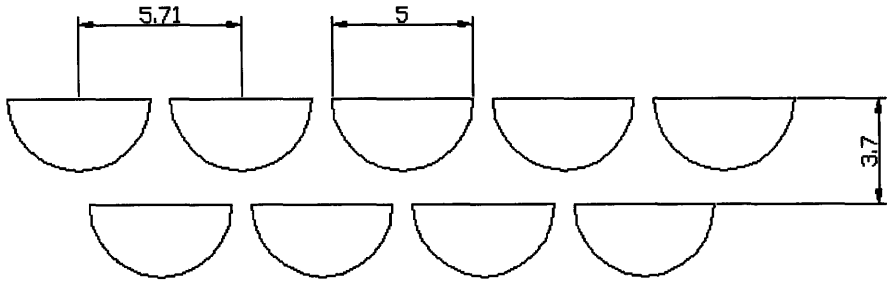

Figure 8.5. Drawing of a segment of one hot and one cold row of channels in the gas/water decay heat removal heat exchangers with dimensions in mm.

The water/water heat exchangers serving as the ultimate heat sink in this design are a variation on a tube-type design by General Atomics (GA) consisting of pipes which conduct the cooling water through water tanks located outside the containment building. The water tanks are connected to spray ponds also located outside of containment. Table 8-2 gives relevant details of the geometry of the heat exchanger such as number and dimensions of pipes within the heat exchanger and in the water loop. Nominal operating conditions are also given as in the case of the gas/water heat exchanger. Again, the performance parameters given are results from a separate-effects RELAP model of the heat exchanger with boundary conditions as indicated in the table.

Table 8-2. General Atomics water/water heat exchanger geometry and nominal operating conditions.

Heat Exchanger Geometry*	
Number of tubes	400
Number of passes	10
Tube length per pass (m)	3.324
Schedule 40 pipe: outside diameter (m)	0.0422
Inside diameter (m)	0.0351
Total hot side flow area (m^2)	0.387
Nominal Operating Conditions†	
Heat load (MW)	48
Water loop pressure (kPa) ‡	500
Water mass flow rate (kg/sec) ‡	459.3
Hot leg temperature (^oC) ‡	100
Cold leg temperature (^oC)	75.1
Sink temperature (^oC) ‡	25
Heat exchanger pressure drop (kPa)	16.98
Additional Water Loop Parameters	
Loop Elevation (m) (volumes 720 and 740 in Figure 9.2)	8.0
Number of supply and return loops	4
Supply and return pipe outside diameter (m)	0.3556
Supply and return pipe inside diameter (m)	0.3333

8.3 Summary

In this chapter, a description was given of the layout of the active SCS/ECS to be used from this point forward in this work. This system is similar to the hybrid active/passive SCS/ECS evaluated in the previous chapter, only now the gas/water heat exchangers are placed inside the PCIV. Some ultimately important design details were not addressed fully in this chapter: the drive mechanism for the SCS/ECS blowers was not described and the

* Geometry parameters refer to 100% decay heat removal for consistency with RELAP modeling methodology. The actual design has 200% decay heat removal capacity.

† These operating conditions are for design purposes and performance data in this table are from a separate-effects RELAP model of the SCS/ECS heat exchangers only.

‡ Indicates an imposed boundary condition in the separate effects model of the General Atomics water/water heat exchanger.

number of blowers, though nominally set at eight, was not investigated in detail. The detailed design of the blowers and check valves is also an open issue requiring further attention. In the next chapter, the final whole-plant RELAP model to be used in the remaining analysis will be described in detail. Geometric and performance parameters were given for gas/water and water/water heat exchangers in Table 8-1 and Table 8-2, but these parameters will be listed again in the following chapter in a format more suitable to documentation of a RELAP model (similar to the format used for Table 7-2 and Table 7-3).

9 RELAP Model of Reference Plant Design

9.1 Introduction

This chapter gives a description of the methodology used in modeling the reference plant design. In Chapter 7, a description was given for a previous core model and SCS/ECS design. The model described here represents the core design and SCS/ECS layout to be used for the remainder of this work. In Chapter 7, the PCS loops shown were identical to the ones used here, but since the analysis presented at that time was not focused on the performance of the PCS loops, a detailed description was withheld until this chapter, where more information regarding recuperators, precoolers and turbomachinery will be given.

9.2 Overall RELAP Model Layout and Nodalization

Figure 9.1 shows the overall layout and basic features of the reference plant with the active SCS/ECS described in the previous chapter. Figure 9.2 and Figure 9.3 show the nodalization scheme used for the whole-plant RELAP model of the reference design. Each region shown is a calculational node used in the model. The numbering scheme used in the RELAP model is shown in the figure and will be referenced in the text. Hatched regions attached to hydrodynamic volumes indicate that RELAP heat structures are used to simulate heat exchanger material, pipe walls, fuel, etc. The heat structures communicate thermally to the hydrodynamic volumes which they are attached to in the figures via convection. Figure 9.2 shows the nodalization of the vessel and core along with the PCS loops with the SCS/ECS and its attachment to the vessel omitted. The PCS loops here are identical to those mentioned in Chapter 7 and diagrammed in Figure 7.2. The left-hand PCS loop (300's) is a

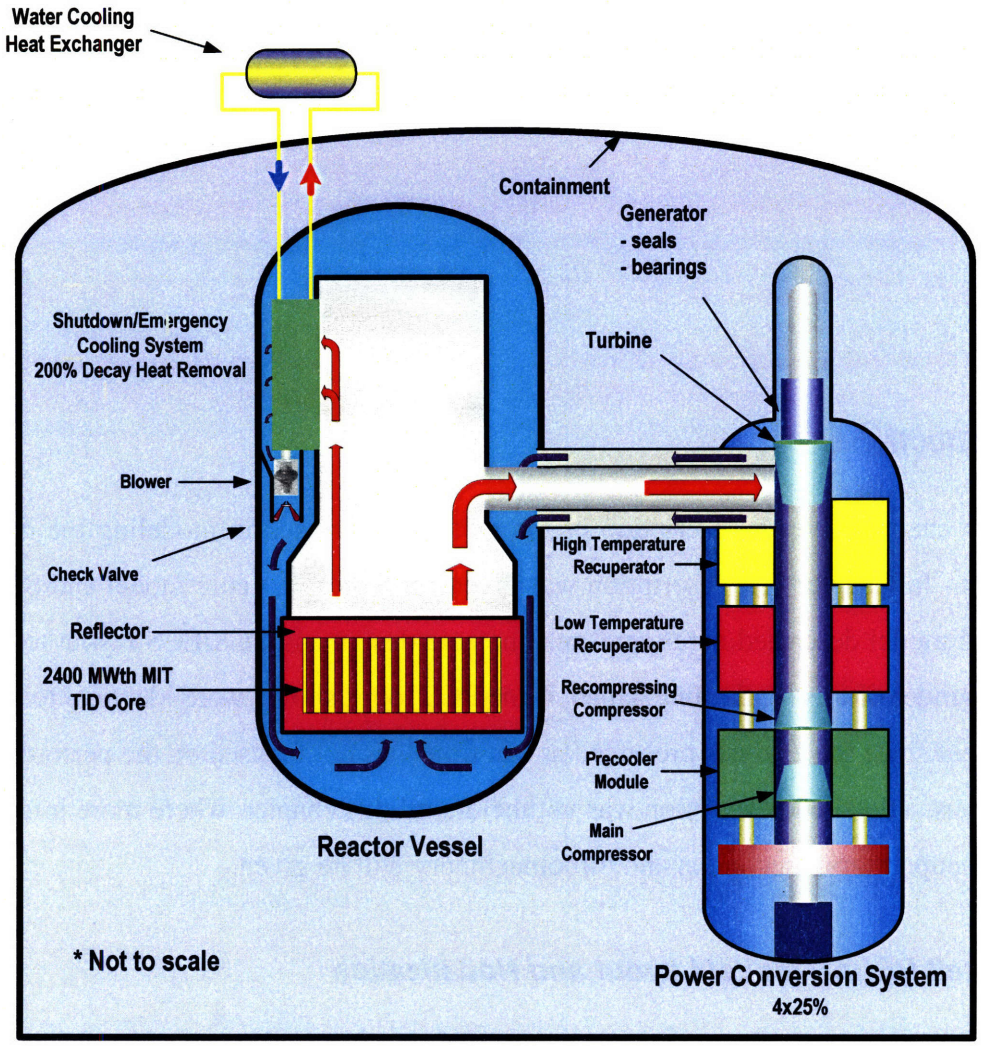

Figure 9.1. Layout of plant with active SCS/ECS.

single 25% loop and the right-hand PCS loop is a lumped 75% loop used to represent the remaining three which would be present in the actual plant. Simulation of pipe breaks or any other transient involving an event initiated in only one PCS loop are typically performed on the single 25% loop and the responses of the three remaining loops are assumed to be identical and captured by the lumped 75% loop. For this reason, the valves used to simulate pipe breaks are located on the ducts leading to and from the 25% PCS loop. To simulate a pipe break, combinations of valves 303, 304, 393 and 394 can be opened to allow coolant to escape to the containment volume. These valves can be sized according to the size of pipe break desired. To simulate complete severance of one of the co-axial PCS ducts (a so-called

400% break), these four valves are opened and valves 302 and 303 are closed to provide the most extreme case. As in the previous model, volumes 397 and 497 attached to the volumes at the main compressor inlets are pressure control volumes used to set the pressure in the system while the model runs to steady state. The valves leading to these volumes (396 and 496) are closed before the outset of a transient. Unlike in the previous plant model, the representation of the core now includes four channel types instead of two due to the addition of a heated inter-assembly gap and an unheated flow path for cooling shielding assemblies. These channels will be described in greater detail in a subsequent section.

The SCS/ECS and its attachments to the core downcomer and chimney are shown in Figure 9.3. As mentioned in the previous chapter, 100% decay heat removal capacity is modeled due to the assumption that half of the 200% capable SCS/ECS is not operational. There are a few key differences between this and the hybrid active/passive SCS/ECS analyzed in Chapter 7 and diagrammed in Figure 7.3. One is that the extended loop height of the CO_2 path to the decay heat removal heat exchanger has been removed since these heat exchangers are now located within the reactor vessel. Another is that the active volume of the gas/water heat exchangers now consists of horizontal channels rather than vertical. The water loop toward the top of the figure is unchanged from the previous revision of the SCS/ECS design.

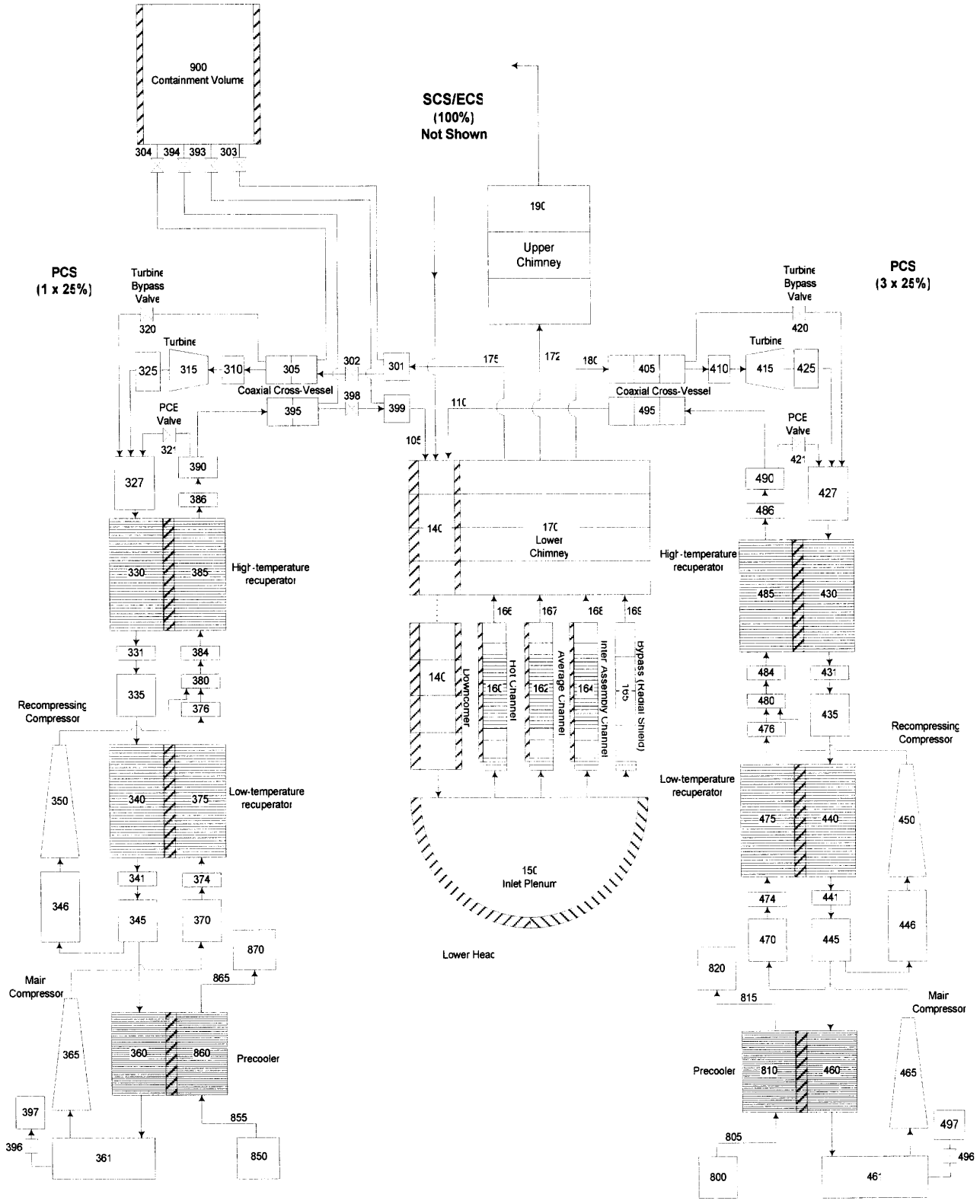

Figure 9.2. Nodalization diagram for RELAP model with SCS/ECS omitted.

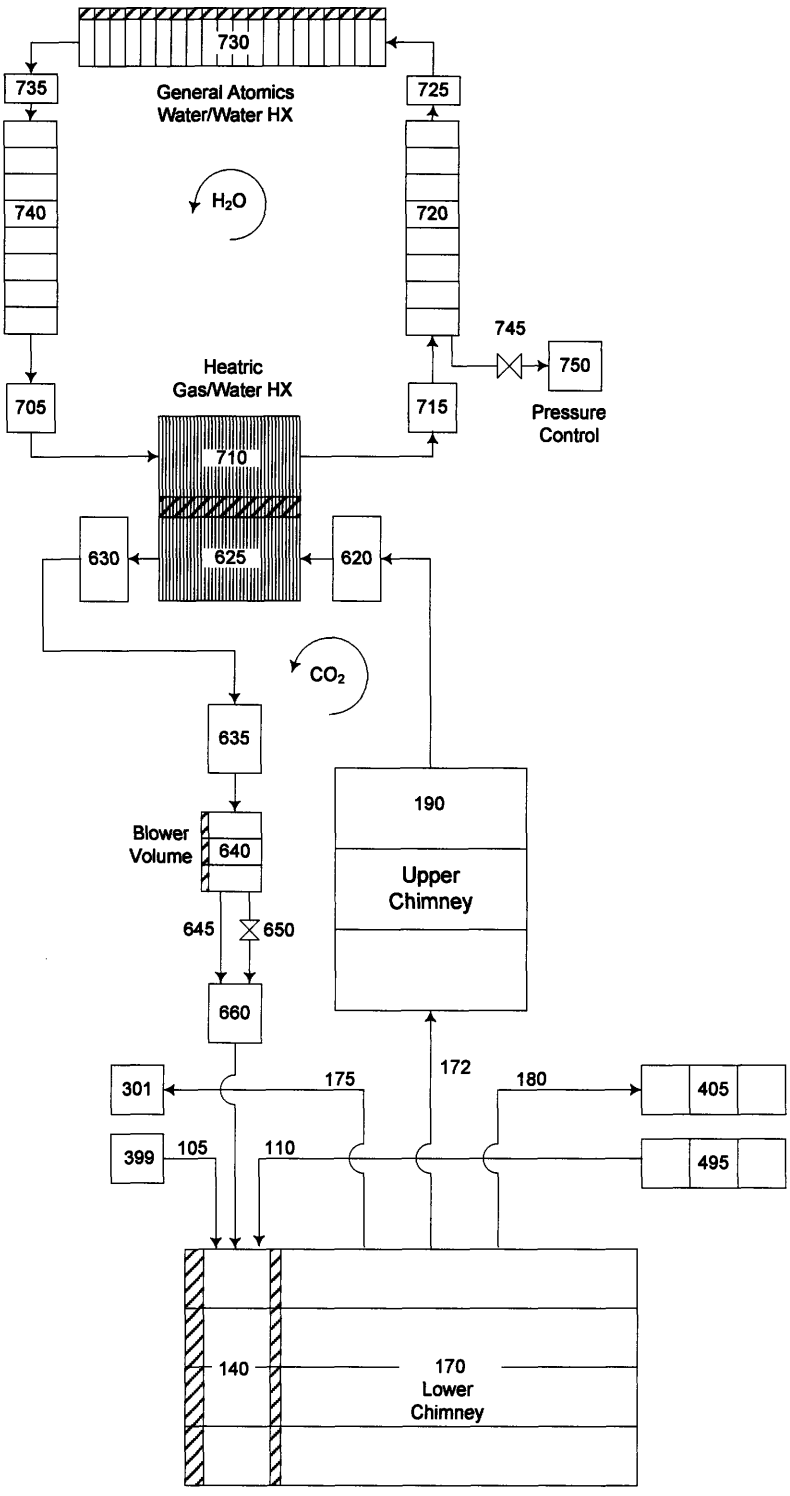

Figure 9.3. Nodalization diagram for RELAP model of SCS/ECS.

9.3 Vessel and Core

Coolant enters the upper downcomer (volume 140) from the PCS cold legs or the SCS/ECS blowers and proceeds downward between the barrel and the vessel wall. The CO_2 then encounters the inlet plenum, a branch which connects the flow to the four channel types used to represent the flow in the core. Figure 9.4 shows a diagram of the nodalization and heat structures used in the core model. Volumes 160, 162, 164 and 165 are used to represent the hot channel, the average channel, the heated inter-assembly flow path and the bypass between radial shielding assemblies, respectively. Table 9-1 shows information about these four channels. The bottom node of each channel represents the passage through the lower flower-box type core plate. Flow to each fueled assembly is assumed to occur through a 17 cm diameter hole. The second node of each channel simulates the expansion of the flow after leaving the passage through the lower plate before entering the coolant channels which carry coolant through the core. The parameters in Table 9-1 only refer to the third node through the last node in each channel. For a more detailed description of these hydrodynamic volumes, see Appendix A for an excerpt of the RELAP input deck.

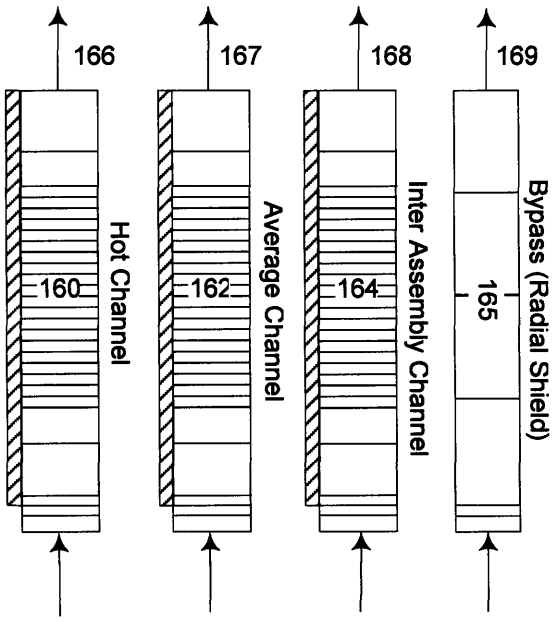

Figure 9.4. Nodalization diagram of core channels in RELAP model.

Table 9-1. Description of hydrodynamic volumes in core.*

Node	Description	D_e (mm)	# of Channels	Length (mm)	Height (mm)	Entrance k_{loss}	Roughness (m)	Flow Area per channel (m^2)
160	Hot Channel	7.0	265	3640	3640	0.1	$1.0x10^{-5}$	$3.848x10^{-5}$
162	Average Channel	7.0	99,905	3640	3640	0.1	$1.0x10^{-5}$	$3.848x10^{-5}$
164	Inter-Assembly Channel	5.635	1	3640	3640	25.0	$4.5x10^{-5}$	0.4191
165	Bypass (Radial Shield)	5.635	1	3640	3640	30.0	$4.5x10^{-5}$	0.3193

The three heated core channels are nodalized such that the segments of coolant channels in the active core are represented by 20 axial nodes (the smaller nodes shown in Figure 9.4). The segment of coolant channels adjacent to upper and lower axial reflectors are represented by one axial node each, as in the case of axial shielding. In the heated channels, the third node from the bottom is the lower plate of the TID fuel assembly. In the bypass channel shown on the right in Figure 9.4, the bottom two nodes are used to represent the passage through the core lower plate and the subsequent expansion in the TID fuel assembly plenum, just as in the case of the heated channels. Beyond this, however, only four nodes are used to represent the remaining bypass flow because no heating is occurring along this length and a simple representation such as this will suffice.

In the calculations performed with the FLOWSPLIT code, heat conduction through the fuel-clad gap was handled iteratively by considering separately the contributions from conduction through the fill gas and radiation heat transfer. RELAP includes a built-in gap conductance model, but it is much more robust than is needed for this work. Also, the model in RELAP is based on pin fuel, and the fuel-clad gap in TID fuel may behave differently. Hence, this model may not be fully applicable to this design. Instead, an effective material is defined such that if placed in the gap between cladding and fuel, the temperature rise for a given heat flux is the same as with the model used in FLOWSPLIT. The required thermal conductivity of this effective gap material can be found using the following relationship;

$$\Delta T_{gap} = \frac{q''_{gap}}{h_{gap}} = \frac{q''_{gap}}{k_{gap}} t_{gap} \qquad \textbf{(9-1)}$$

* The first two nodes of each channel type are not represented here. See Appendix A for an excerpt of the RELAP input deck giving detailed channel information.

where ΔT_{gap} is the temperature rise across the gap in Kelvins, q''_{gap} is the heat flux through the gap in W/m^2, h_{gap} is the gap conductance in W/m^2·K and k_{gap} is the thermal conductivity of the effective gap material in W/m·K. The heat flux is cancelled from the equation giving the following relation giving the thermal conductivity of the effective material as the product of the gap conductance and the thickness of the gap;

$$k_{gap} = h_{gap} t_{gap} \tag{9-2}$$

One complication with this assumed gap material is that as one would expect from the implicit Equation 5-16, the gap conductance changes with heat flux. Here, because we have assumed a constant thermal conductivity of the fill gas, gap conductance increases with heat flux due to the radiation component of heat transfer. For the hot channel in RELAP, the value of gap conductance calculated by FLOWSPLIT in the hot channel at the axial node where the peak fuel temperature was located was used to find the effective conductivity of the gap. For the average channel in RELAP, the axially averaged value of gap conductance calculated by FLOWSPLIT in the average channel was used to find the effective conductivity of the gap. In this way, the peak fuel temperature is preserved in the hot channel and the core-average fuel temperature is approximately preserved in the average channel.

Reactor kinetics parameters can be entered in the RELAP model to simulate power changes resulting from coolant density or fuel temperature feedback, a reactor scram, rod ejection, etc. RELAP has the capability to simulate power level changes based on point or nodal kinetics calculations. In a fast reactor, the neutronic coupling of the reactor is expected to be strong, and so point kinetics can be used with reasonable accuracy. Estimates of delayed neutron fraction (β) and mean prompt neutron lifetime (Λ) are given in Table 9-2 at three points in the cycle, beginning of life (BOL), middle of life (MOL) and end of life (EOL). These values were calculated by [Handwerk (b), 2006] using MCNP. The ratio of delayed neutron fraction to mean prompt neutron lifetime is required in order for reactor kinetics calculations to be performed by RELAP. The β/Λ value selected for this work was 4950 s^{-1} because the lower values of this ratio give the slowest decrease in power following a reactor scram, although the difference between these three values has a very low impact on

the speed of a reactor scram. Figure 9.5 shows the reactivity versus time after a scram is initiated as control rods fall into the core; this curve is similar to a scram curve of a typical pressurized water reactor.

Table 9-2. Best-estimate values of delayed neutron fraction and prompt neutron lifetime. [Handwerk, 2006]

Point in Cycle	β	Λ(s)	β/Λ (s^{-1})
BOL	0.00461	8.69×10^{-7}	5300
MOL	0.00417	8.43×10^{-7}	4950
EOL	0.00438	814×10^{-7}	5380

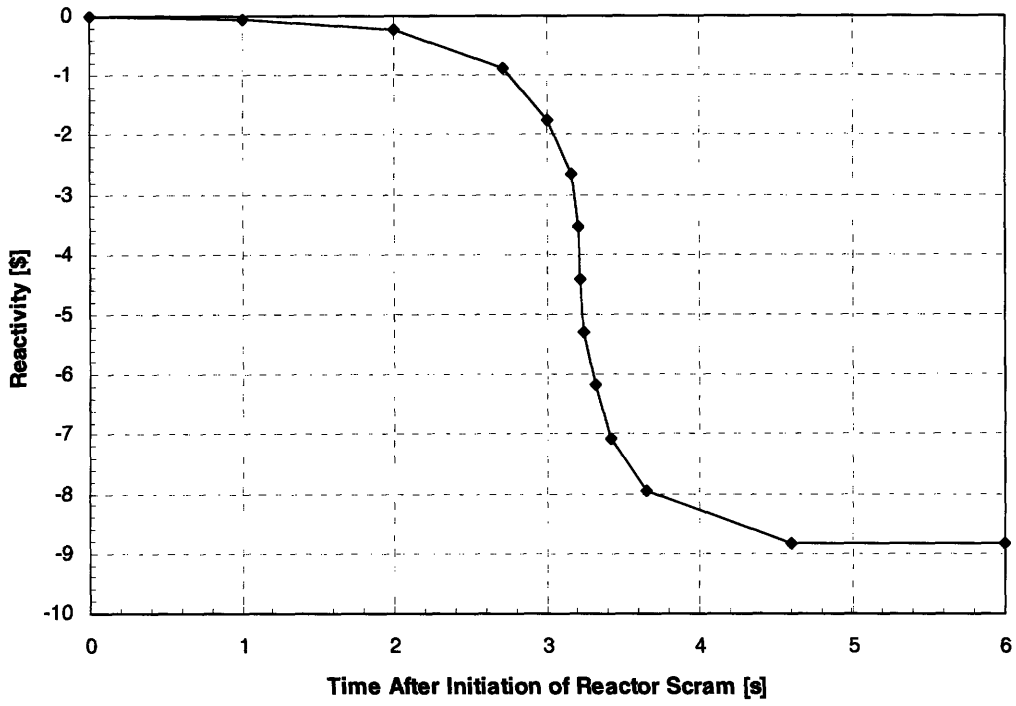

Figure 9.5. Reactivity versus time past the initiation of a reactor scram.

9.4 Power Conversion System

This section provides a description of key PCS component parameters. As mentioned before, the PCS loop model has not changed since the analyses presented in Chapter 7, but since that part of the work did not deal heavily with the PCS loops, description of them was withheld until this section.

9.4.1 Recuperators

Each PCS loop contains a high and a low temperature recuperator. Table 9-3 gives some of the key parameters of the each. They are modeled in RELAP as having straight vertical semicircular channels, though a later design revision may specify zig-zag channels in order to increase heat transfer coefficient and reduce the required heat exchanger volume. In Table 9-3, the total volume represents the active heat exchanger volume only, neglecting headers. The coolant channels in the recuperators and precoolers are semicircular with a diameter of 2 mm.

Table 9-3. Selected high and low temperature recuperator design parameters.*

Recuperator	**High temperature**	**Low temperature**
Total active volume (m^3)*	66.86	43.14
Plate Width (m)	0.6	0.6
Active channel length (m)	2.3	2.00
Total height (m)	48.45	35.95
Height per module (m)	4.845	5.14
Number of modules per HX	10	7
Channel type	Straight	Straight
Semicircular channel diameter (mm)	2.0	2.0
Plate thickness (mm)	1.5	1.5
Total number of cold/hot plates	16150 / 16150	11983 / 11983
Flow area per side (m^2)	6.291	4.668
Channel hydraulic diameter (mm)	1.222	1.222
Channel pitch (mm)	2.40	2.40
Total number of hot-side channels	4,005,200	2,971,867
Total number of cold-side channels	4,005,200	2,971,867
Hot side pressure drop (kPa)	111.8	100.03
Cold side pressure drop (kPa)	40.4	10.22
Total power (MW_{th})	1222	358
Power density (MW_{th}/m^3)	18.27	8.32
Material	stainless steel 316	stainless steel 316

* Parameters are given for a single recuperator, i.e. one PCS loop.

9.4.2 Precoolers

Table 9-4 gives parameters of interest for the precoolers. The water side of the precoolers has an inlet temperature of 20°C. This water flow is simulated by two time dependent volumes to set pressure and inlet temperature and a time dependent junction which forces the water flow rate to 4726 kg/s per precooler (one per PCS loop). Assuming water pump isentropic efficiency of 85%, the pumping power required at steady state full power conditions is 356 kW per PCS loop, or 1.42 MW for the entire plant. S-CO_2 is cooled to 32°C (89.6°F) in the precooler, 1°C higher than its critical temperature.

Table 9-4. Selected precooler design parameters.*

Total active volume (m^3)	10.00
Plate Width (m)	0.60
Active Length (m)	0.9
Total height (m)	18.52
Height per module (m)	4.63
Number of modules per HX	4
Channel type	Straight
Semicircular channel diameter (mm)	2.00
Plate thickness (mm)	1.50
Channel hydraulic diameter (mm)	1.222
Channel pitch (mm)	2.40
Total number of cold/hot plates	6173 / 6173
Channel hydraulic diameter (mm)	1.222
Total number of hot-side channels	1,530,987
Total number of cold-side channels	1,530,987
Water inlet temperature (°C)	20
Water flow rate (kg/s)	4726
Gas side pressure drop (kPa)	25.76
Water side pressure drop (kPa)	63.8
Water side pumping power (kW)	356
Total power (MW_{th})	295
Power density (MW_{th}/m^3)	29.5
Material	titanium

* Parameters are given for a single precooler, i.e. one PCS loop.

The availability of water at 20°C (68°F) is an issue which should be addressed in future work, as this may geographically limit the design to cooler climates. If needed, higher temperature water could be used in the cold side of the precooler, but this would be at the expense of higher water mass flow rates and thus higher pumping power, especially because the heat capacity of S-CO_2 becomes quite large as the fluid approaches its critical point.

9.4.3 Turbomachinery

9.4.3.1 Turbine

The turbine isentropic efficiency is modeled in RELAP as a function of the ratio of turbine work to rated turbine work and is given by;

$$\eta = \eta_R \left[0.9407 + 0.0858\left(\frac{\dot{W}}{\dot{W}_R}\right) - 0.0061\left(\frac{\dot{W}}{\dot{W}_R}\right)^2 - 0.0188\left(\frac{\dot{W}}{\dot{W}_R}\right)^3 \right] \quad \textbf{(9-3)}$$

where η is the turbine efficiency, η_R is the rated turbine efficiency (94%), $\dot{W}$ is the turbine power and $\dot{W}_R$ is rated turbine power (409 MW). This curve was originally developed by [Wang, et. al., 2004] for a lower-temperature power cycle having a turbine inlet temperature of 550°C. For application to this power cycle, the rated power and efficiency were changed to match the expected conditions for this cycle and the off-normal performance was left the same.

9.4.3.2 Compressors

The version of RELAP used for this work has the capability of modeling compressors with detailed performance curves relating efficiency and pressure ratio developed by the compressors to relative corrected flow and relative corrected speed. The relative corrected flow is defined as follows;

$$v = \frac{\dot{m}\rho_R a_R}{\dot{m}_R \rho a} \quad \textbf{(9-4)}$$

where v is the dimensionless relative corrected flow, $\dot{m}$ is the compressor mass flow rate, ρ is the fluid density, a is the sound speed and the subscript R indicates a rated condition. The fluid density ρ and the sound speed a are evaluated at stagnation conditions at the inlet to the compressor. The relative corrected speed is given by;

$$\alpha = \frac{\omega}{\omega_R}\frac{a_R}{a} \tag{9-5}$$

where α is the dimensionless relative corrected speed and ω is the shaft speed in rad/s.

In RELAP, the detailed performance curves for compressors are in the form of tables which give pressure ratio developed by the compressor and isentropic efficiency of the compressor for a given relative corrected flow rate. A table is entered for each relative corrected speed desired. RELAP performs a linear double interpolation to determine the compressor head and efficiency at each time step. Compressor performance characteristics were developed by [Wang, et. al., 2004] for the power cycle having a turbine inlet temperature of 550°C and main compressor inlet temperature of 42°C. These performance characteristics were converted to the format accepted by RELAP by Cliff Davis at the Idaho National Laboratory. Because in this power cycle, the nominal pressure ratio developed by the compressors and isentropic efficiencies are different than the lower-temperature cycle, all values in the characteristic curve of each compressor were multiplied by a constant such that the performance was correct at nominal conditions. Figure 9.6 and Figure 9.7 show pressure ratio versus relative corrected flow for a number of relative corrected speeds for the main and recompressing compressors, respectively. The actual surge and choke lines are shown on each figure, but the line for each relative corrected speed is extrapolated in order to extend the range in which the compressor models can operate without interrupting the transient simulations performed by RELAP. Isentropic efficiency curves for each compressor are not given here.

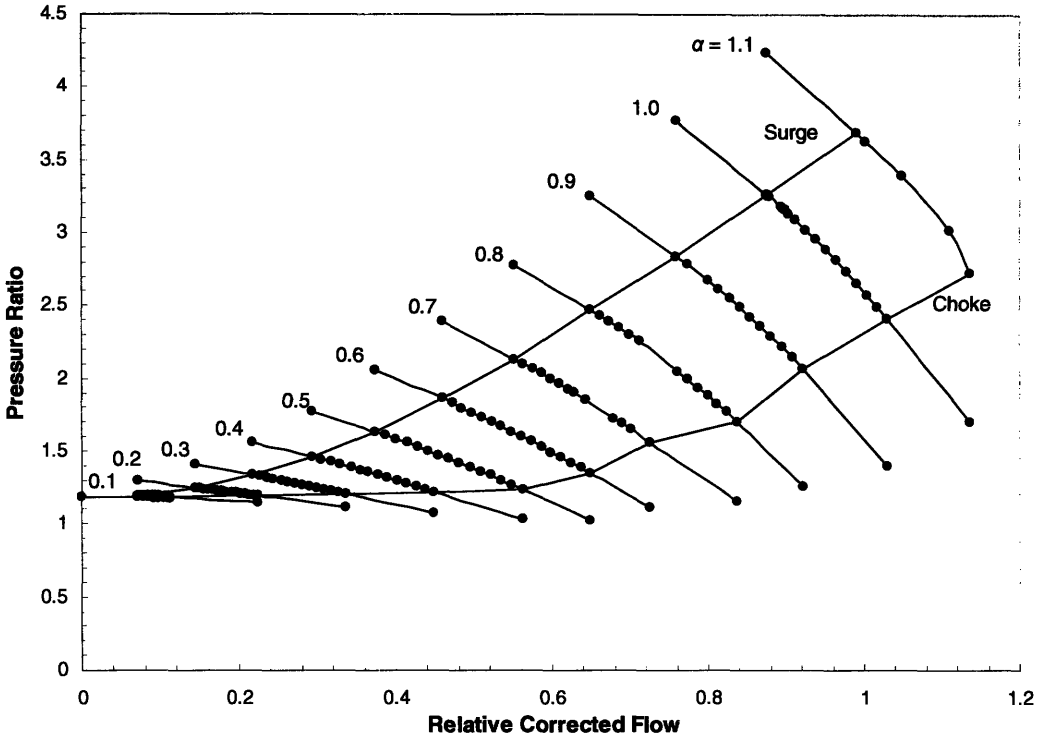

Figure 9.6. Pressure ratio developed by main compressor.

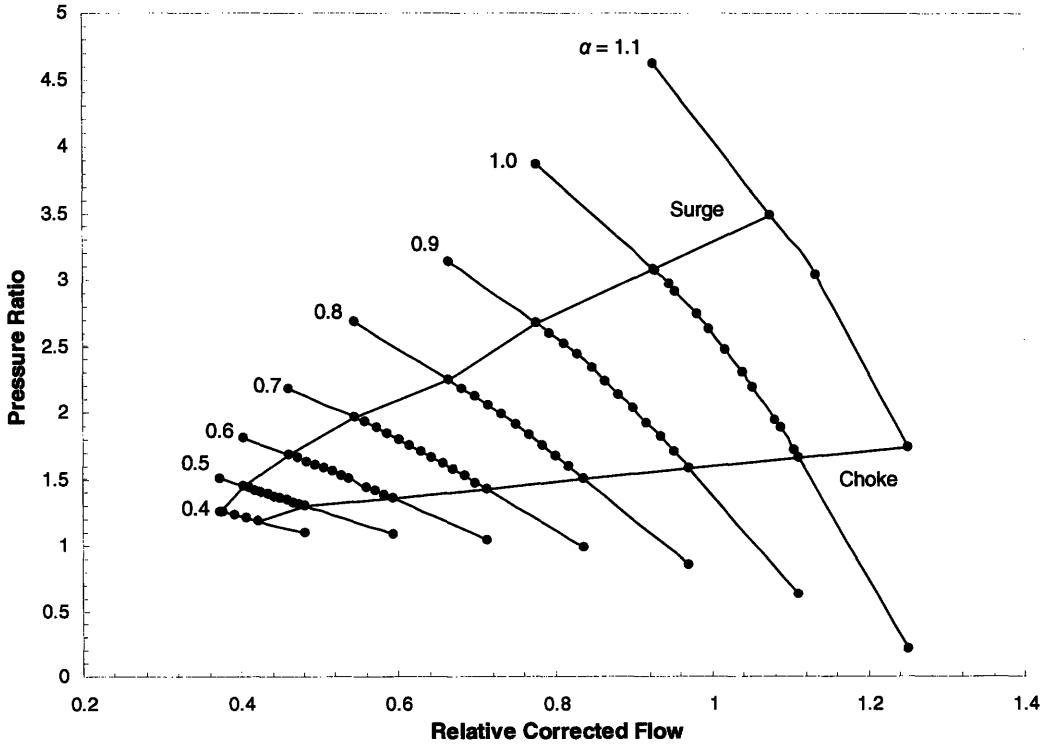

Figure 9.7. Pressure ratio developed by recompressing compressor.

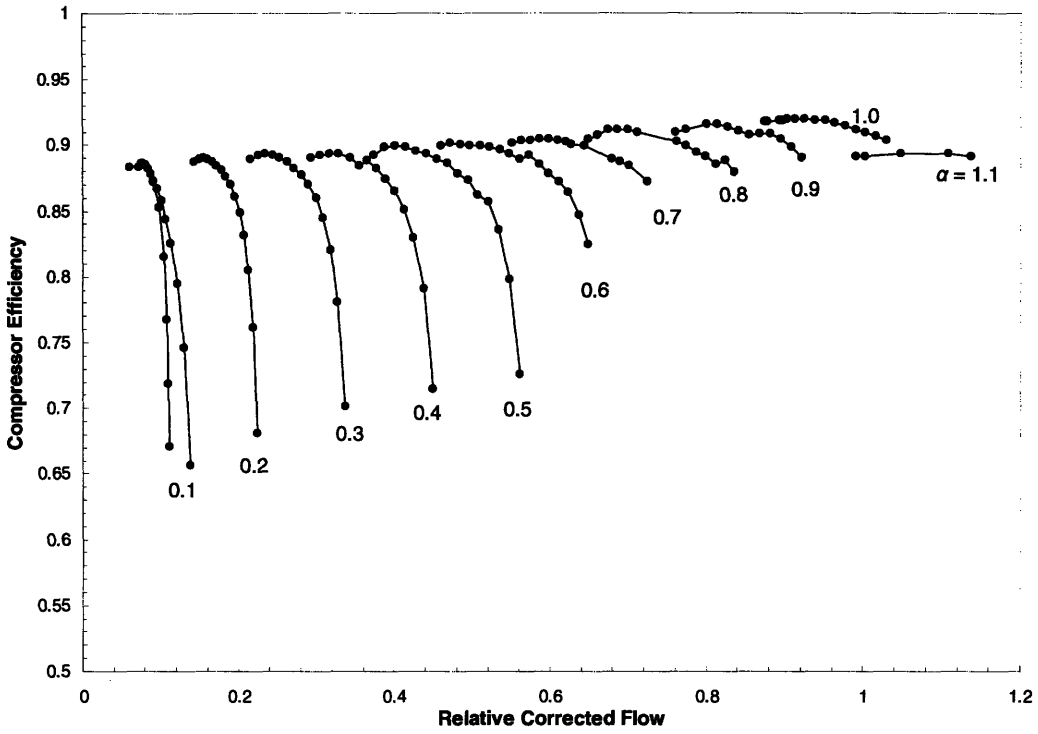

Figure 9.8. Main compressor efficiency versus relative corrected flow.

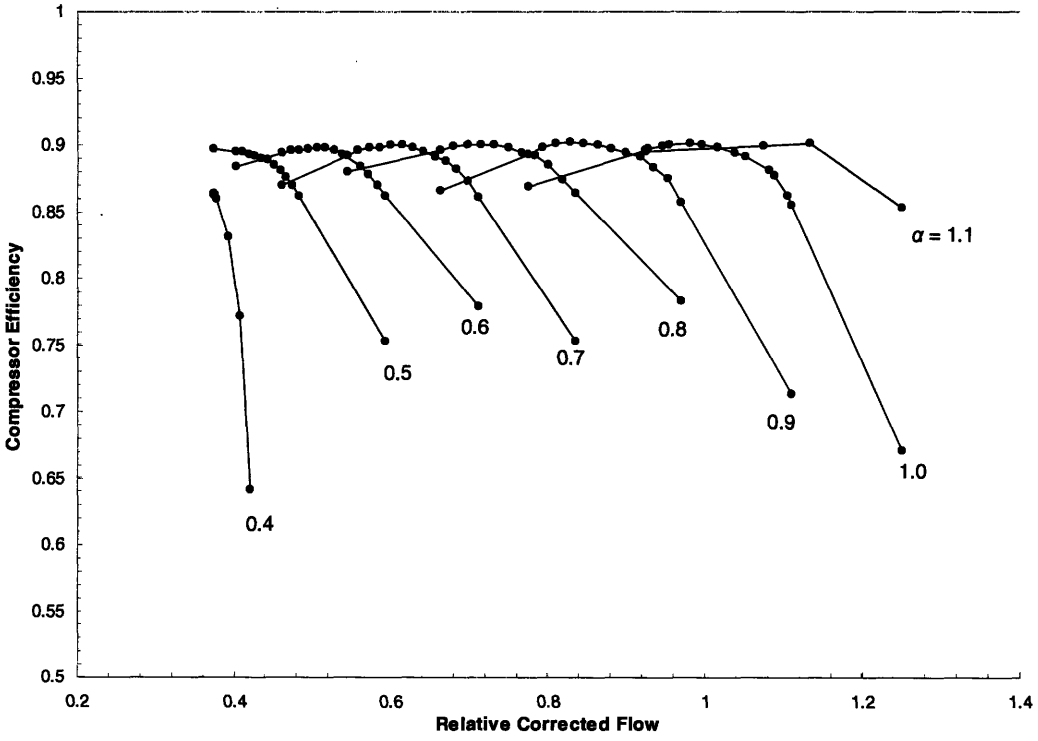

Figure 9.9. Recompressing compressor efficiency versus relative corrected flow

9.4.3.3 Homologous Pump Representation of Compressors

As can be gathered from Figure 9.6 and Figure 9.7 the operating range of the axial compressors specified at this point in the work is quite narrow. This means that many of the transients analyzed will cause a surge or choke and end the simulation. In future work, the use of radial compressors should be investigated as they offer a wider band of operation than the axial type. For this work, however, the RELAP model employed for transient analysis will use homologous pump models to approximate the effects of compressors. This allows the RELAP transient simulations to continue to run although compressors may be operating outside their allowable bands, while RELAP control variables programmed into the decks can tell the user whether or not a compressor has surged or choked. To convert a compressor model to a homologous pump in RELAP, several nominal parameters must be calculated. The following three equations refer to rated conditions, but the R subscript will be left off for clarity. First, the volumetric flow rate is calculated by;

$$Q = \frac{\dot{m}}{\bar{\rho}} \tag{9-6}$$

where Q is the volumetric flow rate, $\dot{m}$ is the mass flow rate in the compressor and $\bar{\rho}$ is the average fluid density in the pump. It should be noted that there is a difference in the way head is added to fluid between pump and compressor models in RELAP. In a compressor, all head is added at the inlet junction whereas in a pump model, half is added at the inlet junction and the rest at the outlet junction. Therefore, if the average density is obtained from a RELAP calculation of compressor performance, the average of the compressor volume and the upstream volume should be used. In the case of the pump, the density in the pump volume should reflect this average density well. The rated head is calculated by;

$$H = \frac{\Delta P}{\bar{\rho} g} \tag{9-7}$$

where H is the head developed by the compressor (or pump), ΔP is the pressure increase across the compressor and g is the gravitational acceleration. The rated torque of the pump is calculated by;

$$\tau = \frac{\bar{\rho} Q g H}{\omega \eta} \tag{9-8}$$

where τ is the torque that the compressor exerts on the shaft, ω is the shaft speed in rad/s and η is the compressor isentropic efficiency. Off-normal performance curves are used to simulate the change in performance as flow rate and shaft speed change. These are given in Appendix B. Once these parameters were calculated from the design and the steady state compressor results, the rated volumetric flow rate was increased to better match the design flow rate.

9.4.4 Shafts and Generators

The RELAP model includes two shafts, one is used to represent the single PCS loop and the other the lumped (3x) PCS loop. In general, the shaft speed is governed by the following equation;

$$\sum_i \tau_i = \sum_i I_i \frac{d\omega}{dt} - \sum_i f_i \omega + \tau_c \tag{9-9}$$

where τ_i is the torque applied to the shaft by component i in N·m, I_i is the moment of inertia of component i in kg·m^2, ω is the angular velocity of the shaft in rad/s, f_i is the friction factor of component i in N·m·s, and τ_c is the torque on the shaft from a control system in N·m. The sign convention is such that the angular velocity during normal operation is positive and torque applied in the direction of normal rotation is positive. The turbine would thus apply positive torque typically with the compressors and generators applying negative torque. During normal operation, there will no torque applied by a control system and friction in the shaft is to be neglected, so the f_i and τ_c terms are zero. Given these assumptions, the equation governing shaft speed can be expanded to include the components used in this work as follows;

$$\tau_{MC} + \tau_{RC} + \tau_T + \tau_G = \left(I_{MC} + I_{RC} + I_T + I_G + I_S\right) \frac{d\omega}{dt} \tag{9-10}$$

where the subscript *MC* refers to the main compressor, the subscript *RC* refers to the recompressing compressor, the subscript *T* refers to the turbine, the subscript *G* refers to the

generator and the subscript S refers to the shaft. During normal operation, the generator is attached to the electrical grid which holds the shaft speed constant at 376.991 rad/s (60 Htz or 3600 rpm). In this case, the right side of Equation 10-10 is zero and the generator torque is determined by;

$$\tau_G = -(\tau_{MC} + \tau_{RC} + \tau_T) \tag{9-11}$$

Table 9-5 gives the moments of inertia for a single shaft and the components attached to it. The moments of inertia for the lumped 3x shaft and components would be three times these values. These components have relatively low moments of inertia for the power delivered by the PCS. This creates a challenge in preventing turbine overspeed during a loss of external load transient, an issue which will be addressed in a later chapter.

Table 9-5. Turbomachinery moments of inertia for a single PCS.

Component	**Moment of Inertia ($kg \cdot m^2$)**
Main Compressor	305.6
Recompressing Compressor	113.1
Turbine	850.0
Generator	1000.0
Shaft	186.0
Total	**2454.7**

9.5 Decay Heat Removal System

The decay heat removal system was described in the last chapter, but the key details of hydrodynamic components are repeated here in a format better suited to understanding RELAP modeling methodology. As was mentioned before, the representation of the SCS/ECS in the RELAP model is designed to account for 100% decay heat removal although the actual system would have twice this capacity. All modeled SCS/ECS components are lumped into one effective loop for simplification of the model and reduction of computation time. Table 9-6 gives a description of the hydrodynamic components in the vessel and

SCS/ECS containing CO_2 omitting the core components. It is assumed that all CO_2 en route to the SCS/ECS heat exchangers travels to the axial midpoint of the heat exchangers. Note that the heights of the volumes in the table do not sum to zero because 1) the core channels are not included in this table and 2) the inlet and outlets to the lower plenum all occur on the top of the volume as shown in Figure 9.2. Table 9-7 gives a description of the hydrodynamic volumes which comprise the water loop of the SCS/ECS. A time-dependent junction connecting volumes 745 and 705 can serve as a water pump for active cooling or a single junction is placed there to allow the water loop to flow purely by natural circulation.

Table 9-6. Description of hydrodynamic volumes in vessel and SCS/ECS with core components omitted.

Node	Description	D_e (mm)	# of Channels	Length (mm)	Height (mm)*	Entrance k_{loss}	Roughness (m)	Flow Area per channel (m^2)
140	Downcomer	600	1	9580	-9580	0.23	$4.5x10^{-5}$	8.124
150	Inlet Plenum	8920	1	1000	1000	1.24	$4.5x10^{-5}$	62.5
170	Lower Chimney	8200	1	5640	5640	1.0	$4.5x10^{-5}$	52.8
190	Upper Chimney	5970	1	6390	6390	0.1	$4.5x10^{-5}$	28.0
620	G/W HX Inlet Plenum	40	48	200	0	0.5	$4.5x10^{-5}$	0.11
625	G/W HX Hot Side	3.055	611,766	567.3	0	0.0	$4.5 x10^{-5}$	$9.817x10^{-6}$
630	G/W HX Outlet Plenum	40	48	200	0	1.0	$4.5x10^{-5}$	0.11
635	HX CO_2 Downcomer	300	8	2750	-2750	1.0	$4.5x10^{-5}$	0.12
640	Blower/Check Valve	1400	4	3000	-3000	1.0	$4.5x10^{-5}$	3.08
660	Lower HX Downcomer	1600	1	640	-640	13.23	$4.5x10^{-5}$	20.0

Table 9-7. Description of hydrodynamic volumes in water loop of active SCS/ECS.

Node	Description	D_e (mm)	# of Channels	Length (mm)	Height (mm)	Entrance k_{loss}	Roughness (m)	Flow Area per channel (m^2)
705	G/W HX Inlet Plenum	130.8	48	2750	-2750	0.5	$4.5x10^{-5}$	$6.25 x10^{-3}$
710	G/W HX Hot Side	3.055	611,766	567.3	0	0.5	$4.5x10^{-5}$	$9.817x10^{-6}$
715	G/W HX Outlet Plenum	130.8	48	2750	2750	1.0	$4.5x10^{-5}$	$6.25 x10^{-3}$
720	Water loop Riser	333.3	4	8000	8000	0.0	$4.5x10^{-5}$	0.087
725	G/A HX Inlet Plenum	35.1	391	500	0	0.5	$4.5x10^{-5}$	$9.676 x10^{-4}$
730	G/A UHS HX	35.1	391	33240	0	0.0	$4.5x10^{-5}$	$9.676 x10^{-4}$
735	G/A HX Outlet Plenum	35.1	391	500	0	0.0	$4.5x10^{-5}$	$9.676 x10^{-4}$
740	Water loop Downcomer	333.3	4	8000	-8000	1.0	$4.5x10^{-5}$	0.087

* Volume heights in this column do not sum to zero because core channels are omitted and because all attachments to lower plenum (volume 150) at the top of this volume as shown in Figure 9.2.

9.6 Performance of RELAP Model in Steady-State Full Power Operation

Each component of the system is modeled separately in RELAP in order to verify that it performs as expected. In some cases, tuning is required at this stage. For example, in the case of the recuperators and precoolers, the design of the headers is not modeled in detail, but rather the inlet and outlet loss coefficients are adjusted such that the overall pressure losses match the design values. Also, because in these heat exchangers, the flow paths are more complex than the straight channels in crossflow modeled in this work, fouling factors are used to match the heat exchanger effectiveness calculated by RELAP to design values. Individual components are combined into larger RELAP models of PCS loops and the reactor vessel. These models are allowed to run to steady state and then are combined to make the final model of the entire plant. Table 9-8 shows a comparison of key core performance parameters from the steady state RELAP model with compressors to the expected values calculated with FLOWPSLIT (in parenthesis). In general, the two show excellent agreement. From the agreement in peak fuel temperatures, it can be concluded that the effective gap material used in the RELAP model represents the gap temperature rise well.

Table 9-8. Whole-plant RELAP core performance parameters with FLOWSPLIT values in parentheses.

Parameter	Hot Channel	Average Channel	Inter-Assembly Channel	Bypass Channel
Mass flow rate* (kg/s)	0.1050 (0.1049)	0.1060 (0.1060)	615.9 (611.0)	459.1 (478.4)
Peak T_{wall} (°C)	788.6 (785.1)	747.1 (743.4)	669.7 (666.4)	
Peak T_f (°C)	1750 (1764)	1594 (1625)	1011 (none calculated)	
Outlet T_{bulk} (°C)	686.6 (686.5)	659.2 (658.6)	626.1 (627.6)	
Total Core ΔP (kPa)	421.5 (412.7)			

* Mass flow rates in hot and average channel types are given on a per channel basis, while mass flow rates in inter-assembly space and bypass are based on total flow in that channel type.

Table 9-9 shows a comparison between the design power cycle statepoints to those of the RELAP model at steady state. Both the model with detailed compressor curves and homologous pumps are included with both showing good agreement. Table 9-10 shows a comparison of selected PCS design parameters with steady state RELAP results with the compressor models. This table refers to the single PCS loop, but exact matching between the single PCS and the 3x PCS was verified using separate effects PCS models of each. If modeled correctly, results from steady state models of each PCS loop should match to all significant figures. The results on this table indicate again that the RELAP model is performing as expected at steady state. Adjustments were made to the RELAP model of the entire plant after its assembly in order to achieve better agreement with the design power cycle statepoints, primarily core outlet temperature. The precooler water side flow rate was adjusted to make the main compressor inlet temperature very close to 32°C and the reactor power was lowered slightly to make the steady state core outlet temperature closer to the target of 650°C. Table 9-10 compares design steady state core flow rate, reactor power and recompressed fraction to results from the RELAP model with compressors and homologous pumps, again showing excellent agreement. The reactor power was lowered to 99.4% of the target 2400 MW_{th} in the model with compressors and 99.7% in the model with homologous pumps.

Table 9-9. Comparison of power cycle statepoints in RELAP model to design values.

Statepoint	Temperature (°C)			Pressure (MPa)		
	Design	RELAP		Design	RELAP	
		Compressors	Pumps		Compressors	Pumps
1	32.0	32.0	32.0	7.69	7.69	7.69
2	60.9	61.1	61.1	20.00	20.05	20.14
3	159.1	159.6	157.8	19.99	20.02	20.11
4	485.5	487.1	486.2	19.95	19.97	20.06
5	650.0	649.3	649.7	19.45	19.41	19.50
6	529.9	531.8	531.6	7.93	7.91	7.91
7	167.3	167.6	165.5	7.82	7.80	7.80
8	70.9	71.0	70.6	7.71	7.71	7.71

Table 9-10. Comparison of PCS performance in RELAP model to design values.*

Component / Parameter	Design	RELAP
High Temperature Recuperator		
Hot side ΔP_{fric} (kPa)	111.8	111.2
Cold side ΔP_{fric} (kPa)	40.4	40.6
Total power (MW_{th})	1222	1225
Low Temperature Recuperator		
Hot side ΔP_{fric} (kPa)	100.0	100.8
Cold side ΔP_{fric} (kPa)	10.2	10.4
Total power (MW_{th})	358.	358
Precooler		
Gas side ΔP_{fric} (kPa)	23.23	22.79
Water side pumping power (MW)	0.31	0.356
Total power (MW_{th})	295	295
Turbine		
Shaft power (MW)	409	400.2
Pressure ratio	2.45	2.45
Efficiency (%)	94.0	94.1
Flow rate (kg/s)	2927	2922.6
Main Compressor		
Shaft power (MW)	34	35.0
Pressure ratio	2.60	2.61
Efficiency (%)	91.0	90.6
Flow rate (kg/s)	1698	1694.8
Recompressing Compressor		
Shaft power (MW)	70	71.0
Pressure ratio	2.59	2.60
Efficiency (%)	90.0	90.0
Flow rate (kg/s)	1229	1227.8
Cycle Efficiency (%)†	50.8	49.3

* Parameters apply to a single PCS loop in RELAP model of entire plant using detailed compressor models.

† Cycle thermodynamic efficiency includes precooler water side pumping power but not generator and switchyard losses. Note the reduction in reactor thermal power listed in Table 9-11 for calculation of efficiency.

Table 9-11. Comparison of overall plant parameters in RELAP model to design values.

Parameter	Design	RELAP	
		Compressors	Pumps
Total mass flow rate (kg/s)	11,708	11,690	11,637
Core Thermal Power (MW_{th})	2400	2385.1	2392.3
Recompressed fraction (%)	42.0	42.0	41.7

Figure 9.10 shows the radial temperature profile in the hot and average channel types at the axial position of maximum fuel temperature, a few centimeters above the axial centerline of the fuel. Data points indicate the locations of radial calculational nodes and the vertical dotted lines show the locations of interfaces between materials. Six nodes were used to model the radial temperature profile and three were used in the cladding for a total of nine radial nodes at each axial location in the fuel channels. The horizontal dotted line indicates the 1800°C limit for peak fuel temperature at steady state. Not shown on this plot, the centerline of the coolant channel would be located at the zero on the abscissa. From this, the significant contribution of the thermal resistance of the fuel-clad gap to overall temperature rise can be observed. In fact, in the hot channel at this axial location, the temperature rise across the gap is 526°C whereas the temperature increase across the fuel only is 426 °C. Therefore, significant benefit would result from increasing the fuel-clad gap conductance in future work. This may be achieved by reduction of the hot gap thickness, but this is limited by manufacturability of the fuel assemblies, especially since the cold gap is smaller than the hot gap. This could also be achieved by use of vibrationally compacted fuel instead of the pellet fuel specified here, but a thorough knowledge of the thermal conductivity of this fuel type as well as its behavior with burnup in this geometry must be acquired, possibly by experiment on a prototypical TID fuel assembly. The solid diamonds and squares shown in Figure 9.10 represent results from FLOWSPLIT for the same axial location in the average and hot channels, respectively. These show excellent agreement with RELAP, actually overlapping the RELAP data in the cases of the clad inner and outer surfaces and only deviating slightly at the fuel maximum temperatures.

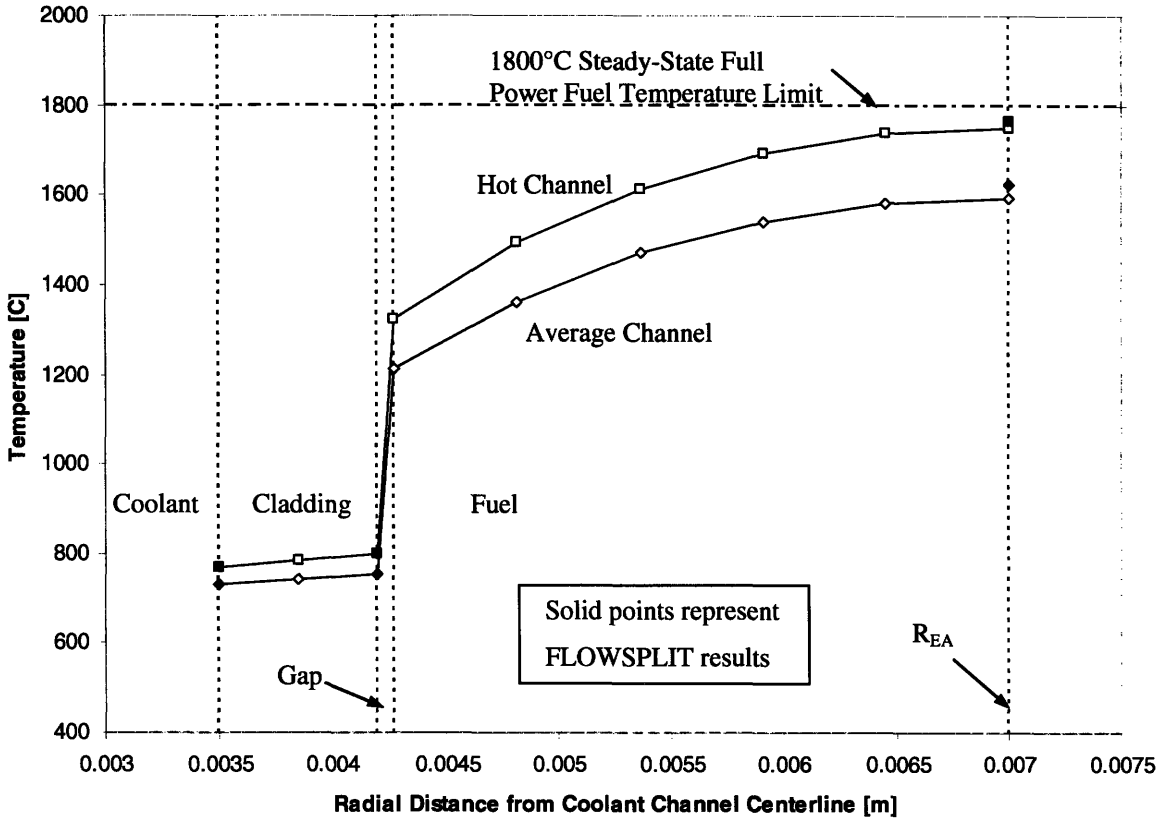

Figure 9.10. Steady-state full power radial temperature distributions in cladding and fuel calculated using RELAP for hot and average channels at the axial location of peak fuel temperature.

9.7 Summary

In this chapter, the methodology used to model the S-CO_2 cooled GFR in RELAP was described. Due to the large quantity of details involved in modeling an entire plant, the majority of the modeling methodology must be left out of the text. For the majority of transient analyses performed in this work, the homologous pumps representation of the compressors will be used rather than the detailed compressor models. The purpose and location of the turbine bypass valves were mentioned in this chapter, but will be revisited in greater detail later.

10 Steady State Natural Circulation in Reference Design

10.1 Introduction

Although the SCS/ECS has been revised such that it relies on active cooling, it is still capable of providing sufficient natural circulation to remove decay heat under certain conditions when emergency blowers and SCS/ECS water pumps are not functioning. In this chapter, the natural circulation performance of the reference design described in Chapter 9 will be assessed. Some sensitivity studies will also be presented which analyze the effects of conduction through the core barrel, functioning of the SCS/ECS water pumps and post LOCA core bypass in the revised design.

10.2 Mapping of Demand for Active Cooling

In this section, steady state natural circulation calculations are used in order to determine the natural circulation decay heat removal capabilities of the redesigned active SCS/ECS. As in the steady state natural circulation calculations presented in Chapter 7, the PCS loops were removed from the RELAP model in order to speed up computation. The water loop was allowed to operate by natural circulation as though the water pumps were not functioning. The primary system pressure was set by a time-dependent control volume and the power was varied until the peak clad surface temperature was at the 1200°C limit with the SCS/ECS check valves left open and the simulated emergency blowers not running. This was repeated for pressures ranging from 4 to 30 bar. The points plotted on Figure 10.1 show the maximum power removable by natural circulation versus backup pressure. The equation for the regression line drawn through them is given on the figure, again showing the near-linear relationship between pressure and decay heat removable by natural circulation. The

dashed line shown on the plot is the decay power produced by the core versus time after shutdown in hours as estimated by the following fit to the ANS standard decay heat curve;

$$\dot{Q} = \frac{0.0147}{t^{0.28}} \tag{10-1}$$

where $\dot{Q}$ is reactor decay power in percent of full power and t is time after shutdown in hours. This correlation was checked against results from decay heat calculations in RELAP, showing good agreement.

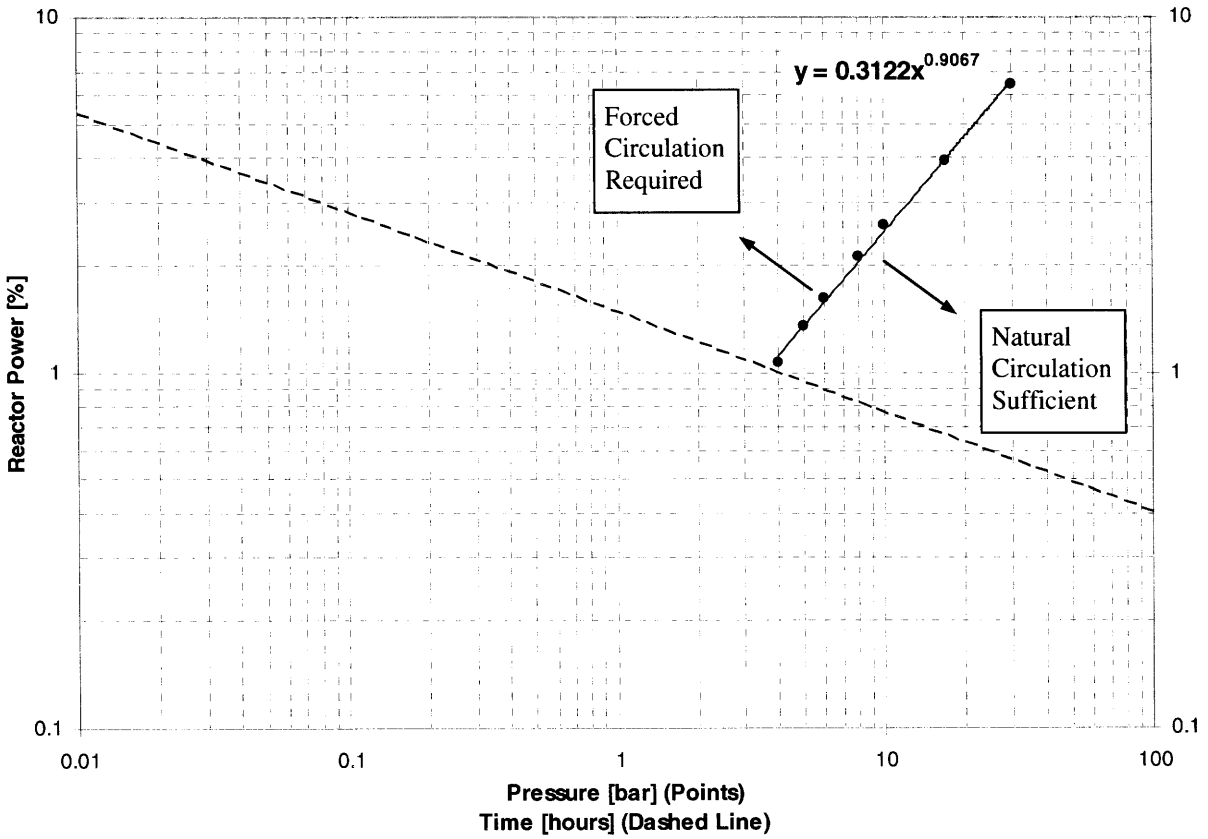

Figure 10.1. Reactor power which can be removed by natural circulation versus pressure (points with line fit) and decay power versus time (dashed line).

The arrows and notations on Figure 10.1 indicate that above the line, forced circulation is required to provide sufficient decay heat removal. Conversely, at powers below the line at a given pressure, natural circulation suffices. Although analysis of the

containment backup pressure will be performed in more detail later, the target design pressure of the containment after a LOCA is 6 bar. At this pressure, the removable decay power is about 1.6 percent, corresponding to 46 minutes after the reactor scram. However, the peak pressure will not be sustained indefinitely as heat is conducted from the containment volume vapor to the structures.

10.3 Steady State Parametric Studies

Three other sets of steady state calculations were also performed with the revised core and SCS/ECS design; one having no heat conduction through the core barrel, another with the SCS/ECS water pumps functioning and a third with core bypass through PCS duct breaks. The results are shown in Figure 10.2. The circular data points in the figure are referred to here as nominal and are the same points shown in Figure 10.1. As mentioned in Section 7.4.2, heat conducted from the fluid in the chimney to fluid in the downcomer through the upper section of the core barrel degrades natural circulation. In the current RELAP model of the plant, the lower chimney section (all four segments of volume 170 in Figure 9.2) conducts to the upper downcomer (the top four segments of volume 140 in Figure 9.2). The upper section of the chimney (volume 190 in Figure 9.2) is adjacent to the decay heat removal heat exchangers and is assumed not to conduct heat through a barrel to the downcomer. The structure of the core barrel is modeled as a 6 cm thick cylinder constructed of Incoloy Alloy 800. In order to quantify the effect of conduction through the core barrel during depressurized natural circulation decay heat removal, heat conduction through the barrel was disabled in the RELAP model. The square data points in Figure 10.2 show the decay heat removable by natural circulation versus pressure with no conduction through the barrel, showing a relatively weak sensitivity.

For all of the natural circulation calculations thus far, the SCS/ECS water pumps were assumed to not be functional and the water was allowed to flow by natural circulation alone. In the next calculation, these pumps were assumed to be pumping water at a mass flow rate of 459.2 kg/s, the design value given in Table 8-2. The resulting power removable by natural circulation (only CO_2 flows by natural circulation) versus backup pressure is shown in Figure 10.2 as the triangles.

The third steady state parametric study performed with the revised core and active SCS/ECS model was an investigation of the effect of core bypass through a so-called "400% break" of a coaxial PCS duct. This is the same scenario as the largest break analyzed in Section 7.5.1, where the full flow area of the cold and hot legs were open to the containment volume and coolant could bypass the core via these pipe breaks. The results of this calculation are shown in Figure 10.2. This shows that the reactor power removable by natural circulation is not as sensitive to core bypass routes as it appeared to be in the previous core revision. This is because the core in this design revision has a larger flow area due to the addition of the reflector cooling and flow between assembly ducts. The revised core design also has larger coolant channel diameters.

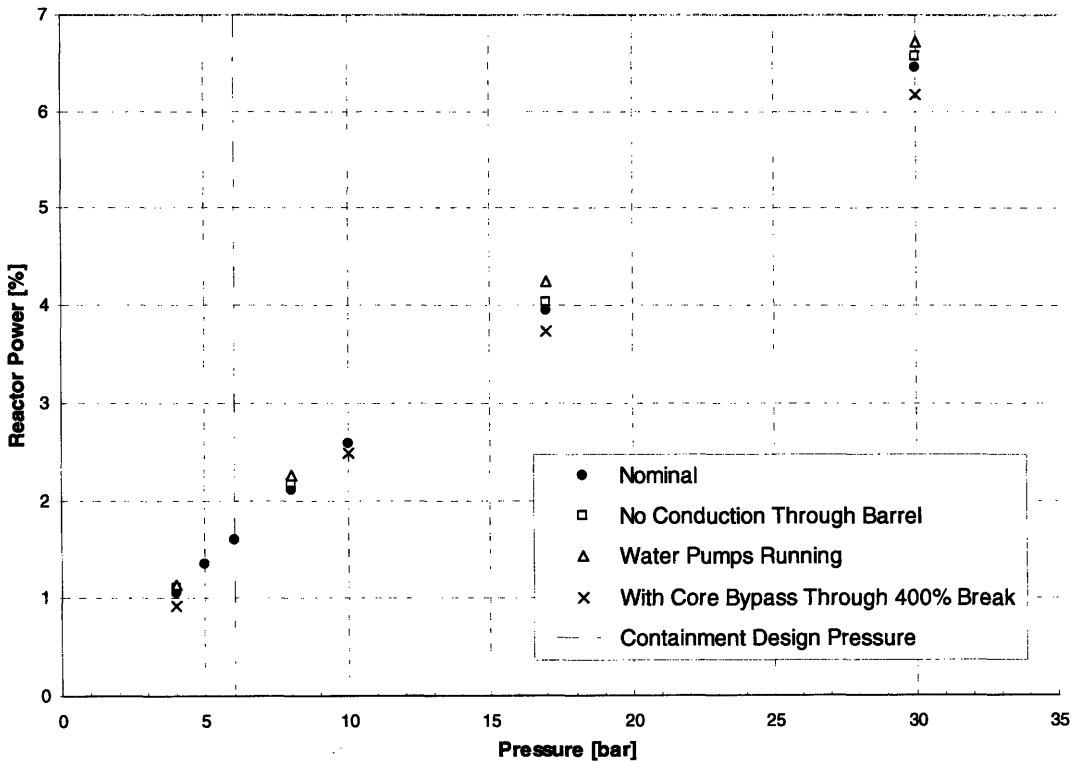

Figure 10.2. Percent reactor power removable by natural circulation versus pressure for four assumed circumstances.

10.4 Temperatures in Water Loop

The decay heat is transferred to the ultimate heat sink via a water loop. Because the water must remain in the liquid phase, the temperature of the water is critical to the function of the system. In the natural circulation calculations presented in the previous section where the powers exceeded 2%, the pressure in the water loop needed to be increased above the 500 kPa loop design pressure printed in Table 8-1 in order to raise the saturation temperature to above the hot leg temperature. Figure 10.3 shows the temperature in the hot leg of the SCS/ECS water loop versus reactor power for various pressures. This shows that the water loop hot leg temperature is insensitive to the pressure in the primary system, and depends only on the reactor power. The water loop hot leg temperatures for the case where the water pumps are functioning are also shown in the figure.

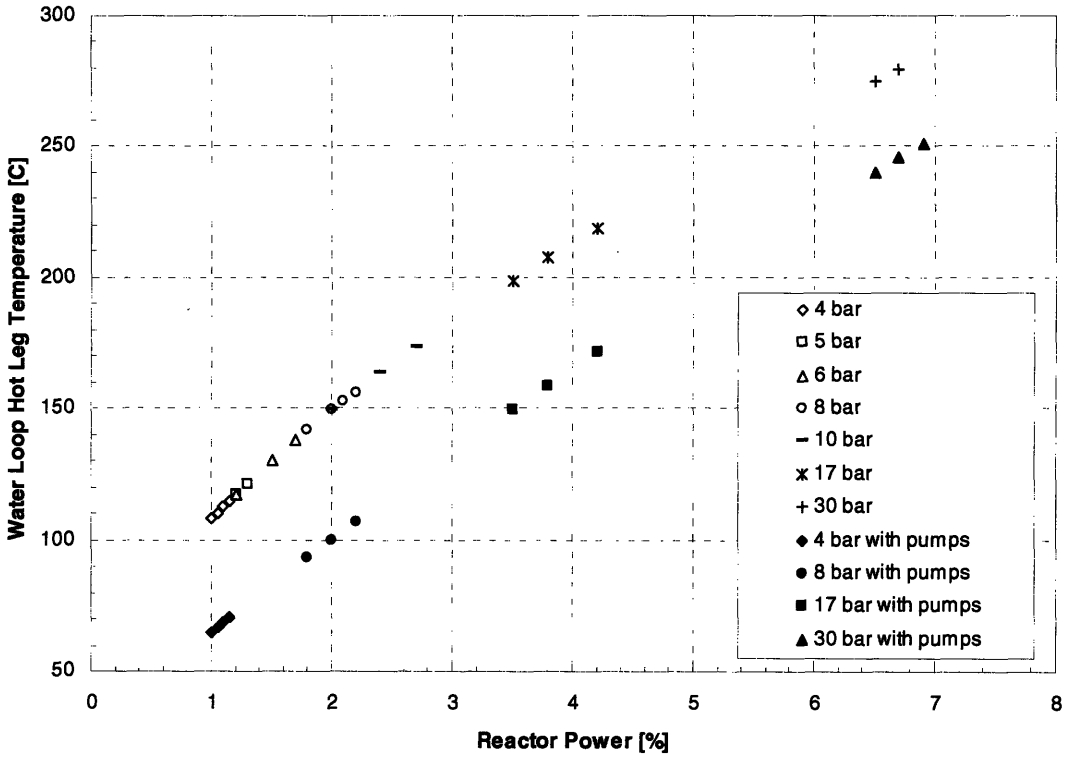

Figure 10.3. Temperature in hot leg of SCS/ECS water loop versus percent of reactor power removed by natural circulation with and without water pump function.

Figure 10.4 shows the saturation pressure corresponding to the hot leg temperature in the water loop versus reactor power. The top data points correspond to the nominal case where both the CO_2 and the water loops flow by natural circulation. The lower points refer to the case where the water pumps are operational. This shows that at the highest powers evaluated here, approximately 6.8%, the saturation pressure corresponding to the temperature in the hot leg of the water loop is in excess of 6 MPa. Having the pumps running reduces this saturation pressure to 4 MPa. Just as the backup pressure in the containment following a LOCA is important in providing sufficient mass flow for natural circulation decay heat removal, the water loop pressure is critical in order to prevent boiling of the water in the decay heat removal heat exchanger. Thus, Figure 10.1 is incomplete in that the water loop pressure which is required to provide heat transfer to the ultimate heat sink increases dramatically at the higher reactor powers.

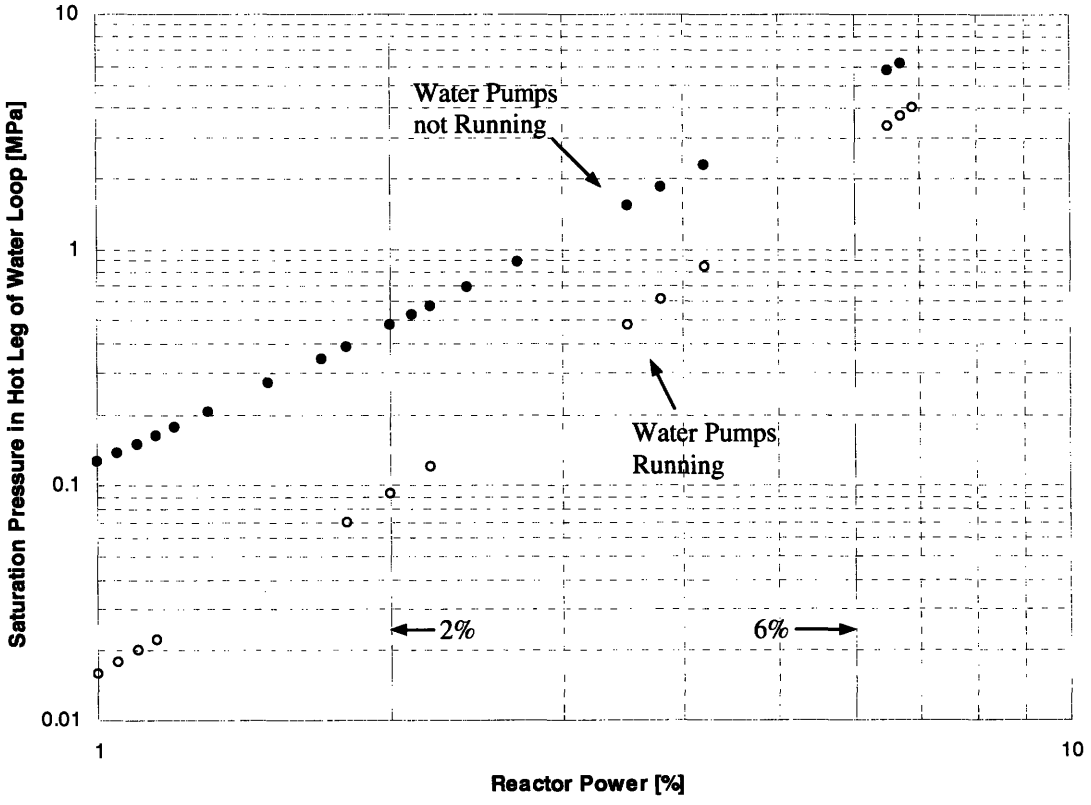

Figure 10.4. Saturation pressure corresponding to temperature of hot leg of SCS/ECS water loop during steady state natural circulation versus power with and without water pump function.

If the pressure in the water loop is much higher than in the primary system, a risk of water ingress into the primary system or depressurization of the water loop into containment could be an issue. A water loop which allows boiling could potentially be designed if either the boiling or condensing regions were made vertical instead of horizontal.

10.5 Summary

In this section, the demand for active cooling was mapped using steady state RELAP calculations. The sensitivity of the passive decay heat removal capability of the system to conduction through the core barrel was shown to be minimal, due in part to our accounting for only the conduction through the lower part of the barrel. Functioning SCS/ECS water pumps was shown to give a noticeable improvement in natural circulation decay heat removal capability. The pumps also lowered the hot leg temperature of the water loop, reducing significantly the required water loop pressure to prevent boiling. Core bypass via a 400% pipe break was shown to have less of an impact on the natural circulation decay heat removal capability of the revised core design due to the larger total core flow area and larger coolant channels.

11 Loss of External Load Transient

11.1 Introduction

During a loss of external load (LOEL) event, an electrical disturbance causes the generator to be decoupled from the electrical power grid. This removes the τ_g term from Equation 10-10. Because this is a large negative term, the left-hand side of the equation becomes positive and so the $d\omega/dt$ term on the right-hand side becomes positive and the shaft experiences a large positive angular acceleration. The initial rate of angular acceleration is determined by the turbine and compressor torques along with the moment of inertia of the shaft plus all the attached components. If the shaft angular velocity reaches too high a value, the turbine can fail catastrophically. Nuclear power Rankine cycle plants employ sophisticated and reliable systems of fast-acting bypass valves and controls in order to prevent shaft overspeed during an LOEL, an event expected to happen several times in the life of any plant. Brayton cycle turbomachinery is smaller (thus smaller moments of inertia and faster acceleration) than that of Rankine cycles making mitigation of an LOEL event more challenging in gas cycles. Because the S-CO_2 cycle has even smaller turbomachinery than that of the typical helium Brayton cycle, the loss of load event is even more challenging in the present design. The LOEL event is analyzed in this section with particular focus on avoiding shaft overspeed and ensuring sufficient core cooling. A maximum shaft speed of 120% of the nominal shaft speed is adopted as the limit for an LOEL event, along with a maximum peak fuel cladding temperature target of 1000°C.

11.2 Power Cycle Bypass

The first option for mitigation of an LOEL event analyzed here will be referred to as power cycle bypass (PCB). Valves are placed as shown in Figure 11.1 which are closed during normal operation. In the event of an LOEL, the valves can be opened to connect volumes from the exit of the high-temperature recuperator cold side (volume 390), which is nominally at 19.95 MPa pressure, with the inlet of the high-temperature recuperator hot side (volume 325), which is at 7.93 MPa pressure. In other words, the reactor inlet is connected to the turbine exhaust so that fluid bypasses both the core and the turbine. This increases the pressure in the turbine exhaust volume, reducing the mass flow rate through the turbine and the positive torque which it applies to the shaft. The result of this is a reduction in the shaft acceleration after the LOEL. The reactor inlet temperature is 485.5°C while the turbine exhaust temperature 529.9°C. Thus during a PCB, the high-temperature recuperator hot side is exposed to a stream which is colder than normal by about 44°C. Thus the location of the PCB valves is favorable from the standpoint of limiting thermal shock to the high temperature recuperator. This is in contrast to a direct turbine bypass where fluid at 650°C from the core outlet would be redirected around the turbine and then would encounter the high-temperature recuperator hot side inlet, exposing it suddenly to higher temperatures by some 120°C, with attendant thermal shock. This turbine bypass scheme will be evaluated later as an alternative means of LOEL mitigation.

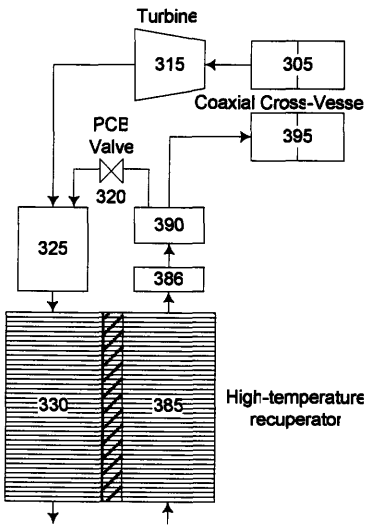

Figure 11.1. Nodalization diagram showing the PCB valve location.

Figure 11.2 shows four different PCB valve opening rates. Because real valves cannot respond instantaneously to an LOEL, a delay is modeled in RELAP. This is captured by the time after actuation of the PCB valves before the valve area increases from zero as shown in Figure 11.2. The valves are actuated at the same instant as the LOEL in the RELAP model and their delay time is captured by the valve opening rate. The delays for the PCB valves to begin opening range from 0.067 seconds in valve type 4 to 0.20 seconds in valve type 1. The total time that the valves take to come fully open ranges from 0.2 to 0.6 seconds in the same valve types, respectively. The total flow area initially used for these bypass valves was 0.5 m^2.

Figure 11.3 shows normalized PCS shaft speed versus time after occurrence of an LOEL at time zero. The top line shows shaft speed if PCB valves do not open. In this case, the shaft reaches the 20% overspeed limit in just under 0.3 seconds, illustrating the need for a very fast response to an LOEL event. The other four lines in the figure show shaft speed versus time following the loss of load, but with immediate actuation of the PCB valves with opening rates given in Figure 11.2. The labels on each line correspond to the numbering in the legend of Figure 11.2. This shows that the fastest-opening PCB valves limit the shaft rotation to just at the limit of 20% overspeed at the peak, which occurs at about 0.7 seconds into the transient.

In these transient simulations, the PCB valves open and remain so until the simulation is terminated. As the shaft spins down, the compressors still develop head and are able to circulate CO_2, but because the PCB valves are left open, a significant amount of the coolant flows through the PCB valves rather than the core. Figure 11.4 shows the core mass flow rate in one case where an LOEL has occurred without PCB and two more where the PCB (valve type 4 in Figure 11.2) occurs immediately. In one of the cases with PCB, the SCS/ECS check valves are not allowed to open, and in the other case, they are set to open when their downstream pressure is less than then their upstream pressure. In the case where the LOEL occurs and no action is taken, the core mass flow rate increases to a new steady state value higher than the nominal full power value because the new steady state shaft speed is higher. In the cases where PCB valves are opened in response to the LOEL, a large reverse flow rate results in the core for a few tenths of a second, then a small positive flow is

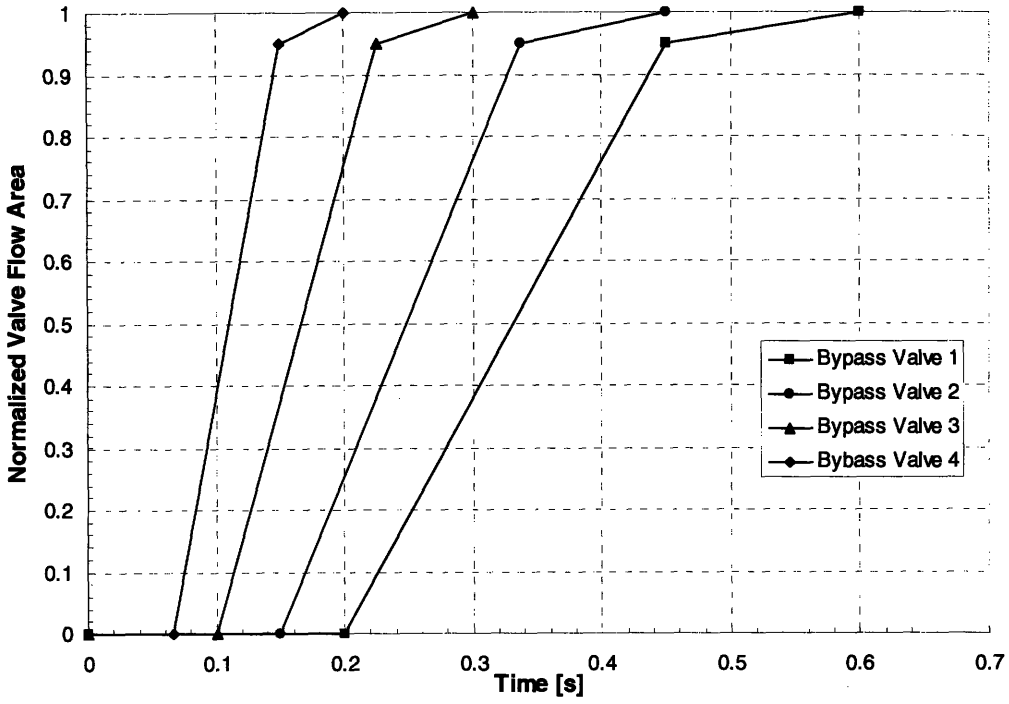

Figure 11.2. Normalized turbine bypass valve area versus time for four opening speeds.

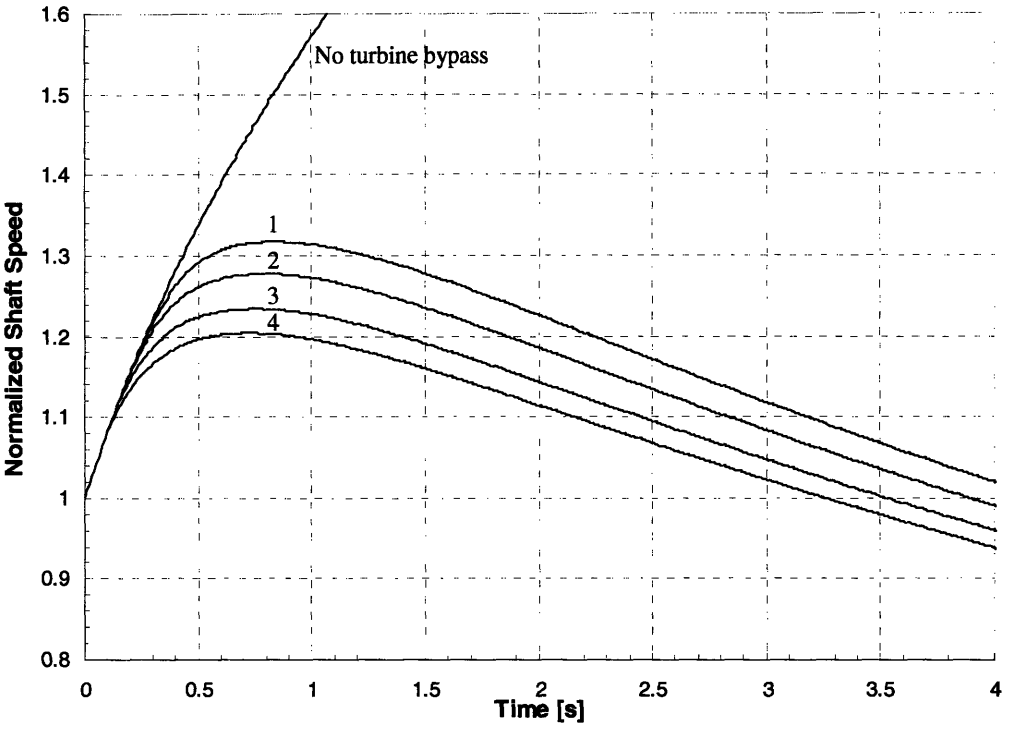

Figure 11.3. Normalized shaft speed versus time following a loss of load event for no turbine bypass and four turbine bypass valve speeds numbered according to Figure 11.2.

restored. The negative core flow results from the sudden rushing of the cold leg fluid to the region of the turbine exhaust, drawing fluid from the core from the downcomer region. The small positive core flow rate which occurs after this is a result of compressors moving CO_2, but much of this flow travels through the open PCB valves rather than through the core. Figure 11.5 shows percent of full reactor thermal power versus time after a scram, showing that the power remains significant for several seconds after the reactor scram occurs, yet the core mass flow rate has fallen to a very low value soon after the initiation of the LOEL event. In the case where the SCS/ECS check valves are allowed to open, the sudden opening of the PCB valves and the resulting drop in downcomer pressure provide the differential across the check valves required for their opening. This aggrevates the core cooling situation because the CO_2 driven by the compressors now has another alternate route by which to avoid flowing through the core, flowing in reverse through the SCS/ECS.

Figure 11.6 shows peak clad surface temperature versus time after the loss of external load for the same cases shown in Figure 11.4. The opening of the PCB valves in the way described above prevents the core from receiving sufficient coolant flow to remove the energy produced, and the 1000°C limit on clad surface temperature for the LOEL event is reached in less than 2 seconds for both cases of PCB bypass, with and without the opening of the SCS/ECS check valves. The 1200°C clad temperature limit for accident conditions is even reached in approximately 6 seconds in the case where the SCS/ECS check valves cannot open and in about 4 seconds in the case where they are allowed to open. Thus a major tradeoff inherent to the placement of these PCB valves is demonstrated between protection of turbomachinery against overspeed and maintaining sufficient core cooling. To limit the shaft to less than 20% overspeed by use of these PCB valves alone is to deprive the core of sufficient cooling in the first few seconds after the scram when core power is still high, Thus a balance must be struck such that both the turbomachinery and the core are protected.

The opening of the SCS/ECS check valves is also a significant disadvantage of this bypass scheme. If these valves are opened following an LOEL and PCB valve opening, the emergency blowers would have to come on or the valves would have to be re-closed automatically in order to prevent reverse flow through SCS/ECS loop from degrading core cooling.

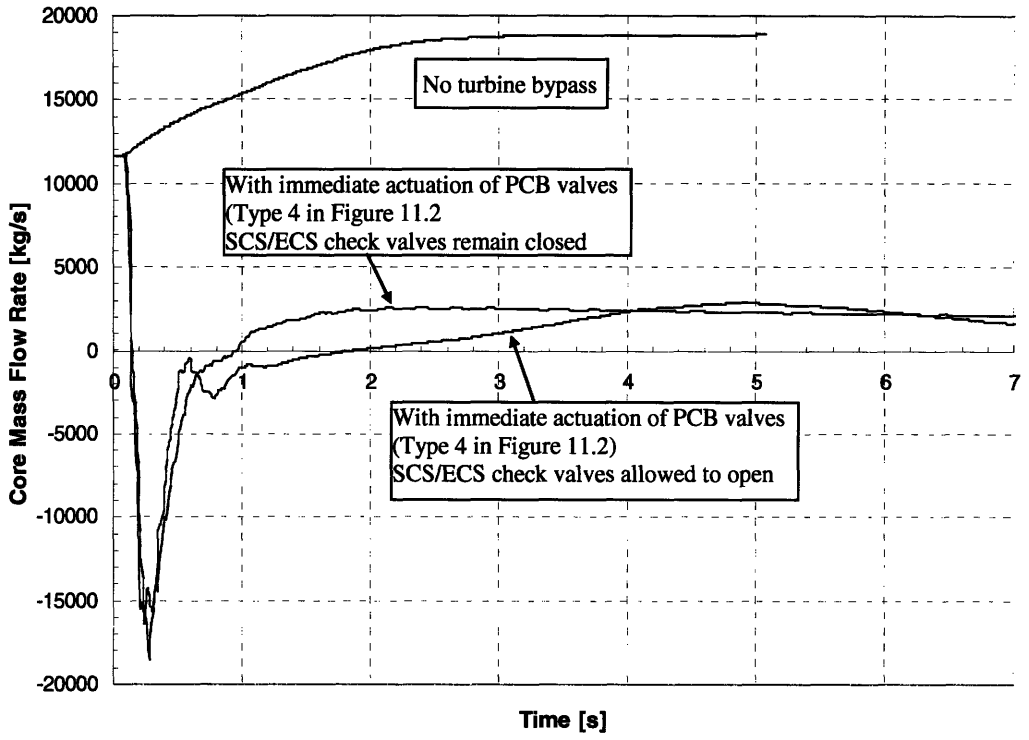

Figure 11.4. Core flow rate versus time following a loss of load event with and without turbine bypass without allowing for opening of SCS/ECS check valves.

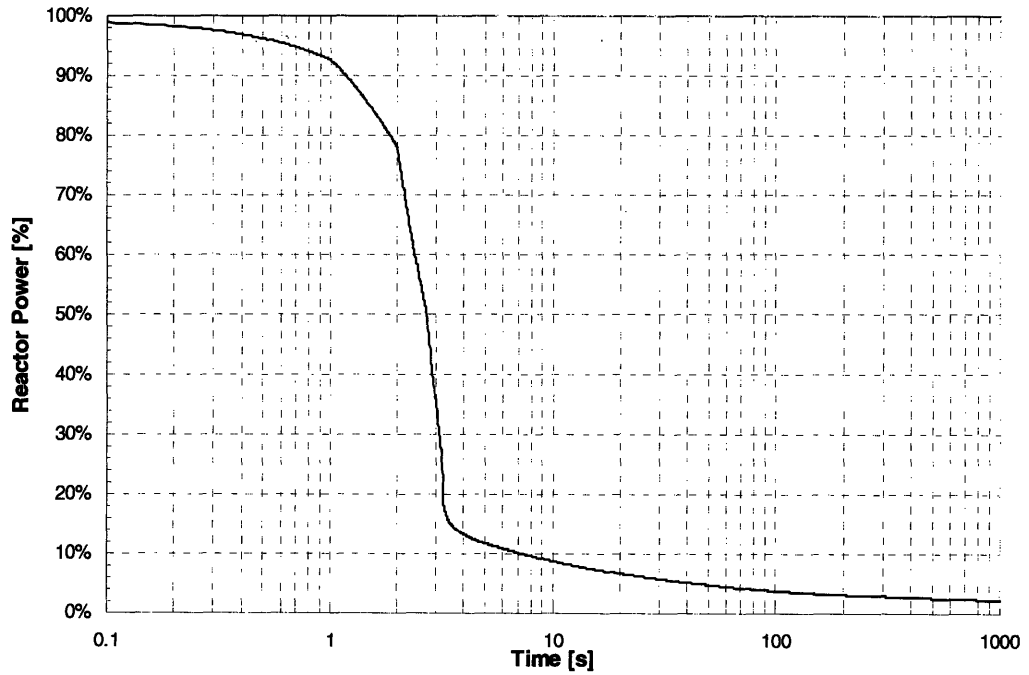

Figure 11.5. Normalized reactor power versus time following a scram at time zero.

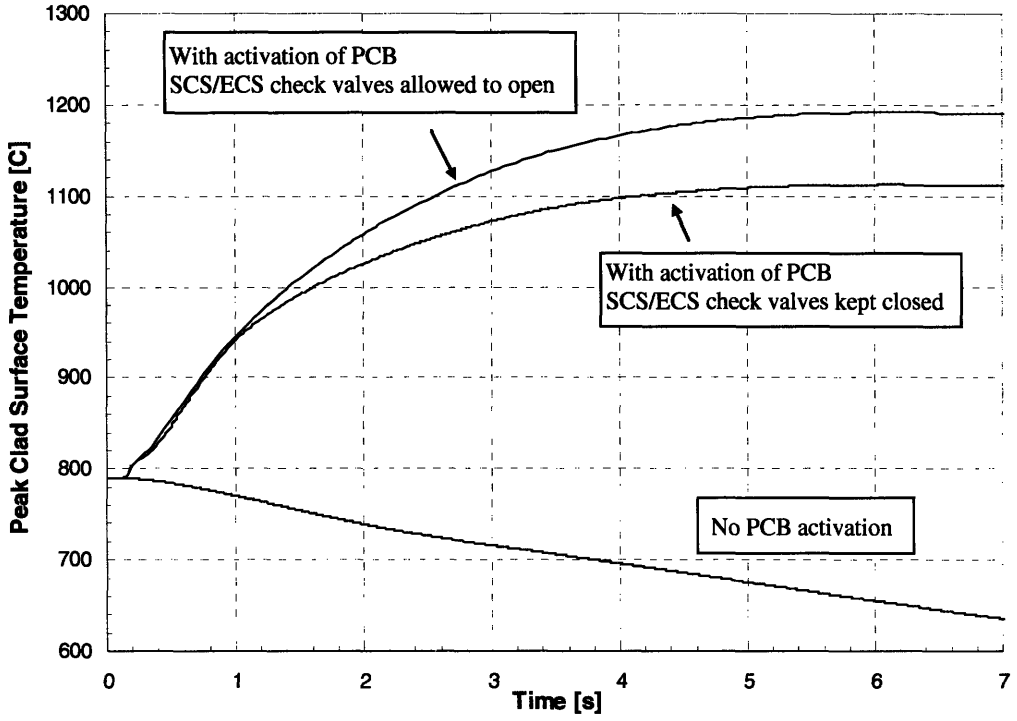

Figure 11.6. Peak clad surface temperature versus time following loss of external load with and without turbine bypass.

11.3 Flywheels and Resistor Banks

One technique to improve the capability of the system to limit shaft overspeed without depriving the core of sufficient flow is to add moment of inertia to the shafts by installing flywheels. This slows the acceleration of the shaft after the LOEL event, thus allowing the design to rely less on fast, large-area PCB valves. If actuation of the PCB valves can be delayed in this way, the reactor has more time to shut down before it occurs. The primary reason that flywheels are not specified in this plant is the significant increase in cost and complexity that would result. The necessary flywheel moment of inertia to significantly reduce the reliance on the turbine bypass would be on the order of that of the generators or greater, thus it is not considered an acceptable approach.

Another method used for slowing the acceleration of a shaft following a LOEL is by using resistor banks. These consist of a set of resistors which can be coupled to the generator

very quickly following an LOEL. They then apply an equivalent negative torque on the shaft in order to slow its acceleration until some other means of reducing shaft acceleration can be activated. Figure 11.7 shows the time it takes for the shaft speed to equal the limit of 120% nominal after an LOEL event versus the negative torque applied by a resistor bank. No bypass valves were used for this set of calculations. It should be noted that both the generator torque and the equivalent resistor bank torque have negative signs by the convention used here, so the normalized resistor bank torques are given in positive percentage values on the abscissa. As shown in Figure 11.5, for the first three seconds after a reactor scram, power decreases quickly, followed by a much slower decline. Based on this, it would be desirable to delay the opening of the PCB valves by that much time, knowing that it will cause flow stagnation in the core. If this margin is to be achieved by a resistor bank alone, then about 80% of the full power steady state generator torque must be applied by the resistor bank beginning at the instant of the LOEL. Though the equivalent torque from the resistor bank is lower than the generator torque, the shaft speed will increase to 120% of its full power steady state value, so the power spent in the resistor bank during those three seconds is slightly greater than the energy that the generators produce in the same amount of time ($> 3.6 \times 10^9$ J in three seconds). This is a prohibitively large amount of energy to be stored as heat in such a short period of time and the possibility of using resistor banks is thus discarded.

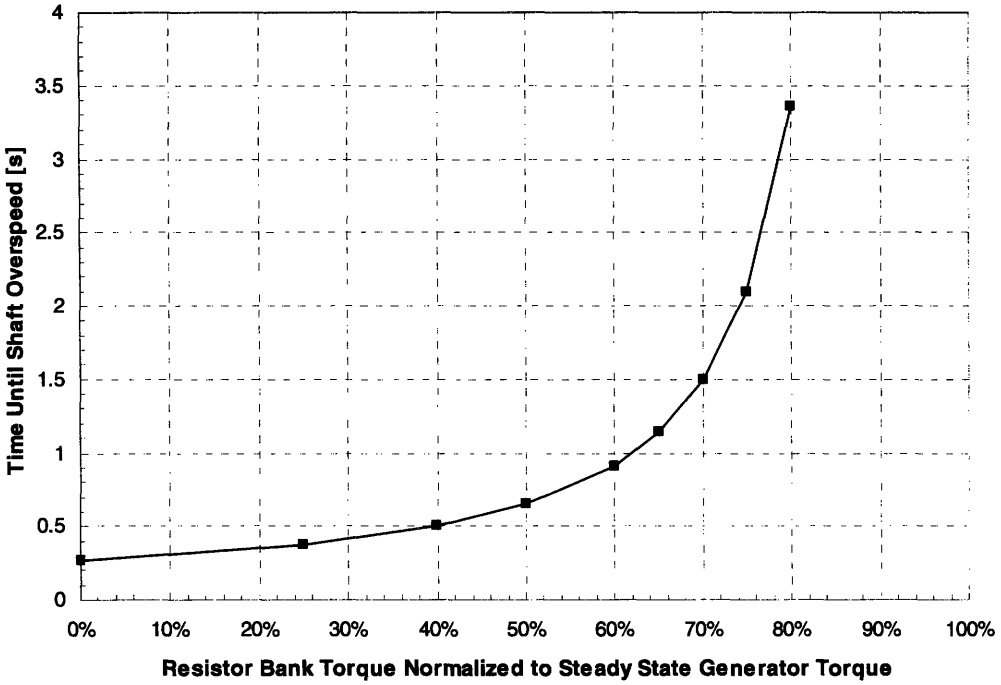

Figure 11.7. Time until 20% shaft overspeed in an LOEL versus constant negative torque applied by a resistor bank normalized to steady state generator torque.

11.4 Turbine Bypass

Mentioned in the previous section as an alternative means of mitigating an LOEL event, a turbine bypass valve is evaluated in this section. In this arrangement, fluid from the core outlet is diverted around the turbine and rejoins the stream in the turbine exhaust. Though this is similar to the turbine bypass strategy used in steam Rankine cycles, this method is often discarded for gas-cooled reactors for two reasons; one is because the turbine bypass valves are exposed to fluid at the core outlet temperature, which is typically higher in gas-cooled reactors than in a Rankine cycle. The other reason is that opening the turbine bypass valves suddenly exposes the inlet of the high-temperature recuperator hot side to fluid at the core outlet temperature. This sudden increase in temperature at the recuperator is a result of the sudden removal of the temperature drop across the turbine; in the present design, this is about 120°C. It should be noted that this is much less severe than the temperature difference across the turbine in a typical helium Brayton cycle (~400°C). Figure 11.8 shows a nodalization diagram of the turbine bypass valve location. Volumes 310 and 327 were added because, in RELAP, faces of volumes which are connected to a turbine must only have

one junction. The steady state performance of the plant with these volumes added was verified to be very close to before their addition so that results can be compared directly between bypass schemes. The addition of volumes was performed on both the single and 3x PCS loops in the RELAP model. Using the valve opening rate given by valve type 4 from Figure 11.2, the area of the turbine bypass valves was adjusted such that the shaft speed reaches a peak just at the 120% limit (settling upon per valve 0.31 m^2). Figure 11.9 shows the shaft speed versus time following an LOEL event where the above described turbine bypass scheme is used. Valves are actuated at time zero and left open for the duration of the transient. When the turbine bypass valve is opened, the turbine, which had been providing a large resistance to flow for the CO_2, is suddenly circumvented. Therefore, the core mass flow rate increases dramatically in the seconds following the actuation of the turbine bypass. Figure 11.10 shows core mass flow rate versus time following the LOEL and turbine bypass. Increasing to 2.3 times the nominal value in around one second, this high a mass flow rate can be damaging to core components. A core mass flow rate limit of 150% of the nominal value is thus adopted for the LOEL event. The nominal mass flow rate and the 150% values are shown in dashed lines in Figure 11.10.

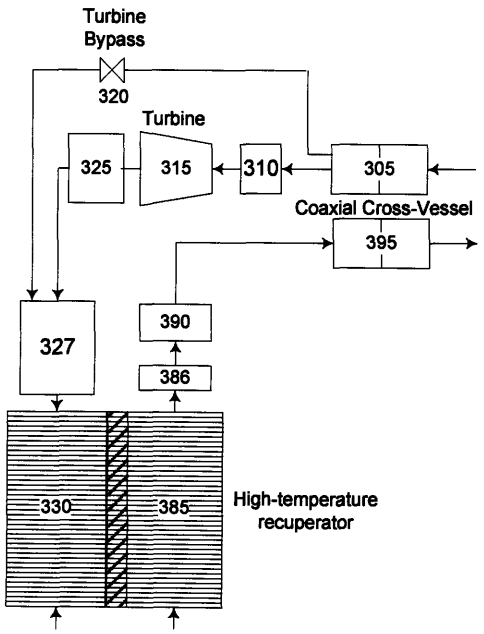

Figure 11.8. Nodalization diagram showing location of turbine bypass valve.

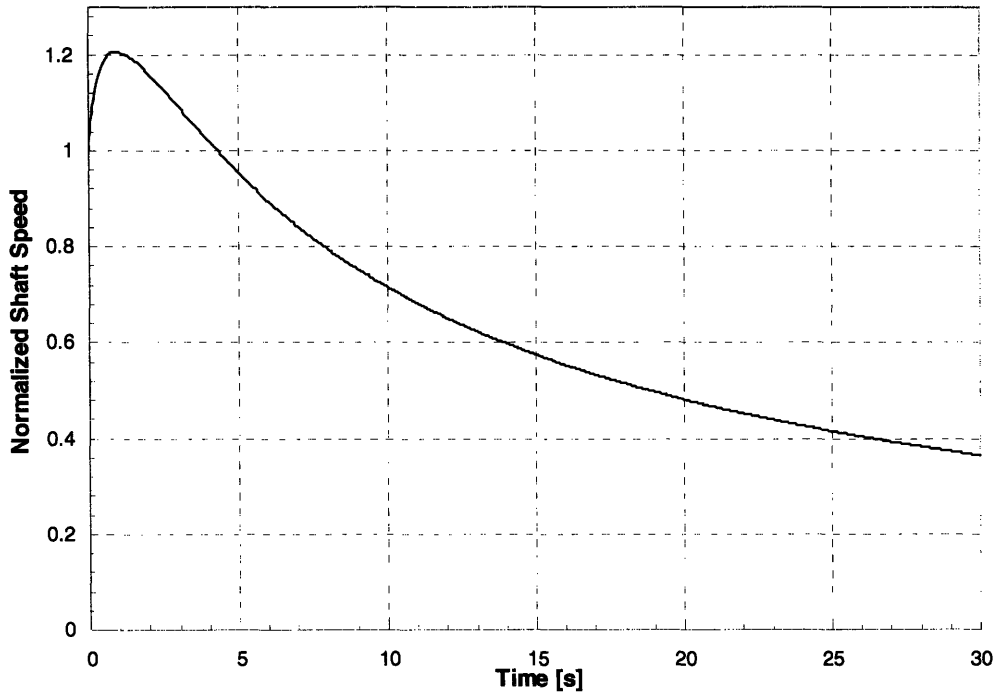

Figure 11.9. Normalized shaft speed versus time after an LOEL event with turbine bypass.

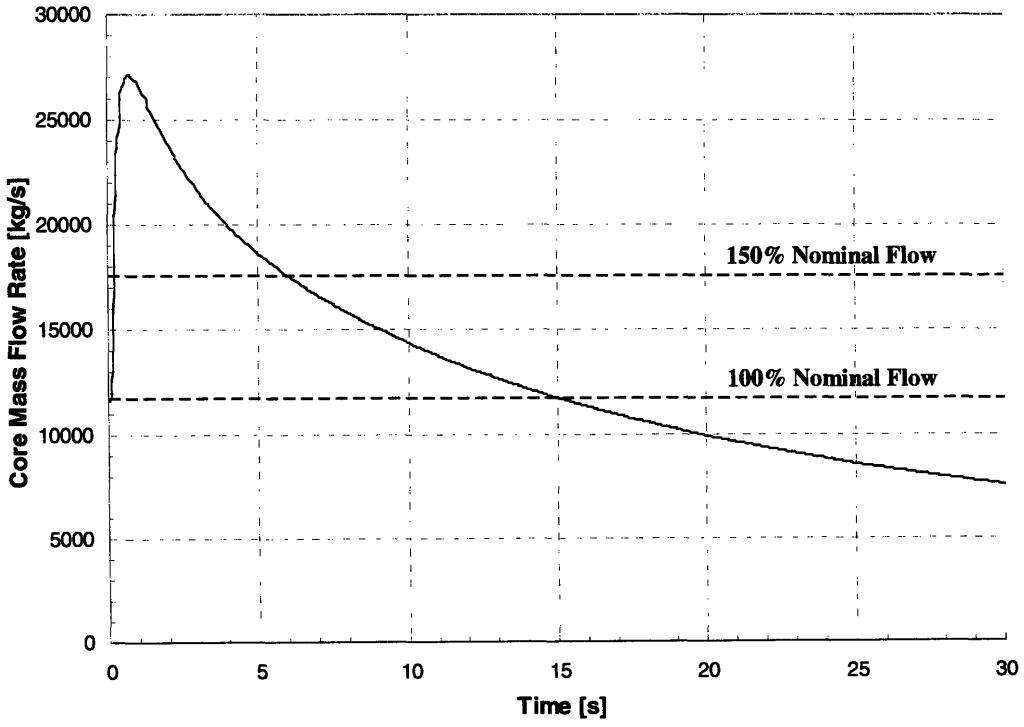

Figure 11.10. Core mass flow rate versus time after LOEL event with turbine bypass.

Because during the turbine bypass, fluid at the core outlet temperature impinges on the inlet to the hot side of the high temperature recuperator, thermal shock is an important issue. Figure 11.11 shows the temperature of the volume at inlet to the hot side for the high temperature recuperator. Nominally at 531.7°C (steady state RELAP result), the temperature increases to 560°C within 0.3 seconds resulting from the sudden inflow of fluid at the core outlet temperature. The temperature increases further to about 567°C by 1.4 seconds, beyond which the temperature excursions are relatively slow.

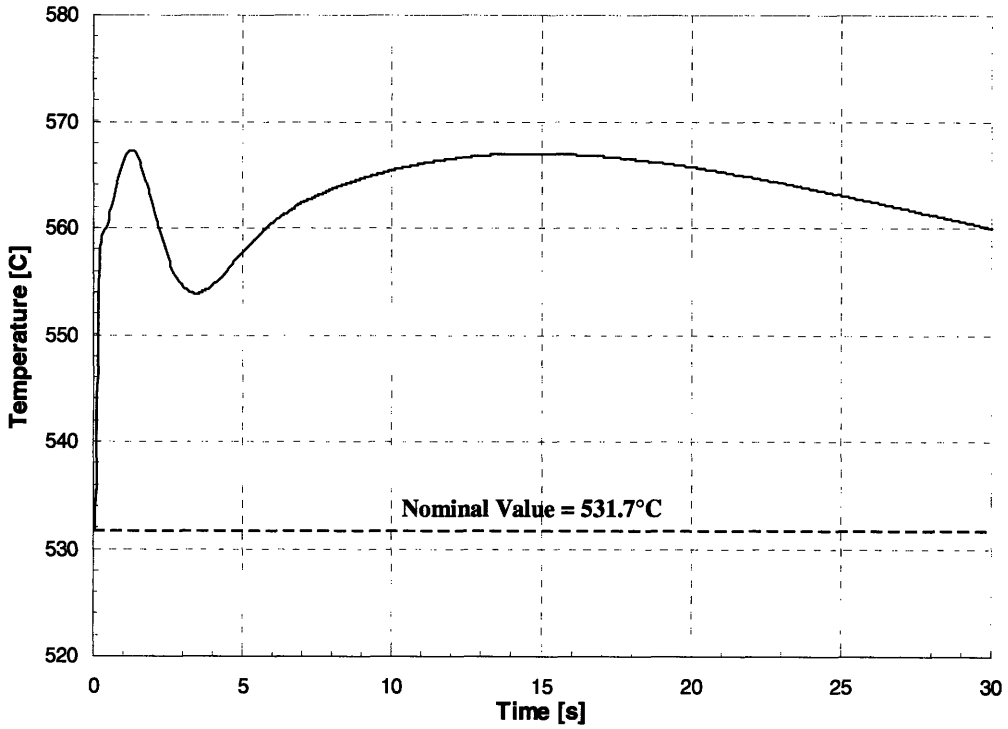

Figure 11.11. Temperature at inlet to high temperature recuperator hot side versus time following an LOEL event and turbine bypass.

The turbine bypass is advantageous in that it does not cause an immediate flow reversal and subsequent stagnation in the core as does the PCB described before. The turbine bypass also does not cause the SCS/ECS valves to come open as does the PCB scheme. There are several prohibitive disadvantages of relying exclusively on this turbine bypass scheme; the bypass valve is exposed to fluid at the reactor outlet temperature (650°C), the mass flow rate in the core is extremely large for a brief time following the actuation of the

turbine bypass valves and turbine bypass causes a rapid temperature increase at the hot side inlet to the high temperature recuperator. A scheme is therefore sought which would combine the positive characteristics of both turbine bypass and PCB.

11.5 Combined PCB and Turbine Bypass

Both the turbine bypass and the PCB valves evaluated above had favorable and unfavorable performance characteristics. In this section, a bypass scheme is suggested which would combine the two valve locations in order to prevent shaft overspeed without too low or too high a core flow rate and without exposing the high temperature recuperator to extreme temperature excursions. This will be referred to as "combined" bypass, since it is essentially a combination of both valve types evaluated above. Figure 11.12 shows a nodalization of the combined bypass scheme. In this scheme, the turbine bypass valve is given a reduced area from before (now 0.25 m^2). This is because the PCB valve will assist the turbine bypass in slowing the shaft and so a smaller flow area is required. This is beneficial since it reduces the size of the valve and pipe used in the bypass. The PCB valve has an area of 0.2 m^2, also reduced from before.

At the instant the LOEL event occurs, the turbine bypass valves were actuated and open according to valve type 4 in Figure 11.2. This bypass slows the acceleration of the shaft while increasing the core flow rate rapidly. The PCB valves are also actuated at the time of the LOEL, but with a slightly slower opening rate of 0.33 seconds (slightly slower than valve type 3 in Figure 11.2). The reason for the PCB valves being slightly slower than the turbine bypass valves is to prevent a negative core flow rate. When the PCB valves open, the shaft acceleration is further reduced and the flow of the coolant moved by the compressors which would have otherwise flowed into the core contributing to the very high core flow rate now bypasses the core in favor of the PCB valves. The valve areas and opening rates were determined by trial and error in order to both keep core flow rate below 150% of the nominal value and to limit the shaft to < 20% overspeed. The opening of the PCB valves allows cooler fluid (485.5°C) into the inlet region of the high temperature recuperator hot side, countering the hotter fluid (650°C) coming from the turbine bypass valves.

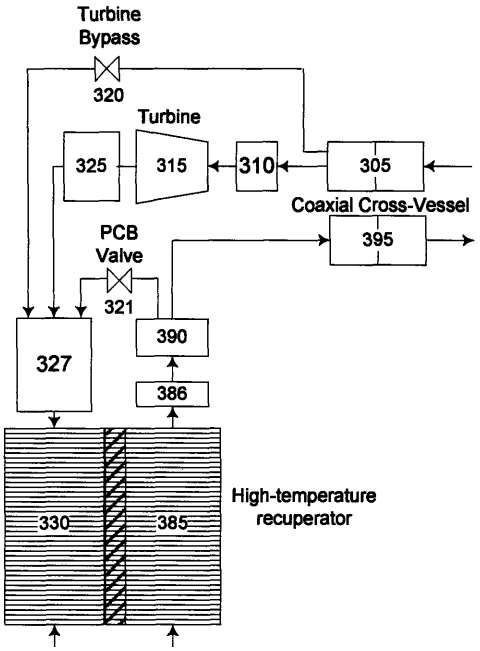

Figure 11.12. Nodalization diagram showing arrangement of "combined bypass" consisting of PCB and turbine bypass valves.

Figure 11.13 shows normalized shaft speed versus time following an LOEL event with combined bypass. The peak shaft speed is just below 120% and the reduction in shaft speed after the peak is faster than both the cases of turbine bypass and PCB alone. Figure 11.14 gives core mass flow rate versus time following the same LOEL event with combined bypass. The opening of the PCB valves has arrested the increase in core flow rate before it reaches the 150% limit. The flow rate then decreases back through the nominal full power value at around 2.5 seconds and slowly decreases after that beyond the 30 second termination of the transient. This flow rate is more than sufficient to remove heat from the core as it shuts down, as can be seen in Figure 11.15. This figure shows peak clad surface temperature versus time following the LOEL event and combined bypass. The clad surface temperature decreases immediately following the bypass actuation as a result of the increased core flow rate. As the mass flow in the core decreases, the peak clad surface temperature increases slightly until around five seconds into the transient when the low reactor power causes a decrease in peak clad surface temperature, which continues for the duration of the simulation.

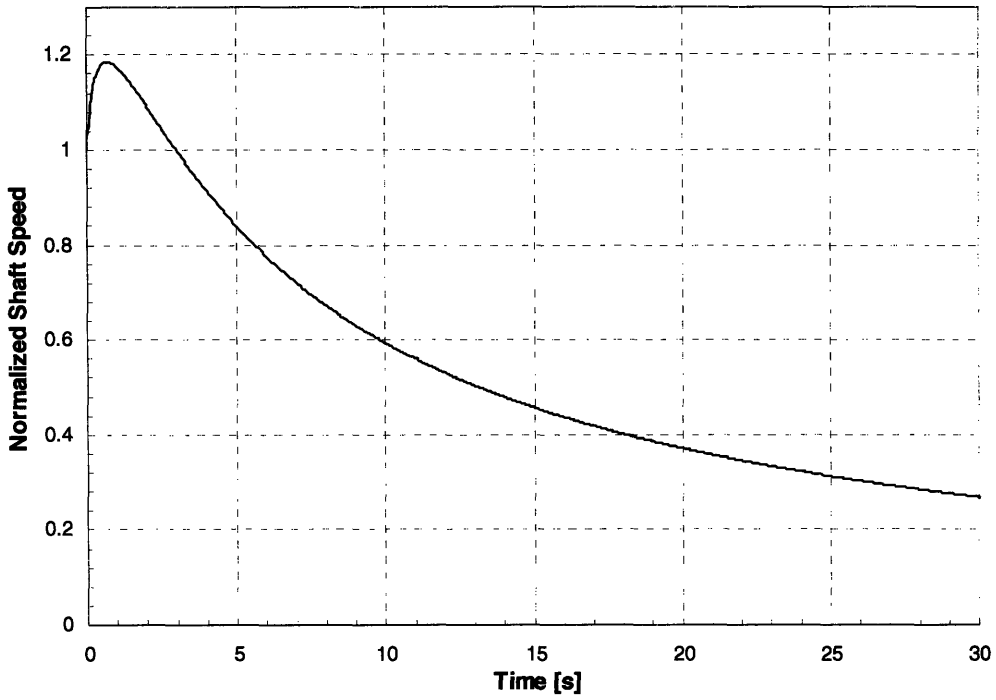

Figure 11.13. Shaft speed normalized to full power value versus time following an LOEL event with combined bypass.

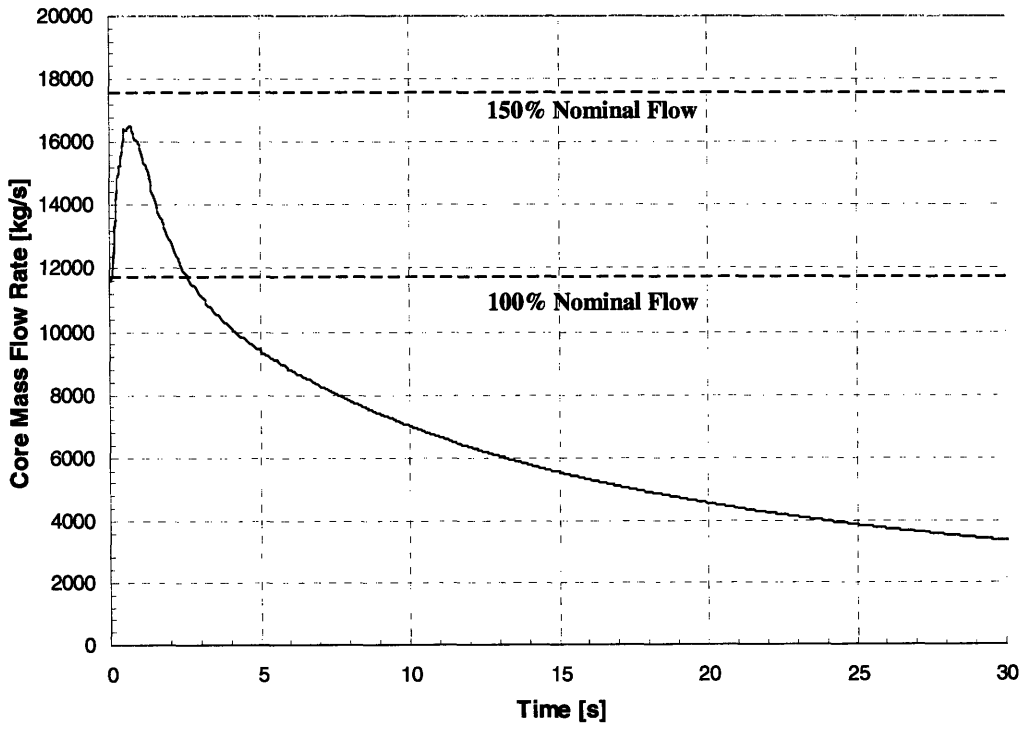

Figure 11.14. Core mass flow rate following an LOEL event with combined bypass.

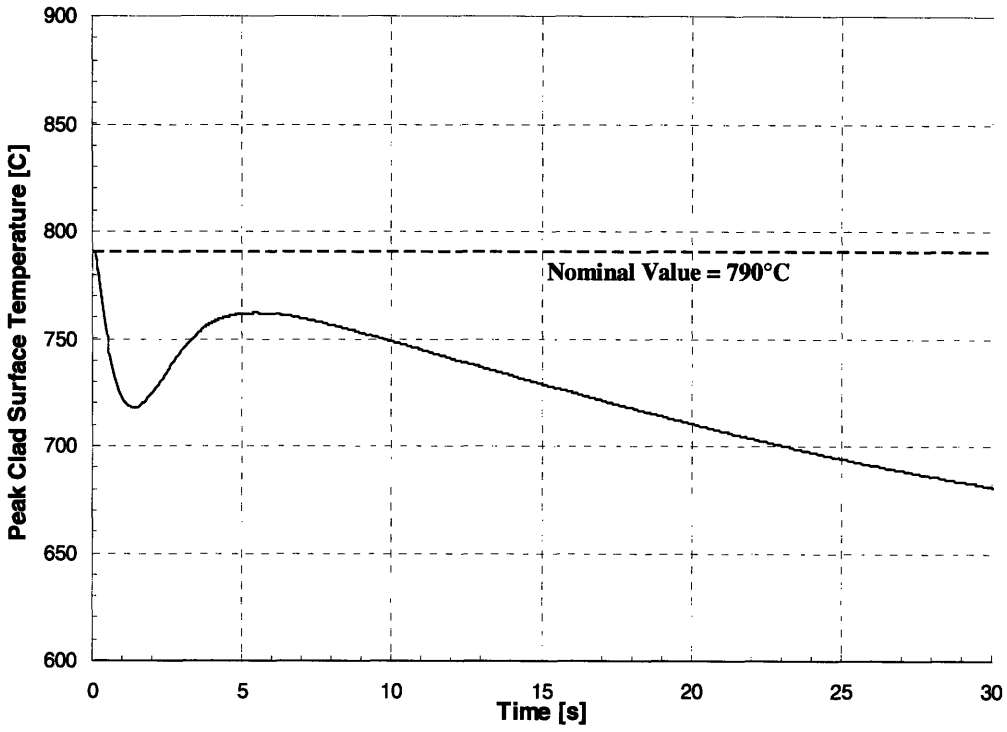

Figure 11.15. Peak clad surface temperature versus time following an LOEL event with combined bypass.

Figure 11.16 shows the temperature at the inlet to the hot side of the high temperature recuperator versus time following the LOEL and combined bypass. The timescale in this figure is limited to five seconds in order to better capture the immediate temperature behavior. The same parameter from the turbine bypass case is included for comparison. In the combined bypass case, the temperature follows the same sharp increase in the first 0.15 seconds as in the turbine bypass case, but then the opening of the PCB valves arrests this temperature rise at about 547°C by adding the lower temperature fluid from the high temperature recuperator cold side outlet to the volume. Between 0.15 and 0.6 seconds, the temperature decreases from 547°C to about 517°C as the fluid from the PCB valve flows into the volume. Figure 11.17 shows the same parameters over the longer timescale of 30 seconds. This shows that after about 7 seconds, the combined bypass case reaches a higher temperature, but this occurs at a slow enough rate that thermal shock is not considered a problem beyond this point. In the turbine bypass scheme, the temperature increases by about 30°C degrees in 0.3 seconds, whereas in the combined bypass scheme, the temperature

increases at the same initial rate, but for less time, followed by a 30°C decrease in temperature over about 0.45 seconds. Although the thermal cycling at the inlet to the hot side of the high temperature recuperator is not totally eliminated by the combined bypass scheme, the situation is somewhat improved and may be improved further during refinement of the bypass design in future work. The reason for the higher eventual temperature (after ~7 seconds) at this location in the combined bypass case than in the turbine bypass case is that the core coolant mass flow rate is much greater for a sustained period of time with the turbine bypass scheme than in the combined bypass scheme, which suppresses the coolant outlet temperature.

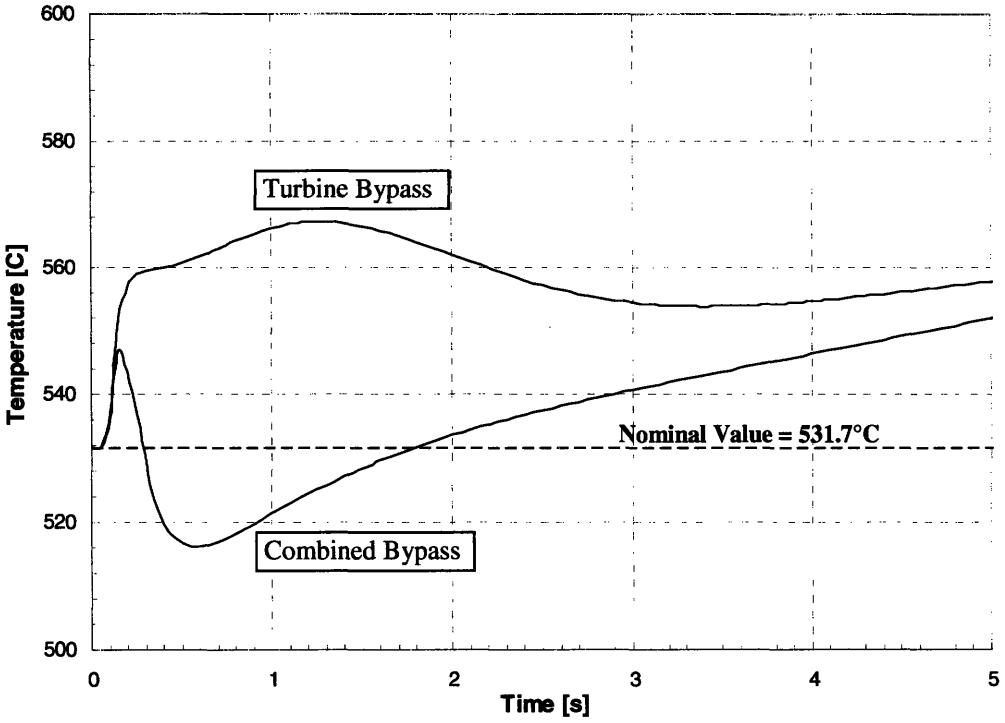

Figure 11.16. Temperature at inlet to high temperature recuperator hot side versus time following an LOEL event with combined bypass (turbine bypass shown for comparison): short time scale.

In later work, a control system should be specified in order to provide the optimal combination of mass flow rate in the core, shaft speed and recuperator temperatures following the LOEL event. This may consist of valves which can be automatically opened or closed to a desired flow area in order to allow the desired flow rate through. For the duration

of this work, however, the valves will remain in the open position for the duration of the transients once the generator is decoupled from the electric power grid and the combined bypass is actuated. Ultimately, bypass valves should be opened and closed by proportional-integral-derivative (PID) controllers to sustain flow rate through the core as long as possible, thus taking advantage of the direct cycle configuration.

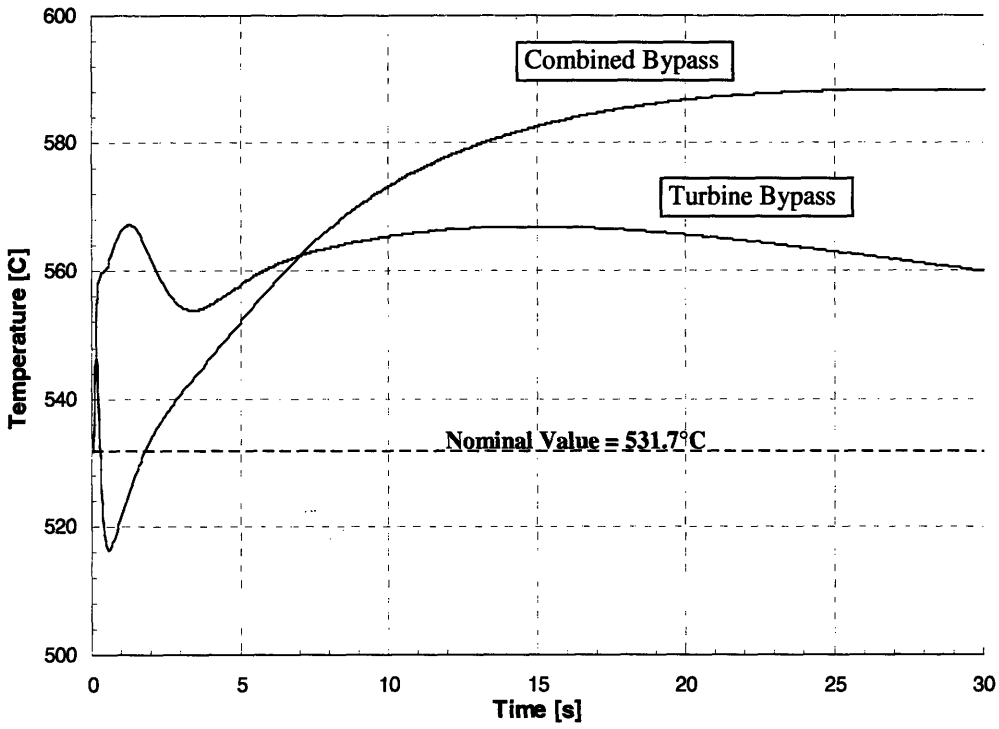

Figure 11.17. Temperature at inlet to high temperature recuperator hot side versus time following an LOEL event with combined bypass (turbine bypass shown for comparison): longer time scale.

Because the duty of slowing the acceleration of the shaft is shared by the turbine bypass valves and the PCB valves, both can have smaller flow areas with the combined bypass arrangement than in either the turbine bypass or PCB cases alone. This allows them also to reside in smaller-diameter piping. The issue of the design of the valves, particularly a turbine bypass valve which would be exposed to coolant at the core outlet temperature of 650°C continuously, is left for future work.

11.6 Summary

In this chapter, methods of mitigating an LOEL event were investigated. The PCB valves, when sized to be just large enough to arrest the shaft acceleration before reaching the 20% overspeed limit, produced a flow reversal in the core, followed by near-stagnation. This caused rapid overheating of the core. The opening of the PCB valves also caused a sudden decrease in pressure in the downcomer region, opening the SCS/ECS check valves. This is an unfavorable result because if the blowers do not come on, the SCS/ECS becomes a route by which coolant circulated by the compressors as the shaft spins down may bypass the core, accelerating the heat up of the cladding. The direct turbine bypass was evaluated as well with mixed results. Usually discarded for helium gas-cooled reactor applications due to the exposure of the bypass valves to coolant at the core outlet temperature, turbine bypass may be feasible in the cooler S-CO_2 (650°C) environment. The core mass flow rate, rather than stagnating as in the PCB case, increased more than twofold in the seconds following the turbine bypass. Turbine bypass also has the advantage of not causing the SCS/ECS valves to come open.

Accordingly, the recommended scheme for mitigating an LOEL event is a combined bypass scheme wherein the turbine bypass valves and PCB valves are opened, the PCB valves having a slightly slower opening rate. The combined opening of the two valves arrests the acceleration of the shaft before reaching the 20% overspeed limit. Opening the turbine bypass valve first ensures that the SCS/ECS check valves will not open and prevents the large flow reversal in the core. The delayed PCB valve opening provides an alternate route for coolant in order to keep the mass flow rate in the core to less than 150% of the nominal value during the transient. The combined bypass scheme can also be used to reduce the thermal shock to the high temperature recuperator during the LOEL event. Smaller valves residing in smaller pipes can also be used with the combined bypass scheme than in either the turbine bypass or the PCB valves alone, since it is their combined flow which reduces the shaft acceleration.

In future work, a PID control system should be devised which maintains a desired shaft speed and core flow rate in the minutes following the LOEL. This can be done by

changing control valve stem position in one or both of the valve types. In this work, however, the valves, once opened, remain open unless their closure is otherwise noted in the description of the transient.

Another important detail not addressed at this point is protection of the compressors from surging and choking. In the LOEL transients simulated here, the compressor choke, but the simulation is allowed to continue because the homologous pump models are used. This is justified because the operational band for axial compressors like the ones specified here are quite narrow. In future work, radial compressors will be specified in order to provide more margin to surging or choking. In real systems, fast-acting protection systems would be in place to prevent damage to the compressors in transients like this. Once detailed performance curves are available for radial compressors, these systems can be designed and tested for the LOEL event and other transients.

12 Loss of Coolant Accident

12.1 Introduction

The LOCA is generally considered to be the most severe accident, particularly in gas-cooled reactors where the rate of coolant inventory loss is larger than in liquid-cooled reactors. The break size which will be analyzed in this section is a 100 in^2 (645 cm^2) break in the cold leg of a PCS duct. This is simulated using a motor valve (valve 394 in Figure 9.2). In the final design, reliable PCS isolation valves will be used in order to quickly shut off the flow to a PCS loop which experiences a break. In this work, however, it is assumed that the isolation valve in the broken loop has failed and the system blows down to equilibrium with the containment. The 100 in^2 break is first used in order to determine the size requirements (and thus type) of the containment required for the present design. Then, the response of the plant to the break is analyzed in order to determine the response needed from the SCS/ECS to prevent core damage.

12.2 100 in^2 Cold Leg Break

In this LOCA scenario, a break having an area of 100 in^2 (645 cm^2) is initiated at time zero using valve 394 in Figure 9.2. The underpressure scram set point is 19.5 MPa in the lower reactor plenum and so is the signal which disconnects the turbomachinery from the grid and initiates the bypass valves immediately. The shaft is then free to turn according to the turbomachinery torques, spinning down over the course of the transient. The bypass valves are sized and timed the same as in the recommended combined bypass scheme in Chapter 11 and once their opening is initiated at the same time as the underpressure scram signal, they are left open for the duration of the simulation. The precooler water flow rate

remains at the full power value for the duration of the transient and pressure control volumes 397 and 497 are disconnected from the system just prior to the occurrence of the break. After about 10 minutes (problem time), the system depressurization is complete and the pressure in the primary system is equal to that of the containment.

12.2.1 Containment Considerations

As mentioned in the introduction to this chapter, the 100 in^2 break is used to size the containment. The LOCA was simulated for different containment sizes ranging from 50,000 m^3 to 80,000 m^3. In the initial cases, no containment structures were modeled. These are shown in the first five rows of Table 12-1. The backup pressures range from 0.895 to 0.620 MPa over this range of containment free volumes. Single large dry containments for present-day Pressurized Water Reactors (PWRs) have free volumes in the range of 60,000 m^3 to 95,000 m^3, with design pressures of 0.4 to 0.65 MPa. [Gavrilas, et. al., 1995] Thus, a large dry PWR containment may be suitable for this design.

In a real system experiencing a LOCA, a significant amount of energy is expended in heating up the containment building and other structures within it, decreasing the final temperature and pressure after the blowdown. The 70,000 m^3 case was selected for further calculations where these heat structures are considered because the backup pressure was expected to decrease into the range of PWR containment design pressures. A typical large dry containment has a non load-bearing carbon steel or stainless steel liner between 0.6 and 1.2 cm thick in order to provide leak tightness. [Gavrilas, et. al., 1995] A stainless steel liner having a thickness of 1.0 cm was selected for this analysis. The modeled containment volume was cylindrical with a flat floor and a hemispherical ceiling. The diameter was set equal to the cylindrical height giving a value of 40.58 m for both. At this stage, the volume of the primary system and structures was neglected in sizing the containment building (the volume of the fluid in the primary system is approximately 2000 m^3). In the RELAP model of the plant, heat structures were added which communicate thermally with the containment volume on one side and are perfectly insulated on the other. The steel liner sections on the flat floor, hemispherical ceiling and cylindrical wall were modeled using three RELAP heat structures, each with 4 radial nodes to represent their thickness. The total volume of steel in

the 1.0 cm-thick liner is approximately 90 m^3. The sixth row of Table 12-1 gives the results of the blowdown with the steel liner included. The backup pressure has decreased from 0.685 MPa to 0.606 MPa and the final temperature decreases from 334°C to 308°C with the inclusion of conduction to the steel liner.

A typical large dry PWR containment also has reinforced or prestressed concrete outside the steel liner with a thickness of 1.0 to 1.5 m in the cylindrical wall and 0.7 to 1.0 m on the hemispherical (or ellipsoid) roof. [Gavrilas, et. al., 1995] Like the steel liner, the concrete absorbs heat and lowers the backup pressure and temperature after a LOCA. The RELAP heat structures were changed in order to quantify the effect of this concrete, again using the 70,000 m^3 containment volume. The thickness of the concrete was taken to be 0.8 m in the hemispherical dome and 1.25 m in the cylindrical walls and floor. Heat is assumed to conduct from the steel liner to the concrete without thermal resistance at the interface, and the outer edge of the concrete is assumed to be perfectly insulated. The last row of Table 12-1 shows the resulting pressure and temperature in the containment with the heat structures modified to account for both the steel liner and the concrete.

Table 12-1. Final containment pressure and temperature following 100 in^2 cold leg break and blowdown to equilibrium.

Containment Free Volume (m^3)	Containment Structures Modeled	Backup Pressure		Peak Containment Temperature (°C)
		(MPa)	(bar)	
50,000	–	0.895	8.86	355
65,000	–	0.726	7.19	338
70,000	–	0.685	6.78	334
75,000	–	0.651	6.45	330
80,000	–	0.620	6.14	325
70,000	Liner	0.606	6.00	308
70,000	Liner + Concrete	0.599	5.93	308

The resulting temperature and pressure in the case with both the steel liner and the concrete structures in the containment is only slightly different than those in the case with the liner alone. This indicates that over the relatively short period of time it takes for the system to blow down (it will be shown that this takes about 10 minutes), the concrete does not absorb a significant amount of energy. As more time passes, however, the concrete heats up, lowering the temperature and presure in the system more than in the case with the liner only. The containment free volume of 70,000 m^3 was thus selected as the reference containment design and the steel liner and concrete heat structures were left in the RELAP model for the remaining analyses.

The containment volume will have other structures than the liner and concrete in the containment walls, such as the outsides of insulated primary system piping, fuel handling structures, PCS piping or vessels, etc. These structures will heat up and further lower the peak temperature and pressure in the containment volume after a LOCA. As the design of the primary system and other contents of the containment mature, more accurate accounting for these structures should be used in the RELAP LOCA simulations. As this information is integrated into the design, the containment size which gives the 6 bar design backup pressure will be found to be smaller than 70,000 m^3, and the resulting peak temperature will be lower. The lower peak temperature expected is important because the current value of 308°C could be too high for some of the more sensitive contents of the containment. This is left for refinement in future work.

12.2.2 100 in^2 Cold Leg Break without SCS/ECS Response

In order to determine what measures must be taken in order to withstand a LOCA, it is first instructive to determine the events and conditions which occur when no action is taken by the SCS/ECS. In this section, this will be done for the 100 in^2 cold leg break. The 70,000 m^3 containment selected in the previous section is used with the steel liner and concrete heat structures included. The break occurs at time zero and the reactor scram is initiated when the 19.5 MPa set point is reached. At the same time as the scram, the generators trip and the combined bypass valves are actuated. After this, no further action is

taken in response to the LOCA. The PCS isolation valve in the faulted PCS loop fails to close and the system blows down completely.

The reactor scram signal occurs at 1.2 seconds into the transient. At the same time as the scram, the generators trip off the grid and the combined bypass valves are actuated. Once opened, they are not reclosed for the duration of the transient. The shafts speed up to just below the 20% overspeed limit and then slow down, as shown in Figure 12.1, reaching very low speeds by the termination of the transient. The faulted PCS shaft speed is very close to that of the other three, thus only one is shown in the figure.

Figure 12.2 shows the core inlet pressure as well as the containment pressure versus time following the break. The 6 bar containment design pressure is also shown on the plot as the dashed line. The pressure in the containment reaches its peak at around 600 seconds (10 min) after the break even though the system is not fully depressurized until around 700 seconds. This is because even as primary coolant system inventory continues to enter the containment free volume, heat is being conducted to the steel and concrete in the containment structures. The relatively large time required for depressurization of the primary system is due to the large coolant inventory of the system (~330,000 kg) and the low sound speed of CO_2. This is in stark contrast to helium cooled systems, which have much smaller coolant inventory and faster depressurization times despite their lower pressure.

Figure 12.3 shows the coolant mass flow rate in the core versus time following the break. The nominal full power flow rate is shown with a dashed line, as is 150% of this value. The lower bound of the time scale is one second, at which time the flow rate has already fallen to around 75% of the nominal value as a result of coolant in the cold leg exiting the break rather than traveling through the core. At about 1.3 seconds, the mass flow rate increases sharply as a result of the opening of the turbine and PCS valves, then falls slowly as the shafts slow down. The slight increase in mass flow rate beginning at 100 seconds is a result of the SCS/ECS check valves opening and the subsequent mass flow rate through them, which will be shown to have a noticeable effect on clad temperatures.

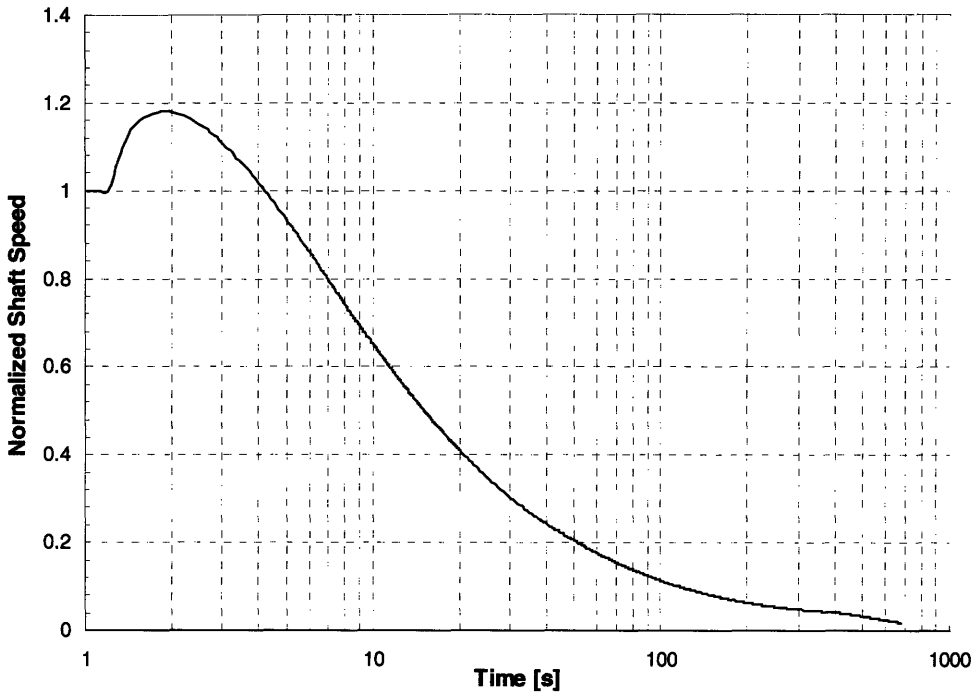

Figure 12.1. Shaft speed versus time following a 100 in^2 break in cold leg.

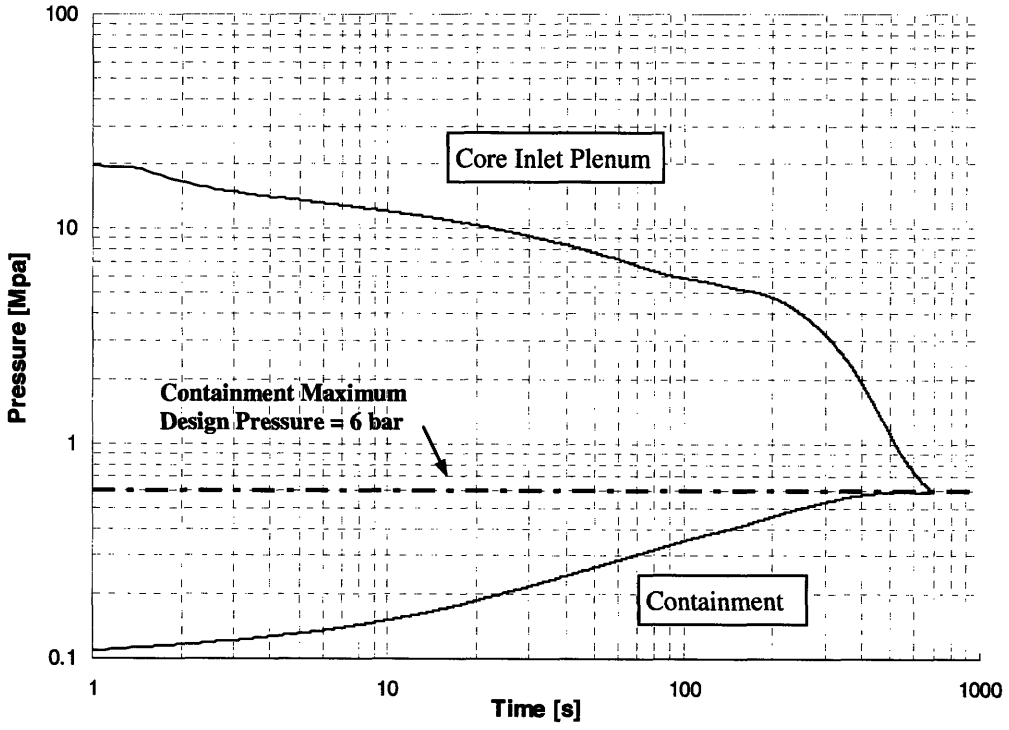

Figure 12.2. Pressure in core inlet plenum and containment building versus time following a 100 in^2 break in a cold leg.

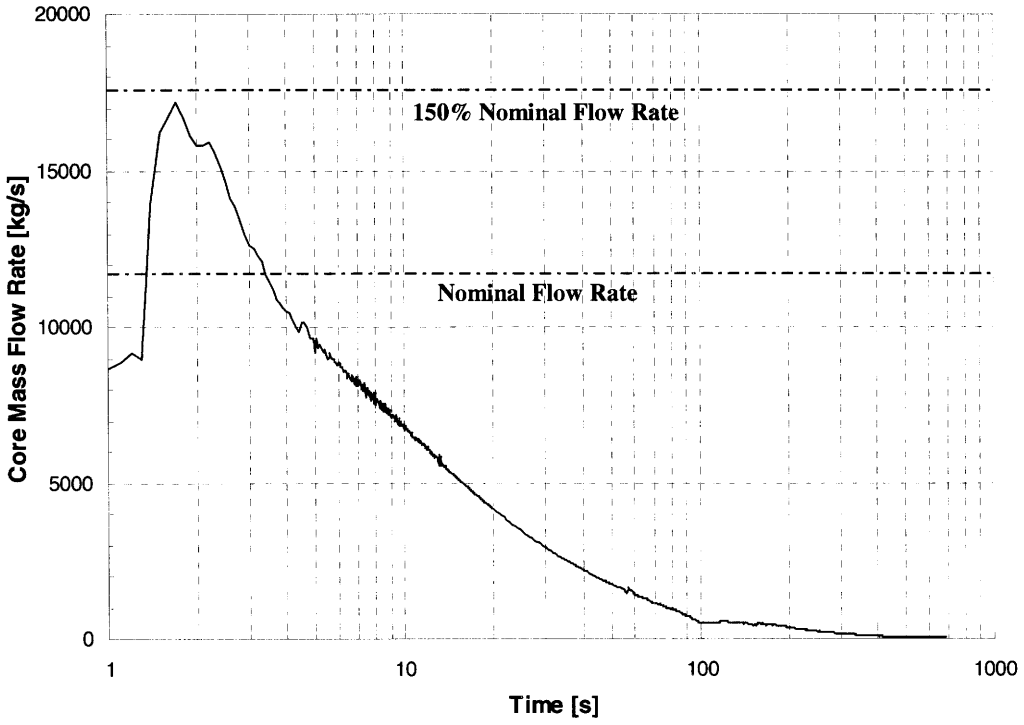

Figure 12.3. Core mass flow rate versus time following a 100 in^2 break in a cold leg.

Beyond 600 seconds (10 minutes) into the transient, the PCS temperatures have become very cold and two-phase CO_2 is present in precoolers and low-temperature recuperators. The very low CO_2 temperatures encountered in the PCS loops during the LOCA transient are not encountered in most other practical applications of the RELAP code. Under these conditions, thermodynamic property errors occur frequently unless the maximum time step is made prohibitively small. In order to circumvent these errors, the PCS loops were removed at t = 600 seconds. By this time in the transient, the shaft speeds are very low, as shown in Figure 12.1, and the coolant in the PCS loops is nearly stagnant. Therefore, removal of these sections can be performed without significant alteration of the results. The removal of the PCS loops, however, also removes potential core bypass routes which could have degraded post-LOCA cooling were they left in the model. This is accounted for by leaving some of the sections in the model as shown in Figure 12.4. The turbine bypass and PCB valves are included and are left open. This simulates all of the bypass valves having been left open after the LOCA, providing a conservatively large core

bypass route. Thus, the calculation of time before the peak clad surface temperature is reached (and the estimation of blower power required to prevent it in the following section) is a conservative one. The simulated cold leg break (valve 394) is also left in the model in addition to the containment volume (volume 900). This is done so that the primary system can continue to communicate with the containment volume as the pressure in both falls during the transients.

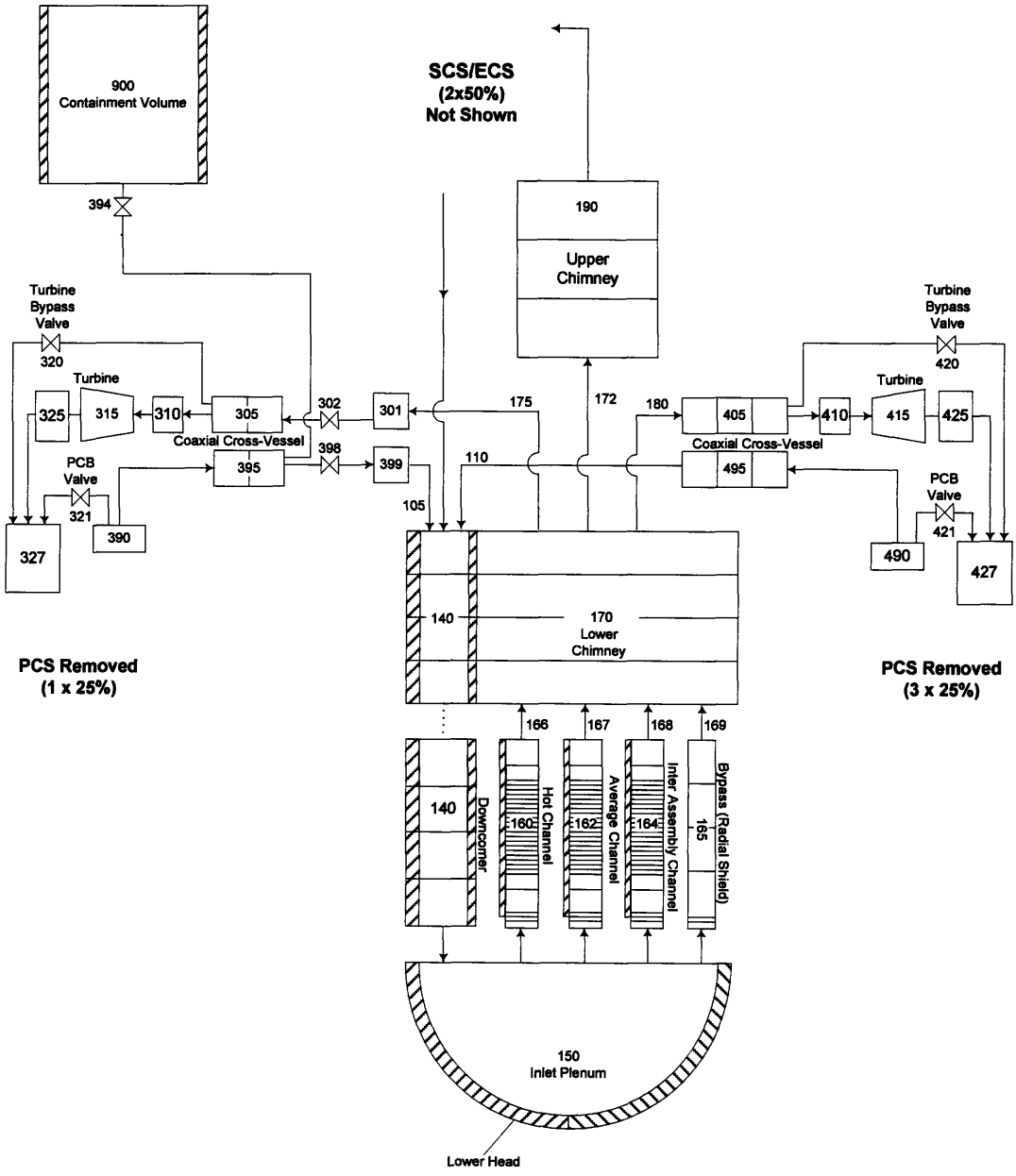

Figure 12.4. Nodalization diagram used after t = 600 seconds with PCS loops removed and core bypass routes (PCB valves) included.

Figure 12.5 shows the peak clad surface temperature versus time following the break with no response from the SCS/ECS system. The temperature experiences a slight increase in the time between the break and the initiation of bypass valves opening. This is because the core mass flow rate is slightly lower than the nominal full power flow rate and the reactor power is still nearly 100%. At around 1.3 seconds into the transient, the increased mass flow rate due to the opening of the bypass valves lowers the clad surface temperature. At approximately two seconds, the mass flow has fallen back to below the full power value and the peak clad temperature increases again. Approximately seven seconds into the transient, the clad temperatures decrease again because the reactor power has fallen significantly by this time. The mass flow rate and the reactor power both decrease until around 80 seconds, when the flow rate becomes very low and the clad temperatures begin to increase slightly. This increase is temporarily arrested by the increase in flow which occurs with the opening of the SCS/ECS check valves. Beyond 200 seconds, the clad surface temperatures increase steadily as the core mass flow rate has become extremely low.

The location along the temperature line indicated by the point and the arrow shows when the PCS loops were removed from the model. From this, it can be observed that the rate of temperature increase remains smooth during this instantaneous change in the model. At t = 600 seconds , the peak clad surface temperature has reached approximately 970°C, still well below the accident limit of 1200°C, which is reached at approximately 890 seconds. This indicates that aside from the reactor scram, generator trips and bypass valve actuation, no further action is required for at least 10 minutes into the transient in the event of a 100 in^2 cold leg break assuming failure of the isolation valves on the faulted PCS. In the following section, operation of the SCS/ECS blowers will be simulated starting at 600 seconds.

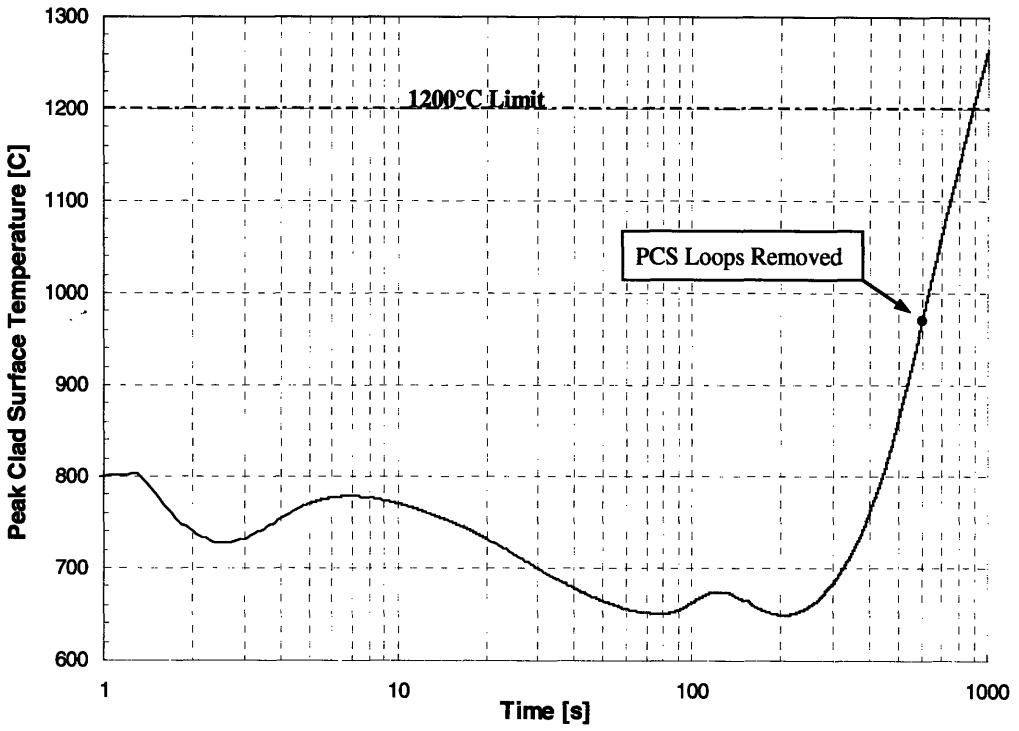

Figure 12.5. Peak clad surface temperature versus time following a 100 in^2 break in a cold leg.

12.2.3 100 in^2 Cold Leg Break with SCS/ECS Response after 10 Minutes

In the previous section, it was observed that in the event of a 100 in^2 break in a cold leg where the isolation valves have failed, no action need be taken by the SCS/ECS for the first 10 minutes following the break. After this time, the clad temperatures increase and reach the 1200°C limit at around 890 seconds. In this section, the response of the SCS/ECS will be assumed to take place at 10 minutes past the initiation of the transient. The same LOCA scenario as the previous section is modeled, only at 10 minutes into the accident, the simulated SCS/ECS blowers are started. As described previously, the PCS loops are removed from the model at t = 600 seconds in order to prevent thermodynamic property errors in these volumes, but conservatively large bypass routes (assuming bypass valves remain open) are left intact.

Because it is not practical at this stage in design to use detailed compressor or pump characteristics to represent the emergency blowers, a RELAP time-dependent junction (junction 645 in Figure 9.3) was used for this evolution. The time-dependent junction imposed a flow rate which was specified using a table of mass flow versus time. The blower power required for the specified mass flow rate was calculated using Equation 7-2, again assuming a constant efficiency of 85%. The initial SCS/ECS blower flow rate upon its actuation at t = 600 seconds was 125 kg/s. This value was obtained from the results of the steady state calculations used to generate the results in Chapter 10, and by trial and error. Approximately 1/3 of the coolant flow forced by the blower bypasses the core through open PCB valves. Figure 12.6 shows the blower mass flow rate versus time on the right-hand axis. As time passes during the transient, the decay power decreases and the blower mass flow rate is decreased as well, as is shown in Figure 12.6, with a final value of 100 kg/s at 10,000 seconds. The other line on Figure 12.6 corresponds to the left-hand axis and gives the calculated SCS/ECS blower power in kW versus time. The blower power required to deliver the prescribed mass flow rate peaks at approximately 2400 seconds with a value of 84 kW.

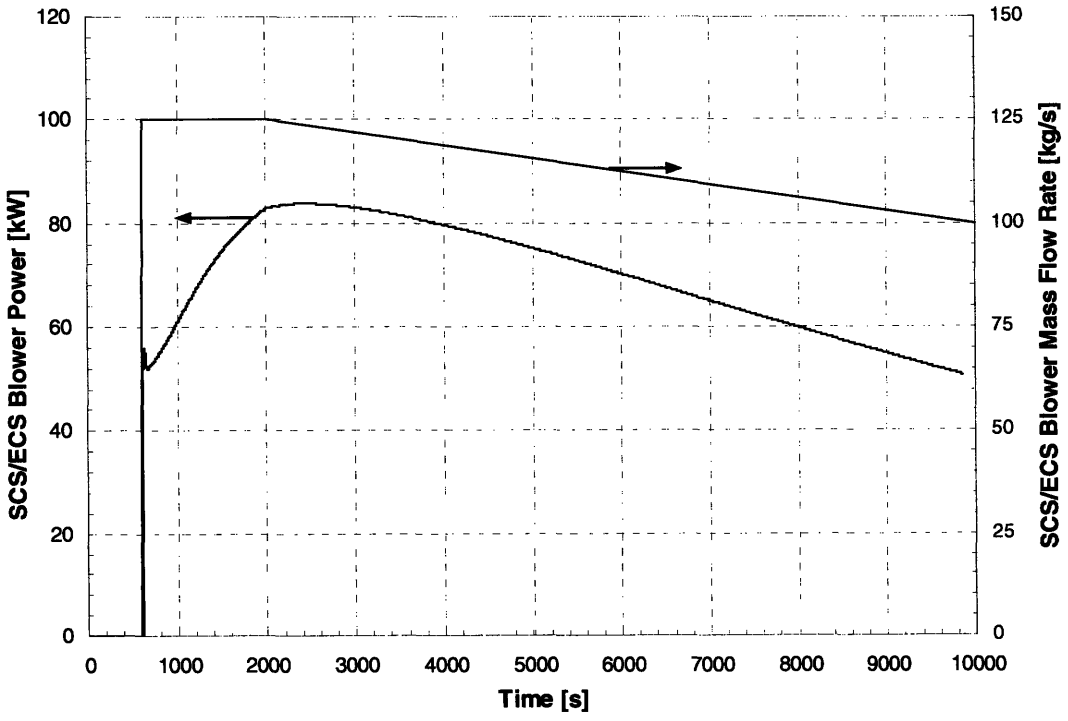

Figure 12.6. SCS/ECS blower mass flow rate and power versus time.

Figure 12.7 shows the peak clad surface temperature versus time for the case with no SCS/ECS response and for the case with the prescribed blower flow rate mentioned above. The 125 kg/s forced by the SCS/ECS blowers limits the peak clad temperature to a maximum of approximately 1100°C just past 1000 seconds. The peak clad temperature then decreases for the duration of this transient, which ends at 10,000 seconds.

Figure 12.8 shows containment pressure versus time following the 100 in^2 cold leg break with the time scale ending at 10,000 seconds. The peak containment pressure occurs between 500 and 600 seconds, followed by a more gradual decrease in pressure resulting from transfer of energy to the containment structures, primarily the stainless steel liner. Because the volume in the containment and that of the primary system are connected by the break (valve 394), the pressure given for the containment in Figure 12.7 is also that of the primary system after approximately 700 seconds. By the termination of the transient simulation at 10,000 seconds, the system pressure has fallen to about 400 kPa. Figure 12.9 shows the containment volume temperature versus time following the 100 in^2 cold leg break.

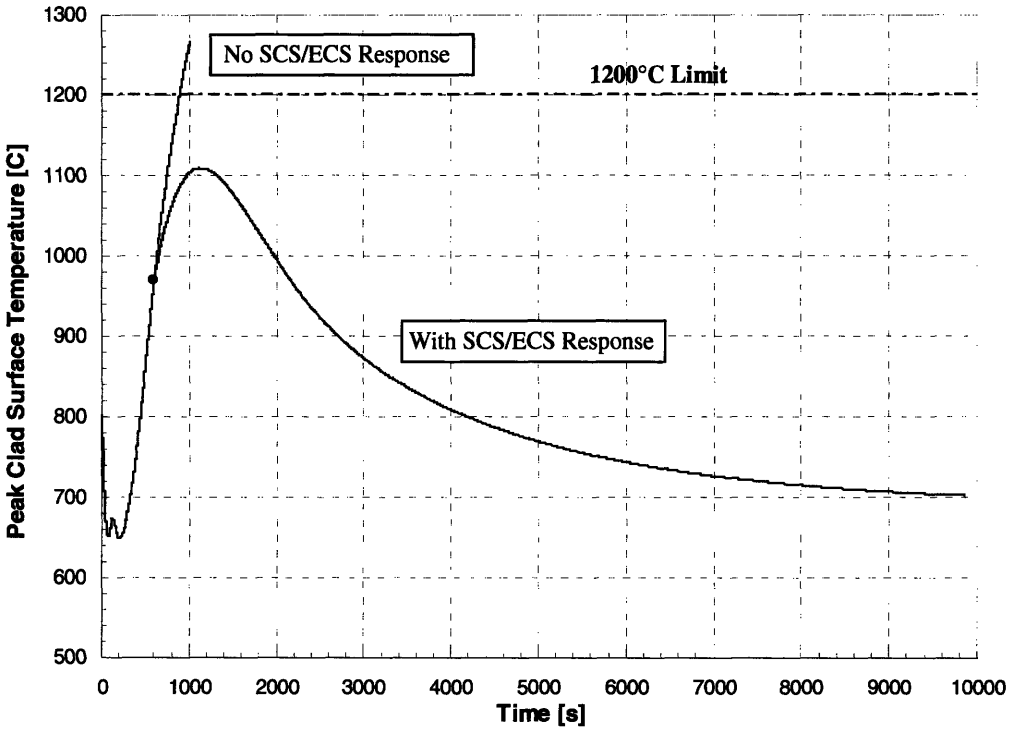

Figure 12.7. Peak clad temperature versus time with and without blower function after a 100 in^2 cold leg break.

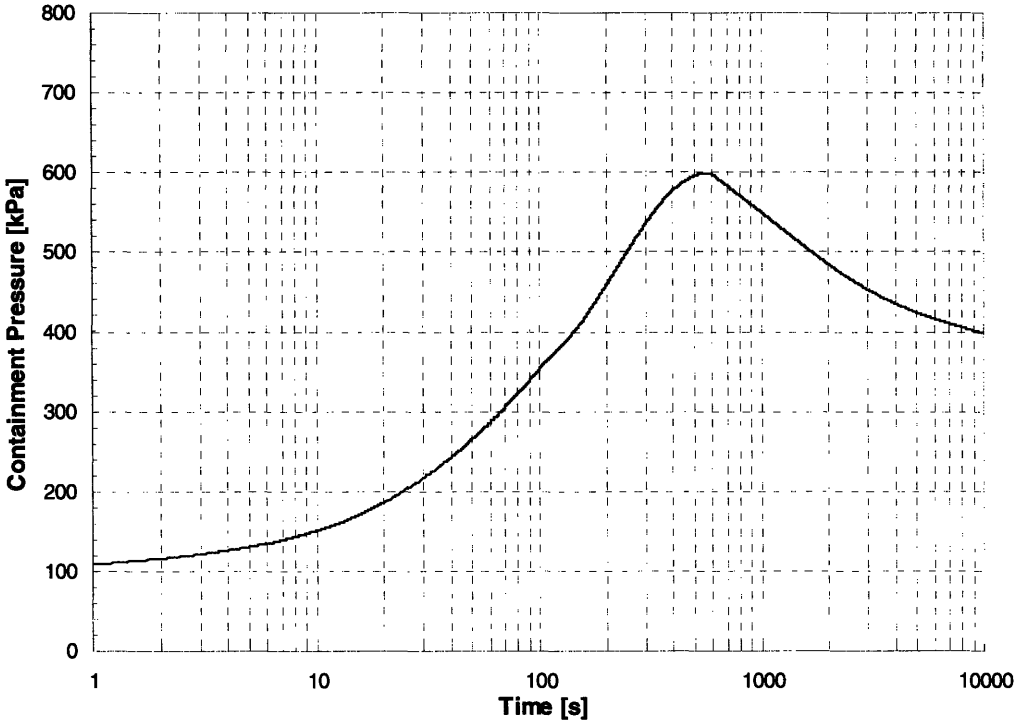

Figure 12.8. Containment pressure versus time following a 100 in^2 break in a cold leg.

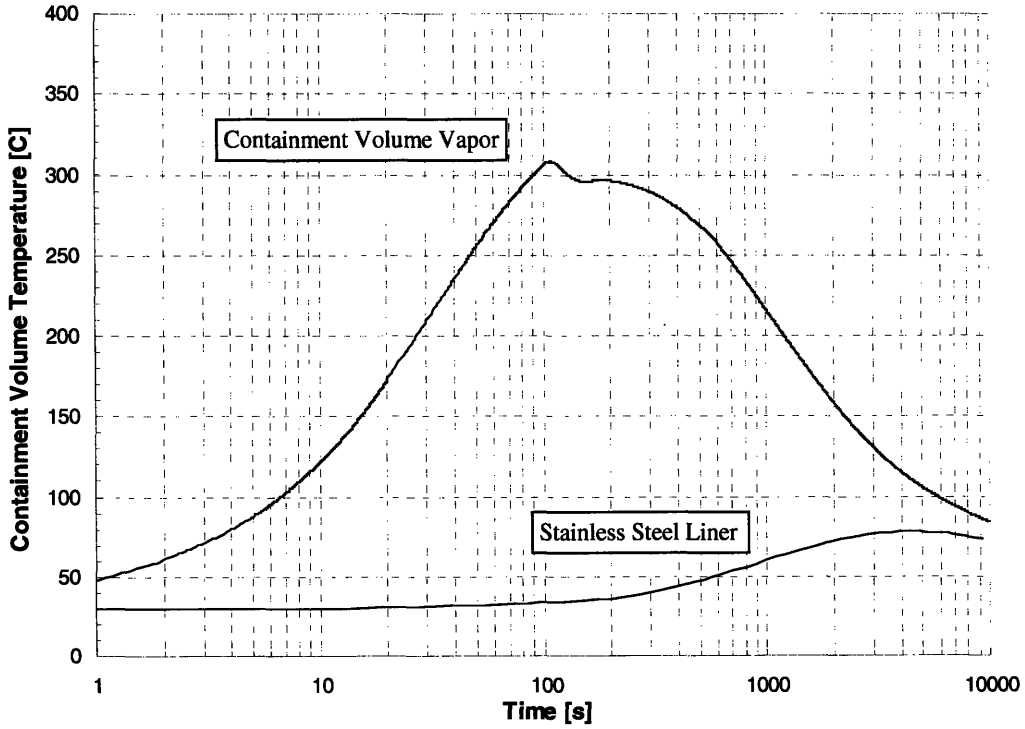

Figure 12.9. Containment volume vapor temperature and steel liner average temperature versus time following a 100 in^2 cold leg break.

The peak containment volume vapor temperature of 308°C occurs at around 100 seconds and is followed by a gradual decline in temperature as heat is transferred to the containment structures. The peak in containment temperature can occur before the peak in pressure because the heat transfer to the containment structures overcomes the continued flow of primary system inventory into the free containment volume. The average temperature of the stainless steel containment liner versus time is also given in Figure 12.9, taken from the cylindrical wall heat structure. This shows that the fall in containment volume vapor temperature corresponds with an increase in the steel liner temperature. Beyond approximately 5,000 seconds into the accident, the steel liner temperature begins to decrease as the rate of heat transfer from the liner to the concrete beyond it begins to exceed the rate of heat transfer from the CO_2 to the steel liner.

12.3 Summary

In this chapter, a 100 in^2 cold leg break was simulated, selected based on its use as a maximum break size in previous gas-cooled reactor designs (specifically, the GA GCFR). The simulated LOCA was first used in order to size the containment free volume. With a free volume of 70,000 m^3 and heat structures included to simulate the steel liner and reinforced concrete in the cylindrical wall, flat floor and dome-shaped roof of the containment, its peak pressure following the LOCA was found to be approximately 6 bar. This size and peak pressure are suitable for a typical large dry PWR containment, and so this type of containment is specified for the present design. Because a great deal of other structures not accounted for here are present in a real containment, the free volume which gives the same peak pressure may be somewhat smaller than 70,000 m^3. This should be re-addressed later after the design is developed further. The peak containment volume vapor temperature of 308°C calculated in this work may also be of concern. However, the temperatures of containment structures remain below about 100°C, an acceptable value.

Assuming that the reactor scrams due to an underpressure signal at 19.5 MPa in the lower core plenum with concurrent trip of the generators and bypass valve actuation, no further action is required for 10 minutes following the initiation of the accident. This is assuming that the SCS/ECS water pumps are operating for the entire time. Beginning 10

minutes after the accident, SCS/ECS blower power of < 90 kW was found to be sufficient to keep the peak clad temperature well below the limit of 1200°C up to 10,000 seconds when the simulation was discontinued. Because this was modeled assuming that 2 of the 4 SCS/ECS units were functioning, this means that 4 units with a 45 kW rating could be specified. By 10,000 seconds, the pressure in the containment and the primary system has fallen to approximately 4 bar. It is worth noting that if this rate of pressure decrease in the containment is extrapolated to 24 hours, (8.64×10^4 seconds), the pressure will not be half its maximum value as commonly required of a PWR. This could become an issue in the licensing process. On the other hand, there is incentive to maintain high pressure to facilitate natural convection (see Chapter 10).

After the blowdown, low temperatures in the PCS loops caused thermodynamic property errors. In order to circumvent these errors, the loops were removed at the 10 minute point at the same time that blower function was initiated. Because at this point, the depressurization was nearly complete and the turbomachinery had all but stopped spinning, the results with the PCS loops removed should be an accurate representation of the actual transient. In future work, however, the root cause of these errors should be investigated.

It should also be noted that this is a very conservative simulation since only half of the SCS/ECS (2x50%) is assumed to be functional. If it were assumed that only one has failed (as in the single failure criterion), this would lead to greater decay heat removal capability by natural circulation.

If a control system is added which maintains the shaft speeds by opening and closing turbine bypass valves, coolant flow could be maintained longer than in the case where the valves are simply left open. This would take advantage of the direct-cycle arrangement and allow for the decay heat to provide the energy to circulate the coolant. In this way, the demand for the SCS/ECS blowers could be postponed or even eliminated. This should be pursued in future work.

13 Loss of Flow Transient

13.1 Introduction

In the 4-loop arrangement of the 2400 MW_{th} S-CO_2 cooled GFR, each PCS loop has valves which provide means for isolating that loop from the rest of the plant. If inadvertent isolation of one of the loops were to occur at full power, a rapid 25% reduction in core coolant flow rate would result before the reactor power could be decreased from its 100% value. Because of the significant decrease in flow resulting from this closure, this event is designated as a loss of flow (LOF) transient. In this chapter, this LOF transient is simulated assuming that no plant response to the LOF occurs (i.e. no reactor scram). Isolation of a PCS loop need not be inadvertent, however, as this is the expected response to a number of PCS loop faults (e.g. small or large LOCA, shaft seizure, compressor or turbine failure). If the plant responds normally to these faults and isolates a PCS loop, the rest of the plant will respond in a way which is independent of what type of fault prompted isolation of that loop. In this way, the LOF transient analyzed in this chapter envelops a number of other types of events assuming that they involve isolation of a PCS loop.

13.2 Methodology for Modeling the LOF Transient

The LOF transient was modeled in RELAP by removing the single PCS loop during a restart. The remaining lumped 3x25% PCS loop responds to this as though the single PCS had been completely and instantaneously isolated from the rest of the plant. The reason for using this method is that one avoids the numerical complications of having the flow suddenly stagnant before the turbomachinery can respond. The weakness of this method is that only the response in the core and the un-isolated PCS loops can be determined. This is, however,

the priority in the hierarchy of plant protection. Once it is verified that core damage can be avoided, only then is the condition of the turbomachinery in the isolated loop of concern. An important assumption made for this analysis is that of no reactivity feedback.

13.3 Results of LOF Analysis

Figure 13.1 shows the core coolant mass flow rate versus time following the initiation of the LOF transient. The initial full power mass flow rate of 11,708 kg/s is shown on the plot as a dashed line. Because the decrease from the nominal value occurs so quickly, it is not visible on this plot. After the initial decrease, the mass flow rate is approximately 75% of the nominal value and then slowly increases. This increase is due to the lower core pressure drop resulting from the lower mass flow rate.

Figure 13.2 shows the temperatures of the coolant at the core inlet and outlet versus time following the LOF. The core oulet temperature begins to increase immediately because the flow rate decrease is nearly instantaneous as modeled here. The core inlet temperature remains constant for a brief time, then begins to increase in a similar way as the core outlet temperature. This delay is due to the fact that the hotter fluid from the core outlet must reach the high-temperature recuperator before the cold leg can be heated from its nominal value. Both the inlet and the outlet temperatures approach new steady state values which could potentially decrease slightly from the value at 400 seconds due to the increase in mass flow. The new core temperature rise is 203°C, up 23% from the nominal value of 164.5°C. If the mass flow rate dropped to 75% of the nominal value and remained there, the increase in core ΔT would be about 33% (factor of 4/3 increase). Because the mass flow rate steadily increases due to the lower core pressure drop, the increase in core ΔT is not this large.

Figure 13.3 shows the peak clad surface temperature versus time following PCS isolation valve closure from a full power steady state condition. This shows that the peak clad temperature approaches a new steady state value after the LOF which appears to be just above 1000°C. This temperature may decrease over a longer time scale as well due to the steady increase in mass flow rate shown in Figure 13.1. These results indicate that even if no

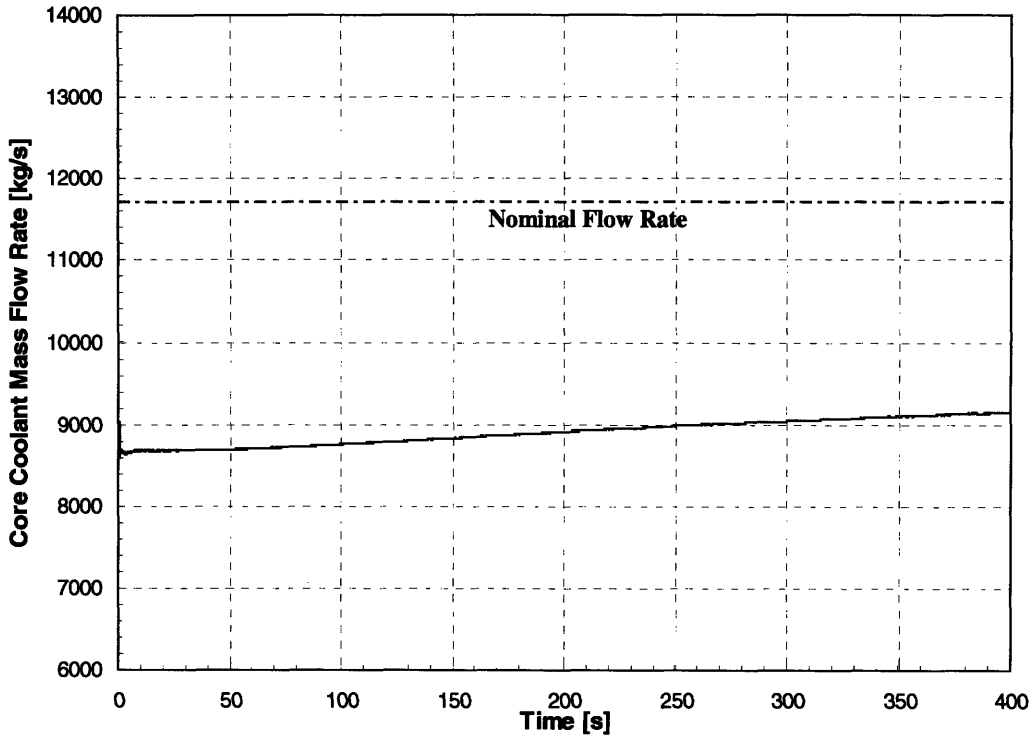

Figure 13.1. Core coolant mass flow rate following PCS isolation valve closure from a full power steady state condition.

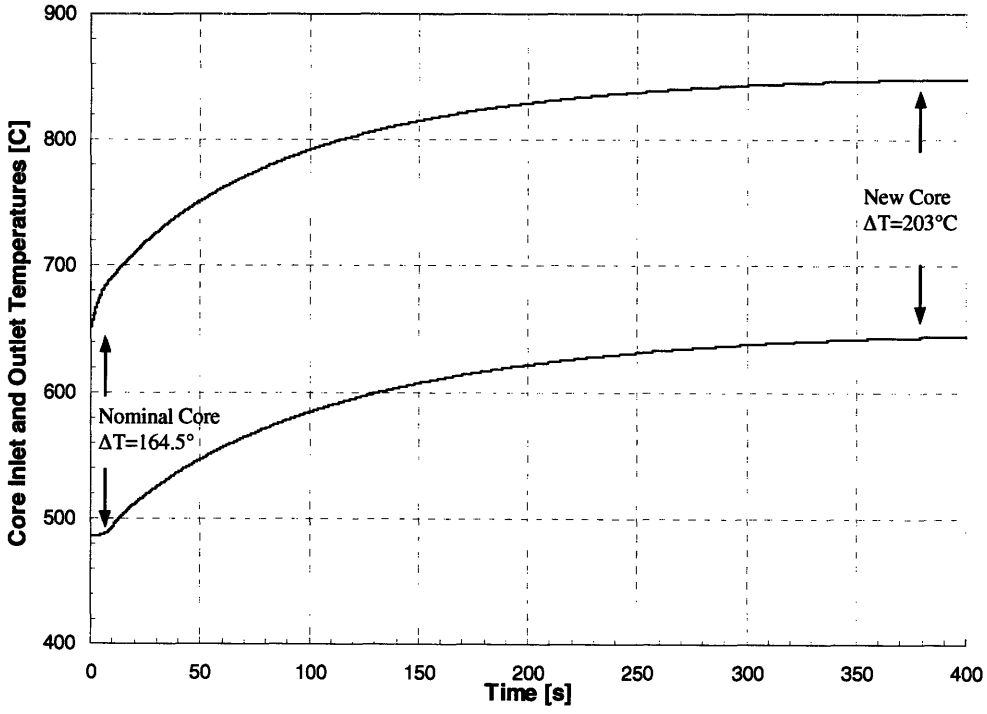

Figure 13.2. Core inlet and outlet temperature versus time following PCS isolation valve closure from a full power steady state condition.

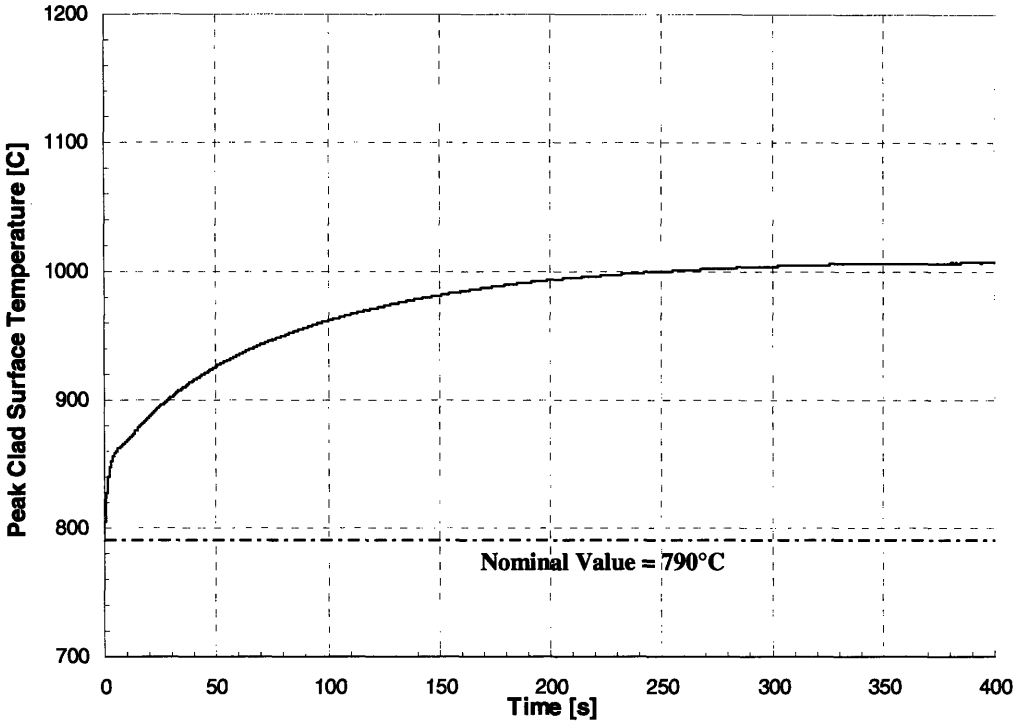

Figure 13.3. Peak clad surface temperature versus time following PCS isolation valve closure from a full power steady state condition.

action were taken either automatically or by operators to mitigate this LOF event*, clad temperatures in excess of the accident limit of 1200°C would not result. Furthermore, the new steady state peak clad surface temperature which the system appears to be approaching is approximately 1000°C, which was the limit previously selected for an LOEL transient, an event expected to occur more than once in the life of any plant.

13.4 Summary

In this chapter, an LOF transient was analyzed in which one of the four PCS loops was suddenly isolated from the rest of the plant. The core flow rate decreases almost instantaneously to approximately 75% of its nominal value and then increases slowly due to

* Normally, reactor power will be reduced by 25% automatically after isolation of a PCS loop.

the lowered core pressure drop. The core inlet and outlet temperatures increase over the first few hundred seconds following the LOF, approaching new steady state values. The peak clad surface temperature also increased to a new steady state value of approximately 1000°C. This shows that in the event of an LOF event such as this, there is no immediate threat of core damage and there is sufficient time for mitigating action to be taken either automatically or by an operator (e.g. reactor power ramp down or scram).

The response of the isolated PCS loop, though not simulated in this work, should consist of rapid decoupling of that generator from the electrical grid. Actuation of the combined bypass valves should not be necessary in this case because the stagnation of flow will arrest the shaft rotation rapidly.

Although the sudden isolation of a PCS loop was identified as one of the more severe LOF transients which is likely to occur, other types of events which cause a decrease in flow may be identified for analysis in future work; for example, a compressor failure or shaft seizure without response of the isolation valves. Also, if the check valve also fails to close, a bypass backflow could occur.

It is also worth noting that these calculations were performed assuming no reactivity feedback, and so the reactor power remained perfectly constant throughout. Reactor physics parameters such as coolant void or fuel temperature coefficients of reactivity should be integrated into future LOF calculations. However, if the coolant void reactivity is zero or negative, as is the goal in the present design, this should not add to the severity of the LOF transient.

14 Summary, Conclusions and Recommended Future Work

14.1 Summary

The gas-cooled fast reactor (GFR) has received new attention due to its selection as a Generation-IV (Gen-IV) contender by the Gen-IV International Forum. The mainstream GFR design is a 600 MW_{th} helium-cooled direct Brayton cycle plant with core outlet temperatures in the range from 850°C to 1000°C. These very high temperatures are being pursued in the interest of high cycle efficiency and to provide high-temperature heat for hydrogen production by thermochemical water cracking. Operating a reactor at these temperatures presents a number of materials challenges which may prove difficult to overcome. The 2400 MW_{th} direct S-CO_2 cooled fast reactor under investigation at MIT is a lower-temperature alternative to the reference GFR concept. Taking advantage of the high density and low compressibility of CO_2 just above its critical point, the S-CO_2 recompression cycle gives efficiencies of approximately 48% with a core outlet temperature of 650°C. However, this requires a relatively high peak pressure of 20 MPa, a somewhat challenging but not unprecedented condition. This cycle is very compact with a single shaft and no intercoolers, providing significant reduction of capital cost. Power conversion is performed by four 600 MW_{th} power conversion system (PCS) loops. The S-CO_2 recompression cycle was selected as the most promising S-CO_2 cycle for Gen-IV service, and its optimization was performed in previous work at MIT [Dostal, et. al., 2004].

The general objective of this work is to contribute to the design process from the standpoint of thermal-hydraulics. This includes design of the reactor core and other reactor vessel internals, design and analysis of the Shutdown/Emergency Cooling System (SCS/ECS) and analysis of the performance of the plant during various events and accidents

using RELAP5-3D. Based on historical precedent for GFR type reactors, the transients selected for analysis were the loss of external load (LOEL), the loss of coolant accident (LOCA) and a loss of flow (LOF). Design of the core and reactor vessel internals was performed in collaboration with C.S. Handwerk (MIT), who provided reactor physics analysis in support of this effort.

14.1.1 Core Design

Chapters 2 through 6 of this thesis deal with the design of the core and reactor vessel internals. The results of these studies are summarized in this section.

14.1.1.1 Motivation for High Fuel Volume Fraction and Inverted Fuel Geometry

Fast reactors are typically designed with conversion ratios greater than unity in order to achieve high burnup and thus high natural uranium resource utilization. In the past, this has been done by using natural uranium blankets, which produce significant amounts of plutonium with high ^{239}Pu content. From the standpoint of proliferation resistance, this is not a favorable practice since the plutonium could potentially be used to make nuclear weapons. The use of fertile blankets was therefore discarded for this design. In the absence of these blankets, a high fuel volume fraction (low coolant volume fraction) is necessary to boost the reactivity-limited burnup. A coolant volume fraction of 25% was selected as a goal for this design.

It is also desirable to use fuel which is chemically stable in CO_2. Carbide and nitride fuels, which are favorable neutronically due to their high heavy metal densities, are oxidized in CO_2 at the temperatures of present interest. Oxide fuel was therefore selected as the reference fuel form. The relatively low heavy metal density of oxide fuel further necessitates a high fuel volume fraction in the core.

Another factor motivating the use of low coolant volume fraction is the desire for low coolant void reactivity, which is typically positive in fast reactors. Having low coolant volume fraction reduces the spectral hardening which takes place upon voiding the coolant from the core, thus reducing the resulting reactivity increase.

In this work, the concept of "inverted" fuel geometry is used to denote an arrangement where fuel resides not in cylindrical pins surrounded by coolant, but rather surrounding cylindrical coolant channels. The most common example of an inverted geometry is the block-type fuel found in the HTGR or VHTR designs. It was shown that due to the inherent characteristics of inverted and pin-type fuel geometries, a given fuel temperature limit can be met using an inverted fuel geometry with a lower pressure drop than a conventional pin-type arrangement. As coolant volume fraction decreases, this difference is magnified. Use of inverted fuel geometry also eliminates the need for grid spacers, further reducing the pressure drop. The decrease in pressure drop resulting from using inverted fuel geometry becomes available in the clad and fuel temperature reduction tradeoff process. In the design of present interest, a high coolant mass flow rate and low coolant volume fraction make pressure drop a major constraint, thus pin-type fuel was discarded in favor of inverted fuel geometry.

14.1.1.2 Consideration of Matrix Fuel

Matrix fuel forms are essentially blocks of structural material having fuel dispersed within and coolant channels running through them. Fuel exclusion zones surrounding coolant channels provide a buffer between coolant and fuel. Matrix fuels can consist of ceramic fuel and matrix (cer-cer), ceramic fuel and metallic matrix (cer-met) or both metallic fuel and matrix (met-met). In early work by [Kaufmann, 1962], it was recommended that no more than 30% fuel by volume be used in matrix fuel so that it retains structural integrity during burnup. Previous studies at MIT concluded that in order to achieve sufficiently high burnup in a fast reactor using $(U,Pu)O_2$ fuel and no fertile blankets, approximately 60% fuel by volume or greater is necessary, thus precluding the use of matrix fuels in this design. [Pope, et. al., 2004]

14.1.1.3 Vented Tube-In-Duct Fuel Assembly

In order to achieve high fuel volume fraction with inverted-geometry fuel elements which would not be corroded excessively by high-temperature CO_2 and maintain structural integrity with burnup, a Tube-In-Duct (TID) fuel assembly was conceptualized. A TID fuel assembly consists of a hexagonal duct with coolant tubes inside. Fuel is placed around

coolant tubes and inside the hexagonal duct. Figure 14.1 shows a horizontal cross-sectional view of a TID fuel assembly. Figure 14.2 shows a vertical cross-sectional view of a TID fuel assembly with some of its features sketched schematically. This figure shows only one coolant tube whereas there actually would be many per assembly as is shown in Figure 14.1. Axial reflector and shielding materials are placed at the top and bottom of the assembly inside the same cell volume envelope as the fuel. Coolant enters the assembly from the bottom through a debris filter and flows into the coolant channels. Because some of the heat generated in the assembly will be transferred through the outer duct wall, a fraction of flow is diverted just before the coolant channels through holes in the duct wall to the outside of the duct.

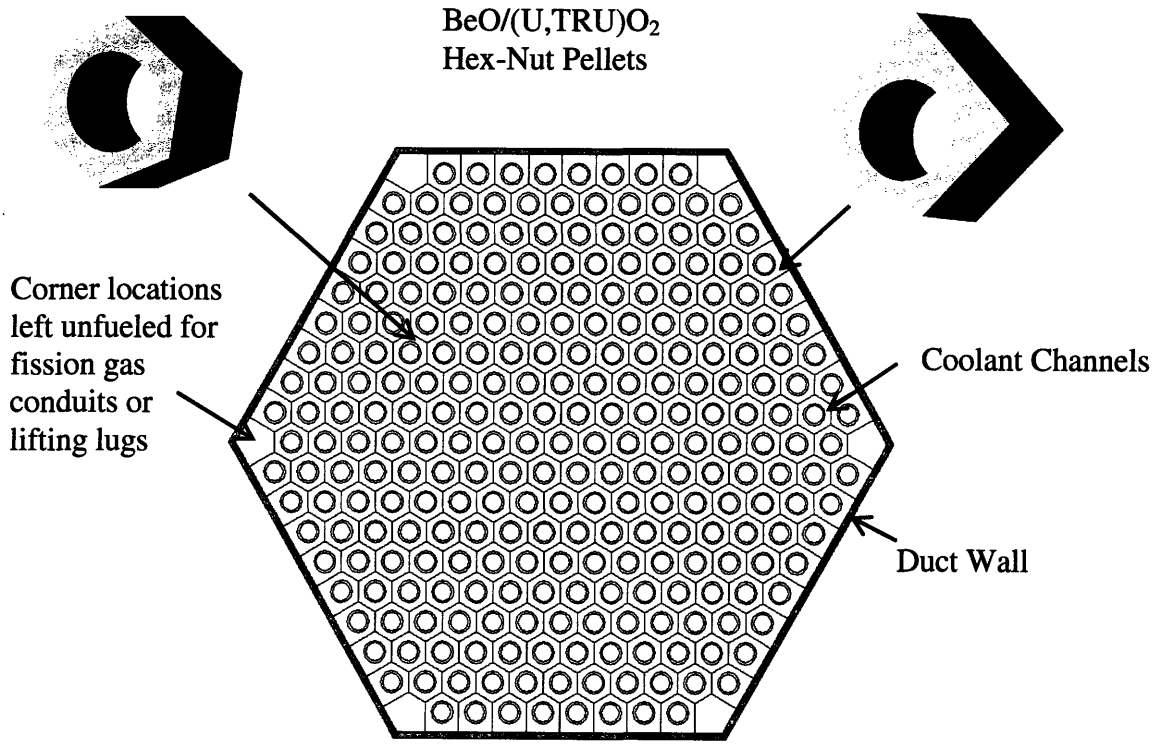

Figure 14.1. Horizontal cross-section view of TID fuel assembly.

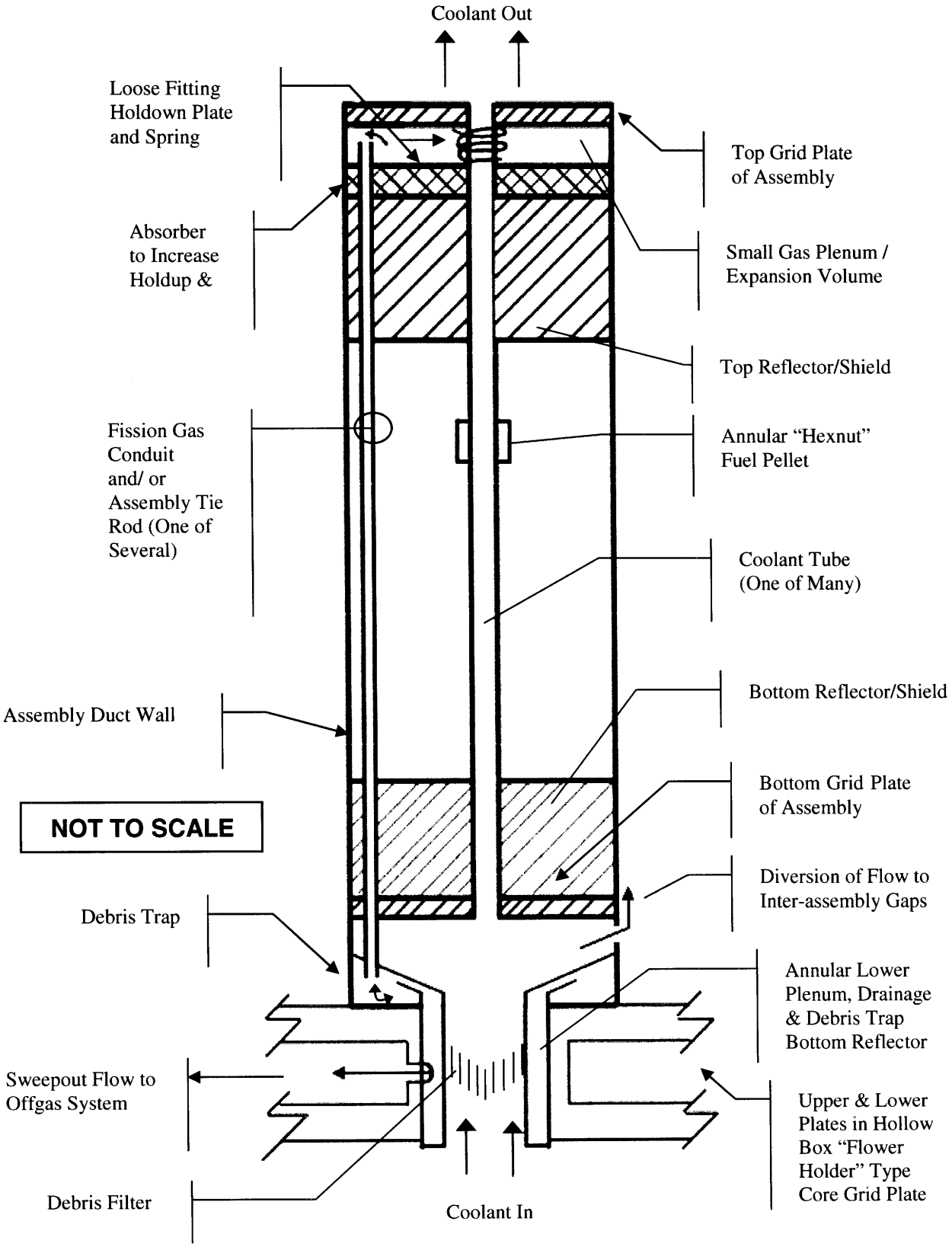

Figure 14.2. Vertical cross-section view of TID fuel assembly features.

The duct wall and the coolant tubes (cladding) are susceptible to pressure induced creep. The fueled region therefore must be vented to an offgas system to reduce wall stresses during steady state and LOCA conditions. A venting system similar to this was specified in the design of the General Atomics pin-type GCFR of the 1970's. [Capana, et. al., 1974] Vented fuel was also evaluated favorably for LMFBR service [O'Neill, et. al., 1965] and was used successfully on the Peach Bottom HTGR. [de Hoffmann, et. al., 1965] In addition to virtually eliminating wall stresses in the cladding and duct walls, venting the fuel region eliminates the need for a long fission gas plenum, which further reduces the core pressure drop.

Because the TID fuel assembly features a somewhat irregularly shaped fuel volume and must be capable of remote loading to allow for transuranic enrichment, use of VIPAC (or sphere-pac) fuel was a natural candidate. This fuel form could potentially offer some advantages such as small thermal resistance at the fuel-clad interface in addition to greater ease in remote fuel loading. However, due to uncertainty in the behavior of such fuel with the BeO diluent, its lower unsintered thermal conductivity and density, and the unusual geometry specified for this design, these fuel forms were not selected for the reference design, but rather left as possible alternatives to the "hex-nut" fuel conceptualized here.

Figure 14.1 shows how annular pellets having circular holes and hexagonal outer shapes (here called "hex-nut" pellets) can fit into the TID assembly. Peripheral pellets would have one flat side which would fit adjacent to the duct wall. Annular oxide fuel pellets have been successfully manufactured at Westinghouse as part of a NERI project. [Hejzlar, et. al., 2004] Manufacturing hex-nut pellets is expected to be possible by a similar process with an appropriately-shaped die.

14.1.1.4 Use of BeO Diluent in Fuel

BeO is specified for use as a diluent in the fuel for a number of reasons. If (U,TRU)O_2 fuel were to be used without this diluent, the reactor would exhibit a large high positive coolant void reactivity (in excess of $1). The radial power shape without diluent would change dramatically during a cycle and the reactivity swing would be very large, required a large number of high-worth control rods. It has been shown that addition of BeO

to the fuel matrix reduces coolant void reactivity and provides the means to flatten the radial power over a very long cycle. BeO also increases the critical enrichment which can lower the conversion ratio to just above unity, giving a relatively flat reactivity during core life and also reducing the reactivity hold-down burden on control rods. [Handwerk, et. al., 2006]

With an unusually high thermal conductivity for an oxide, BeO also has been shown to augment significantly the thermal conductivity of UO_2 pellets. Enhanced thermal conductivity oxide fuels have been developed by [Sarma, et. al., 2005] by pressing cylindrical pellets of UO_2 with a continuous BeO inert matrix. This fuel has exhibited a 50% higher thermal conductivity than ordinary UO_2 fuel with 10% BeO by volume present, an increase which was observed over a range of temperatures. [Solomon, 2005]

14.1.1.5 Core Parameters

Calculations were performed in order to determine how best to meet the relevant design limits while respecting the constraint of a 25% coolant volume fraction. Those limits were a peak clad surface temperature of 800°C, core pressure drop of 500 kPa and a peak fuel temperature of 1800°C. Though not a necessarily a hard constraint, keeping the core diameter to a minimum is also desirable as it directly impacts the size of the reactor vessel required. This was done using FLOWSPLIT, a parallel channel thermal hydraulic code written by [Hejzlar, 1994], modified to include the ability to calculate fuel temperatures.

Initially, the core power density was set to 100 kW/liter (similar to that of a present day PWR, but half that of the GFR designs of the 1970's) and two channels, hot and average, were assumed. Because the coolant volume fraction was set at 25%, the channel P/D was also set at 1.905. For a given core height, the core diameter which gave 24 m^3 of active core was calculated. Then, the channel pitch and diameter were varied while preserving P/D. For each case, the number of channels needed to given the proper coolant flow area was found (that giving 25% coolant) and the corresponding peak fuel and clad surface temperatures were calculated along with pressure drop. This process was repeated for a range of core H/D. The smallest core diameter which could be used to satisfy the above limits was determined. The result of this calculation was a set of parameters (core height and diameter, channel pitch

and diameter and number of coolant channels) which served as a baseline from which to construct a more realistic core.

The transition to a more realistic core involved addition of more flow channels in the modeling methodology. Spaces between the duct walls of adjacent fuel assemblies were accounted for and a preliminary estimate of the heat flux through the duct walls was made and included in the calculation. A core bypass channel was also added to represent coolant flow around radial shielding assemblies. Table 14-1 gives parameters of interest of the final core design. Note that the active core H/D is 0.32. Cores with low H/D values such as this one are referred to as "pancake" core designs, which are common in fast reactors. Pancake cores are used because the small core height gives a low pressure drop and because they have a higher surface area to volume ratios (thus higher leakage) than a configuration where the height and diameter are approximately equal (e.g. in a PWR). This leaky configuration lowers coolant void reactivity by providing a greater increase in leakage upon coolant voiding.

Figure 14.3 shows a horizontal cross section of the core, barrel and reactor vessel. Of the 397 assembly locations in the active core, 19 are reserved for control assemblies. The three rows of radial reflectors actually consist of a S-CO_2 "reflector" which provides additional enhanced neutron leakage upon voiding the coolant. The coolant is held in a near stagnant condition by orifices at the top of these assemblies. These channels are not accounted for in the thermal-hydraulic simulations, but play a major role in the neutronic behavior of the core. [Handwerk, et. al., 2006]

The power density in the final design is slightly lower than the 100 kW/liter which was originally assumed (the new value is 85.7 kW/liter if control assemblies are included and 90.0 if they are not). This is because the steel in the duct walls, the coolant between assemblies and the empty corner locations of the assemblies are now accounted for. Because these are not fueled regions, the power density is reduced without significantly affecting the specific power (in kW/kg HM), which is the more important parameter in determining the fuel cycle economics of the plant.

Table 14-1. Summary of parameters of active core.*

Parameter (units)	Value
Coolant Channels	
Inner diameter (mm)	7.0 (6.93)
Cladding thickness (mm)	0.7
Outer diameter (mm)	8.4 (8.32)
Channel pitch (mm)	13.3 (13.21)
Channel roughness (m)	$1x10^{-5}$
Lower inactive length (m)	1.1 (1.094)
Active length (m)	1.54 (1.530)
Upper inactive length (m)	1.0 (0.992)
Fuel Assembly Geometry	
Fueled locations per assembly	265
Unfueled locations per assembly (corners)	6
Duct wall flat-to-flat inner dimension (cm)	22.3 (22.1)
Duct wall thickness (mm)	2
Duct wall flat-to-flat outer dimension (cm)	22.7 (22.5)
Core Geometry	
Inter-assembly spacing (mm)	2.8 (5.0)
Fuel assemblies	378
Control assemblies	19
Reflector assembly locations	234
Shielding assemblies	288
Active core volume including control assemblies (m^3)	28.0
Active core effective diameter (m)	4.81
Active core H/D	0.32
Active core area including control assemblies (m^2)	18.2
Active core area excluding control assemblies (m^2)	17.3
Area Fractions (neglecting control assemblies)	
Coolant flow area (%)	24.7
Coolant in channels (%)	22.3
Coolant in inter-assembly gaps (%)	2.4
Steel (%)	13.2
Steel in coolant channel cladding (%)	9.8
Steel in duct walls (%)	3.4
Fuel (%)	59.6
Corner locations for vent tubes or lifting lugs (%)	2.5

* Hot dimensions are given with selected cold dimensions in parenthesis.

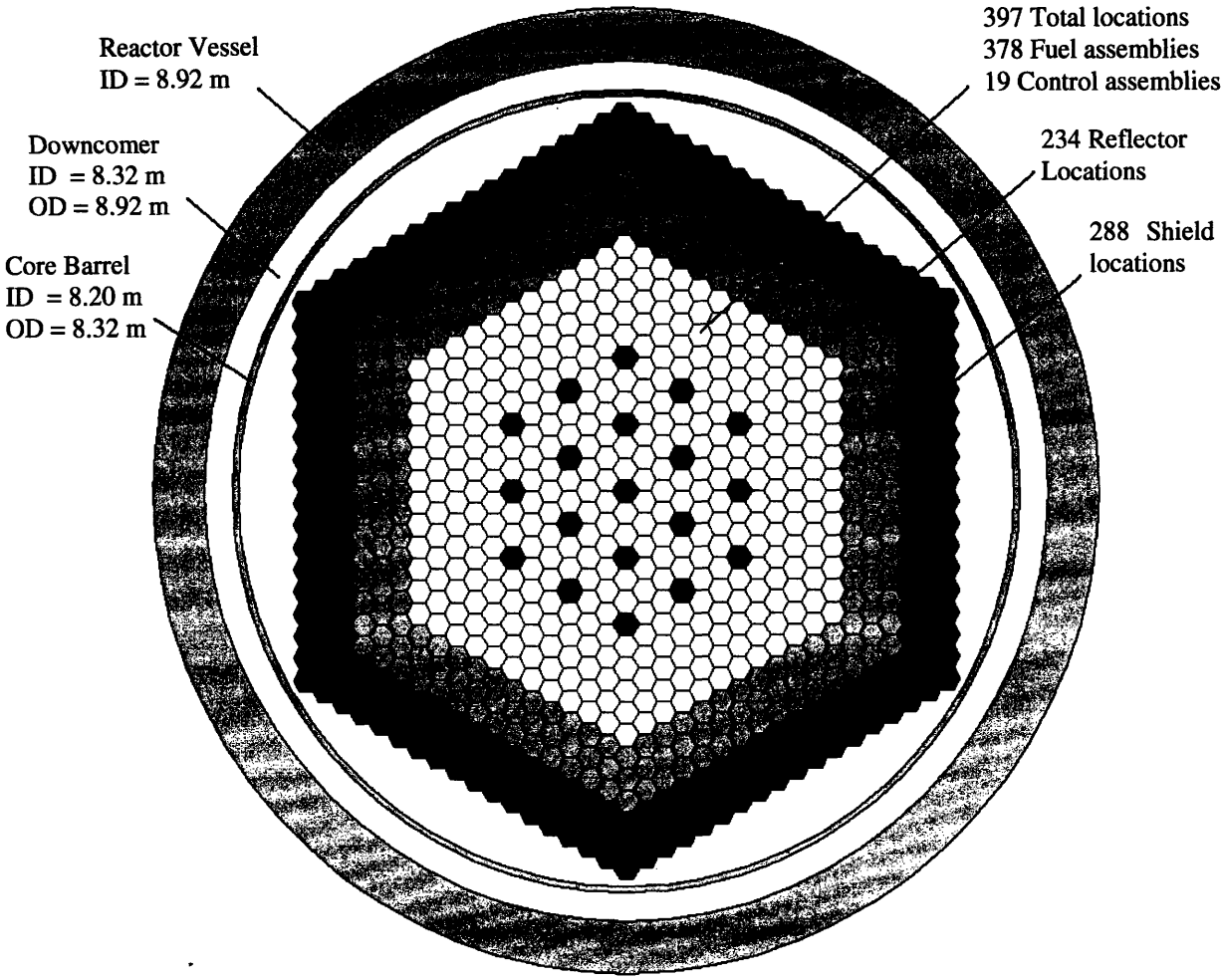

Figure 14.3. Horizontal cross-section view of core layout.

Because the reactor vessel inner diameter is rather large (8.92 m), as is the pressure which it must withstand (20 MPa), a prestressed cast iron vessel (PCIV) is specified for use in this design.

Figure 14.4 shows the steady-state full power radial temperature distributions in cladding and fuel calculated using RELAP, for hot and average channels at the axial location of peak fuel temperature. From this, it can be observed that the peak fuel temperature is close to the limit of 1800°C. This is because even with the augmentation provided by the BeO diluent, oxide fuel has a relatively low thermal conductivity, a characteristic which is

especially penalizing in a core with low coolant volume fraction. The pressure drop in the reference core design is also near the limit of 500 kPa.

Neither coolant channel orificing nor heat transfer augmentation is specified for this design because of the already-constraining pressure drop and fuel temperatures. If heat transfer augmentation were to be used, it would increase the pressure drop, which would have to be decreased by increasing the channel diameter (and thus pitch). This would increase fuel temperatures to beyond the limit since the lowering of the clad temperature which would result is small compared to the temperature rise across the fuel. Orificing is not specified in fueled channels at this point because the radial power peaking factor is kept quite low using the BeO diluent zoning. [Handwerk, et. al., 2006]

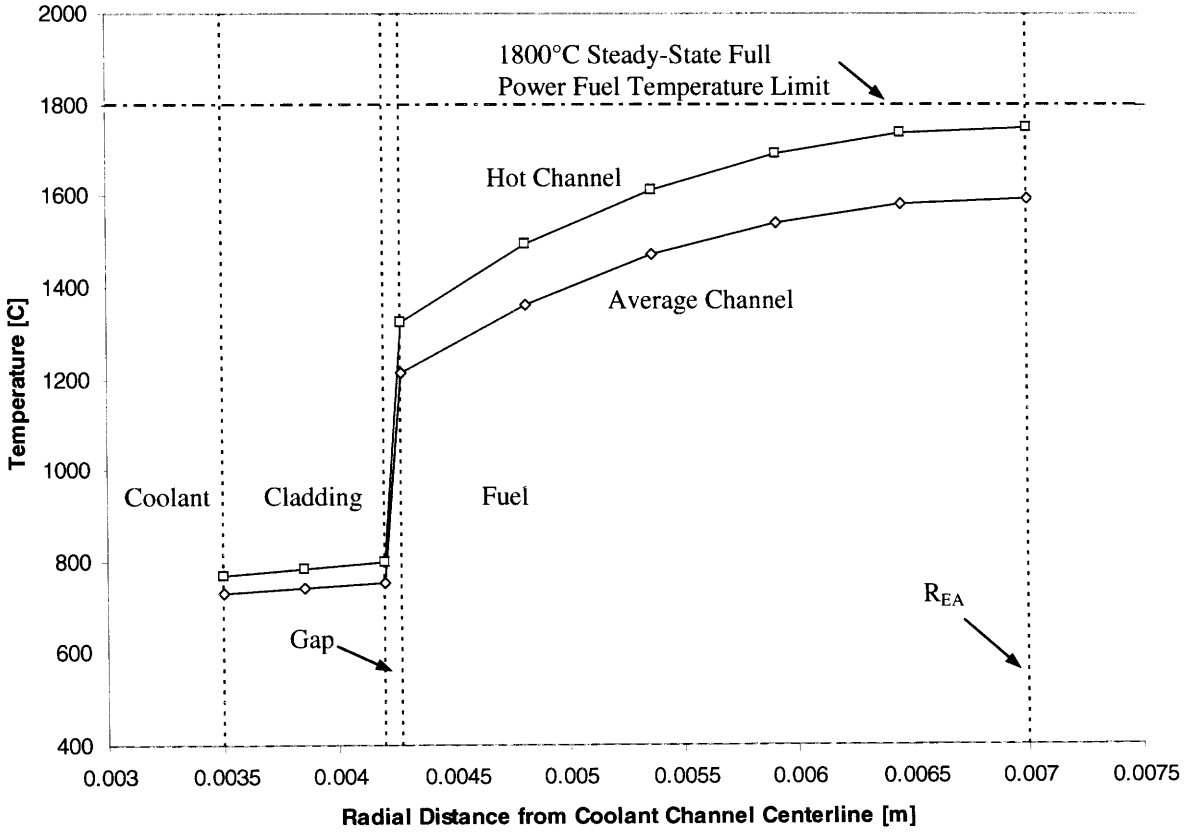

Figure 14.4. Steady-state full power radial temperature distributions in cladding and fuel calculated using RELAP for hot and average channels at the axial location of peak fuel temperature.

Table 14-2. Selected plant parameters.

Parameter (unit)	**Value**
Thermal Power (MW)	2400
Coolant Type	Supercritical CO_2
Coolant Peak Pressure (MPa)	20
Reactor T_{in} (°C)	485.5
ReactorT_{out} (°C)	650
Power Density [kW/liter core]	85
q''' [kW/liter fuel]	151
Cycle thermal efficiency [%]	50.8
Specific Power [kW/kg HM]	**20.7**
PCS loops	4 x 25%
Cladding material	ODS MA956
Reflector material	Titanium

14.1.2 Post-LOCA Core Bypass

In an earlier iteration of the design, the Shutdown/Emergency Cooling System (SCS/ECS) was a hybrid active/passive type having 4 loops, each capable of 50% decay heat removal (i.e. 4x50% or a 2 out of 4 system). During the course of an evaluation of the steady state natural circulation capabilities of this SCS/ECS, routes were identified by which coolant may bypass the core after a LOCA. This was shown to be capable of degrading natural circulation decay heat removal significantly depending on the size and type of the bypass route. The two bypass routes analyzed were through PCS duct breaks in which the hot and the cold legs are both breached (shown in Figure 14.5) and by reverse flow through the PCS loops once the turbomachinery has stopped. In the case of core bypass flow via PCS loops, all four loops without isolation valves and with turbomachinery stopped provide a relatively small resistance to flow and thus give rise to a large bypass mass flow rate (~19% of total SCS/ECS flow). Implementation of reliable isolation valves would eliminate this route of core bypass. If isolation valves are not used or have malfunctioned, active cooling using modestly-sized blowers can provide adequate decay heat removal to the core. Operation of PCS startup motors also can prevent this bypass mechanism from occurring.

In the case of a break in both the hot and cold legs of a PCS duct, the percent of flow which bypasses the core is dependent primarily on the pipe break size and shape and is relatively insensitive to total system mass flow rate. This was shown to be true whether free or forced circulation is employed. The use of a reliable and appropriately-sized active system can provide sufficient core cooling even in the extreme case of the maximum possible break sizes (entire flow area of both hot and cold ducts) without excessive power demand.

The exclusion of these routes of core bypass without more knowledge of these mechanisms is difficult to defend. Natural circulation cooling may be aided by increasing the height of the convection loop or increasing the backup pressure, but these means are not cost effective, and a maximum credible bypass has not been identified at this time. On the other hand, relying on blowers capable of delivering mass flow rates of interest here would result in a modest cost penalty since blowers were already specified in the hybrid active/passive decay heat removal system. In the remainder of this work, it was therefore recommended that an active decay heat removal system with highly reliable blowers be specified. Since active decay heat removal will be relied upon, this removes the need for the extended heights of the decay heat removal loops. Decay heat removal heat exchangers could therefore be placed inside the reactor vessel along with the blowers. In the main text, the design of this type of active SCS/ECS is presented.

Another course of action which could be pursued is the limitation of duct break size, for example by clamping strongbacks onto the PCS ducts with circumferential rib cages. Instrumentation to detect leaks before breaks should also be provided. As noted earlier, reliable isolation valves are a high priority system design goal. It should also be noted that a break in both the hot and cold leg of a PCS duct is probably more severe than would be considered credible. It is nonetheless concluded that there is sufficient uncertainty in the occurrence of various bypass routes to warrant further examination.

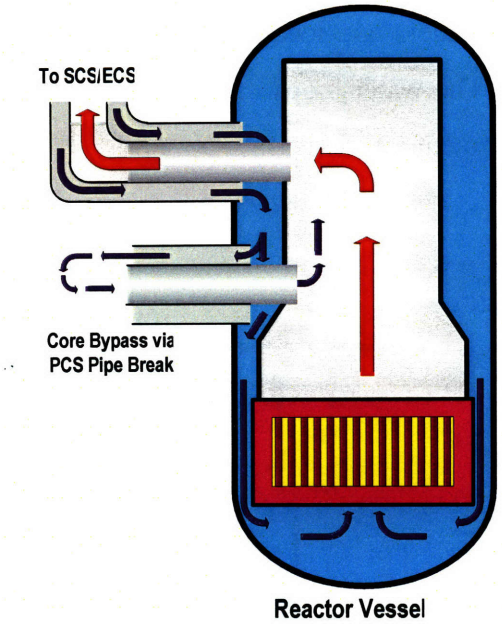

Figure 14.5. Post-LOCA core bypass through pipe break in both hot and cold legs.

14.1.3 Description of Reference Design

The reference design arrived at in this work is briefly summarized in this section. Figure 14.6 shows a schematic of its features. There are four PCS loops attached to the reactor vessel with coaxial ducts. Although a vertical integrated PCS loop is shown in this diagram and is used in this work, a horizontal dispersed arrangement is likely to be adopted in future work.

14.1.3.1 Description of Active SCS/ECS

In the upper left corner of Figure 14.6, an SCS/ECS heat exchanger is shown attached to the side of the upper core barrel. This represents one of several Heatric® PCHE's arranged around the cylindrical barrel. When the SCS/ECS is functioning, hot CO_2 from the core enters the PCHE's and is cooled by counterflow with water as it moves toward the reactor vessel wall. After exiting the PCHE, the CO_2 turns downward and encounters a blower, followed by a check valve. The check valve is held shut by the core ΔP under normal operating conditions. The heat exchanger sizes are the same as were specified in the active/passive hybrid design inherited from previous work at MIT [Williams, et. al., 2004],

only now fitted with different headers and located inside the reactor vessel rather than in a loop with an extended height. The water loops carry heat to the ultimate heat sink, a spray pond located outside the containment.

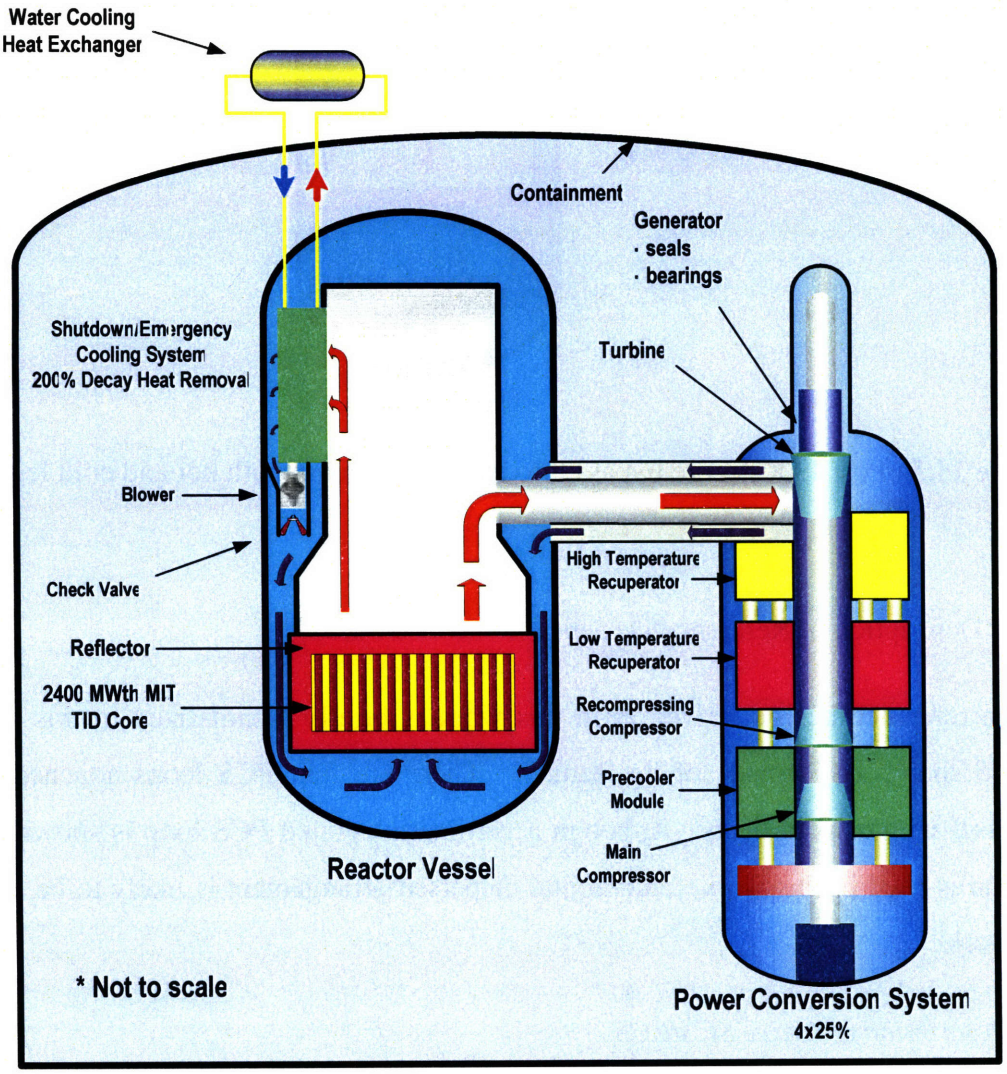

Figure 14.6. Layout of plant with active SCS/ECS.

14.1.3.2 RELAP Model of Reference Design

Figure 14.7 shows a RELAP nodalization diagram of the reactor, vessel and PCS loops; the SCS/ECS is omitted from this figure. The PCS loops are represented by a single 25% loop which is shown on the left side of the figure and a lumped 3x25% loop which is

shown on the right. Transients which are initiated in a single PCS, such as a LOCA or a LOF, are assumed to occur in the single loop and the behavior of all of the remaining three loops is assumed to be identical. The containment volume is shown in the upper left corner of the figure (volume 900). The valves connecting the coaxial duct of the single PCS to this volume are fast-acting RELAP motor valves used to simulate breaks.

Detailed axial compressor performance curves were initially used in RELAP to represent main and recompressing compressors. Because of the relatively narrow band of operation of axial compressors, however, the need for transient simulations necessitated the use of homologous pump models to approximate the compressors. This allowed simulations to continue running though the compressors may have reached a surge or choke condition. In later work, not only should protection be designed to prevent choking or surging, but radial compressors should be pursued, as they have a wider band of operation.

All of the recuperators and precoolers are assumed to be vertical counter-flow heat exchangers. This is a simplification since the actual flow in these Heatric® PCHE's is more complicated than this. The cold side of the precooler is a water stream which enters at 20°C.

A nodalization diagram of the SCS/ECS and its attachments to the core downcomer and chimney are shown in Figure 14.8. Note that, as indicated in Figure 14.7, 100% decay heat removal capacity is modeled in the SCS/ECS due to the assumption that half of the 200% capable SCS/ECS is not operational.

Before steady state shutdown cooling or transient calculations were performed, the steady state performance of the RELAP model was compared to design values, showing excellent agreement.

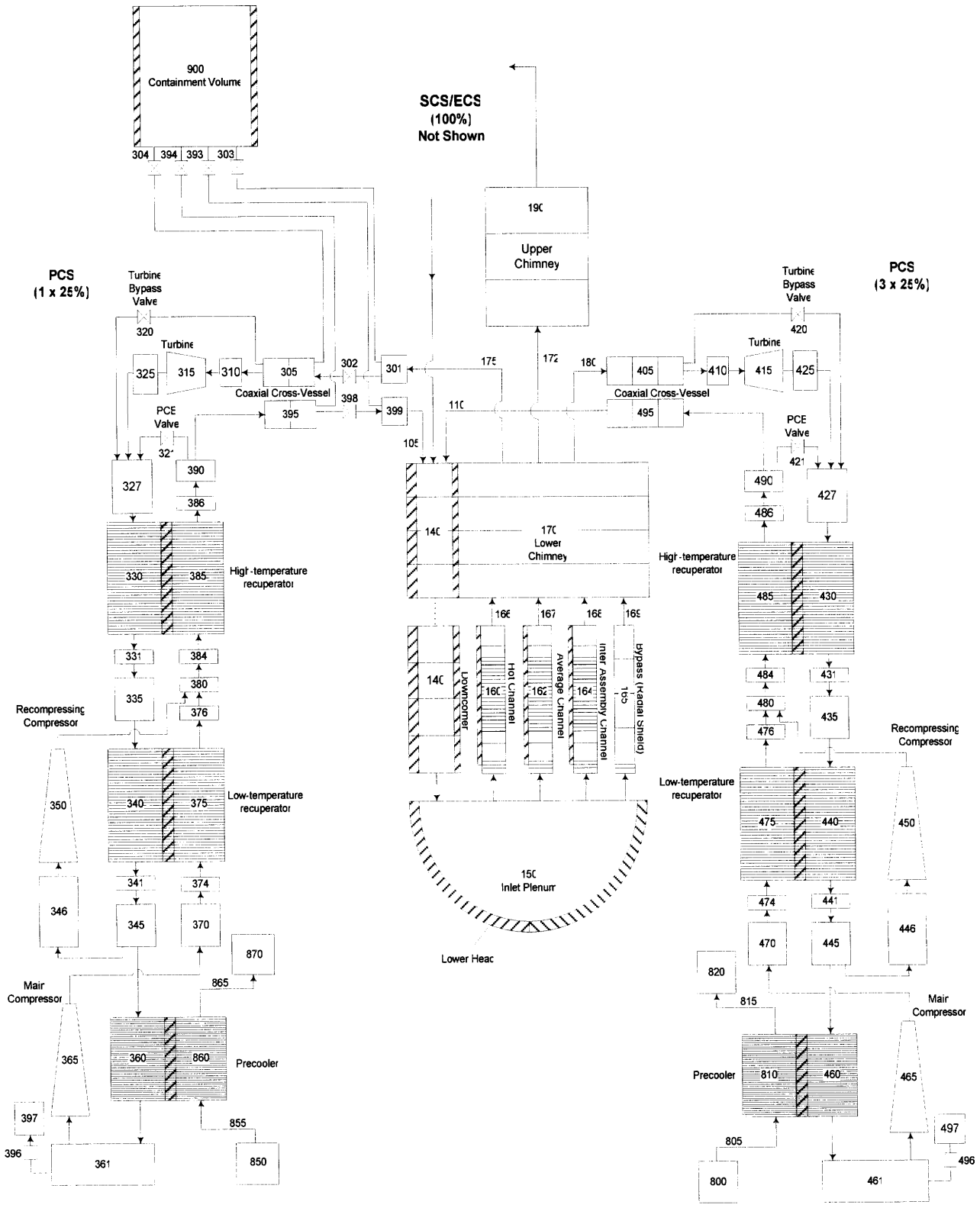

Figure 14.7. Nodalization diagram for RELAP model with SCS/ECS omitted.

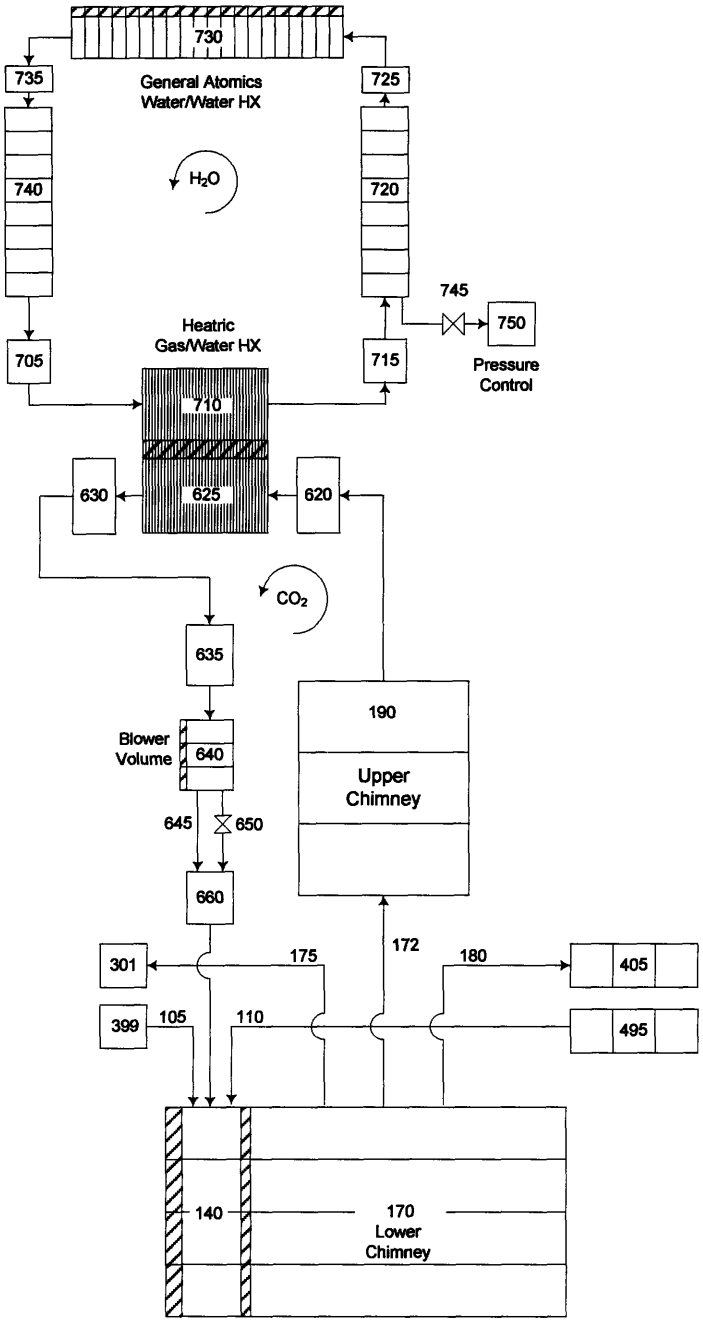

Figure 14.8. Nodalization diagram for RELAP model of SCS/ECS.

14.1.3.3 Steady State Demand for Active Cooling

Although the reference design has an active SCS/ECS, it is still capable of some natural circulation decay heat removal at elevated pressure. The steady state demand for active cooling was mapped using the RELAP model of the reference design. Figure 14.9

shows the reactor power removable by natural circulation versus backup pressure (points with a regression line) assuming that no coolant bypasses the core, but only half of the SCS/ECS is operational. Above the line, blower-driven circulation is required to cool the core, whereas below the line, natural circulation is sufficient. The dashed line on the figure shows decay power versus time past shutdown of the reactor.

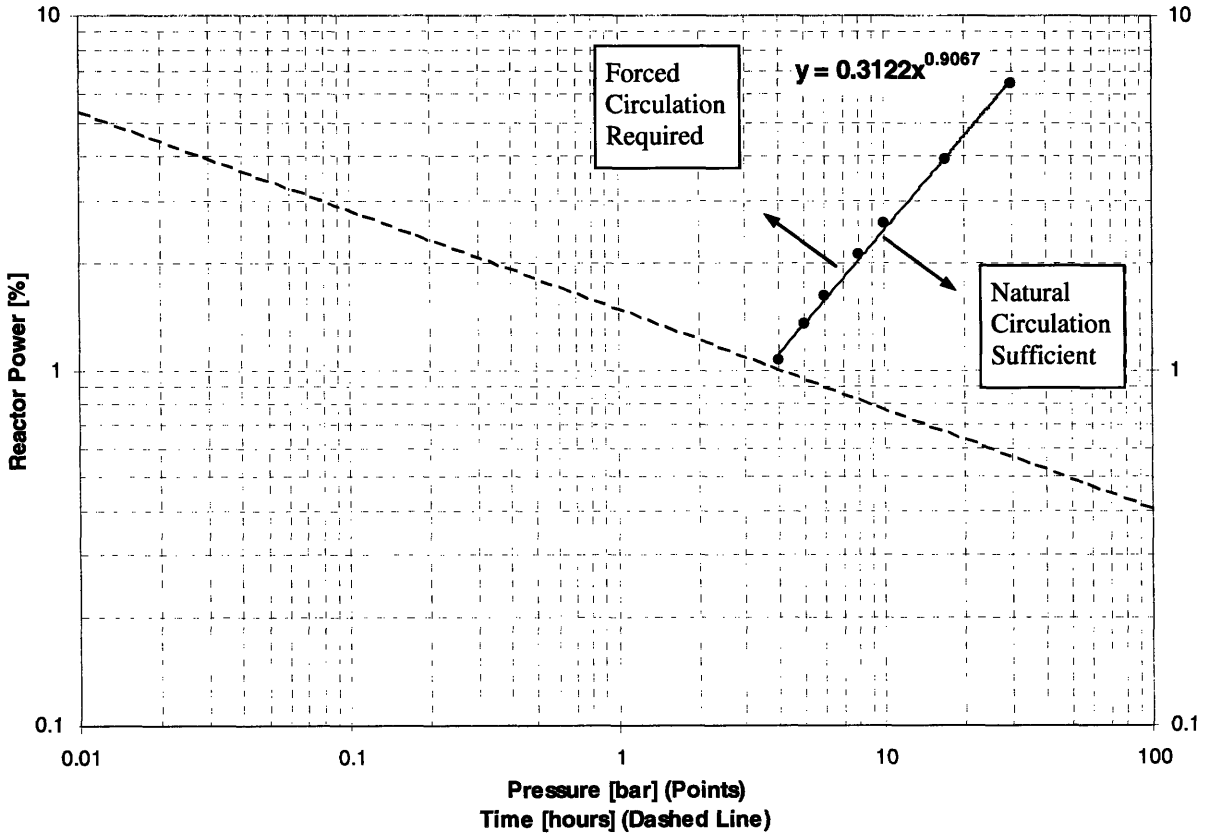

Figure 14.9. Reactor power which can be removed by natural circulation versus pressure (points with line fit) and decay power versus time (dashed line).

14.1.4 Transient Analyses of Final Design

14.1.4.1 Loss of External Load

In the loss of external load (LOEL) transient, the generator becomes decoupled from the electrical grid. This removes the large negative torque on the generator, causing rapid acceleration of the shaft. Fast-acting bypass valves are used in order to prevent shaft over-

speed and damage to turbomachinery. Because the turbomachinery is smaller in gas cycles than that of steam Rankine cycles, this transient is particularly challenging due to the small moments of inertia of components attached to the shafts. S-CO_2 turbomachinery is even smaller than helium turbomachinery, and so the LOEL transient is even more challenging in this design. A conventional turbomachinery shaft overspeed limit of 20% was set for this work.

Methods of mitigating an LOEL event were investigated. The first method was placement of a fast-acting valve connecting the flow which is about to return from the PCS to the reactor vessel to the turbine exhaust. This is here called a power cycle bypass (PCB) valve and is shown in Figure 14.7 (valves 321 and 421). The PCB valves, when sized to be just large enough to arrest the shaft acceleration before reaching the 20% overspeed limit, produced a flow reversal in the core followed by near-stagnation resulting in rapid overheating of the core. The opening of the PCB valves also caused a sudden decrease in pressure in the downcomer region, opening the SCS/ECS check valves. This is an unfavorable result because if the blowers do not come on, the SCS/ECS becomes a route by which coolant circulated by the compressors as the shaft spins down may bypass the core, accelerating the heat up of the cladding.

The other bypass valve location evaluated provided a connection, when opened, between the turbine inlet and exhaust. This direct turbine bypass, also shown in Figure 14.7 (valves 320 and 420) was evaluated as well, with mixed results. Usually discarded for helium gas-cooled reactor applications due to the exposure of the bypass valves to coolant at the core outlet temperature, turbine bypass may be feasible in the cooler S-CO_2 (650°C) environment. The core mass flow rate, rather than stagnating as in the PCB case, increased by more than twofold following the opening of the turbine bypass valves. This is an unacceptably large core flow rate. Turbine bypass does, however, have the advantage of not causing the SCS/ECS valves to come open.

Accordingly, the recommended scheme for mitigating an LOEL event is a combined bypass scheme wherein both the turbine bypass valves and PCB valves are opened, the PCB valves having a slightly slower opening rate. The combined opening of the two valves

arrests the acceleration of the shaft before reaching the 20% overspeed limit. Opening the turbine bypass valve first ensures that the SCS/ECS check valves will not open and prevents the large flow reversal in the core as in the case of the PCB valves alone. The delayed PCB valve opening provides an alternate route for coolant in order to keep the mass flow rate in the core to less than 150% of the nominal value during the transient. The combined bypass scheme can also be used to reduce the thermal shock to the high temperature recuperator during the LOEL event since the PCB valves allow cooler CO_2 to mix with the hot CO_2 from the turbine bypass valves. Smaller valves residing in smaller pipes can also be used with the combined bypass scheme than in either the turbine bypass or the PCB valves alone, since it is their combined flow which reduces the shaft acceleration.

14.1.4.2 Loss of Coolant Accident

The LOCA is generally considered to be the most severe accident, particularly in gas-cooled reactors where the rate of coolant inventory loss is larger than in liquid-cooled reactors. The break analyzed in this work is a 100 in^2 (645 cm^2) break located in the cold leg of a PCS duct. The 100 in^2 break size is the same as that assumed for the GA GCFR. The break is simulated using a motor valve (valve 394 in Figure 14.7). In the final design, reliable PCS isolation valves will be used in order to quickly shut off the flow to a PCS loop which experiences a break. In this work, however, it was assumed that the isolation valve in the broken loop had failed and the system was allowed to blow down to equilibrium with the containment. The reactor underpressure scram setpoint was 19.5 MPa in the inlet plenum and the generator trip and combined bypass were set to begin at the same time as the scram.

Calculations were performed in order to determine an appropriate containment size for the design of present interest. With a containment having a free volume of 70,000 m^3, the peak pressure during the blowdown was found to be 6 bar. This volume and peak pressure could be accommodated by a large dry PWR containment, and so this type of containment was adopted for the present design.

Figure 14.10 shows the pressure in the core inlet plenum and the containment volume versus time following a 100 in^2 cold leg break. This shows that the primary system depressurization is quite slow. Coolant flows through the core during this time, first as a

result of the turbomachinery as the shafts spin down to a stop. Natural circulation then moves sufficient coolant to avoid overheating the cladding while the pressure is still somewhat high. No action is required of the SCS/ECS for at least 10 minutes following the break. At ten minutes following the break, the SCS/ECS blowers were activated. The blowers are modeled as a RELAP time dependent junction, and so a mass flow rate is prescribed which will provide sufficient cooling (determined approximately from the results of steady state calculations) and the blower power required is calculated assuming an efficiency of 85%. Figure 14.11 shows SCS/ECS blower mass flow rate versus time following the LOCA on the right-hand axis and calculated blower power versus time on the left-hand axis. Figure 14.12 shows peak clad surface temperature versus time following the LOCA. The point along the line indicates where the SCS/ECS blowers were turned on. This shows that a relatively low blower power < 90 kW is required to keep the clad surface temperature below the 1200°C limit.

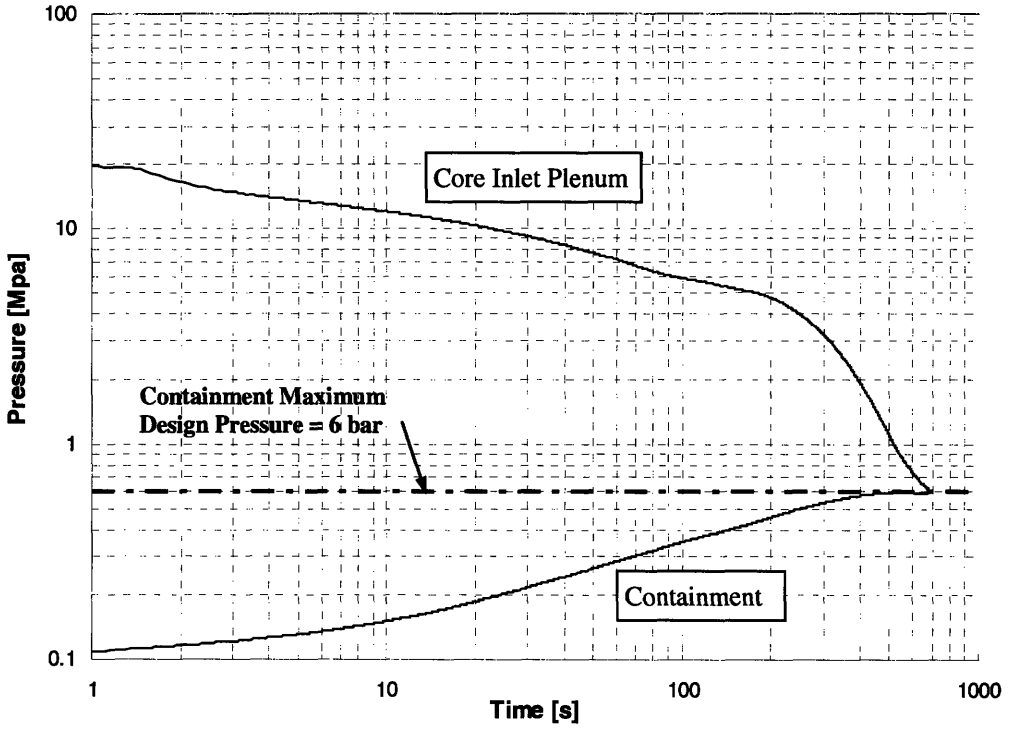

Figure 14.10. Pressure in core inlet plenum and containment building versus time following a 100 in^2 break in a cold leg.

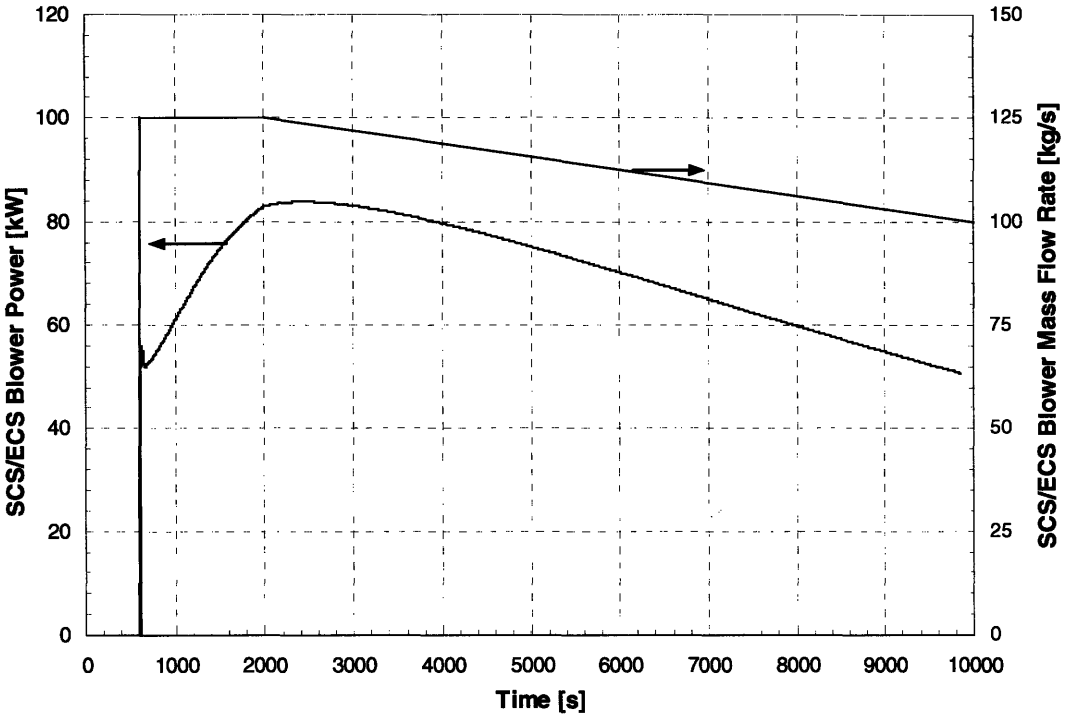

Figure 14.11. SCS/ECS blower mass flow rate and power versus time.

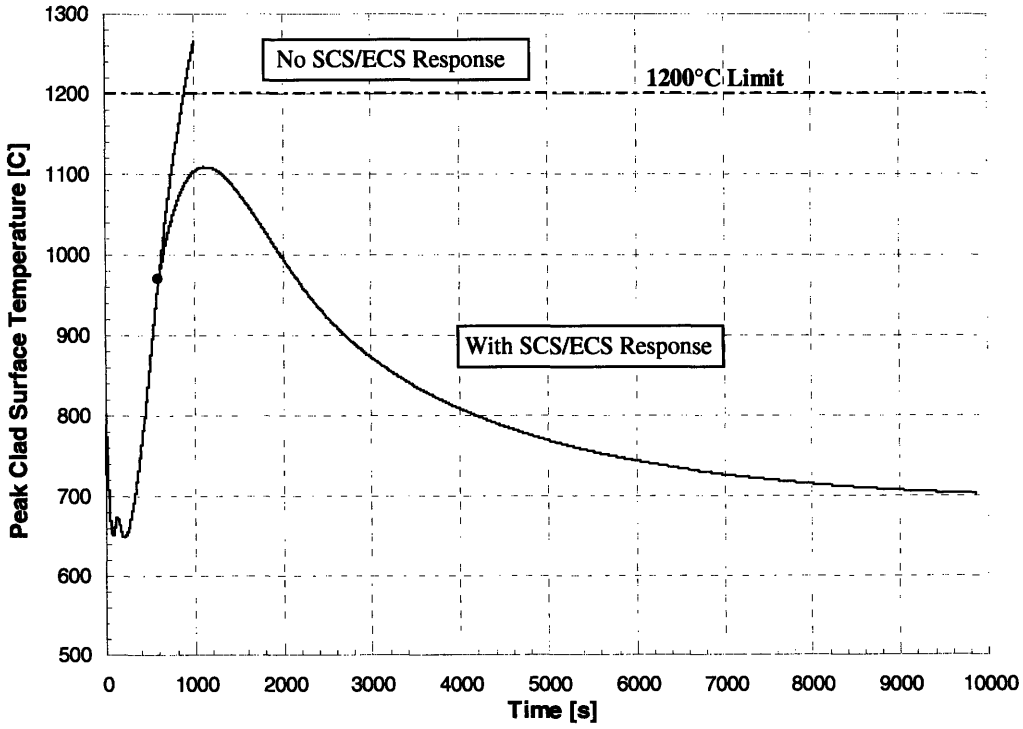

Figure 14.12. Peak clad temperature versus time with and without blower function 10 minutes after a 100 in^2 cold leg break.

14.1.4.3 Loss of Flow Transient

In general, a loss of flow (LOF) transient is a sudden loss of coolant flow in the core such that the power/flow ratio increases and the core heats up unless some action is taken. In water-cooled reactors, LOF transients can be initiated by circulating pump failures of various kinds. In the S-CO_2 direct cycle where turbomachinery is on a single shaft, an LOF could occur as a result of damage to a compressor or a shaft seizure.

In the 4-loop arrangement of the GFR under investigation here, isolation valves will be included in order to seal individual PCS loops in case of a serious fault. For example, in the case of a LOCA in one of the PCS loops, the isolation valves to that loop should close immediately upon its detection, suddenly decreasing core flow by 25%. After the isolation of the PCS loop, the rest of the system will function independent of it. Isolation valve closure could also be initiated inadvertently even if no PCS loops are faulted. In this case, the analysis does not change significantly from that of a small break LOCA or other fault in which the response of the system is relatively slow. Therefore, isolation valve closure alone envelopes other transients involving faults in PCS loops so long as the valves are assumed to function as designed.

An LOF transient was analyzed in which one of the four PCS loops was suddenly isolated from the rest of the plant at full power. The core flow rate decreases almost instantaneously to approximately 75% of its nominal value and then increases slowly due to the lowered core pressure drop. The core inlet and outlet temperatures increase over the first few hundred seconds following the LOF, approaching new steady state values. The peak clad surface temperature also increased to a new steady state value of approximately 1000°C as is shown in Figure 14.13. This shows that in the event of an LOF event such as this, there is no immediate threat of core damage and there is sufficient time for mitigating action to be taken either automatically or by an operator (e.g. reactor power ramp down or scram).

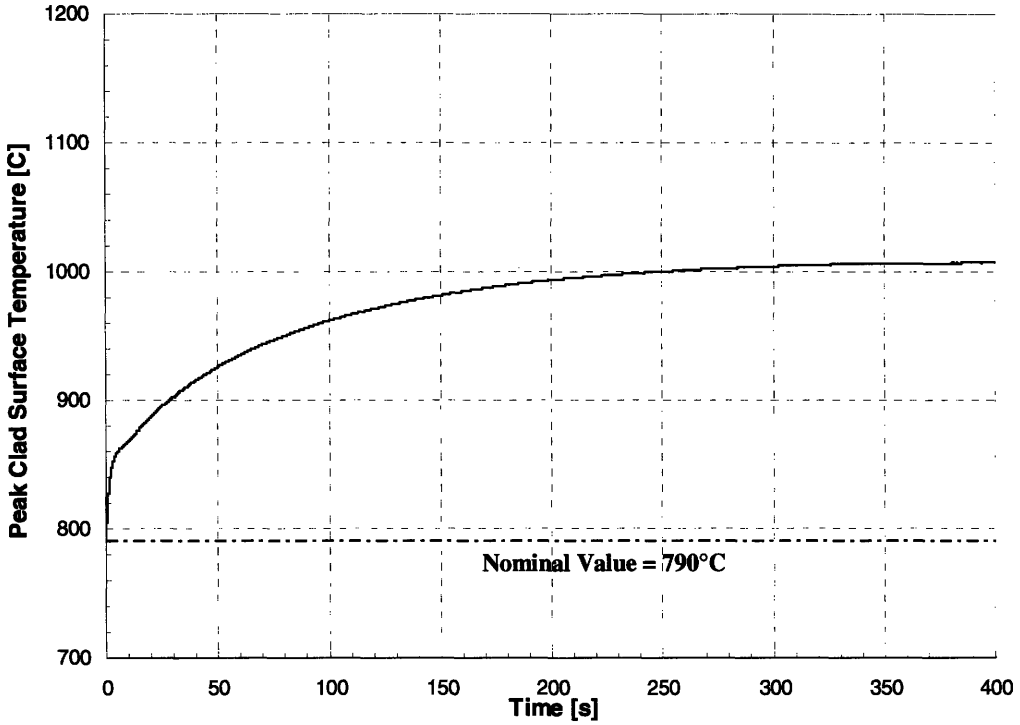

Figure 14.13. Peak clad surface temperature versus time following PCS isolation valve closure from a full power steady state condition.

14.2 Conclusions

The design of a four loop, 2400 MW_{th} direct S-CO_2 cooled fast reactor has been advanced in this work based on thermal hydraulic analyses. In order to accommodate the unique operating conditions and design constraints presented in this design, an innovative Tube-In-Duct fuel assembly was conceptualized. This fuel assembly shows promise in providing a corrosion resistant interface with the S-CO_2 coolant while allowing high enough fuel volume fraction to reach high burnup without fertile blankets. The fuel form in the reference design is a BeO/(U,TRU)O_2 blend pressed into pellets having a hex-nut shape which fits into the TID fuel assemblies.

A core design was developed which satisfies limits on peak clad surface temperature, peak fuel temperature and core pressure drop while maintaining the relatively low coolant volume fraction of approximately 25%.

During the course of evaluating the steady state natural circulation decay heat removal capability of a hybrid active/passive SCS/ECS, routes were identified by which coolant may bypass the core after a LOCA, degrading decay heat removal. This was shown to be true independent of whether coolant circulation was free or forced. Depending on the size and type of these bypass routes, the reactor power and the primary system pressure, natural circulation decay heat removal could be eliminated as a viable cooling method by these bypass routes. Moderately-sized SCS/ECS blowers were shown to be effective at providing sufficient cooling in even the most extreme cases of post-LOCA core bypass. An active SCS/ECS with reliable blowers was thus adopted as the means of decay heat removal in the reference design.

For mitigation of the LOEL transient, a combined bypass scheme was recommended which consists of two valve locations on each PCS loop. The combined effect of these valves opening in response to an LOEL is such that the core coolant mass flow rate does not exceed 150% its nominal value, the acceleration of the shaft is arrested before reaching 20% overspeed and the clad temperatures do not increase in an unacceptable way.

A 100 in^2 break in a cold PCS duct was used to determine a suitable containment size and type for this reactor. Results showed that a large dry PWR containment with free volume of 70,000 m^3 and a peak pressure of 6 bar is well suited to the 2400 MW_{th} S-CO_2 cooled GFR. However, the pressure did not appear to be decreasing fast enough to meet the requirement of being reduced to half the peak value after 24 hours, which is a typical regulatory requirement for this type of containment. This should be evaluated further in future work.

The depressurization time in the event of a 100 in^2 break was shown to be quite long (about 10 minutes) and SCS/ECS blower function was not required before this time. After this time, the blower power requirement was shown not to exceed 90 kW at any time during the 10,000 seconds analyzed.

A LOF transient was simulated where an entire PCS loop is shut off from the rest of the plant from a full power condition. This resulted in a near-instantaneous 25% reduction in core mass flow rate, followed by a slow increase due to the lowered core pressure drop. The

core inlet and outlet temperatures increased over the first few hundred seconds following the LOF, approaching new steady state values. The peak clad surface temperature also increased to a new steady state value of approximately 1000°C. This indicated that in the event of an LOF event such as this, there is no immediate threat of core damage and there is sufficient time for mitigating action to be taken either automatically or by an operator (e.g. reactor power ramp down or scram).

The 2400 MW_{th} direct S-CO_2 cooled fast reactor performs well in the accidents and transients evaluated in this work. Overall, this design shows promise as a next generation nuclear power plant.

14.3 Recommendations for Future Work

The basic concept of the TID fuel assembly was introduced and some of dimensions and features were determined in this work. Much remains in producing a detailed design for this assembly type, which is left for future work. This should include a more detailed procedure for manufacturing the assemblies and design of the fission gas venting system. In the design of the venting system, sufficiently slow release of radionuclides to the offgas system should be ensured.

Because the fuel type specified for this design is relatively new, significant data is not readily available related to its thermal conductivity. Furthermore, in the TID fuel assembly, its behavior with burnup may not be predictable. In this work, conservatism was used in lieu of precise data for similar fuel (i.e. BeO/(U,TRU)O_2 in hex-nut pellets or VIPAC in a TID fuel assembly at high burnup). While the fuel thermal conductivity does not significantly affect any of the transient analyses performed in this work, it will in the case of reactivity-initiated transients. The question of whether VIPAC fuel would be useable should be revisited in future work as more relevant data becomes available.

In this work, detailed compressor performance curves were provided for axial compressors. These curves were then used in the RELAP model in order to establish the steady state full power condition. For the transient analyses, however, the compressor models were replaced with a homologous pump representation in order to allow the

simulations to continue after compressors would have surged or choked. Although preliminary estimates of radial CO_2 compressor performance curves have been made by [Gong, et. al., 2006], more work is required in this area. Also, once the compressors are modeled in a more realistic way, a system should be devised which protects them from the surge and choke conditions.

In this work, SCS/ECS blowers were simulated using RELAP time dependent junctions and the power required was estimated assuming a constant efficiency. The question of what will supply the modest power required by these blowers is an open issue which should be addressed in future work. Other project researchers have evaluated the use of fuel cells in lieu of and in addition to conventional diesel engines.

The PCIV specified for this design has very large side penetrations for connections to the coaxial PCS ducts. Any large penetration like this creates a zone where axial and radial pre-stressing tendons cannot be located. The structural integrity of the specified design should be examined more carefully in future work.

In this work, a combined bypass scheme was developed which prevents shaft overspeed and overheating the core. This is done by opening the two valve types and leaving them open for the remainder of the simulation. An actual plant would have a sophisticated control system which adjusts the stem position of these two valves to keep the shafts spinning longer than if the valves were simply left open. A control system for these valves should be developed in future work.

The PCS layout was assumed to be vertical and integrated in this work. Currently, work is ongoing to design a horizontally dispersed version. This could have an impact on the LOCA if the volumes of the pipes are significantly different. This is because the CO_2 densities in the PCS are large and small changes in these volumes could significantly impact the primary system inventory. If major changes in the PCS take place, LOCA analyses should be repeated with the new design.

References

Capana, R.J., and J.R. Lindgren, "Irradiation Testing of Design Models for the GCFR Fuel Pressure Equalization (Vent) System," *Nuclear Engineering and Design*, **26**, p. 201 (1974).

Chauvin, N., J.C. Garnier, J.L. Seran and P. Brossard, "Requirements for Fuel and Structural Materials of Gas Cooled Fast Reactors," *Proceedings of ICAPP '03*, May 4-7 (2003).

de Hoffmann, F. and C.L. Rickard, "High Temperature Gas-Cooled Reactors," *Proceedings. of the 3rd ICPUAE*, Vol. 5 (1965).

de Podesta, M., *Understanding the Properties of Matter*, Taylor and Francis, 1996.

Dostal, V., M.J. Driscoll, and P. Hejzlar, "A Supercritical Carbon Dioxide Cycle for Next Generation Nuclear Reactors," MIT-ANP-TR-100, March 2004.

Dostal, V., P. Hejzlar and M.J. Driscoll, "High-Performance Supercritical Carbon Dioxide Cycle for Next-Generation Nuclear Reactors," *Nuclear Technology*, **154**, No. 3, June (2006).

Dostal (b), V., P. Hejzlar and M.J. Driscoll, "The Supercritical Carbon Dioxide Cycle: Comparison to Other Advanced Power Cycles," *Nuclear Technology*, **154**, No. 3, June (2006).

Driscoll, M.J. and P. Hejzlar, "Reactor Physics Challenges in Gen-IV Reactor Design," Nuclear Engineering and Technology, **37**, No. 1, February (2005).

Eaton, T.E., D.D. Lanning, N.E. Todreas, "Gas-Cooled Breeder Reactor Fuel Element Thermal-Hydraulic Investigations," *MITNE-172,* August (1975).

Fishkin, L.B., "Prestressed Cast Iron Vessel (PCIV) Use for Gen-IV GFR Applications," MIT-GFR-006, April (2004).

Garnier, J.C., N. Chauvin, P. Anzieu, G. Francois, T.Y.C. Wei, T. Taiwo, M. Meyer, P. Hejzlar, H. Ludewig and A. Baxter, "Feasibility Study of an Advanced GFR, Design Trends and Safety Options, Status of France and U.S. Studies," *Proceedings of GLOBAL 2003*, November 16-20 (2003).

Gavrilas, M., P. Hejzlar, N.E. Todreas and Y. Shatilla, *Safety Features of Operating Light Water Reactors of Western Design*, CRC Press, Inc., 1995.

General Atomic Company, "Gas-Cooled Fast Breeder Reactor Preliminary Safety Information Document: Amendment 10," *GA-10298*, September (1980).

Gezelius, K., M.J. Driscoll, P. Hejzlar, "Design of Compact Intermediate Heat Exchangers for Gas Cooled Fast Reactors," MIT-ANP-TR-103, May (2004).

Gilbreath, J.R. and O.C. Simpson, "The Effect of Reactor Irradiation on the Physical Properties of Beryllium Oxide," *2nd U.N. International Conference on the Peaceful Uses of Atomic Energy*, P/621 (1958).

Gnielinski, V., "New Equations for Heat and Mass Transfer in Turbulent Pipe and Channel Flow," *Forschung im Ingenieurwesen* 41, No. 1, Federal Republic of Germany, 1975. Reprinted in *International Chemical Engineering: Translations of the Best in Chemical Engineering*, April 1976.

Gong, Y., N.A. Carstens, M.J. Driscoll and I.A. Matthews, "Analysis of Radial Compressor Options for Supercritical CO_2 Power Conversion Cycles," MIT-GFR-034, June (2006).

Handwerk, C.S., M.J. Driscoll, P. Hejzlar, P. Yarsky, and M.A. Pope, "Power Shaping of a Long-Lived GFR Core Using Diluents," *Transactions of the American Nuclear Society*, **93**, Nov. 13-17 (2005).

Handwerk, C.S., M.J. Driscoll, P. Hejzlar, "Use of Beryllium Oxide to Shape Power and Reduce Void Reactivity in Gas Cooled Fast Reactors," *Proceedings of PHYSOR '06*, Sept. 10-14 (2006).

Handwerk (b), C.S., Personal Communication, July 2, 2006.

Hankel, R. "Stress and Temperature Distributions," *Nucleonics*, **18**, No. 11, November (1960).

Hejzlar, P., "Conceptual Design of a Large, Passive, Pressure-Tube Light Water Reactor," Sc.D. Thesis, Massachusetts Institute of Technology, May (1994).

Hejzlar, P., D. Feng, Y. Yuan, M. S. Kazimi, H. Feinroth, B. Hao, E. J. Lahoda, and H. Hamilton, "The Design and Manufacturing of Annular Fuel for High Power Density and Improved Safety in PWRs", *2004 International Meeting on LWR Fuel Performance*, Orlando, Florida, September 19-22 (2004).

Hejzlar, P., S.J. Kim and W.C. Williams, "Transient ATHENA/RELAP-3D Calculations for a 600 MW_{th} Plate-Type Helium GFR," MIT-GFR-026, April (2005).

Hejzlar, P., V. Dostal and M.J. Driscoll, "A Supercritical CO_2 Cycle- a Promising Power Conversion System for Generation IV Reactors," *Proceedings of ICAPP '06*, Paper #6307, Reno, NV, June 4-8 (2006).

Hickman, B.S., and A.W. Pryor, *Journal of Nuclear Materials*, **14**, pp. 96-110 (1964).

Holden, A.N., *Dispersion Fuel Elements*, Gordon and Breach, New York, NY (1967).

Idelchik, I.E., *Handbook of Hydraulic Resistance: 3rd Ed.*, CRC Press, Boca Raton, FL (1993).

INL, Idaho National Laboratory website, *www.inl.gov/gen4/gfr.shtml*, 2006.

INL (b), Idaho National Laboratory, "RELAP3-3D© Code Manual," INEEL-EXT-98-00834, Rev. 2.3, April (2005).

Jourdan, G. and M. Golay, "Using Risk-Based Regulations for Licensing Nuclear Power Plants: Case Study of the Gas-Cooled Fast Reactor," MIT-ANP-TR-106, December (2004).

Kaufmann, A.R., *Nuclear Reactor Fuel Elements: Metallurgy and Fabrication*, Interscience Publishers, New York, NY (1962).

Kreith, F. and M.S. Bohn, *Principles of Heat Transfer, 4th Ed.*, pp. 628, Harper and Row (1986).

Lee, B., Y. Koo, J. Cheon, J. Oh, and D. Sohn, "A Unified Thermal Conductivity Model of LWR MOX Fuel Considering its Microstructural Characteristics," *Journal of Nuclear Science and Technology*, Supplement 3, pp. 705-708, 2002.

Ligrani, P.M., and M.M. Oliveira, "Comparison of Heat Transfer Augmentation Techniques," AIAA Journal, **41**, No. 3, March (2003).

Ligrani, P.M., N.K. Burgess and S.Y. Won, "Nusselt Numbers and Flow Structure on and Above a Shallow Dimpled Surface Within a Channel Including Effects of Inlet Turbulence Intensity Level," *Journal of Turbomachinery*, **127**, pp. 321, April (2005).

O'Neill, G.E. et. al., "A Technical and Economic Evaluation of Vented Fuel for Sodium-Cooled Fast Ceramic Reactors," GEAP-4770, May 1965.

Pope, M.A., P. Yarsky, M.J. Driscoll, P. Hejzlar, and P. Saha, "An Advanced Vented Fuel Assembly Design for GFR Application," *Trans. Am. Nuc. Soc.*, **92**, June 5-9 (2003).

Pope, M.A., M.J. Driscoll, P. Hejzlar, "Reactor Physics Design of Supercritical CO_2-Cooled Fast Reactors," MIT-ANP-TR-10, September (2004).

Pryor, A.W., R.J. Tainsh and G.K. White, "Thermal Conductivity at Low Temperature of Neutron-Irradiated BeO," *Journal of Nuclear Materials*, **14**, pg. 208-209 (1964).

Ravets, J.M. and J.M. Tobin, "The Very High Temperature Reactor for Process Heat," *Transactions of the American Nuclear Society*, **22**, November (1975).

Ravigururajan, T.S. and A.E. Bergles, "Development and Verification of General Correlations for Pressure Drop and Heat Transfer in Single-Phase Turbulent Flow in Enhanced Tubes," *Experimental and Fluid Science*, **13**, pg. 55-70 (1996).

Ribeiro, A.A.T., "Flow Orificing in Nuclear Power Reactors," S.M. Thesis, Massachusetts Institute of Technology, May (1974).

Rohsenow, W.M., J.P. Hartnett and Y.I. Cho, "*Handbook of Heat Transfer, 3rd ed.*," McGraw-Hill, New York (1998).

Sarma, K.H., J. Fourcade, S-G Lee and A.A. Solomon, "New Processing Methods to Produce Silicon Carbide and Beryllium Oxide Inert Matrix and Enhanced Thermal Conductivity Oxide Fuels," *E-MRS*, Strasbourg, France, May 31-June 3 (2005).

Schilling, F.E., B. Beine and H. Gross, "The Prestressed Cast-Iron Pressure Vessel: Its Applicability for Gas and Water Cooled Nuclear Power Reactors and for Impact Load Protection, *2nd International Conference on Structural Mechanics in Reactor Technology (SMiRT-2)*, Berlin, Germany, September 10-14 (1973).

Smith, R., "The Development of Beryllia-Based Fuels for HTGC Reactor Systems," *3rd U.N. International Conference on the Peaceful Uses of Atomic Energy*, Geneva, pp.543, September (1964).

Solomon, A.A., Personal Communication, October 19, 2005.

Special Metals, Inc., Publication number SMC-008, September (2004).

Stacey, S.M., *Proving the Principle*, DOE/ID-10799, Idaho Operations Office of the Department of Energy, Idaho Falls, ID (2000).

U.S. DOE, "A Technology Roadmap for Generation IV Nuclear Energy Systems: Ten Nations Preparing Today for Tomorrow's Energy Needs," U.S. DOE Nuclear Research Advisory Committee (NERAC) and the Generation IV International Forum, GIF-002-00, December (2002).

Todreas, N.E. and M.S. Kazimi, *Nuclear Systems I: Thermal Hydraulic Fundamentals*, Hemisphere Publishing Corporation, New York, NY, 1990.

Waltar, A.E. and A.B. Reynolds, Fast Breeder Reactors, Pergamon Press, New York, 1981.

Wang, Y., G. Guenette Jr., P. Hejzlar and M.J. Driscoll, "Supercritical CO_2 Turbine and Compressor Design," MIT-GFR-015, June (2004).

Williams, W.C., P. Hejzlar, and P. Saha, "Analysis of a Convection Loop for GFR Post-LOCA Decay Heat Removal," ICONE12-49360, *Proc. of ICONE12*, Arlington, VA, April 25-29 (2004).

Yildiz, B., K.J. Hohnholt and M.S. Kazimi, "Hydrogen Production Using High-Temperature Steam Electrolysis Supported by Advanced Gas Reactors with Supercritical CO_2 Cycle," *Nuclear Technology*, **155**, July (2005).

Zigrang, D.J., and N.D. Sylvester, "A Review of Explicit Friction Factor Equations," *Transactions of ASME, Journal of Energy Resources Technology*, 107, 1985, pp. 280-283.

Appendix A

The following is a listing of input for the hydrodynamic volumes which comprise the core (volumes 160, 162, 164 and 165). These are given because the handling of the inlet to the channels is somewhat complicated to convey using a simple table as was done with other parts of the model.

```
*---- ----1---- ----1---- ----1---- ----1---- ----1---- ----1---- ----1---- ----1----
* Fuel hot channel  (265 channels represent 1 hot assembly)
*---- ----1---- ----1---- ----1---- ----1---- ----1---- ----1---- ----1---- ----1----
*hydro    name      type
1600000   hotchan   pipe
*HYDRO    VOLS
1600001   27
*HYDRO    AREA      VOL
1600101   2.2698E-2   1        * flow area for 17 cm dia. hole in lower plate
1600102   4.1920E-2   2        * just after lower core plate and before channels
1600103   1.01984E-2  27        * flow area for 265 7mm diameter channels
*HYDRO    LEN       VOLS
1600301   0.2         1          * 0.2  m passage through core lower plate
1600302   0.1         2          * 0.1  m expanded area before channels
1600303   0.1         3          * 0.1  m lower TID ass'y plate
1600304   0.6         4          * 0.6  m lower shield
1600305   0.4         5          * 0.4  m lower reflector
1600306   0.077      25          * 1.54 m core
1600307   0.4        26          * 0.4  m upper reflector
1600308   0.6        27          * 0.6  m upper shield
*HYDRO    VOL       VOLS
1600401   0.0       27
*HYDRO    AZIM      VOLS
1600501   0.0       27
*HYDRO    VERT      VOL
1600601   90.0      27
*HYDRO    ROUGH     Dh        VOL
1600801   45.e-6   0.170       1     * del = 45 um
1600802   45.e-6   0.215       2     * del = 45 um
1600803   10.e-6   0.007      27     * del = 10 um
*HYDRO    Kf       Kr     jun
1600901   1.0     0.5      1
1600902   0.1     1.0      2
1600903   0.0     0.0     26
*HYDRO    TLPVBFE   VOL
1601001     11000   27
*HYDRO    JEFVCAHS  JUNC
1601101     000000  26
*HYDRO    EBT       PRES       TEMP       0.0        0.0        0.0      VOLS
1601201   0         20019022. 809297.    809297.    1.         0.       1
1601202   0         20017158. 809287.    809287.    1.         0.       2
1601203   0         19984614. 809155.    809155.    1.         0.       3
1601204   0         19954418. 809294.    809294.    1.         0.       4
1601205   0         19911236. 809258.    809258.    1.         0.       5
1601206   0         19890374. 814528.    814528.    1.         0.       6
1601207   0         19883188. 821344.    821344.    1.         0.       7
1601208   0         19875846. 829525.    829525.    1.         0.       8
1601209   0         19868328. 838952.    838952.    1.         0.       9
1601210   0         19860640. 849503.    849503.    1.         0.       10
1601211   0         19852782. 860999.    860999.    1.         0.       11
1601212   0         19844756. 873287.    873287.    1.         0.       12
1601213   0         19836568. 886188.    886188.    1.         0.       13
1601214   0         19828228. 899486.    899486.    1.         0.       14
1601215   0         19819744. 913048.    913048.    1.         0.       15
1601216   0         19811132. 926609.    926609.    1.         0.       16
1601217   0         19802404. 939965.    939965.    1.         0.       17
```

```
1601218   0          19793576. 952933.   952933.   1.        0.      18
1601219   0          19784666. 965312.   965312.   1.        0.      19
1601220   0          19775690. 976926.   976926.   1.        0.      20
1601221   0          19766670. 987586.   987586.   1.        0.      21
1601222   0          19757620. 997143.   997143.   1.        0.      22
1601223   0          19748564. 1005452.  1005452.  1.        0.      23
1601224   0          19739524. 1012374.  1012374.  1.        0.      24
1601225   0          19730514. 1017806.  1017806.  1.        0.      25
1601226   0          19703598. 1017960.  1017960.  1.        0.      26
1601227   0          19647494. 1018073.  1018073.  1.        0.      27
*HYDRO    VEL/FLW
1601300   0
*HYDRO    F_FLW      G_FLW     J_FLW     JUNC
1601301   8.96084    8.96084   0.        1  * 27.6809
1601302   19.94506   19.94506  0.        2  * 27.6809
1601303   19.97137   19.97137  0.        3  * 27.6809
1601304   20.0034    20.0034   0.        4  * 27.6809
1601305   20.04254   20.04254  0.        5  * 27.6809
1601306   20.21507   20.21507  0.        6  * 27.6809
1601307   20.41986   20.41986  0.        7  * 27.6809
1601308   20.6646    20.6646   0.        8  * 27.6809
1601309   20.94514   20.94514  0.        9  * 27.6809
1601310   21.25402   21.25402  0.        10 * 27.6809
1601311   21.59027   21.59027  0.        11 * 27.6809
1601312   21.94717   21.94717  0.        12 * 27.6809
1601313   22.31834   22.31834  0.        13 * 27.6809
1601314   22.70096   22.70096  0.        14 * 27.6809
1601315   23.0857    23.0857   0.        15 * 27.6809
1601316   23.4709    23.4709   0.        16 * 27.6809
1601317   23.84697   23.84697  0.        17 * 27.6809
1601318   24.2114    24.2114   0.        18 * 27.6809
1601319   24.55876   24.55876  0.        19 * 27.6809
1601320   24.88264   24.88264  0.        20 * 27.6809
1601321   25.1811    25.1811   0.        21 * 27.6809
1601322   25.44873   25.44873  0.        22 * 27.6809
1601323   25.6814    25.6814   0.        23 * 27.6809
1601324   25.8773    25.8773   0.        24 * 27.6809
1601325   26.03344   26.03344  0.        25 * 27.6809
1601326   26.0709    26.0709   0.        26 * 27.6809
*HYDRO    J_DYD      FLD       INTCPT    SLOPE     JUNC
1601401   0.0        0.0       1.0       1.0       26   *
*
*
*---- ----1---- ----1---- ----1---- ----1---- ----1---- ----1---- ----1----
* Fuel average channel (377 fuel assemblies)
*---- ----1---- ----1---- ----1---- ----1---- ----1---- ----1---- ----1----
*hydro    name       type
1620000   avechan    pipe
*HYDRO    VOLS
1620001   27
*HYDRO    AREA       VOL
1620101   8.5571E+0   1      * 377 17cm diameter holes in lower plate
1620102   15.800E+0   2      * again same as average channel
1620103   3.8448E+0   27     * 377x265=99905 channels with 7mm diameter
*HYDRO    LEN        VOLS
1620301   0.2         1           * 0.2  m passage through core lower plate
1620302   0.1         2           * 0.1  m expanded area before channels
1620303   0.1         3           * 0.1  m lower TID ass'y plate
1620304   0.6         4           * 0.6  m lower shield
1620305   0.4         5           * 0.4  m lower reflector
1620306   0.077       25          * 1.54 m fueled core height
1620307   0.4         26          * 0.4  m upper reflector
1620308   0.6         27          * 0.6  m upper shield
*HYDRO    VOL        VOLS
1620401   0.0        27
*HYDRO    AZIM       VOLS
1620501   0.0        27
*HYDRO    VERT       VOL
1620601   90.0       27
*HYDRO    ROUGH      Dh        VOL
1620801   45.e-6     0.170       1      * del = 45 um
```

```
1620802   45.e-6   0.215       2     * del = 45 um
1620803   10.e-6   0.007      27     * del = 10 um
*HYDRO    Kf       Kr      jun
1620901   1.0    0.5       1
1620902   0.1    1.0       2
1620903   0.0    0.0      26
*HYDRO    TLPVBFE   VOL
1621001     11000   27
*HYDRO    JEFVCAHS  JUNC
1621101     000000   26
*HYDRO    EBT       PRES       TEMP       0.0        0.0        0.0      VOLS
1621201   0         20018858.  809296.    809296.    1.         0.       1
1621202   0         20016962.  809286.    809286.    1.         0.       2
1621203   0         19983776.  809152.    809152.    1.         0.       3
1621204   0         1.9953+7   809293.    809293.    1.         0.       4
1621205   0         19908976.  809256.    809256.    1.         0.       5
1621206   0         19887734.  813782.    813782.    1.         0.       6
1621207   0         19880478.  819652.    819652.    1.         0.       7
1621208   0         19873084.  826697.    826697.    1.         0.       8
1621209   0         19865538.  834810.    834810.    1.         0.       9
1621210   0         19857838.  843888.    843888.    1.         0.       10
1621211   0         1.985+7    853786.    853786.    1.         0.       11
1621212   0         1.9842+7   864355.    864355.    1.         0.       12
1621213   0         19833850.  875453.    875453.    1.         0.       13
1621214   0         19825574.  886903.    886903.    1.         0.       14
1621215   0         19817170.  898551.    898551.    1.         0.       15
1621216   0         19808650.  910227.    910227.    1.         0.       16
1621217   0         19800028.  921708.    921708.    1.         0.       17
1621218   0         19791318.  932853.    932853.    1.         0.       18
1621219   0         19782534.  943506.    943506.    1.         0.       19
1621220   0         19773694.  953484.    953484.    1.         0.       20
1621221   0         19764810.  962645.    962645.    1.         0.       21
1621222   0         19755904.  970868.    970868.    1.         0.       22
1621223   0         1.9747+7   978008.    978008.    1.         0.       23
1621224   0         19738090.  983957.    983957.    1.         0.       24
1621225   0         19729218.  988625.    988625.    1.         0.       25
1621226   0         19702616.  988772.    988772.    1.         0.       26
1621227   0         19647128.  988881.    988881.    1.         0.       27
*HYDRO    VEL/FLW
1621300   0
*HYDRO    F_FLW     G_FLW     J_FLW     JUNC
1621301   9.04927   9.04927   0.        1  * 10538.55
1621302   20.14177  20.14177  0.        2  * 10538.55
1621303   20.16887  20.16887  0.        3  * 10538.55
1621304   20.20185  20.20185  0.        4  * 10538.55
1621305   20.24215  20.24215  0.        5  * 10538.55
1621306   20.39493  20.39493  0.        6  * 10538.55
1621307   20.57405  20.57405  0.        7  * 10538.55
1621308   20.78793  20.78793  0.        8  * 10538.55
1621309   21.0335   21.0335   0.        9  * 10538.55
1621310   21.3043   21.3043   0.        10 * 10538.55
1621311   21.59776  21.59776  0.        11 * 10538.55
1621312   21.91094  21.91094  0.        12 * 10538.55
1621313   22.23632  22.23632  0.        13 * 10538.55
1621314   22.57024  22.57024  0.        14 * 10538.55
1621315   22.91015  22.91015  0.        15 * 10538.55
1621316   23.2464   23.2464   0.        16 * 10538.55
1621317   23.57733  23.57733  0.        17 * 10538.55
1621318   23.8982   23.8982   0.        18 * 10538.55
1621319   24.20233  24.20233  0.        19 * 10538.55
1621320   24.48814  24.48814  0.        20 * 10538.55
1621321   24.7513   24.7513   0.        21 * 10538.55
1621322   24.98607  24.98607  0.        22 * 10538.55
1621323   25.19153  25.19153  0.        23 * 10538.55
1621324   25.3646   25.3646   0.        24 * 10538.55
1621325   25.50283  25.50283  0.        25 * 10538.55
1621326   25.5391   25.5391   0.        26 * 10538.55
*HYDRO    J_DYD     FLD       INTCPT    SLOPE     JUNC
1621401   0.0       0.0       1.0       1.0       26   *
*
*
```

```
*---- ----1---- ----1---- ----1---- ----1---- ----1---- ----1---- ----1----
* Fuel Inter-assembly channel (heated by HS-5004)
*---- ----1---- ----1---- ----1---- ----1---- ----1---- ----1---- ----1----
*hydro    name      type
1640000   Intr-asy   pipe
*HYDRO    VOLS
1640001   27
* because the pressure drop is dominated by form pressure losses at the
* diversion to inter-assembly flow and friction in the flow between assemblie,
* the first two areas listed are arbitrarily chosen to give little resistance
* to flow.  The third area and its form loss coefficient are the significant
* numbers.
*HYDRO    AREA      VOL
1640101   2.00E+0   1      * not meaningful
1640102   2.00E+0   2      * not meaningful
1640103   0.41912  27      * total active core interassembly flow area
*HYDRO    LEN       VOLS
1640301   0.2        1           * 0.2  m passage through core lower plate
1640302   0.1        2           * 0.1  m expanded area before channels
1640303   0.1        3           * 0.1  m lower TID ass'y plate
1640304   0.6        4           * 0.6  m lower shield
1640305   0.4        5           * 0.4  m lower reflector
1640306   0.077     25           * 1.54 m fueled core height
1640307   0.4       26           * 0.4  m upper reflector
1640308   0.6       27           * 0.6  m upper shield
*HYDRO    VOL       VOLS
1640401   0.0       27
*HYDRO    AZIM      VOLS
1640501   0.0       27
*HYDRO    VERT      VOL
1640601   90.0      27
*HYDRO    ROUGH     Dh        VOL
1640801   45.e-6   0.100       1     * del = 45 um
1640802   45.e-6   0.215       2     * del = 45 um
1640803   45.e-6   0.005635   27     * del = 45 um
*HYDRO    Kf       Kr      jun
1640901   1.0     0.5       1
1640902  25.0    25.0       2
1640903   0.0     0.0      26
*HYDRO    TLPVBFE   VOL
1641001     11000   27
*HYDRO    JEFVCAHS  JUNC
1641101     000000   26
*HYDRO    EBT       PRES       TEMP       0.0        0.0        0.0      VOLS
1641201   0         20026740. 809340.    809340.    1.         0.       1
1641202   0         20026186. 809337.    809337.    1.         0.       2
1641203   0         19819310. 808206.    808206.    1.         0.       3
1641204   0         19801328. 808287.    808287.    1.         0.       4
1641205   0         19775686. 808264.    808264.    1.         0.       5
1641206   0         19763400. 811957.    811957.    1.         0.       6
1641207   0         19759334. 816724.    816724.    1.         0.       7
1641208   0         19755226. 822445.    822445.    1.         0.       8
1641209   0         19751066. 829034.    829034.    1.         0.       9
1641210   0         19746852. 836389.    836389.    1.         0.       10
1641211   0         19742586. 844424.    844424.    1.         0.       11
1641212   0         19738264. 853007.    853007.    1.         0.       12
1641213   0         19733886. 862003.    862003.    1.         0.       13
1641214   0         19729452. 871284.    871284.    1.         0.       14
1641215   0         19724964. 880743.    880743.    1.         0.       15
1641216   0         19720424. 890202.    890202.    1.         0.       16
1641217   0         19715834. 899501.    899501.    1.         0.       17
1641218   0         19711198. 908548.    908548.    1.         0.       18
1641219   0         19706522. 917178.    917178.    1.         0.       19
1641220   0         19701808. 925262.    925262.    1.         0.       20
1641221   0         19697062. 932688.    932688.    1.         0.       21
1641222   0         19692292. 939350.    939350.    1.         0.       22
1641223   0         19687502. 945136.    945136.    1.         0.       23
1641224   0         19682696. 949956.    949956.    1.         0.       24
1641225   0         19677884. 953738.    953738.    1.         0.       25
1641226   0         19663140. 953816.    953816.    1.         0.       26
1641227   0         19632286. 953873.    953873.    1.         0.       27
```

```
*HYDRO    VEL/FLW
1641300   0
*HYDRO    F_FLW     G_FLW     J_FLW     JUNC
1641301   2.25229   2.25229   0.        1  * 613.234
1641302   10.74794  10.74794  0.        2  * 613.234
1641303   10.8341   10.8341   0.        3  * 613.234
1641304   10.8445   10.8445   0.        4  * 613.234
1641305   10.85716  10.85716  0.        5  * 613.234
1641306   10.92158  10.92158  0.        6  * 613.234
1641307   10.99875  10.99875  0.        7  * 613.234
1641308   11.09102  11.09102  0.        8  * 613.234
1641309   11.19703  11.19703  0.        9  * 613.234
1641310   11.3152   11.3152   0.        10 * 613.234
1641311   11.44223  11.44223  0.        11 * 613.234
1641312   11.57749  11.57749  0.        12 * 613.234
1641313   11.71923  11.71923  0.        13 * 613.234
1641314   11.8647   11.8647   0.        14 * 613.234
1641315   12.01137  12.01137  0.        15 * 613.234
1641316   12.15812  12.15812  0.        16 * 613.234
1641317   12.30247  12.30247  0.        17 * 613.234
1641318   12.44098  12.44098  0.        18 * 613.234
1641319   12.57333  12.57333  0.        19 * 613.234
1641320   12.69755  12.69755  0.        20 * 613.234
1641321   12.81146  12.81146  0.        21 * 613.234
1641322   12.91303  12.91303  0.        22 * 613.234
1641323   13.00167  13.00167  0.        23 * 613.234
1641324   13.07605  13.07605  0.        24 * 613.234
1641325   13.1351   13.1351   0.        25 * 613.234
1641326   13.14546  13.14546  0.        26 * 613.234
*HYDRO    J_DYD     FLD       INTCPT    SLOPE     JUNC
1641401   0.0       0.0       1.0       1.0       26   *
**
*---- ----1---- ----1---- ----1---- ----1---- ----1---- ----1---- ----1---- ----1----
* Bypass flow channel (unheated flow between radial shielding assemblies)
*---- ----1---- ----1---- ----1---- ----1---- ----1---- ----1---- ----1---- ----1----
*hydro    name      type
1650000   bypass    pipe
*HYDRO    VOLS
1650001    6
* because the pressure drop is dominated by form pressure losses at the
* diversion to inter-assembly flow and friction in the flow between assemblie,
* the first two areas listed are arbitrarily chosen to give little resistance
* to flow.  The third area and its form loss coefficient are the significant
* numbers.
*HYDRO    AREA      VOL
1650101   2.00E+0   1     *
1650102   2.00E+0   2     *
1650103   0.3193    6     * total radial shielding inter-assembly flow area
*HYDRO    LEN       VOLS
1650301   0.2        1       * 0.2  m passage through core lower plate
1650302   0.1        2       * 0.1  m expanded area before channels
1650303   0.91       6       * 3.64 m length of radial reflector/shield assy
*HYDRO    VOL       VOLS
1650401   0.0        6
*HYDRO    AZIM      VOLS
1650501   0.0        6
*HYDRO    VERT      VOL
1650601   90.0       6
*HYDRO    ROUGH     Dh        VOL
1650801   45.e-6    0.100       1     * del = 45 um
1650802   45.e-6    0.215       2     * del = 45 um
1650803   45.e-6    0.005635    6     * del = 45 um
*HYDRO    Kf       Kr     jun
1650901   1.0     0.5      1
1650902  30.0    30.0      2
1650903   0.0     0.0      5
*HYDRO    TLPVBFE   VOL
1651001     11000    6
*HYDRO    JEFVCAHS  JUNC
1651101     000000   5
*HYDRO    EBT       PRES      TEMP      0.0       0.0       0.0     VOLS
```

```
1651201   0          20026974. 809341.   809341.   1.        0.      1
1651202   0          20026576. 809339.   809339.   1.        0.      2
1651203   0          19770940. 808167.   808167.   1.        0.      3
1651204   0          19726178. 808180.   808180.   1.        0.      4
1651205   0          19681298. 808192.   808192.   1.        0.      5
1651206   0          19636326. 808205.   808205.   1.        0.      6
*HYDRO    VEL/FLW
1651300   0
*HYDRO    F_FLW      G_FLW     J_FLW     JUNC
1651301   1.6793     1.6793    0.        1  * 457.23
1651302   10.5188    10.5188   0.        2  * 457.23
1651303   10.62672   10.62672  0.        3  * 457.23
1651304   10.64932   10.64932  0.        4  * 457.23
1651305   10.67209   10.67209  0.        5  * 457.23
*HYDRO    J_DYD      FLD       INTCPT    SLOPE     JUNC
1651401   0.0        0.0       1.0       1.0        5   *
```

Appendix B

Homologous Head and Torque for Pump Models used to Represent Compressors

Definition of terms

$$\alpha = \frac{\omega}{\omega_R}$$

$$v = \frac{Q}{Q_R}$$

Q = pump volumetric flow rate (m^3/s)

ω = pump speed (rad/s)

R = rated condition

The homologous head and torque curves are given on the following two pages for the pump representation of the recompressing and main compressors. Each segment of a curve has a three-letter designation (e.g. HAD) These three letters indicate the type of curve, the denominator of the variables on the axes and which quadrant on a four-quadrant head or torque curve the pump is operating in.

First Letter (Curve Type)

H = head curve
B = torque curve

Second Letter (Denominator)

A = denominator is α or α^2
V = denominator is v or v^2

Third Letter (Operation Mode)

N = normal pump operation ($\omega > 0$ and $Q > 0$)
D = dissipation ($\omega > 0$ and $Q < 0$)
R = reverse pump ($\omega < 0$ and $Q > 0$)
T = normal turbine ($\omega < 0$ and $Q < 0$)

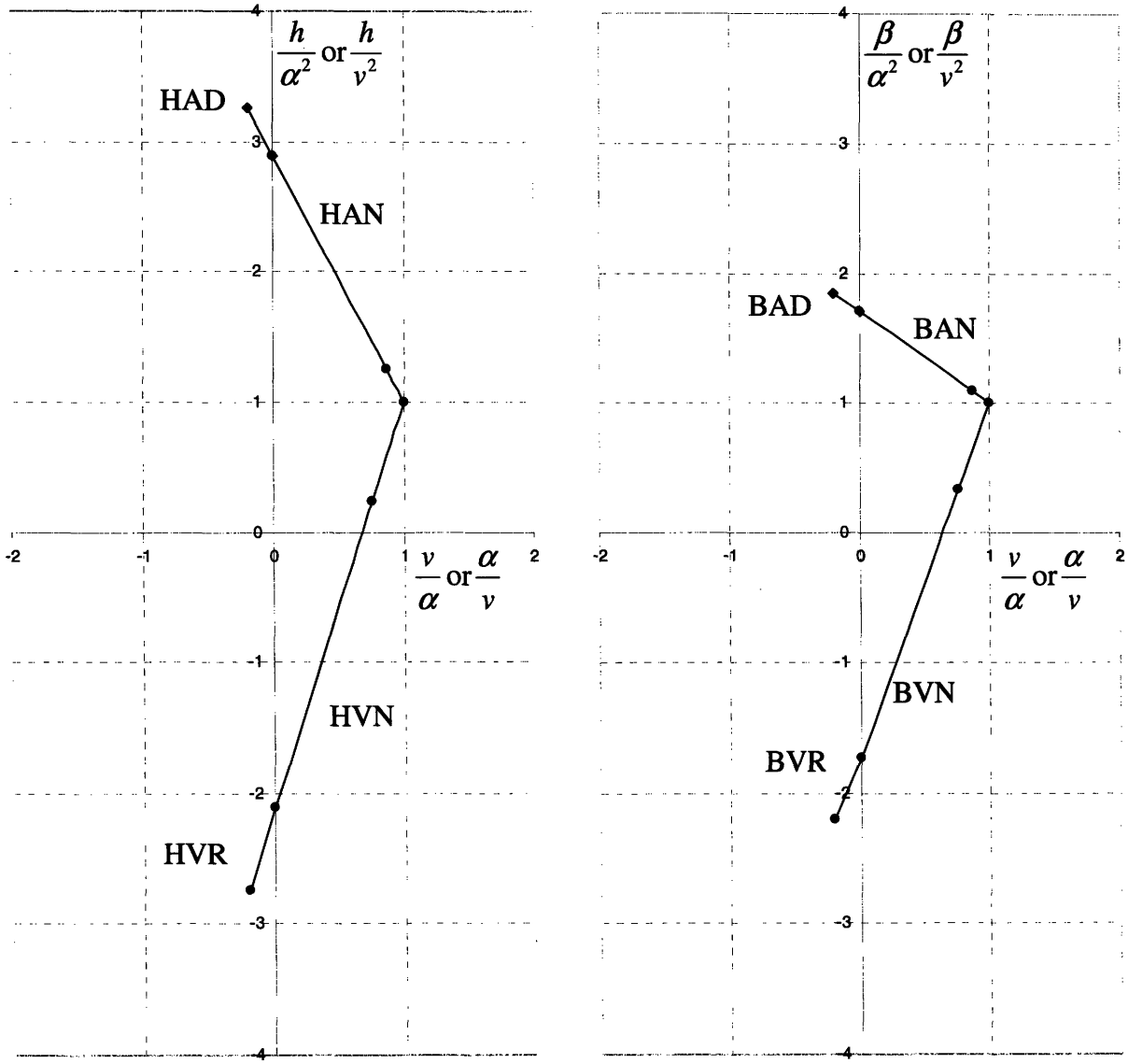

Figure B1. Homologous head (left) and torque (right) curves for pumps representing recompressing compressors.

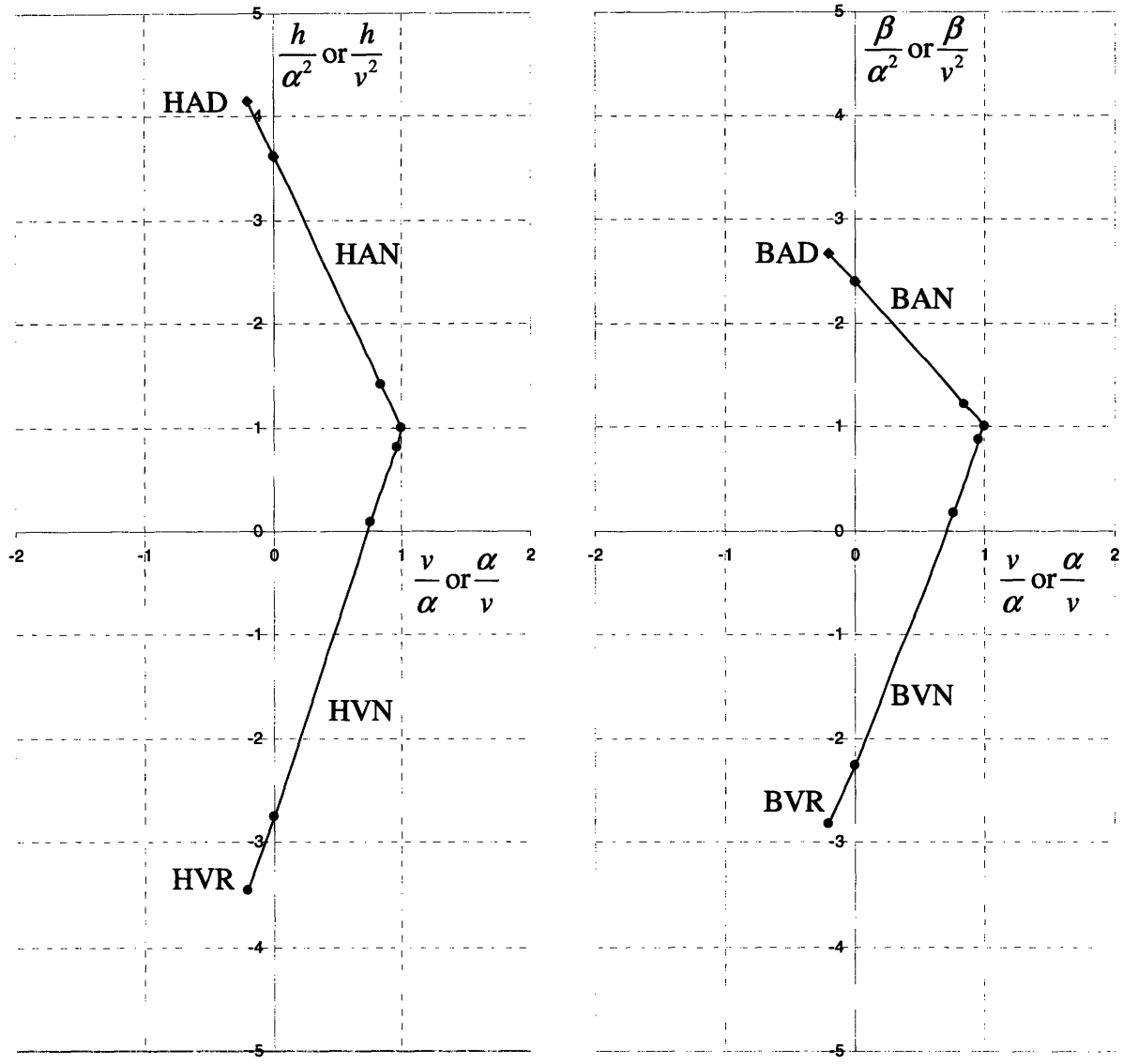

Figure B2. Homologous head (left) and torque (right) curves for pumps representing main compressors.

Appendix C

Proposed manufacturing sequence for the TID assembly.

The first step (see Fig. C1) is to assemble all individual fuel rods by sliding hexnut pellets of fuel or reflector material onto the individual flow tubes. A fitting is welded to the bottom of each tube before assembly. Steel rods are inserted into the flow tubes to stiffen them during the pellet addition process and to hold them in a vertical position: e.g. by inserting the bottom of these support rods into a "flowerholder" block. A loose fitting axial trough aligns the hexnut stack.

The second step is to move the assembled rods, one-by-one, over and into the hexagonal bottom assembly grid plate: a metal puck perforated by a triangular array of holes sized to accommodate the bottom fitting on each flow tube. The fuel rods are loaded progressively down each row of holes, moving from one side of the grid plate to the other. Fission product vent tubes are pre-positioned at, and welded into, the six outer corners of the hexagonal grid plate to help maintain alignment in the assembly process.

Once all of the bundle is in place the tubes are e-beam welded to the grid plate from underneath, with the bundle held in the vertical position.

The next step is to slide the loose-fitting stack holdown plate over the top of the flow tubes, followed by spacer springs over (for example, six) selected flow tubes. The top grid plate is then added and all flow tubes e-beam welded to it, in the same manner as was done for the bottom grid, but this time vertically from above.

The final step is to slide the hexagonal assembly duct up over the fuel bundle and weld it to the bottom and top assembly grid plates. Note that the bottom of the duct contains an end-fitting configured to act as a lower plenum and is necked-down to fit into the bottom core grid plate (this could be pre-attached to the duct, or added later).

When assembly is complete, the channel stiffener rods are removed.

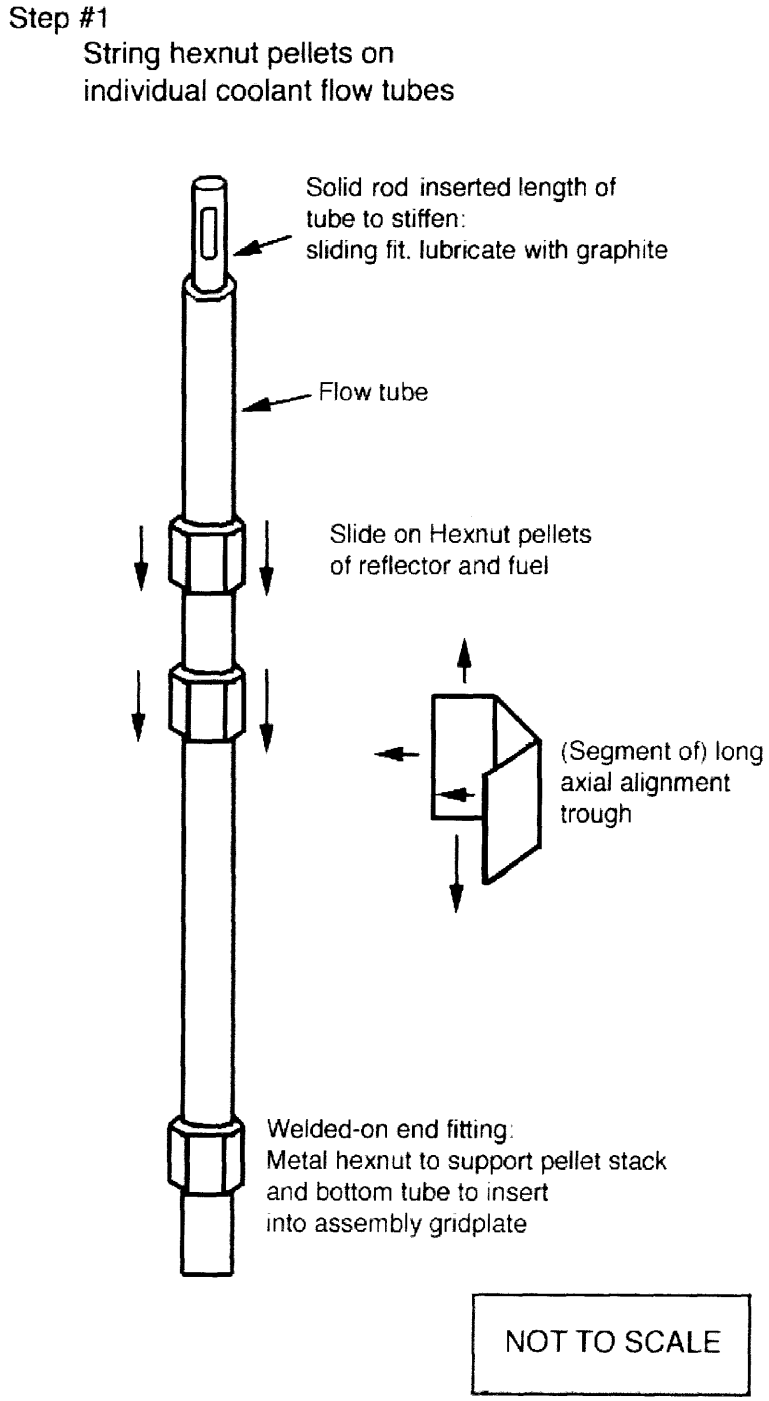

Figure C1. Manufacturing Sequence for TID Assembly using "Hexnut" Fuel Pellets.